Cranfield University

Birute Bunkute

Burning Velocities of Coal-derived Syngas Mixtures

School of Engineering

PhD Thesis

Cranfield University
School of Engineering

Ph.D. Thesis

2008

B. Bunkute

Burning Velocities of Coal-derived Syngas Mixtures

Supervisor: Prof J. B. Moss

January 2008

This thesis is submitted in partial fulfilment of the requirements for the Degree of Doctor of Philosophy.

Summary

Integrated gasification combined cycle (IGCC) systems, which utilize coal, petroleum coke, heavy oil, biomass and waste materials as a feedstock, continue to enter the power generation market. The gasification products from gasifiers using these feedstocks are mixtures of hydrogen, carbon monoxide and inerts like nitrogen, carbon dioxide and water. These mixtures are then used as a fuel in low-emission power generation applications. Unlike natural gas or methane, which has been widely used and researched for many years, these mixtures have not been widely investigated. Thus the aim of this study is to provide data on the combustion properties of syngas mixtures, mainly focusing on laminar burning velocities and critical strain rates to extinction. These combustion properties data are essential for gas turbine combustor modelling using turbulent burning velocity closure models.

The establishment of such a database in this study mainly relies on numerical computations. Therefore, the experimental campaign was limited to investigation of several $CO/H_2/N_2$ fuel mixtures fuel mixtures at different equivalence ratios and operating conditions. The laminar burning velocity values, obtained from the experimental campaign were used mainly for validation of the chemical kinetics model and reaction mechanism.

The principal outcome from this study is that at ambient conditions and reactant preheat temperatures up to 400K experimental laminar burning velocity values compare well with numerical predictions. The laminar burning velocity tests at high pressure presented a number of complications due to the formation of cellular flames and the flow in the

burner tube entering the transitional laminar to turbulent regime. As a result the numerical model could not be fully validated experimentally for high pressure conditions.

A comprehensive combustion properties database has been created using numerical simulations, based on comprehensive descriptions of the chemical kinetics and extensions using neural networks.

CFD simulations of reacting flows in a practical combustor geometry demonstrated the importance of obtaining accurate laminar burning velocities and critical strain rates to extinction data.

Acknowledgements

Here I would want to thank people and organisations without whom I would not have written this thesis.
Prof. J.B. Moss for giving an opportunity to do my PhD studies, his guidance and help during my research and writing up the thesis.
Mr. Dick Kennewel for his help in setting up the test rig and spending long hours with me in the lab during experiments.
Dr Les Oswald for his support and help in resolving numerous issues with High Performance Computing and Fluent.
Miss Delia Alana Richardson and Mr. Gautam Pulugundla for their support during past couple of months and proof reading my thesis.

My mother Vanda, sisters Ruta and Eglute and brother Valdemaras for their support and encouragement during all time of my studies. My uncle Kazimieras for his encouragement to study engineering.

I also would want to thank my friends Jimmy McIntosh, Fernando Colmenares Quintero, Josue Gomez Parada and many others for your friendship and support during these three years. I also would want to thank Roy Chamberlain for your support and help during my last year at Cranfield by letting me to work as your assistant in the Fitness Centre.

This project was funded by British Coal Utilisation Research Association (BCURA) and carried out with cooperation with Alstom Power.

Thank you very much to all of you!

Table of contents

List of figures

List of tables

Nomenclature

Latin letters

Capital letters

0D	zero dimensional
1D	one dimensional
A	cross section area of the stream tube surrounding the flame
A_{flame}	flame surface area
C_i	concentration of combustible component
D	diameter
F	transfer function of ANN
G	stretch factor
K	flame stretch rate
K_g	gas species
L	nozzle separation length
L_f	flammability limits
L_i	flammability limit of combustible component
N	number of moles
P	pressure
R	universal gas constant
R_f	flame radius
S_b	flame velocity (burnt side)
S_c	reaction progress source term
S_{lam}	laminar burning velocity
S_s	initial spherical flame propagation
T	temperature (K)
U	internal volume
V	mole fraction
V_k	diffusional velocity of the k species
$\overline{W}$	mean molecular weight of the mixture
W_k	molecular weight of the k species
Y_k	mass fraction of the k species
Z	weighted sum of the input

Small letters

b	bias of ANN
c	mean reaction progress variable
c_p	heat capacity (constant pressure)

c_{pk}	heat capacity of k species (constant pressure)
f	focal length of the Schlieren mirror
g_{cr}	critical strain rate
h_k	specific enthalpy of the k species
l_r	reaction zone thickness
l_t	turbulence length scale
$\dot{m}$	mass flow rate
m_{fr}	mixture fraction
n	unit vector of the surface
r_e	final soap bubble radius
r_o	initial soap bubble radius
t	time
u’	root-mean-square turbulence velocity
v	flame motion velocity
v_u	reactants stream velocity
w	scalar weight of ANN
x	spatial coordinate
x_{ki}	scalar input of ANN

Greek letters

α	thermal diffusivity of the unburnt reactants
α_d	density ratio
β	flame half cone angle
χ	Thermal diffusivity
χ_{O2}	O_2 mole fraction
ε	turbulence dissipation rate
ε_{cr}	turbulence dissipation rate at the critical strain rate
ϕ	equivalence ratio
λ	thermal conductivity of the mixture
η	Kolmogorov length scale
μ_{str}	a constant in the flame stretch model
μ_t	turbulent viscosity
θ	apex angle
ρ	mass density
σ	standard deviation of the distribution of the turbulence
τ_c	chemical time scale
τ_t	turbulence time scale
$\dot{\omega}$	molar rate of production by chemical reaction of the k species per unit volume

$\tilde{\xi}$	mean mixture fraction
$\tilde{\xi}^2$	mixture fraction variance
ψ	learning rate of ANN

Symbols

Over bars

$\overline{()}$	Reynolds average
$\tilde{()}$	Favre average

Subscripts

A	related to air
b	related to burnt
u	related to unburnt
D	related to preheat zone
R	related to reaction zone
mix	related to mixture
t	related to tangential component
i	related to i^{th} component

Dimensionless Groups

Ka	Karlovitz number
Le	Lewis number
Re	Reynolds number
Sc_t	turbulent Schmidt number

Abbreviations

AFR	air to fuel ratio
ANN	artificial neural network
HHV	higher heating value
LHV	lower heating value
RMSE	Root Mean Squared Error
SSE	Sum of Squares due to Error
TFC	turbulent flame speed closure

1 Introduction

1.1 Overview

Integrated gasification combined cycle (IGCC) systems continue to penetrate the power generation market and there are now a number of IGCC projects in design, construction or operation around the world. In principle, coal, petroleum coke, heavy oil, biomass and waste materials can be employed as a feedstock in these cycles. The gasification products from these feedstocks are mixtures of mainly hydrogen and carbon monoxide, with inert gases (nitrogen, carbon dioxide and water). These mixtures are employed as a fuel in low-emission power generation applications. Unlike natural gas or methane, which has been used over many years and for which much combustion data are collected, these gaseous fuel mixtures have not been widely investigated.

The design of stable low NO_x emission, lean-burning combustion systems is a challenge, even for natural gas. The combustion developments for syngas mixtures, with its variations in composition, water content, temperature and calorific value, depending on the gasification process, are very complex and challenging.

The present study addresses the combustion aspects of medium calorific value syngas from a fundamental point of view. The main focus in this work is on the premixed combustion of carbon monoxide, hydrogen and diluent mixtures involving investigations on laminar burning velocity and flame structure. Of the many combustion characteristics the major ones are the laminar burning velocity, flammability limits, autoignition delay and temperature and critical strain rate to extinction. Out of these the most important property is the laminar burning velocity, which is

applied in the modelling of engines, the design of combustors and burners and the design and validation of chemical kinetic schemes. Especially for syngas combustion the knowledge of flame structure and burning velocity is essential for maintaining a stable flame. Since the diffusion coefficient of hydrogen is very high in comparison to other syngas fuel components, it is interesting to investigate the flame structures. These mixtures are susceptible to irregularities through cellular flame formation due to preferential diffusion effects. The following section presents a brief background of the concepts required for further reading.

1.2 Background

1.2.1 Flame Structure

A flame can be described as a reaction zone that travels in the gas holding it. This term is usually used to describe fast exothermic reactions which are often accompanied by the emission of light. Flames may be either stationary, stabilised on a burner (propagating into gas flow from a burner) or freely propagating flames, which travel in an initially quiescent reactant mixture.

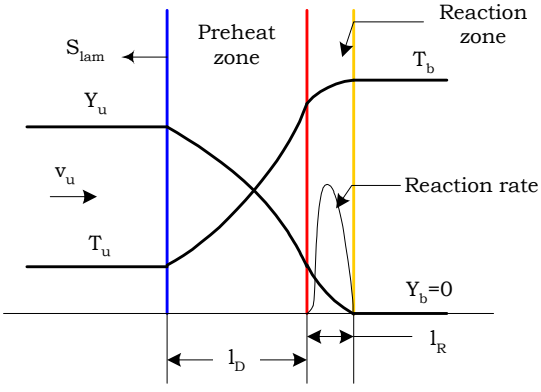

Figure 1.1: Flame structure of 1D freely propagating planar premixed flame

Figure 1.1 shows the steady propagation of a planar flame into a combustible mixture with velocity S_{lam}. The upstream mixture approaches the flame with velocity $v_u = S_{lam}$ and temperature T_u and leaves the reaction zone with velocity $v_b=S_b$ and temperature T_b. S_{lam} and S_b are velocities of the flame with respect to unburnt and burnt gases, which are assumed to be equal at ambient pressure.

The flame front consists of two zones: the preheat zone and the reaction zone. The preheat zone is dominated by heat diffusion and mass diffusion of the reactants and the reaction zone is dominated by chemical reaction and mass diffusion. In the preheat zone the reactants approaches the flame, gradually heats up by the heat transferred from the chemical heat release in the reaction zone. The temperature continuously increases from T_u to T_b. The temperature profile is not linear due to the presence of the convective transport. The continuous heating of the reactants will eventually lead to its ignition and subsequent reaction.

1.2.2 Definitions

The premixed flame has a defined adiabatic flame temperature and laminar burning velocity. The latter may be defined as the plane flame front velocity normal to itself and relative to the unburned reactant mixture.

In addition, premixed flames can only be obtained if the fuel and oxidiser mixture lies between certain composition limits called the limits of flammability. All these definitions are discussed in following sections.

The definition of artificial neural network (ANN) is given as well because ANN was used as a method to predict correlations for laminar burning velocities, critical strain rates to extinction and autoignition delays

as a function of temperature, pressure, equivalence ration and mixture composition for syngas mixtures.

1.2.2.1 Flame temperature

The adiabatic flame temperature is the temperature of the gases leaving the reaction zone. For the premixed flame, the adiabatic flame temperature can be calculated from the thermodynamic properties of the reactant mixture because the reactant mixture composition is well defined and reactants enter the flame at a fixed temperature and pressure. For stoichiometric mixtures of most fuels with air, the adiabatic flame temperature is about 2000 – 2200K. Near the flammability limits, the flame temperature is lower; it is only about 1400 – 1500K.

1.2.2.2 Laminar burning velocity of a premixed flame

Laminar burning velocity is defined as the velocity with which a planar flame front in a 1D flow system moves normal to its surface through the unburned gas. It is also the volume of combustible mixture consumed in a unit of time by the unit of area of the flame front. Laminar burning velocity is independent of flame geometry, burner size and flow rate; it is fundamentally a measure of the overall reaction rate of the flame. The laminar burning velocity is affected by flame radiation and flame temperature, and by local gas properties such as thermal conductivity, viscosity and diffusion coefficient. It can also be varied by changing such variables as pressure, temperature, equivalence ratio and mixture fuel composition.

However, even if its theoretical definition is straightforward, it is difficult to measure. Therefore, there are considerable differences between the results obtained by the various experimental methods. The main

problem of the laminar burning velocity is that it is very difficult practically to obtain a plane flame front. In all practical cases, the flame front is curved or it is not normal to the direction of the reactant stream.

There are two types of measurements of laminar burning velocity; one employs flames travelling through stagnant mixtures, the other uses flames which are held stationary by a counter flow of unburned reactant mixture [1]. These methods will be presented later.

1.2.2.3 Flammability limits

If small amounts of combustible fuel are added gradually to an oxidiser, a point will be reached at which the mixture becomes flammable. The fraction of fuel at the point is called the lower or lean flammability limit. If more fuel is added another point will be reached at which the reactant mixture will no longer burn. This point is called upper or rich flammability limit. The flammability range can be widened by increasing the unburned reactant temperature and operating pressure. The rich end of the flammability region is mainly affected.

One might expect the burning velocity to fall to zero at the flammability limit, but the limiting burning velocity is found to be finite at around 3 to 5 cm/s [1].

1.2.2.4 Ignition

There are two types of ignition: homogenous ignition and point ignition. The homogenous ignition is the ignition when it occurs simultaneously through the reactant volume without any external source of energy. If the temperature of the flammable mixture in the vessel is raised up to the level required to supply the activation energy needed for the reactions to initiate, homogeneous ignition will occur. This

phenomenon is also called self-ignition or auto-ignition. The criterion for the auto-ignition is the net rate of the heat loss or gain in a given volume of the reactants. If the heat production rate released by chemical reactions is greater than a heat loss then the chemical reactions will accelerate and the mixture will self-ignite.

The auto-ignition phenomenon is widely investigated because it is associated with spark ignition engine knocking. In the spark ignition engine, when the flame travels across the combustion space, the pressure and temperature increases in the unburned gas. Under certain conditions the rapid reactions are initiated within the unburned gas leading to a very rapid combustion through the volume. This rapid combustion is accompanied with a rapid pressure rise, which creates sound of engine knock. Knock is an undesirable phenomenon in the engine. In compression-ignition or diesel engines however, by design, autoignition is employed to initiate the combustion process [2].

As it was mentioned earlier, premixed combustion technology is widely employed in gas turbines, which operate under high pressure and temperature conditions. One of the major concerns of this technology is avoiding the autoignition phenomenon in the fuel/air mixture prior to combustion to protect the engine components and to limit pollutant emission levels.

The auto-ignition is described by two criteria: autoignition delay and temperature. Autoignition delay is the time required for formation of sufficient concentrations of intermediate radicals, which initiate rapid oxidation reactions. The autoignition temperature is the lowest temperature at which the mixture will spontaneously ignite without an

external source of energy. This temperature is needed to supply the activation energy for chain propagation reactions.

In the instantaneous point ignition case the flame develops from the high temperature ignition source (spark) and then spreads through the reactant volume.

1.2.2.5 Flame stretch

In practical combustion systems flames do not have the ideal planar configuration. Instead they are wrinkled and in most cases also unsteady. In addition, flames also exist in flow fields, which are non-uniform. Therefore it is expected that flame characteristics, like laminar burning velocity and flame thickness, are affected by these so-called stretch effects.

Flame stretch is considered to be a combined effect of flame curvature, flame motion and flow non-uniformity [3, 4]. The concept of flame stretch was proposed by Karlovitz et al. [5]. They define flame stretch at any point of the flame surface through the change of the flame area of an infinitesimal element of flame surface:

$$K = \frac{1}{A}\frac{dA}{dt} \qquad \textbf{(1.1)}$$

where the surface boundary is moving tangentially in respect to the surface of the local tangential component of the fluid velocity [6].

In respect to flow variables, it can be shown that:

$$K = \left|\nabla_t v_t + (v \cdot n)(\nabla \cdot n)\right|_s \qquad \textbf{(1.2)}$$

where ∇_t and v_t are the tangential components of ∇ and v evaluated at the surface; n is the unit vector of the surface, pointed in the direction of the unburned gas. The unit of the stretch rate K is sec^{-1}.

There are two stretch sources represented in the equation above. The first ($\nabla_t v_t$) is the influence of flow non-uniformity along the flame surface. The second, is the stretch, experienced through the flame motion (velocity v) and flame curvature ($\nabla \cdot n$). From this equation it is evident that flame curvature contributes to stretch, if it is moving ($V \neq 0$) and flame propagation contributes to the stretch if the flame is curved [6]. Therefore, stationary spherical flames and propagating planar flames are unstretched. On the other hand, the flow field strain can contribute to stretch even if the flame is stationary and not curved.

For common flame configurations flame stretch rate can be computed using the following equations:

a) Bunsen burner flame:

$$K = -\frac{u_\infty \sin\theta}{2R_f} \quad \textbf{(1.3)}$$

where, u_∞ is the uniform upstream velocity, θ is the apex angle and R_f is flame radius at a given axial cross section [6].

b) Opposed-flow planar flame [7]:

$$K = \frac{2v_1}{L}\left(1 + \left(\rho_1 v_1^2 / \rho_2 v_2^2\right)^{1/2}\right) \quad \textbf{(1.4)}$$

where L is the nozzle separation length, and v_1 and ρ_1 are the exit velocity and density for nozzle i and the subscripts 1 and 2 refer to arbitrary choices of the opposed jet nozzles. When the momentum flux of the two jets is equal (two premixed fuel-air jets configuration), the equation reduces to $4v_1/L$.

c) Outwardly propagating spherical flame [6]:

$$K = \frac{2}{R_f}\frac{dR_f}{dt} \quad \textbf{(1.5)}$$

where R_f is the instantaneous flame radius

These equations are valid if flames are assumed to be infinitely thin.

The stretch rate can be non-dimensionalised by the characteristic flow time within the flame:

$$Ka = \left(\frac{l_r}{S_{lam}} \right) K \qquad \textbf{(1.6)}$$

Here l_r is the reaction zone thickness and S_{lam} is the laminar burning velocity.

In addition to the mentioned effects, the flame can be subjected to stretch, caused by preferential diffusion. For mixtures with Le>1, an increase in the stretch rate would reduce the flame temperature and consequently, the laminar burning velocity. Flames for mixtures with Le<1 will experience opposite effects of stretching [4].

Another important characteristic of the flame is the critical strain (stretch) rate to extinction.

The critical strain rate to extinction can be defined as the flow velocity corresponding to the state beyond which the flame would extinguish with a slight increase in flow rate [8].

1.2.2.6 Artificial neural network

Artificial neural networks (ANNs) are powerful modelling tools that are analogous to the behaviour of biological neural structures. They have an ability to identify relationships from given input and output data, rather than by describing them analytically.

ANNs consist of simple elements (neurons), which operate in parallel. As in nature, the network function is determined by the connections

between neurons. A neural network can be trained to perform a particular task by adjusting the values of the weights between neurons.

Normally ANNs are trained in a way, in which a particular input leads to a specific target. ANN is adjusted, based on a comparison of the network output and target until the difference between those is zero or within the value of acceptable error. Usually many such input/target pairs are used to train the network. This type of training is called supervised training [11].

ANNs can handle tasks involving incomplete data sets, fuzzy or incomplete information, highly complex and poorly defined problems, where humans would usually make decisions intuitively. ANNs are also able to handle noisy data. [9, 10]

ANNs have been applied successfully in various fields including aerospace, business, automotive, banking, industrial, manufacturing, robotics and telecommunications fields.

ANNs are categorized by their architecture (number of layers), topology (feedforward or recurrent, etc.) and learning algorithm. A multilayered feedforward ANN with back-propagation learning is widely used in the above mentioned applications [9-11].

A feedforward, back-propagation artificial neural network was chosen to correlate the mixture combustion properties with temperature, pressure, mixture strength and composition. This network is most common and widely employed for function approximation problems and is easy to implement.

1.3 Motivation for the present work

Motivation for the present investigation comes from the fact that there are limited data available on laminar burning velocities for carbon

monoxide hydrogen mixtures and particularly for coal-derived syngas. In addition, most of the available data are at ambient pressure and temperature. The aim of present study is to produce a database of laminar burning velocities of CO/H_2/Diluents fuel mixtures at various mixture compositions, equivalence ratios, temperatures and pressures.

1.4 Specific objectives

The specific objectives of the research are threefold:

1. To establish a database of combustion properties – notably, laminar burning velocity, ignition delay and critical strain rate to extinction – for syngas fuel mixtures, representative of gasified coal at conditions relevant to the gas turbine.
2. To combine measurement and numerical simulation such that a robust methodology can be identified which both validates results obtained under common conditions and permits their prediction for mixtures and conditions that are not accessible experimentally.
3. To demonstrate their application in a representative gas turbine combustor simulation.

1.5 Structure of the thesis

The thesis is organized in eight chapters, which describes the conducted research. The next chapter gives a brief literature review on the laminar burning velocities of single fuels and multi-component fuel mixtures and their measurement techniques and computational methods. In this chapter other combustion properties like flammability limits, critical strain rate to extinction and autoignition parameters are also discussed. Chapter 3 lays out the details of the experimental setup of the

Bunsen burner, which was employed to measure the laminar burning velocities for several syngas mixtures under high temperatures and pressures. Chapter 4 discusses experimental and numerical methodologies adopted to gather required data for the combustion properties database. Chapter 5 presents results from the Bunsen burner experiments for lean flames of several $CO/H_2/N_2$ fuel mixtures at reactant preheat temperatures up to 600K and pressures up to 7bar. This chapter also presents a comparison of experimental and computational results of laminar burning velocities for fuel mixtures investigated experimentally. Chapter 6 discusses the results obtained using computational methods for laminar burning velocities for various $CO/H_2/CH_4$/Diluents mixtures for a wide range of temperatures and pressures. This chapter also presents computations of critical strain rates to extinction and autoignition delays for various $CO/H_2/N_2$ mixtures. The effects of the different parameters, like fuel mixture composition, operating conditions and mixture strength on the combustion parameters are discussed in this chapter. Chapter 7 presents simulations of the real combustor fuelled with methane and several $CO/H_2/N_2$ mixtures. The first part of this chapter covers the theory of turbulent flame speed closure (TFC) model and the application of the laminar burning velocity and critical strain rate to extinction data. In the second part the results of the combustor simulations and demonstration of combustion properties data implementation and comparison with reference fuel (methane) are presented. The thesis finishes with Chapter 8, where conclusions and discussion on the scope for future work are presented.

2 Literature study

Among the combustion characteristics of premixed gaseous fuel/air mixtures the laminar burning velocity is generally the most significant one, although other combustion characteristics such as flammability limits, extinction strain rates and auto-ignition temperature may be important in some situations.

Firstly a literature review on the composition of syngas, obtained from various gasifiers, is presented. It is followed by a comprehensive review of experimental techniques for laminar burning velocity measurement, computational methods for laminar burning velocity determination and flame structure investigation, and data on laminar burning velocities. A brief review on flammability limits, critical strain rates to extinction and autoignition delays is presented towards the end of this chapter.

2.1 Syngas compositions from gasifiers

Gasifiers are often classified into three main categories depending on their characteristics: moving-bed, fluid-bed and entrained-flow [178, 179]. The more detailed information on gas compositions for these processes along with information on several IGCC plants around the world and their gas compositions is given in Appendix A.

Figure 2.1 shows that H_2 and CO compositions from gasifiers vary and do not lie in a specific range for any particular category. Some technologies, like moving bed gasifiers, are more feedstock specific: anthracite and coke are preferred. Therefore, the composition range for this category of technologies does not vary very significantly.

Fluid-bed technologies are more suitable for reactive feedstock gasification, such as low-rank coals or biomass (due to temperature restrictions). But new developments, able to operate at higher temperatures, are available and for this reason the fluid-bed gasifiers are more flexible with regard to feedstock.

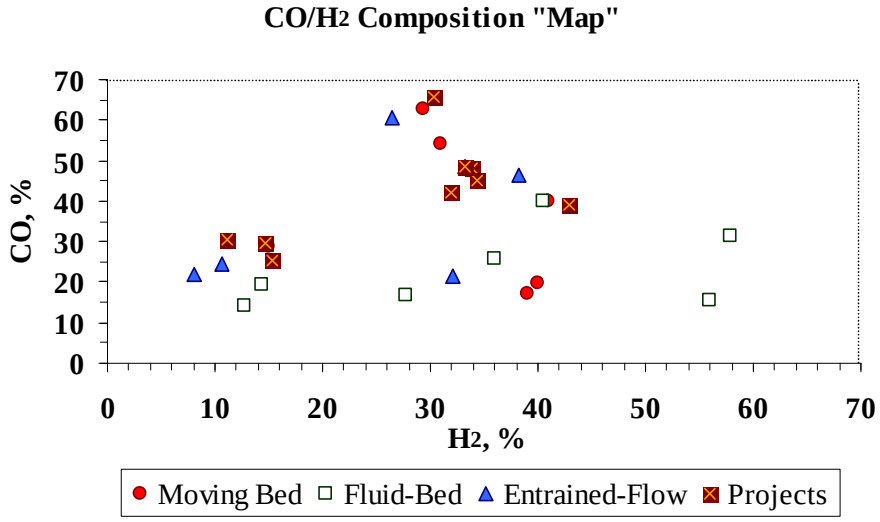

Figure 2.1: H_2/CO Composition "Map" for gasification technologies and existing projects

All gasification technologies can be classified into two major groups based on the gasification blast used: steam/air gasification and steam/oxygen gasification. The gas composition from these processes varies depending on the blast used (air or oxygen). If air is used for gasification, considerable amounts of nitrogen are present in the gas and it has a low calorific value, see Figure 2.2. If oxygen and steam are used for gasification, the amounts of nitrogen are very small and the calorific value of the gas is much greater. For processes using oxygen, the expensive oxygen separation plant should be included in any economic analysis.

In some entrained flow gasifiers inert gas, mainly nitrogen, which is a by-product from the oxygen separation plant, is used as the coal particle carrier. For this reason higher amounts of nitrogen can also be present in the gas.

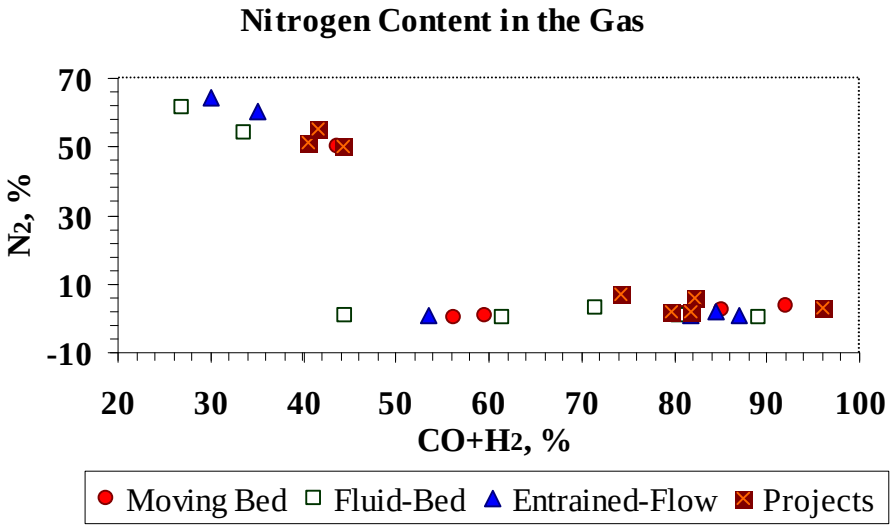

Figure 2.2: Nitrogen content in the gas for gasification technologies and existing projects

Having established a broad basis for describing the product gases, reflecting the gasification technology employed, the combustion implications of such components will now be considered.

2.2 Combustion Characteristics of Mixtures

2.2.1 Laminar burning velocity

Laminar burning velocity is the measure of burning rate of a reactant mixture. It is an intrinsic combustion property of gaseous fuel-air mixtures.

Over several decades researchers have attempted to determine laminar burning velocity experimentally and computationally. They have

used various experimental techniques to perform measurements and a number of models with varying chemical kinetics mechanisms to compute it. In this section selected literature on various laminar burning velocity measurement techniques is presented.

2.2.1.1 Bunsen burner method

Bunsen burner flames have been extensively investigated for laminar burning velocity measurements and flame studies for over 50 years now. Most of the laminar burning velocity data available in the literature prior to 1970 were obtained with Bunsen burner experiments. The main reason for the popularity of this technique is that the Bunsen burner experiment is relatively simple and inexpensive and it produces reasonable results. The method involves establishing laminar flow in a tube and stabilising a stationary flame on the top of the burner by adjusting the flow velocity of the combustible gases.

Very early literature sources on Bunsen burner flames report laminar burning velocity measurements of various single fuel mixtures performed using Schlieren, shadowgraph or direct photography to obtain images of flame geometry. Only since the early 80s has the Bunsen burner method been widely used to investigate the formation of polyhedral flames (their mathematical analysis and stretch analysis) [12-21] and open-tip flame formation [22]. This method also permits flame stability analysis to establish the stable flame region between flashback and blowout [23].

Literature sources indicate however that, given the occurrence of various complex phenomena like preferential diffusion, flame stretch, heat loss and rim aerodynamics, laminar burning velocity measurement by the Bunsen burner technique is not free of error. The clear advantage of this technique is that it is very straightforward and simple to construct and

therefore it was chosen for laminar burning velocity measurement of syngas fuels in the present study where a wide range of conditions is to be investigated.

2.2.1.2 Flat Flame Method

This method provides a close approximation to the ideal 1D flat flame, but is limited to low burning velocities. In this setup the flow is maintained laminar, but not fully developed in the main burner tube. The flame is then stabilised on a perforated plate or wire gauze by setting up a system of vortices on the flame rim. The flame has the shape of a disk with slightly curled edges. Laminar burning velocity is computed by the dividing volumetric flow rate of the mixture by flame area. Since the flow rates can by measured accurately, the accuracy of method depends on the accuracy of flame area measurement.

The sources of inaccuracies in this method are due to some unburned gas escaping at the flame edges, resulting in estimation of lower laminar burning velocity in comparison to the actual one. Due to mixing and cooling by the surrounding nitrogen the exact position of the flame edge is uncertain. In addition, the heat loss from the flame and associated heating of the stabilising matrix makes the method unreliable: flame is non-adiabatic (due to heat loss) therefore the estimated laminar burning velocity will be lower; on another hand, the pre-heating of the unburned mixture will result in rise of the laminar burning velocity. This method can by refined by making provision for quantifying the heat loss from the flame to the perforated burner plate and controlling the heating of the unburned fuel-air mixture. These flames are essentially stretch free due to absence of tangential velocity gradients, because the flame is planar. This burner

arrangement is called the adiabatic burner and the laminar burning velocity measurement method is called the heat flux method [24-26].

2.2.1.3 Flame Propagating in Tubes

The tube method consists of a long cylindrical tube closed at one end and filled with the gas mixture. When ignited, the initially uniform flame travels towards the closed end of the tube. The laminar burning velocity is obtained from uniform velocity during the initial stages of flame propagation S_s and flame front area A_f using the following equation:

$$S_{lam} = \frac{S_s \pi R^2}{A_f} \quad \textbf{(2.1)}$$

here R is the tube radius.

Some investigators claim that if a small hole at the closed end of the tube and a larger one at the open end of the tube are present, the flame movement will be uniform, stable and reproducible. This method was used by many researchers. The laminar burning velocity is calculated from:

$$S_{lam} = \frac{(S_s - v_u)\pi R^2}{A_f} \quad \textbf{(2.2)}$$

Here v_u is the unburnt gas velocity, which is determined from the displacement of a soap bubble formed over the orifice at the unburned-gas end.

Nevertheless, these results are prone to discrepancies because the flame is interacting with the tube wall and its front is deformed and it is also wrinkled. In addition, flame is also self accelerating because of the density change. Thus, the spatial velocity of the flame may increase many times leading to formation of the detonation waves. Actually, the self-accelerating waves were widely studied during the early 70s after the work

of Markstein [101]. It was observed that the use of larger diameter tubes will help to get rid of the serious effects created by the flame-wall interaction, but then the flame-front shape tends to become irregular and difficult to measure. In addition, the laminar burning velocity values differ depending on whether they were obtained from the measurements with the flames propagating upward, downward or horizontally.

2.2.1.4 Spherical flames in a constant volume bomb

This technique is considered to be the powerful method for determining the laminar burning velocity. In this method, a premixed combustible mixture contained in a thick-wall spherical vessel is ignited at the centre. If the differences in concentration and diffusivity between components in the mixture are small enough and the spatial velocity is sufficiently large, the created combustible wave is generally isotropic. The propagation of the flame towards the wall of the vessel is accompanied by the pressure rise and temperature rise associated with it. When pressure and temperature changes are accurately measured along with the position of the flame, this method becomes extremely adaptable. Data on laminar burning velocities for a wide range of pressures and temperatures can be obtained from a single experiment.

This method for the measuring the laminar burning velocities was developed by Lewis et al. [27] and Fiock et al. [28].They developed a methodology for extracting the velocity of the flame relative to the mass movement of the gases in a closed spherical vessel from an analysis of pressure-time record of the detonation. This expression is valid during the early stages of combustion when the pressure rise is small. The laminar burning velocity can be determined during this stage. They compared their experimental results with values obtained from the flame-front movement

and found a very good agreement. Estimation of the flame stretch created by flame curvature can be quantified with help of computational methods. It is proven that the errors involved due to discard of stretch effects are smaller than the experimental uncertainties [29].

2.2.1.5 Freely expanding spherical flames in constant pressure environment

The first derivative of this measurement technique is called the soap bubble method. It was proposed in the early 60s by Price and Potter [30]. Here the combustible mixture is used to blow a spherical bubble around the spark gap in the centre. Assuming that such bubble doesn't resist the gas expansion, ignition of the mixture results in the propagation of a spherical combustion wave at a constant pressure. The flame ball expansion is then recorded with a high speed camera in order to obtain the spatial velocity S_s, which is assumed to remain constant through the flame propagation. The laminar burning velocity can be obtained from the measured or calculated density ratio α_d and the spatial velocity S_s determined from the images using the equation:

$$S_l = \alpha_d S_s \quad \textbf{(2.3)}$$

where $\alpha_d = \rho_u/\rho_b$ with ρ_b and ρ_u – the burnt and unburnt gas densities respectively.

Generally the density ratio can be obtained from the bubble radii as well ($\alpha_d = (r_o/r_e)^3$) where r_o is the initial bubble radius and r_e is the final bubble radius. The accuracy of the method is very sensitive to discrepancies in r_o and r_e measurements. An alternative method of determining density ratio α_d is from thermodynamic calculations.

In order to get accurate measurements a large vessel with optical access is needed. Spherically expanding flame propagations needs to be captured in the early stage when the pressure inside the vessel is not changed yet. The flame stretch due to spherical flame curvature is corrected by obtaining laminar burning velocities at various stretch rates and extrapolating to zero stretch. This method is popular for the global flame structure investigations as well since it can be employed for observing cellular flame formation, depending on the type of the fuel and operating conditions. In addition, many researchers use this technique for investigating the stretch effects on the flame.

2.2.1.6 Counterflow (Stagnation) Flame Method

The counterflow technique for the laminar burning velocity measurement is well known in the combustion community. This technique was proposed by Wu and Law [4]. It includes several arrangements in which the flames are stabilised by the induced aerodynamic strain rate in the flow field. In one of these arrangements the two-dimensional, laminar, steady flame is established in the forward stagnation region of the porous cylinder immersed in a uniform air stream by ejecting fuel-air mixture from the cylinder surface.

One or two planar, steady, nearly one-dimensional laminar flames are established by directing a uniform combustible stream either normally onto a flat plate or counter to an identical combustible stream [31]. The main advantage of such a configuration is that the flame(s) produced is (are) flat and can be arranged to have negligible heat loss. The main difference with the ideal 1D model is that the flames are stabilised by employing aerodynamic strain rate. The burning velocity of this stretched flame can be identified as a propagation velocity of the upstream boundary

of the preheat zone, which corresponds to the minimum value of the velocity profile at the region, see Figure 2.3:.

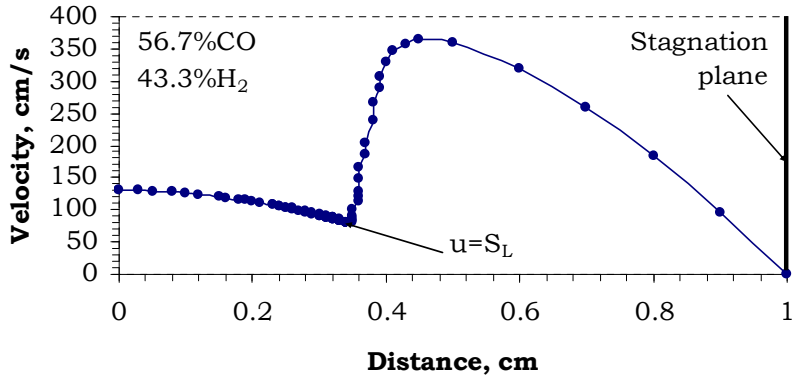

Figure 2.3: Typical axial velocity profile, showing a stagnation flame; SL definition is shown here as well

The set of laminar burning velocities at different strain rates can be determined by varying the free stream velocities. For small values of the stretch (up to 350 s^{-1}), both theory and experiment have shown that the burning velocity varies linearly with stretch [32]. As a result, the unstretched laminar burning velocity can be obtained by linearly extrapolating laminar burning velocities to the zero strain rate. This technique became very popular within the combustion community in recent decades [31-38]. However, the main limitation of the method was that laminar burning velocities could not be measured at pressures higher than 2.5 atm [34]. Most of the laminar burning velocities, reported in the literature, are obtained at ambient conditions.

2.3 Computational methods for determination of laminar burning velocity

Computational simulations are widely used by various researchers for calculating laminar burning velocity as well as investigating flame structure, response of flame to strain, preferential diffusion an other phenomena. There are number of commercial and free-source codes available. The most commonly used commercial codes are CHEMKIN and RUN1DL (COSILAB). These codes assist investigators in understanding the physical phenomenon of the flame propagation.

2.3.1 Numerical codes

Most of the researchers have used their own numerical codes. These codes are mostly one-dimensional due to stiffness of the governing equations, which is introduced through the chemical source terms. Laminar burning velocity can be computed by solving mass, momentum, energy and species conservation equations. The most common methods of solving governing equations are the Euler extrapolation and Newton method.

The most popular one dimensional laminar premixed flame code is PREMIX module in the CHEMKIN package. It was developed by Kee et al [142]. It is a FORTRAN program that computes temperature profiles and species concentrations for freely-propagating and burner stabilized flames. PREMIX uses finite-rate chemistry and molecular transport. This code is applicable for laminar burning velocity computations for variety or fuel-air mixtures with single, binary and multicomponent fuel mixtures.

Another popular CHEMKIN module is OPPDIF. The OPPDIF is derived from the model which was originally developed by Kee et al. [39]. It is a

FORTRAN program that predicts species concentrations and temperature profiles of one dimensional opposed-flow flames, which are stabilised by the impinging separate fuel and oxidiser streams (diffusion flame) or by two premixed streams (two premixed flames). This code can handle single, binary or multicomponent fuel-air mixtures.

Another tool for one-dimensional flame computations is an open-source, object-oriented software, called Cantera. Two one-dimensional steady flame models are available. First one is suitable for flat flame predictions (similar to PREMIX) and another is applicable for axi-symmetric, stagnation-point flow modelling (similar to OPPDIF). Cantera is designed to model CVD or catalysis processes, but it can also be employed for gaseous fuels combustion. Both models use a damped Newton method. If Newton method fails to converge, it is supplemented by time-stepping. The algorithm of Cantera is based on one proposed by Grcar [40, 141].

RUN-1DL is another well known laminar flame code, which was created by Rogg [41]. In this code one-dimensional governing equations are solved for steady and unsteady propagation of the outwardly/planar flames. Researchers have used this model for predicting laminar burning velocities and flame structures for a number of fuel-air mixtures for freely propagating spherical flames [166].

2.3.2 Chemical Kinetic Schemes

There has been a tremendous growth of detailed chemistry knowledge since the late 1970s. The first work on the detailed chemistry in flame simulations was done by Dixon-Lewis [42]. Since then various detailed and reduced mechanisms have been developed. The well known detailed chemical kinetics mechanisms for methane combustion are the following: C1-Mechanism, C1-C3-Mechanism [43], GRI-Mech 2.1, GRI-Mech 3.0 [44].

This is a short-list of a large number of the reaction mechanisms published in the literature. Although the progress in chemical kinetics mechanism developments is significant, the concerns regarding the mechanism performance beyond their range of validity are growing. The main issue of all mechanisms is the comprehensiveness [45]. Chemical reaction rates and pathways are coupled and nonlinear in nature with respect to temperature, pressure and species concentrations. In addition, these parameters can vary locally within the flame structure or globally through the operating conditions of the combustion system. The mechanism can be considered as comprehensive if it can predict accurately the chemical responses over the wide ranges of conditions that are expected to appear. Law et al. [46] demonstrated that mechanisms, which could be considered comprehensive and applied for any operating conditions, do not exist. Authors claim that even mechanisms for hydrogen, which is considered to be simplest fuel, or simple hydrocarbon fuels like methane and benzene, are not sufficiently comprehensive.

One very common method for mechanism validation is to make a comparison between calculated and experimental results of laminar burning velocities of premixed flames. Law et al. [46] compared the predicted laminar burning velocity for hydrogen flames using a kinetic mechanism proposed by Mueller at al. [47], with experimental data obtained from constant-pressure, outwardly propagating spherical flames [48]. The comparison showed an inaccuracy in the predictions for the rich flames and the high pressure tests. This disagreement suggests some deficiency of the hydrogen oxidation chemistry and uncertainty over transport coefficients.

Although progress in developing kinetic mechanisms is substantial, the prospects of developing a full comprehensive mechanism for hydrocarbon oxidation are uncertain; presently no comprehensive mechanism exists for hydrogen, methane or any hydrocarbon fuel [46]. Also, all reduced mechanisms derived from large mechanisms are limited in their application, at least quantitatively.

2.3.3 Transport properties

Since most combustion processes take place in nonhomogeneous media, transport properties of species need to be specified properly. Of all the transport properties, the diffusion coefficients play a very important role. Law et al. [46] showed that for hydrogen flames the computed sensitivity coefficients for the binary diffusion coefficients of $H\text{-}N_2$ were larger than the sensitivity coefficients for the rate constant of $H+O_2 \rightarrow O+OH$, which is the main chain branching reaction for hydrogen/air flames. For hydrocarbon fuels the influence of H radical diffusion was found to be similar to the rate constant of $H+O_2 \rightarrow O+OH$ [46]. It is evident, that there are very few experimental data reported for the diffusion coefficient of H radicals in inert gases; all of them were obtained at room temperature.

Since the laminar burning velocities are very sensitive to the diffusion coefficients of the H radical, the large errors between experimental and predicted values of laminar burning velocity of $H_2/O_2/He$ mixtures can be attributed to the uncertainty in the diffusion coefficient of H radicals [48].

From the discussion above it can be concluded that the reliability of computational models of determining laminar burning velocity is affected by uncertainties in the reaction mechanism and transport properties of

species. Accurate measurements of laminar burning velocities will therefore continue to play an important role in combustion studies.

2.3.4 Fuel variations

2.3.4.1 Methane flames

Methane is the most widely investigated fuel for many years. The reason for such extensive research is its simple structure and extensive use in the form of natural gas, which consists primarily of methane with very small quantities of other hydrocarbons. It was used by various researchers for calibrating experimental devices, development and calibration of computational methodologies and chemical kinetics schemes [29, 49-57, 161]. There are a lot of literature sources available on methane combustion; only a few selected ones are cited here.

Bosschart [58] performed an extensive literature review study on the laminar burning velocity for methane. He presented comparison of his results from measurements on an adiabatic burner with the values presented by various researchers. His findings revealed that there is a wide spread in the laminar burning velocity data available in the literature for different measurement techniques and unaccounted stretch effects.

2.3.4.2 Pure hydrogen flames

Hydrogen combustion was investigated by a number of researchers via the laminar burning velocity and flame structure, because of its wide use in industry and different behaviour in comparison to hydrocarbon fuels [59-63]. Hydrogen behaves differently in comparison to hydrocarbons, because it has a high diffusion coefficient and laminar burning velocity.

The presence of hydrogen in a flame also results in cellular flame surfaces formation due to hydrodynamic and thermal-diffusive instabilities [64].

2.3.4.3 Mixtures of fuels

In comparison to literature available on laminar burning velocities for the single fuel and air mixtures, literature on mixtures of fuels is limited. Several fuel mixtures have been studied. Among those are acetylene-Freon [65], H_2 with C_2H_2, C_3H_8, CH_4 [60], ethanol/iso-octane blends [66], mixtures of either H_2 or CH_4, along with diluents such as N_2, Ar, He, CO_2 and steam [67], gas mixtures containing CO, O_2, and inerts, and trace amounts of H_2-containing species [68], fuel mixtures of CO with H_2 and CH_4 [69,70], CO and H_2 fuel mixture [71, 72] and CH_4 and H_2 fuel mixture [73].

2.3.4.4 Syngas flames

There is some literature available for the combustion characteristics of fuel-air mixtures, including CH_4/Air, H_2/Air and hydrocarbon/Air mixtures. Research on the fundamental combustion characteristics of medium and low calorific value gaseous fuels is limited, even though their application in various combustion systems has been tested.

Chomiak et al. [74] presented a comprehensive review of the problems and prospects of low calorific value gas combustion. They investigated problems of gas composition, flame chemistry and pollutant emissions, flammability limits, laminar burning velocities, flame stability and catalytic wall effects, as well as the effects of mixing and intense swirl on combustor operation.

Cho et al. [75] measured the laminar burning velocity of multicomponent mixtures derived from various coals. They investigated fuel mixtures involving CO, CO_2, H_2, H_2O and C_2H_2.

Natarajan et al. [144] measured laminar burning velocities for lean $H_2/CO/CO_2$/Air mixtures over a range of fuel compositions and reactants preheat temperatures up to 700K using Bunsen burner flames. They compared their measurements with numerical computations based on H_2/CO mechanism developed by Davis et al. [76] and GRI-Mech3.0. For CO/H_2/Air mixtures at ambient temperatures their experimental results compare well with numerical simulations.

2.3.5 Parametric variation – equivalence ratios, pressure and temperature ranges

Even though most of the literature on laminar burning velocities presents values of various fuel/air mixtures over the range of equivalence ratios, very few studies deal with laminar burning velocities at higher temperatures and pressures. The main reason is that even the most sophisticated experimental techniques are not able to operate at the conditions of some practical combustion devices such as gas turbines or internal combustion engines. Therefore the present data sets are restricted to a limited range of temperatures and pressures, mostly close to ambient conditions.

The maximum pressure achieved with the counterflow technique was 2 – 2.25 atm as reported in the work of Zhu et al. [33] and Egolfopoulos et al. [34]. For the heat flux method, laminar burning velocity data were obtained only at ambient conditions as reported by De Goey [24], Maaren et al. [25, 26].

Freely propagating spherical flames in large vessels proved to be slightly advantageous over the burner techniques because experiments could be conducted up to a maximum pressure of 10 atm. Hassan et al. [55] determined unstretched laminar burning velocities of CH_4/Air mixtures up to 4 atm pressure. Gu et al. [56] measured laminar burning velocities for CH_4/Air mixtures up to 10 atm. The only one work presenting laminar burning velocity values at operating pressure, similar to the internal combustion engine, was done by Tse et al. [64]. They presented laminar burning velocity data for pressures up to 20 atm, while their experimental facility could be operated at a maximum pressure of 60 atm. For pressures higher than 20 atm, flames were becoming cellular.

Natarajan et al. [144] presents Bunsen burner results for temperatures up to 700K, but they performed their experiments only at ambient pressure. Authors also showed that with increase in reactant preheat temperature the discrepancy between experimental and numerical computations is large for temperatures higher than 500K.

2.3.6 Laminar burning velocity – computations

Computational investigations are widely used for the laminar burning velocity determination. They can also assist in understanding the fundamental phenomena of flame stretch, flame/stretch interaction, extinction behaviour and preferential diffusion mechanisms of various single fuels, as well as multi-component fuel and air mixtures. In most of the cases computational studies were performed to either deduce reduced kinetic schemes using experimental values or to validate the experimental results alongside more in-depth study of flame structures. There is plenty of literature on computational studies available; a few citations are given in the Table 2.1.

From this table it can be seen that the literature covers a wide range of single fuel and multicomponent fuel mixtures, but laminar burning velocity and flame structure results are available only for ambient conditions. Only very few sources report laminar burning velocity values at high pressures. Tse et al. [64] reported laminar burning velocity values for H_2/Air mixture at 20 atm and Gu et al. [56] presented laminar burning velocity values for CH_4/Air mixture at 10 atm. The reason for the lack of literature is that reaction mechanisms for high pressure and temperature conditions have large uncertainties. All multicomponent fuel mixtures are investigated under ambient conditions because of the complex nature of the kinetic reaction system when several combustible components are involved.

Table 2.1: Summary of Earlier Computational Work for the Burning Velocity Predictions for Premixed Fuel-Air Flames

Source	Fuel	Pressure, atm	Temperature, K	Mechanism
Egolfopoulos et al. [34]	$H_2/O_2/N_2$	0.2-2.5	298	20 reactions
Vegelopoulos et al. [36]	H_2&CH_4&C_3H_8	1	298	C2&C3
Vagelopoulos et al. [35]	CO/H_2&CO/CH_4	1	298	C2
Cho et al. [75]	$H_2/CO/CH_4/C_2H_2$	1	298	C1&C2
Bradley et al. [77]	CH_4	1	298	C1 reduced
Aung et al. [61]	H_2	1	298	
Hassan et al. [144]	CO/H_2	0.5-4.0	298	GRI-Mech 2.1
Aung et al. [62]	H_2	0.45-4.00	298	GRI-Mech 2.1
Hassan et al. [55]	CH_4	0.5-4.0	298	GRI-Mech 2.1
Tse et al. [64]	H_2/Diluents	20	298	21 Reactions
Gu et al. [56]	CH_4	1.0-10.0	300-400	GRI-Mech 2.1
Qin et al. [78]	CH_4	1	298	GRI-Mech 3.0
Ren et al. [79]	$CH_4/CO/H_2/CO_2/H_2O$	1	298	GRI-Mech 3.0

Ren et al. [150]	$CH_4/CO/H_2/CO_2$	1	298	GRI-Mech 3.0
Zhou et al. [80]	$CO/H_2/CH_4/CO_2$	1	298	GRI-Mech 3.0 & Reduced
Hirasawa et al. [38]	Ethylene/n-Butane/ Toluene	1	298	621 Reactions
Aung et al. [81]	H_2&CH_4&C_3H_8	0.5-4.0	298	GRI-Mech 2.1
Hermanns et al. [73]	CH_4/H_2	1	298	GRI-Mech 2.1 & GRI-Mech 3.0
Huang et al. [82]	n-heptane&iso-octane its lends $H_2/CO/N_2$	1 1	298 298	GRI-Mech 2.1 & GRI-Mech 3.0
Natarajan et al. [144]	$H_2/CO/CO_2$	1	300-700	GRI-Mech 3.0 & H_2/CO [76]

2.3.7 Extinction strain rate

Another very important combustion characteristic is the critical strain rate to extinction (extinction strain rate). It is a flow field state beyond which a flame cannot be self-sustaining and is extinguished.

This parameter is mainly investigated by employing the counterflow flame method with several geometrical arrangements (twin-flames with two opposed burners, single burner with stagnation surface, etc.). Very few literature sources on critical strain rate to extinction are available. Most of the experimental work has been performed on methane and propane flames [83-86]; there are several papers on CH_4/H_2 flames [87], non-premixed and premixed flames of ethylene (C_2H_4), ethane (C_2H_6), propene (C_3H_6) and propane (C_3H_8) [88], benzene/air mixtures [89], n-decane/air and n-dodecane/air mixtures [90].

By way of illustration, Jackson et al. [87] studied the effects of H_2 addition to lean premixed CH_4 flames in highly strained fields. They performed counterflow burner experiments and numerical simulations. These authors indicate that both experimental and numerical results show that the addition of H_2 in the fuel significantly increases laminar burning velocities and extinction strain rates. The predicted species profiles suggest that with H_2 addition the CH_4 burning rates are enhanced due to early H_2 breakdown. This breakdown increases radical production rates early in the flame zone and improves CH_4 ignition under conditions where it would be prone to extinction.

2.3.8 Auto-ignition

Autoignition delay time is another important parameter in premixed combustion, traditionally for gasoline engines, but increasingly in respect

of gas turbine combustor design and safety. Autoignition delay is characterised by a time scale which corresponds to an increase in the pool of radicals, followed by a thermal path where product concentrations and temperatures increase exponentially.

Most of the available literature focuses on the internal combustion engine applications and their fuels [91, 92]. There are several recent sources on CO/H_2 and methane or propane autoignition delay under gas turbine operating conditions for kinetic mechanisms validation [93-95].

Wang et al. [96] studied auto-ignition characteristics of H_2/air/steam mixtures at various temperatures, pressures and gas compositions behind the shock wave in a shock tube test rig. These authors established that ignition delay was strongly influenced by the steam concentration and the temperature, while the pressure effect was small. Their measured ignition delay times are consistent with theoretical prediction only in the high temperature region, while for low temperatures the measured ignition delay times are shorter than theoretical values.

Walton et al [97] performed experiments in a rapid compression facility to investigate the ignition of simulated syngas mixtures of H_2, CO, O_2, N_2 and CO_2. They obtained ignition delay times for the pressure (P) range from 7.1 up to 26.4 atm and temperature (T) range from 855K up to 1051K, equivalence ratios (ϕ) from 0.1 to 1, oxygen mole fractions (χ_{O_2}) from 15% to 20% and H_2:CO ratios from 0.25 to 4.0 (mole basis). Authors proposed a correlation of ignition delay with the above mentioned parameters to be:

$$\tau_{ign} = 3.7 \times 10^{-6} P^{-05} \phi^{-0.4} \chi_{O_2}^{-5.4} \exp\left(12500/R_{[cal/mol/K]} T\right) \quad \textbf{(2.4)}$$

Petersen et al. [98] presented ignition data for syngas under practical conditions. They performed shock tube experiments with gas mixtures

consisting of 7.33% H_2, 9.71% CO, 1.98% CO_2, 17.01% O_2 and 63.97% N_2 in the pressure range from 18.7 up to 32.7 atm and temperature range 943-1148K. They also performed ignition delay numerical simulations using five kinetics mechanisms containing H_2/CO chemistry. They found that for lower temperatures there is great disagreement between experimental data and numerical simulations; at 700-800K temperatures the measured autoignition delay times are two to three orders of magnitude lower than numerically predicted ones.

2.3.9 Flammability limits

The study of flammability limits for fuel-air mixture is very important not only as a design parameter for safety against explosions and fire risks but also it is an essential parameter governing flame propagation.

For the purposes of risk management from accidental fires, flammability limits are obtained from experiments in large volumes of gas mixtures. One of the first works of standardization of the measurement technique was published by Coward et al. [99]. This method was modified recently by ASTM [100]. In the ASTM method a spherical glass chamber of 5 litre capacity instead of a vertical tube was adopted. The reason for these changes was the formation of unstable, turbulent and self accelerating flames which were observed in long tubes with the ends either open or closed. The change of tube to a spherical chamber was prompted by Guenoche [101] who studied flame acceleration in vertical tubes. Although the spherical chamber method is the most popular one [102-107], there are a number of publications on flammability limit measurements in flame tubes [108-110], large vessels [111] and rapid compression machines [112].

Shebeko et al. [113] measured flammability limits and laminar burning velocities of methane-air and hydrogen-air mixtures at elevated temperatures and pressures. They showed that with increase in reactants temperature, the flammable region for both mixtures is widened.

Heffington et al. [114] measured flammability limits of coal-derived low calorific value gas mixtures, containing large amounts of inert gases at ambient conditions. They compared their experimental results with the calculations performed using LeChatelier's law, presented by Zabetakis [115]:

$$L_f = \frac{100}{\sum_{i=1}^{n}(C_i/L_i)} \quad \textbf{(2.5)}$$

L_f is the flammability limit for the mixture containing n number of combustible gases, L_i is the flammability limit of the combustible component i and C_i is the concentration of the combustible component i. This equation can be used to compute both, lower and higher, flammability limits.

Heffington et al. [114] demonstrated that the LeChatelier's empirical law is not valid for flammability limits estimations because of the complex nature of the hydrocarbons. This conclusion seems to be ambiguous as the flame propagation tube experimental setup is not a very accurate method for flammability limit measurements.

Law et al. [116] performed an experimental and theoretical investigation of lean and rich flammability limits of the C-H-O-Diluents (H_2, H_2/CH_4, H_2/CO with O_2/N_2) system. The authors claim that flammability limits are primarily controlled by the kinetic processes of chain branching versus chain termination reactions. Their computed results agree very well with experimental values for both lean and rich

limits. Their study shows that at rich and lean limits the chain branching reaction $H+O_2 \rightarrow O+OH$ is the dominant one. For lean limits the dominant chain termination reaction is $H+O_2+M \rightarrow HO_2+M$ and for the rich limit the dominant reaction is mixture specific. When the flammability limit is approached, the maximum termination rate is close to the maximum branching rate. Thereby all the most efficient radicals are consumed and further reactions cannot be initiated. They also applied this theory to investigate the effects of initial temperature and pressure.

Wierzba et al. investigated flammability limits of CO/H_2 mixtures [117] and $CO/H_2/CH_4$ mixtures [118] in air using upward flame propagation in a stainless-steel test tube apparatus over the wide range of fuel mixture compositions, atmospheric pressure and initial temperature up to 573 K (300°C). Their experimental results show that lean flammability limit mixtures obeyed LeChatelier's rule. On the other hand, for the rich flammability limits the experimental results deviated significantly from the ones obtained by LeChatelier's rule, especially for the fuel mixture compositions with very small amounts of hydrogen.

Liao et al. [119] investigated flammability limits of natural gas/diluent mixtures in air. They performed experiments in a constant volume bomb. These authors proposed to determine flammability limits based on critical burning velocity. They demonstrated that the accuracy of the method depends on the accuracy of laminar burning velocity determination. They used cut-off laminar burning velocities of 1, 5 and 8 cm/s and demonstrated that a critical laminar burning velocity of 5 cm/s gives the most accurate results in comparison to experimental values. They also indicated that this method is not accurate enough for upper flammability

limit estimation, while it works very well for the lean flammability limit for natural gas/diluent mixtures at high temperatures and pressures.

2.4 Discussion and conclusions

From the literature review on the determination of laminar burning velocity from Bunsen burner flames it can be noted that this technique has been employed for over 50 years now. Furthermore, most of the laminar burning velocity data reported in the literature prior to 1970 were obtained from Bunsen burner experiments. This technique was so popular because it is relatively simple and inexpensive, and produced reasonable results.
The Bunsen burner technique is also useful to determine the onset of cellular instabilities of syngas. This phenomenon will be discussed in more detail in Chapter 5.

There are several major gaps in the literature:

- ◊ There is a lot of information on the determination of laminar burning velocity of pure fuels like methane, hydrogen, propane and others, but few on mixtures of fuels and medium calorific value gaseous fuels. Laminar burning velocity values are scarce at pressures and temperatures close to gas turbine operating conditions.
- ◊ There is no comprehensive computational data available so far to cover medium calorific value syngas at various compositions, equivalence ratios, temperatures and pressures.

The following major conclusions are drawn from the literature review on combustion characteristics:

1. There are various experimental techniques employed for the laminar burning velocity determination. However, most of the laminar

burning velocity data obtained with those techniques are limited to ambient or slightly higher than ambient pressures.

2. Different fuel mixtures are investigated in the literature, from the mixtures used in the present study. However, there are some data on a fuel mixture with 50%CO/50%H_2 available [76, 144]. An investigation of burning velocity and flame structure with coal-derived syngas would contribute to the knowledge of complex combustion phenomena.
3. Out of the investigated parametric ranges like fuel mixture composition, equivalence ratio, temperature and pressure, equivalence ratios are the most common. They occur in almost every study, but not temperature or pressure due to the limitations imposed by experimental facilities, or the limitations imposed by chemical kinetics mechanisms and transport properties for numerical simulations.
4. Computational studies are greatly limited to ambient conditions as well, because most of the present chemical kinetics mechanisms and transport properties databases are developed, tested and verified under ambient conditions.

The next chapter describes the experimental facility developed to measure laminar burning velocities for low and medium calorific value gas.

3 Experimental facility

As mentioned before, the primary aim of this study is to create a database of combustion properties of syngas. By employing chemical kinetics models, the data can be flexibly extended, but these models need to be validated experimentally. The focus of the experimental part of the study is on the laminar burning velocity at high pressures and temperatures. A Bunsen burner configuration was selected to collect experimental laminar burning velocity data. The principal influence on the choice of experimental method was that this method is relatively simple, lending itself to measurements over a wide range of conditions, and it could be comparatively easily set up within an existing high pressure experimental rig.

3.1 Test rig

Figure 3.1 provides a schematic of the experimental set-up employed for the measurement of laminar burning velocity of rim-stabilised Bunsen burner flames. Fuel mixtures and air were metered through rotameters, each selected (tube diameter and float) based on the required mass flow range. For different gas fuel mixtures different mass flow ranges are required because the burning velocities differ quite substantially and in order to stabilise flames, the reactant mass flow can vary significantly. The following ABB Glass Rotameters (Purgemaster) were employed during 5mm burner tube measurements:

1) Fuel: 1/8-08-SA (0.0008-0.039g/s) & air: 1/8-16-SS (0.004-0.175g/s) for fuel mixture 67%CO/33%H_2 and 50%CO/50%H_2

2) Fuel: 1/8-12-SS (0.002-0.104g/s) & air: 1/8-16-SS (0.004-0.175 g/s) for fuel mixture 1.5%CO/28.5%H_2/70%N_2

3) H_2: 1/16-16-SA (0.00008-0.0045g/s), N_2: 1/16-20-TA (0.0015-0.056g/s) & air: 1/8-16-SS (0.004-0.175g/s) for fuel mixture 57%H_2/43N_2.

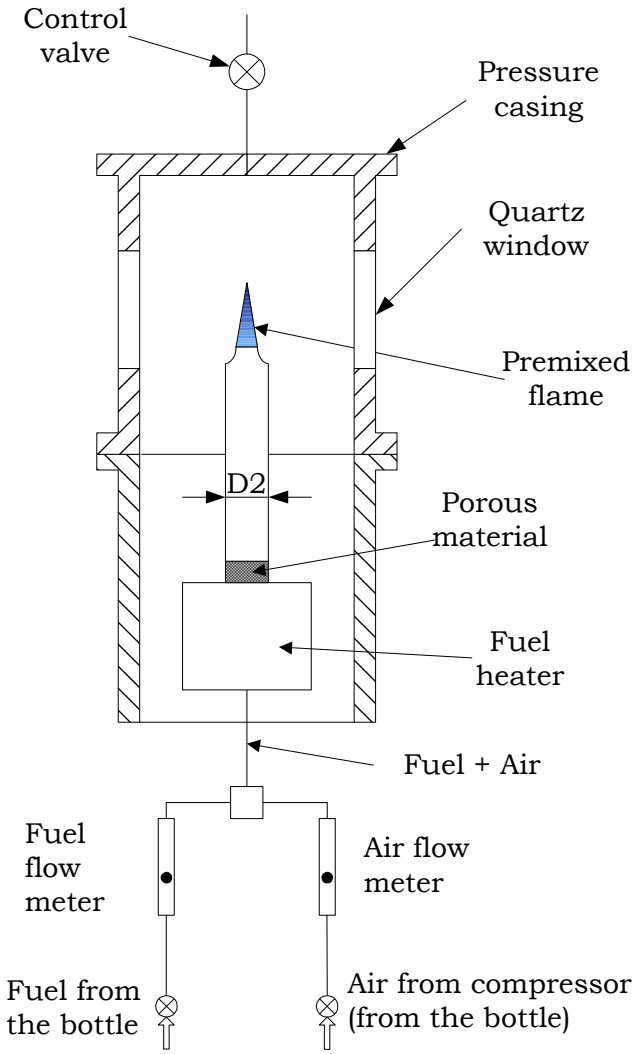

Figure 3.1: Schematics of the experimental setup

During a test, the meter reading and gauge pressure were recorded and the mass flow obtained from the calibration software, provided by the manufacturer (ABB).

The fuel-air mixture then passes through the heater coil, where it can be preheated to the required temperature (described later). At the bottom of the burner tube a porous material disk is placed, that is used to damp any oscillations appearing in the fuel supply system.

3.2 Mixture preparation

The investigated fuel mixtures with 67%CO/33%H_2, 50%CO/50%H_2 and 1.5%CO/28.5%H_2/70%N_2 were drawn from commercially premixed gas cylinders, supplied by BOC. This arrangement ensures that the fuel mixture composition is constant. Only the fuel mixture 57%H_2/43%N_2 was prepared by mixing the H_2 and N_2 streams.

Air was drawn from the laboratory compressor line or from a cylinder. Most of the experiments were performed using air from cylinder because the required mass flows were very small and small fluctuations in flow meter reading were observed while running from the compressor line. These fluctuations introduce errors in the air flow measurements.

3.3 Burners

Two burners have been investigated: a convergent nozzle of 10mm exit diameter, machined in stainless steel and incorporating a 4:1 contraction and 10 diameters in length, and a straight cylindrical tube of internal diameter 5mm, 50 diameters in length. The former gives an essentially uniform exit velocity profile with only a thin wall boundary layer

(see Figure 3.2) whilst the latter produces fully developed laminar pipe flow.

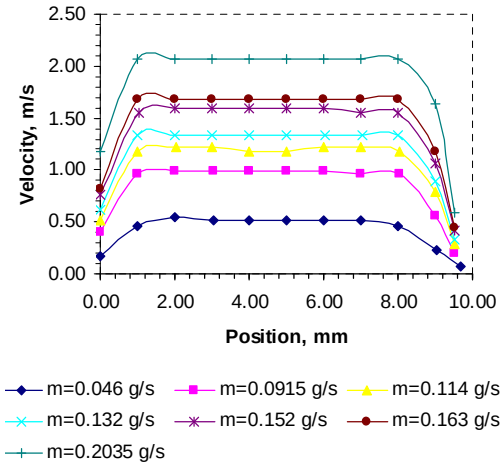

Figure 3.2: Velocity profiles at different mass flows across the burner measured with hot wire anemometry

The hydrodynamic strain in the reactant mixture is then different in the two cases and comparison between the two sets of results introduces an opportunity to examine the influence of such strain on both the measured burning velocity and the stability of lean rim-stabilised laminar flames.

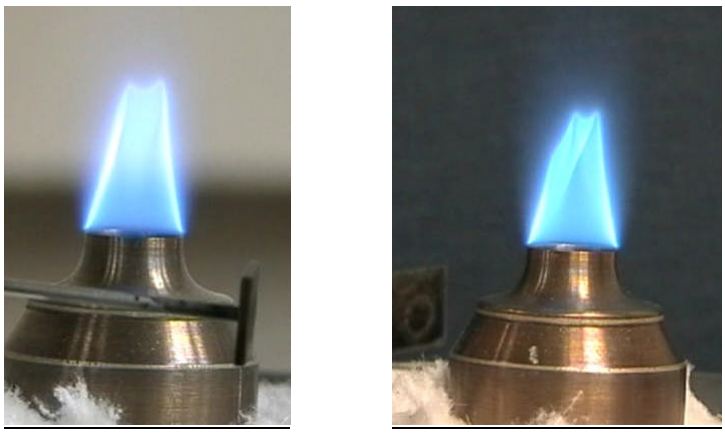

Figure 3.3: Flame images from several angles (approximately 90° and 45° angle to the semitransparent screen) to display flame shape irregularities

Initially the experimental setup with the convergent nozzle was selected, because it was expected to provide laminar burning velocity data of aerodynamic stretch free flames or flames with very low strain/stretch rates. It proved very difficult to obtain laminar burning velocity data with this burner for the higher equivalence ratios, however, because such flames attain irregular cellular shapes at the range of equivalence ratios from 0.8 to 1.1, see Figure 3.3. These flame shapes were observed for the richer fuel mixture 1.5%CO/28.5H_2/70N_2 on the 10 mm nozzle and the 67%CO/33%H_2 fuel mixture on both burner arrangements. This phenomenon will be discussed in detail later.

3.4 Reactant mixture preheat

As mentioned before, the reactant mixture is heated in an electrically heated coil heater. The maximum heater capacity is 750 W. In the original test rig design, this heater was used to vaporize liquid fuels; therefore its power output is much larger than that required to simply preheat the reactant mixture for the present experimental campaigns.

The amount of heat supplied to the mixture was controlled by maintaining a prescribed heater wall temperature constant.

It is impractical to measure directly the temperature of the reactant mixture exiting the burner nozzle in the presence of the flame. It is also not possible to place the thermocouple inside the burner tube because it will perturb the flow and in turn affect the flame shape. Placing it on the tube wall close to the exit is not practical as well because the burner wall temperature is influenced by heat transfer from the flame to the burner rim. Therefore, other means of estimating reactant temperature prior to the preheat zone are used.

3.4.1 Temperature calibration

During tests with reactant preheat it was observed that the burner exit temperature is strongly dependent solely on the reactants mass flow: with increase in reactant mass flow the temperature recorded at the burner exit is increased (while the temperature of the heater wall is kept fixed), see Figure 3.4.

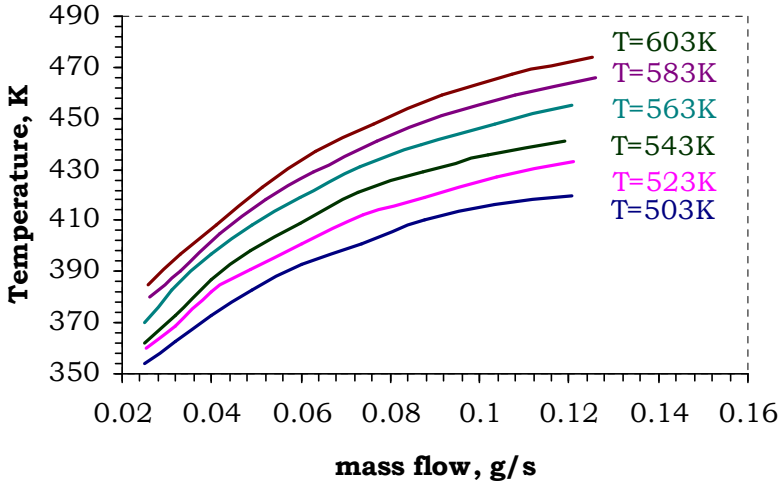

Figure 3.4: Temperature at burner exit dependence on mass flow (temperature of heater wall was kept constant)

That is due to a shorter residence time in the burner tube and also, with increase in stream velocities, more heat is transferred from the heater wall to the gas.

The calibration graph, given in Figure 3.4, was obtained using only heated air.

The actual temperature of the air/fuel mixture can differ slightly due to differences in the c_p value, as the c_p for air/fuel mixture is higher in comparison to pure air. For example for pure air c_p=1002.9 J/kgK (at T=300K, P=1atm) and for fuel mixture 67%CO/33%H_2 at stoichiometric

equivalence ratio, c_p=1116.16 J/kgK (at T=300K, P=1atm). These differences are not taken into account during the temperature calibration. The temperature at the burner exit varies linearly with change in heater wall temperature (heat flux) at fixed mass flow. Using Figure 3.4 the heater wall temperature can be estimated if the mass flow is known prior to the experiment; the desired burner exit temperature is then achieved by setting the heater wall temperature appropriately.

In some experiments the reactant mixture can be electrically preheated together with the wire wrapped burner tube. During the experiments with the converging nozzle, the burner tube was also electrically heated in order to minimise the heat loss through the tube wall. This approach was not adopted with the plain 5 mm tube.

The burner rim itself is generally more problematic, however, and a number of variants have been investigated with a view to extending the stable burning regime. In the presence of the flame, heat is transferred to the rim – principally by conduction since the flame is barely luminous. Locally the metal temperature can exceed the planned level of preheat and therefore, at low heating rates, some rim cooling was introduced through a water jacket extending over the last 10 mm of the 5 mm cylindrical burner.

3.5 Pressure vessel

The burners are mounted within a stainless steel pressure vessel of internal diameter 300mm, fitted with optical quality quartz windows of 75mm diameter that provide line-of-sight access. Additional smaller ports provide access for probes and a retractable heated coil igniter. The top of the pressure vessel is closed with a pressurising valve. The pressure in the vessel is controlled by manually adjusting the position of this restricting

valve. A bursting disk is also installed. Shielding air is supplied to the pressure vessel by a surrounding manifold. This air is used to prevent window fogging by condensing product water especially during high pressure tests.

The vessel can be pressurised using the variable area exhaust orifice up to a casing limit of 15bar. As later results show, it has not proved possible in practice to stabilise flames beyond a 7bar chamber pressure. Whilst reactant heating provides some relief from the effects of increasing chamber pressure on pipe Reynolds number, through the increased viscosity, this effect is not sufficient to delay transition to turbulent flow in the tube. Since the reduction in laminar burning velocity with increased pressure (and hence reactant flow velocity) is comparatively modest, the influence of density predominates and transitional Reynolds numbers ~ 2000 are reached.

3.6 Igniter

Initially a retractable spark-plug igniter was used to ignite the flame. At the start of the experiment it was placed close to the burner rim and retracted, when flame was stabilised on the burner rim.

For later experiments the spark igniter was replaced by a heating coil. This proved difficult to operate for lean near limit flames and it was much harder to get a spark arc at higher pressures. At first the flame would stabilise on the coil igniter, which was positioned several millimetres above the burner, and would then stabilise on the burner rim as mixture composition and velocity were reduced below the blowout limit.

3.7 Schlieren system

The flame is imaged and digitally recorded using a conventional Z-type Herschellian[a] system [120], incorporating 10 cm diameter mirrors with a focal length of 1m, see Figure 3.5. The distance between the mirrors is 2f, where f is the mirror focal length.

The Schlieren image of the flame was projected onto a semitransparent screen (made from paper) and filmed using Panasonic NV-DS11B Digital Video Camera.

The Z-type Schlieren system is comparatively straightforward to setup, but there are several aberrations that need to be taken into account, in particular coma and astigmatism. Most available optical elements are designed for on-axis use; their optical and geometrical axes are coincident. If this is disturbed, there is the price to pay. Both, coma and astigmatism, lead to errors in the production of the light-source image in the cut-off plane.

By definition, coma occurs when the direction of the light reflected from a mirror depends on the position of the point of reflection [120]. This happens if Schlieren field mirrors are tilted off their optical axes. As a result, a comatic optical system will spread a point focus into a line. The point focus becomes smeared into the region of flare with one bright core at one end.

This distortion grows in proportion to the offset angle θ. It can be minimised by keeping a small offset angle and using long focal length mirrors. As coma is generated by both mirrors, it is possible to cancel this effect by tilting both mirrors at equal angles in opposite directions from the

[a] Sir William Herschel (1738-1822), a great astronomer; he tilted his parabolic telescope mirror off its axis in order to gain access to the image [120].

centre optical axis, forming a "z". It is also necessary to use identical mirrors and all optical elements need to be centred in a common plane.

This is an advantage of a "Z-type" Schlieren system: it is free of coma if the mirrors are perfectly and identically configured [120].

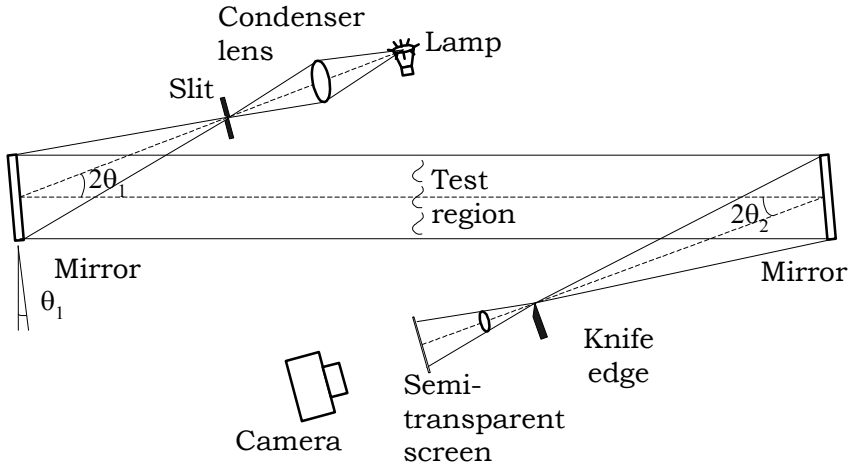

Figure 3.5: Schlieren setup [120]

Unlike coma, astigmatism cannot be removed from the Z-type Shlieren or any off-axis mirror system. Astigmatism is a failure to focus point-to-point. It arises from differences in the mirror periphery and path length along the optical centreline. Due to finite axis angles θ_1 and θ_2, a point light source is imaged as two short lines at right angles to one another and spaced at small distance along the optical axis [120, 121]. Even these angles are minimised and large focal length mirrors are used, some astigmatism is always present [120].

Due to astigmatism vertical and horizontal lines in the test area are not sharply focused simultaneously. This leads to distortion errors in the image.

Astigmatism severity can be evaluated using the following equation [120, 122, 123]:

$$\Delta f = f \cdot \sin^2 \theta / \cos \theta \quad (3.1)$$

In summary, it is recommended to use larger focal distance mirrors and restrict the angle θ in order to minimise astigmatism and coma [120]. The digitisation of the image is described in the Chapter 4.

4 Experimental and numerical methodologies

4.1 Background

To fulfil the objectives of the present study, both computational and experimental approaches were adopted, one complementary to the other. The major objective of this investigation was to create a combustion characteristics database (mainly focusing on laminar burning velocities) for coal derived gas, which primarily consists of hydrogen, carbon monoxide, methane, nitrogen, carbon dioxide and water. Since laminar burning velocity is one of the most important combustion characteristics, it was investigated in more depth. From the many studies identified in the literature survey it is well-established that laminar burning velocity is a function of mixture composition, equivalence ratio, reactant preheat temperature and operating pressure. The present study therefore focused on the influence of these parameters on syngas mixtures broadly representative of those likely to be encountered in future applications.

Of the several configurations that have been previously investigated we chose to make measurements in Bunsen-type flames. Its comparative simplicity leant itself to a wide range of measurement conditions and could be readily accommodated in an existing pressure vessel. Measurements were performed using several $CO/H_2/N_2$ mixtures at different equivalence ratios, temperatures and pressures.

These experiments also allowed observations of the flame shape, tip geometry and luminosity. Preferential diffusion plays an important role in the structure of hydrogen flames because it drives some of the flame instabilities observed. These instabilities cause the formation of cellular structures in the flames. Since little information is available on the flame

structures of syngas, it was informative to be able to observe the flame behaviour on the Bunsen burner.

For laminar burning velocity determination the flames were imaged using Schlieren photography and the flame cone area was calculated. The implications of this method are discussed later in this chapter.

The Bunsen burner provides reasonably accurate laminar burning velocity values; the major limitations of this method are associated with flame stretch due to flame curvature and non-uniform inlet conditions. Although flame stretch values can be calculated, their effect on laminar burning velocity cannot be readily measured. In addition, the flame stretching across the entire flame envelope is not uniform; it is much greater at the tip and base of the flame. Therefore, some assumptions need to be made in interpreting the measurements.

Along with the flame stretch, preferential diffusion is important for the stability of premixed flames, especially in the present fuel/air mixtures due to several reactants involved in the multicomponent mixture with different diffusion coefficients like H_2, CO and N_2. Analysis of flame structure/stretch/preferential diffusion interaction for the fuel/air mixtures was done computationally. Flame codes PREMIX (a premixed flame solver of the numerical code CHEMKIN) and Cantera were employed for these simulations.

As mentioned earlier, there are several ways of estimating average laminar burning velocity from observations of the flame cone. The simplest approach is based on the area-averaged reactant velocity at the exit of the burner and the flame cone angle. Since the spatial velocity of the flame is zero, the laminar burning velocity S_l at any point of the flame front cone is numerically equal to the normal component of gas velocity at that point.

The laminar burning velocity at that point can be computed by using the following equation:

$$S_{lam} = v_u \sin\beta \quad \textbf{(4.1)}$$

where S_{lam} is the laminar burning velocity, v_u – unburned reactant velocity and β is a half cone angle.

A more robust strategy is to determine the area-averaged global laminar burning velocity by dividing the volume flow of the reactant mixture by the total flame surface area. The laminar burning velocity is computed using the following equation:

$$S_{lam} = \frac{\dot{m}}{\rho_u \cdot A_{Flame}} \quad \textbf{(4.2)}$$

where $\dot{m}$ is the mass flow rate, ρ_u is unburned reactant density and A_{Flame} is flame surface area.

From the definition of the laminar burning velocity, the actual flame area should be that immediately upstream of the preheat zone. Therefore, the flame area from the Schlieren images tends to be slightly over-predicted, since the edge of the flame cone is representing the outer envelope of the reaction zone, resulting in laminar burning velocity under-prediction.

A description of the experimental and computational methodologies is presented below.

4.2 Experimental methodology

The Bunsen burner adopted in the present study, is presented below along with its limitations, experimental procedure and calculation procedure.

4.2.1 Experiments

In the Bunsen burner method the fuel/air mixture flows up a cylindrical tube long enough to ensure well developed flow at the exit. The gas burns at the rim of the burner tube and the shape of the premixed cone is recorded and cone area is determined.

4.2.2 Required measurements

The required measurements for laminar burning velocity determination are flow rates of fuel and air in order to calculate the equivalence ratio, mixture composition (for H_2/N_2 fuel mixture) and premixed flame cone area required for the equation above.
The air and fuel flows were metered by rotameters of various ranges, as discussed in Chapter 3.

4.2.3 Preparation of fuel mixtures

Cylinders with fuel mixtures of compositions of 67%CO/33%H_2, 50%CO/50%H_2 and 1.5%CO/28.5%H_2/70%N_2 were prepared by BOC. Fuel and air cylinders were connected to the flow control panel to the inlet of individual rotameters via double stage pressure regulators at the cylinder end. These regulators reduced a cylinder pressure of 200bar to a pressure of around 3-11bar. For experiments with mixture of 57%H_2/43%N_2 pure hydrogen and nitrogen were drawn from the pressurized cylinders, which were connected to the flow control panel to the inlets of individual rotameters, and mixed in required proportions to achieve the required H_2/N_2 fuel mixture composition.

4.2.4 Flow rate setting

During online test, the required air mass flow rate was set at first and then fuel flow rate was adjusted to achieve required equivalence ratio. For fuel with 57%H_2/43%N_2, the test procedure was similar. At first the air mass flow rate was adjusted, then the required nitrogen mass flow rate was supplied and in the end the hydrogen was added.

Air and fuel (or nitrogen and hydrogen) rotameters were set after suitable calculations to the required flow rates with the help of an online calibration program.

4.2.5 Flame imaging and image processing

The fuel/air mixture was lit using the hot wire igniter, placed 1 mm above the burner rim. A conical flame then develops and anchors to the rim of the burner.

As was mentioned before, for laminar burning velocity calculations the required measurements are the air and fuel flow rates and flame area.

To compute the cone area the flame edge from the Schlieren image is digitized using specialist digitising software Digitize-Pro [124]. The edge of the cone is then divided into a number of segments and the areas of the frustum for a number of cones are calculated and the area is then inferred from symmetry, see Figure 4.1. The same procedure is performed for the other half of the flame cone image. The change of the flame area between these two sections usually is less than 5%. The average of these two flame areas was used to determine laminar burning velocity.

For each experimental condition, typically 20 images were extracted from the video and the corresponding flame areas were calculated.

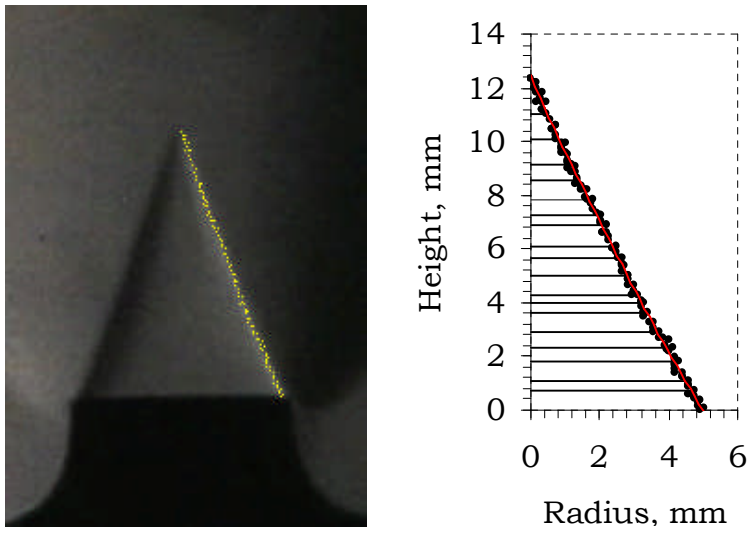

a) b)

Figure 4.1: Determination of the flame cone: a) image with digitized edge; b) surface of the half cone

4.2.6 Uncertainty in the measured components

An uncertainty analysis was performed based on the method of Kline and McClintock [125]. All uncertainties accommodate the accuracies of the measuring instruments.

The uncertainties in the values of air-fuel ratio are found to be within 2.0% and the corresponding values of equivalence ratio are within 2.5%. Uncertainties in laminar burning velocities are within 5.5%. The detailed uncertainty analysis is given in the Appendix C.

4.2.7 Validation of the experiments

Since newly developed facilities require to be validated against published data in order to ensure that their results are correct, tests were conducted with a CO/H_2 mixture composition, which was studied earlier by Natarajan et al. [144]. Mixture with composition of 50%CO/50%H_2 was

used for validation tests. Experiments were conducted at ambient conditions. Laminar burning velocities of this mixture are given in Figure 5.4. As can be seen the present result compares very well with the ones presented in the literature. This indicates that the present facility is well able to predict laminar burning velocities for the investigated fuel mixtures.

4.3 Computational methodology

Computations were performed to quantify the effects of pressure, temperature, mixture composition and equivalence ratio on laminar burning velocities. Other combustion parameters such as critical strain rates to extinction, flammability limits and autoignition parameters were numerically investigated as well.

The computational simulations of the freely propagating planar flames were carried out using the laminar flame code called PREMIX, developed by Kee et al. [142], to compute laminar burning velocities. This algorithm allows mixture-averaged, multicomponent diffusion, thermal diffusion, variable thermochemical properties, and variable transport properties for the computations.

It employs self-adaptive gridding to accommodate the sharp gradients and curvatures developed across the flame zone, which is computationally efficient due to addition of extra grid points at the regions of steep gradients.

For critical strain rate to extinction simulations, another code, called OPPDIF, developed by Kee et al. [39] was employed. It solves governing equations for one-dimensional, opposed-flow flames. This algorithm also

employs the self-adapting gridding approach, similar to the one in PREMIX.

Autoignition delay was modelled using the AURORA algorithm, available in CHEMKIN. This transient algorithm solves conservation equations of mass, energy and species for a closed well-mixed reactor, including the net generation of chemical species within the reactor volume [126].

4.3.1 Selection of chemical kinetics mechanism

Selection of suitable kinetic mechanism out of the many mechanisms available for pure fuels is an important task in computational investigations. But as noted by Law et al. [46] and discussed in section 2.3.2, no comprehensive mechanism is available even for simple fuels such as hydrogen, carbon and methane. Present investigations of combustion characteristics of syngas fuels were performed using GRI-Mech 3.0 mechanism with 375 reactions. Even though this mechanism is designed for methane simulations at ambient conditions; it also contains chemical reaction sets for H_2 and CO combustion.

4.3.2 Features of PREMIX model

For the computations of unstretched laminar burning velocities calculations were performed using the PREMIX code of Kee et al. [142]. This model solves the set of conservation equations that describe the dynamics of the flame. It uses implicit difference methods and a combination of time-dependent and steady-state methods. The algorithm performs coarse-to-fine grid refinement in order to enhance the solution convergence and provide optimal mesh distribution [126]. With assumptions, such as, no body forces, no Dufour effect, zero bulk

viscosity, no viscous dissipation, ideal gas, a constant pressure and no radiation heat losses, the final form of governing equations are the following [126]:

Continuity:

$$\dot{m} = \rho v A \tag{4.3}$$

Energy:

$$\dot{m}\frac{dT}{dx} - \frac{1}{c_p}\frac{d}{dx}\left(\lambda A\frac{dT}{dx}\right) + \frac{A}{c_p}\sum_{k=1}^{K}\dot{\omega}_k h_k W_k = 0 \tag{4.4}$$

Species:

$$\dot{m}\frac{dY_k}{dx} + \frac{d}{dx}\left(\rho A Y_k V_k\right) - A\dot{\omega}_k W_k = 0 \quad \left(k = 1,\ldots,K_g\right) \tag{4.5}$$

Equation of state:

$$\rho = \frac{P\overline{W}}{RT} \tag{4.6}$$

where x is the spatial coordinate; $\dot{m}$ - mass flow rate; $\dot{\omega}$ - molar rate of production by chemical reaction of the k species per unit volume; T – temperature; P – pressure; u – velocity of the fluid; ρ – mass density; Y_k – mass fraction of the k species (K_g – gas species); W_k – molecular weight of the k species; $\overline{W}$ - mean molecular weight of the mixture; λ – thermal conductivity of the mixture; R – universal gas constant; c_p – heat capacity (constant pressure); c_{pk} – heat capacity of k species (constant pressure); h_k – specific enthalpy of the k species; V_k – diffusional velocity of the k species; A – cross section area of the stream tube surrounding the flame.

Boundary conditions

The employed boundary conditions are the known temperature and fuel/air mixture composition (unburned state) and zero-gradient condition

of species and temperature profiles for combustion products (burned state) [126].

Numerical method

In freely-propagating flames, the mass burning rate must be determined as a part of the solution. Therefore the flame location needs to be fixed at a specified temperature to remove one degree of freedom from the conservation equations. The conservation equations and boundary conditions are transformed into a system of algebraic equations with finite difference approximations. The modified damped Newton's method is used to solve non-linear algebraic equations. This method is a combination of two methods: damped Newton's and time-stepping. Initially the damped Newton's method is used and if it fails to converge, time-stepping is employed to bring the solution within the Newton's convergence domain. Depending on the problem, the solver switches between the Newton's method and time stepping to reach the desired convergence. In addition, the solver employs grid adaptation by solving the problem on a coarse grid and then mapping the solution onto a refined grid and solving again to achieve desired tolerances. The structure of PREMIX is available in the manual [126].

4.3.3 Features of OPPDIF model

In the analysis of opposed flames, the conservation equations are reduced to a boundary-value problem. Here assumptions of stagnation-point potential flow and boundary layer are made. In this approach the strain field is characterized only by the potential flow velocity gradient. Even if most of the flame experiments have not reproduced the ideal flow, realized in the analysis, comparison of strained flame experiments can be made with acceptable accuracy [39].

The mass conservation equation for the steady state is the following [39]:

$$\frac{\partial(\rho v)}{\partial x}+\frac{1}{\zeta^{n-2}}\frac{\partial\left(\rho v_{\zeta}\zeta^{n-2}\right)}{\partial\zeta}=0 \qquad (4.7)$$

where v and v_{ζ} are the axial and cross-flow velocity components, and ρ is the mass density.

If v_{ζ}/ζ and other variables are functions of x only, then [39]:

$$G(x)=\frac{\rho v_{\zeta}}{\zeta} \text{ and } F(x)=\frac{\rho v}{(n-1)} \qquad (4.8)$$

The continuity equation for axial velocity u reduces to:

$$G(x)=\frac{dF(x)}{dx} \qquad (4.9)$$

Momentum equation [39]:

$$H-(n-1)\frac{d}{dx}\left(\frac{FG}{\rho}\right)+\frac{nG^2}{\rho}+\frac{d}{dx}\left[\mu\frac{d}{dx}\left(\frac{G}{\rho}\right)\right]=0 \qquad (4.10)$$

$$\text{with} \quad H=\frac{1}{\zeta^{n-2}}\frac{\partial p}{\partial\zeta}=\text{const}$$

Energy and species [39]:

$$\rho u\frac{dT}{dx}-\frac{1}{c_p}\frac{d}{dx}\left(\lambda\frac{dT}{dx}\right)+\frac{\rho}{c_p}\sum_k c_{pk}Y_kV_k\frac{dT}{dx}+\frac{1}{c_p}\sum_k h_k\dot{\omega}_k=0 \qquad (4.11)$$

$$\rho u\frac{dY_k}{dx}+\frac{d}{dx}(\rho Y_kV_k)-\dot{\omega}_kW_k=0 \qquad k=1,\ldots,K \qquad (4.12)$$

Boundary conditions

The boundary conditions employed are the mixture composition, temperature, and the inlet velocity. Symmetry conditions are applied at the stagnation or symmetry plane [39].

Numerical method

The computational approach, which is employed in the OPPDIF was first developed for premixed flame modelling [142]. It reduces the boundary value problem to a system of algebraic equations by making second order finite difference approximations. The initial discretisation is performed on a coarse grid containing few points. After obtaining the solution on the coarse grid, the grid is refined in the regions where large gradients are present and the solution changes rapidly. The solution for the finer grid is initialized from the one obtained on the coarse grid. This iterative solution procedure is continued until new points are not needed to resolve the problem with the desired accuracy. As for PREMIX, the modified damped Newton's algorithm is employed to solve non-linear algebraic equations.

In addition to the flame structure predictions, the flame extinction limits prediction needs to be considered. The flame extinction limits are predicted by using the arc-length continuation methods [39].

Continuation methods are an extension of Newton algorithms. Their most important characteristic is their behaviour near the extinction limit, which is a turning point in the solution, where the Jacobian in the original algorithm becomes singular. If the Jacobian approaches singularity the solution faces computational difficulties, but the continuation method proceeds easily through the turning point and obtains solution.

4.3.4 Features of AURORA model

Autoignition (spontaneous ignition) is investigated by using a closed perfectly stirred reactor model, which is a part of AURORA code.

There are several assumptions made in the model. The contents of the perfectly stirred reactor are assumed to be spatially uniform; this means that conversion of reactants to products is controlled solely by chemical

reaction rates. Therefore the reactor model can be described well by spatially averaged (bulk) properties. The major advantage of such an approximation is that this model does not demand a lot of computational resources, allowing investigating and analysing complex reactor networks or large chemical reaction mechanisms.

In addition, the flow though the reactor is characterized by a nominal residence time.

Governing equations for mass, energy and species for the perfectly stirred reactor include net generation of chemical species within the reactor volume and net loss of species to surface walls [126].

A perfectly stirred reactor consists of a chamber with inlet and outlet ducts. It is possible to define more than one inlet for each reactor. The closed reactor does not have inlets or outlets.

Homogeneous zero-dimensioned reactor equations can be employed for steady-state and transient problems.

The general mass conservation equation for the zero-dimensional reactor(mass change in the reactor is related to the difference between the inflow mass and outflow mass) [126] is:

$$\frac{d}{dt}(\rho V)^{(j)} = \sum_{i=1}^{N_{inlet(j)}} \dot{m}_i^{*(j)} + \sum_{r=1}^{N_{PSR}} \dot{m}^{(r)} R_{rj} - \dot{m}^{(j)} + \sum_{m=1}^{M} A_m^{(j)} \sum_{k=1}^{K_g} \dot{s}_{k,m}^{(j)} W_k \qquad j = 1, N_{PSR} \tag{4.13}$$

where j – reactor number, ρ – mass density, V – reactor volume, $\dot{m}^*$ - inlet mass flow rate, $\dot{m}$ - outlet mass flow rate. $N_{inlet(j)}$ - number of inlets for reactor j, N_{PSR} – total number of reactors in the reactor network, R_{rj} – fraction of the outflow from r recycled into reactor j, A_m – surface area of the m^{th} material, $\dot{s}_{k,m}$ - molar surface production rate of the k^{th} species on

the m^{th} material per unit surface area, K_g – gas-phase species, M – materials.

Species conservation equation [126]:

$$\left(\rho_k V\right)^{(j)} \frac{dY_k^{(j)}}{dt} = \sum_{i=1}^{N_{inlet(j)}} \dot{m}^{*(j)}\left(Y_{k,i}^{*} - Y_k\right) + \sum_{r=1}^{N_{PSR}} \dot{m}_k^{(r)} R_{rj}\left(Y_k^{(r)} - Y_k^{(j)}\right) - Y_k^{(j)} \sum_{m=1}^{M} A_m^{(j)} \sum_{k=1}^{K_g} \dot{s}_{k,m}^{(j)} W_k + \left(\dot{\omega}_k V\right)^{(j)} W_k + \sum_{m=1}^{M} A_m^{(j)} \dot{s}_{k,m}^{(j)} W_k \quad \textbf{(4.14)}$$

where Y_k – mass fraction of k^{th} species, W_k – molecular weight of the k^{th} species, $\dot{\omega}_k$ - molar rate of production of k^{th} species. Inlet stream quantities are indicated by superscript *.

The nominal residence time of the reactor:

$$\tau = \frac{\rho V}{\left[\sum_{i=1}^{N_{inlet(j)}} \dot{m}_i^{*(j)} + \sum_{r=1}^{N_{PSR}} \dot{m}^{(r)} R_{rj}\right]} \quad \textbf{(4.15)}$$

Energy equation [126]:

$$\frac{dU_{sys}^{(j)}}{dt} = \sum_{i=1}^{N_{inlet(j)}} \dot{m}_i^{*(j)} \sum_{k=1}^{K_g} \left(Y_{k,i}^{*} h_{k,i}^{*}\right)^{(j)} + \sum_{r=1}^{N_{PSR}} \dot{m}^{(r)} R_{rj} \sum_{k=1}^{K_g} \left(Y_k h_k\right)^{(r)} - \left(\dot{m} \sum_{k=1}^{K_g} Y_k h_k\right)^{(j)} - Q_{loss}^{(j)} + Q_{source}^{(j)} - P^{(j)} \frac{dV^{(j)}}{dt} \qquad j = 1, N_{PSR} \quad \textbf{(4.16)}$$

Here the total internal energy U_{sys} comprises of the internal energy of the gas and surface phases, solid phases (deposited or etched), and walls.

Solution variables for the model

The total number of species:

$$K = K_g + \sum_{m=1}^{M}\left[K_s(m) + K_b(m)\right] \quad \textbf{(4.17)}$$

where K_g – number of gaseous species, $K_s(m)$ – number of surface species on m^{th} material, $K_b(m)$ – bulk-phase species on the m^{th} material, M – total number of different species in the reactor.

Then the maximum number of unknowns is [126]:

$$J = \left[L_n + K_n + \sum_{m=1}^{M} N_\rho(m) \right] \times N_{PSR} \quad \textbf{(4.18)}$$

Here L_n is for the additional equations for gas temperature or surface temperature. These equations are solved for all N_{PSR} reactors.

4.4 Artificial neural network application

Data obtained from the chemical kinetics simulations are used to train artificial neural networks (ANNs) to get correlations between input values (fuel/air composition, temperature and pressure) and output values (laminar burning velocities, critical strain rate to extinction and autoignition delays). The optional method for obtaining these correlations is the multiple regression analysis.

The ANNs have been chosen because they are able to identify relationships only from given input and output data. A very important feature of the ANNs is the capability of handling tasks involving incomplete data sets, and fuzzy and incomplete information for highly complex and poorly defined problems, where humans usually would make decisions based on intuition. They also are tolerant to noise variations. It is expected that the ANNs will give acceptable results with much smaller data sets in comparison to linear regression analysis.

A new approach, suggested by Sencan et al [9, 200], was used. These authors propose to use weights, biases and activation functions of ANNs to derive sets of simple algebraic equations to predict output from inputs.

Sufficient amounts of data patterns are still needed for efficient ANNs training.

4.4.1 Data Gathering

As was discussed earlier, this study is limited to the investigation of several combustion characteristics, which are laminar burning velocities, critical strain rate to extinction and autoignition delays.

Laminar burning velocities

Data of laminar burning velocities for CO/H_2/Diluents mixtures were generated using the PREMIX code. Simulations were carried out for a broad range of conditions: for pressures from 1 to 50 bar, temperatures from 300 to 900 K and equivalence ratios from 1 down to close to the lean flammability limit. Various CO/H_2/Diluents fuel mixture compositions were covered, see Table 4.1.

Table 4.1: The list of mixture compositions and composition ranges along with data patterns of laminar burning velocities for ANNs training

	CH_4, %	CO, %	H_2, %	N_2, %	CO_2, %	H_2O, %	Data
1	0	1.5	28.5	70	0	0	57
2	0	40	40	20	0	0	164
3	0	50	50	0	0	0	180
4	0	67	33	0	0	0	430
5	0	10-80	90-20	0	0	0	261
6	0	0	100-20	0-80	0	0	232
7	100-1	0-99	0	0	0	0	696
8	5-95	0	95-5	0	0	0	240
9	X	X	X	0	0	0	477
10	X	X	X	X	up to 10	up to 10	491

The inputs for the network are pressure, temperature and fuel/air mixture composition, whereas the output is laminar burning velocity.

Critical strain rates to extinction

Data for critical strain rate to extinction were generated using the OPPDIF code. The mixture compositions were limited to $CO/H_2/N_2$ mixtures. Simulations were carried out for a similar range of conditions as for laminar burning velocities: pressures from 1 to 50 bar, temperatures from 300 to 900 K and equivalence ratios from 1 down to close to the lean flammability limit.

1220 data patterns for various $CO/H_2/N_2$ fuel mixture compositions were collected, see Table 4.2. Mixtures with compositions of 67%CO/33%H_2 and 50%CO/50%H_2 were investigated in more detail.

Table 4.2: The list of mixture compositions along with data patterns of critical strain rate to extinction for ANNs training

	CO, %	H_2, %	N_2, %	Data
1	40	40	20	147
2	67	33	0	470
3	50	50	0	154
4	60	40	0	70
4	40	60	0	59
5	80	20	0	70
6	0	100-20	0-80	250

The inputs for the network are pressure, temperature and fuel/air mixture composition, whereas the output is critical strain rate to extinction.

Autoignition delay

Autoignition delay data for various $CO/H_2/N_2$ fuel mixture compositions were generated using the AURORA code. Computations were performed for air fuel mixtures with equivalence ratio equal to 1, a pressure range from 1 up to 30 bars and a temperature range from 600K to 1300K. For each fuel mixture composition 56 data patterns were generated, see Table 4.3. The reason for investigating only the

stoichiometric mixtures is that ignition delay is not sensitive to equivalence ratio, in comparison to temperature, pressure or mixture composition.

Table 4.3: The fuel mixture compositions investigated for ignition delay data

CO/H_2 mixtures			H_2/N_2 mixtures			$CO/H_2/N_2$ mixtures		
CO	H_2		H_2	N_2		CO	H_2	N_2
10	90		100	0		40	40	20
20	80		90	10		30	30	40
30	70		80	20		20	20	60
40	60		70	30		20	60	20
50	50		60	40		20	40	40
60	40		50	50		10	30	60
70	30		40	60		60	20	20
80	20		30	70		40	20	40
90	10					30	10	60
						10	70	20
						10	50	40
						30	50	20
						50	10	40
						50	30	20
						70	10	20

4.4.2 Artificial neural networks training

The Levenberg–Marquardt variant of the back propagation algorithm was used for the feedforward network with one and two hidden layers. All data were normalized to fit into the range (0,1). A logistic sigmoid (logsig) transfer function has been used for the input, hidden and the output layers. The transfer function used can be expressed as:

$$F(Z) = \frac{1}{1+e^{-Z}} \quad \textbf{(4.19)}$$

where Z is the weighted sum of the inputs.

ANN simulations were performed in the MATLAB environment using the Neural Networks Toolbox. Several ANNs with different numbers of

neurons in the hidden layer(s) were used in order to define output accurately.

The available data sets were divided into three sets: a training set with a size of $0.5*N_{tot}$, a testing set with $0.25*N_{tot}$ and a validation set with $0.25*N_{tot}$ (Here N_{tot} is total number of data patterns). Here the training set was used for network training; the testing set was employed to evaluate the network's ability to generalize data and the validation set was used for early network stopping. More information on artificial neural network theory is given in Appendix B.

For neural network evaluation and selection, several statistical criteria were used: goodness of the fit for output values and predicted output values by the ANN (RMSE - Root Mean Squared Error, R^2 and SSE - Sum of Squares Due to Error):

$$SSE = \sum_{i=1}^{n} \omega_i (y_i - \hat{y}_i)^2 \quad \textbf{(4.20)}$$

with SST, which is called the sum of squares about the mean:

$$SST = \sum_{i=1}^{n} \omega_i (y_i - \bar{y}_i)^2 \quad \textbf{(4.21)}$$

The R^2 value can be expressed as:

$$R^2 = 1 - \frac{SSE}{SST} \quad \textbf{(4.22)}$$

and

$$RMSE = \sqrt{MSE} \quad \textbf{(4.23)}$$

where MSE is the mean square error of the residual mean square

$$MSE = \frac{SSE}{\upsilon} \quad \textbf{(4.24)}$$

where y is the response value and $\hat{y}$ is the predicted response value and the w_i are the weights, which determine the extent to which each response value influences the final parameter estimated; υ indicates the number of independent pieces of information involving all the n data points that are required to calculate the sum of squares [203].

4.4.2.1 ANN for Laminar burning velocities

Artificial neural networks, unlike any other modelling technique, need to be designed and trained properly in order to get optimal and accurate results. In order to achieve optimal results, different number of neurons (9-19) in one and two hidden layers were used. It was decided to limit the number of hidden layers to two, because more complex networks tend to have poor generalisation abilities and memorise the data patterns.

It is evident that by increasing the number of hidden neurons the training accuracy improves, as indicated by smaller RMSE and SSE values and or R^2 value approaching unity.

In addition, the networks' generalisation ability was also evaluated. Some networks with very high training performance were having very poor generalisation ability as the error of their testing set was very large.

Table 4.4: Statistical values for ANNs with one hidden layer (laminar burning velocities)

Number of Neurons	RMSE	R^2	SSE
LM 9-9-1	0.002663	0.9995	0.01885
LM 9-10-1	0.00367	0.999	0.03581
LM 9-11-1	0.00265	0.9995	0.01867
LM 9-12-1	0.002227	0.9996	0.01319
LM 9-13-1	0.002015	0.9997	0.0108
LM 9-14-1	0.001917	0.9997	0.009773
LM 9-15-1	0.002037	0.9997	0.01103
LM 9-16-1	0.001868	0.9997	0.009281

LM 9-17-1	0.001853	0.9997	0.00913
LM 9-18-1	0.00186	0.9997	0.009204
LM 9-19-1	0.001799	0.9998	0.008606

Table 4.5: Statistical values for ANNs with two hidden layers (critical strain rate to extinction)

Number of Neurons	RMSE	R2	SSE
LM 9-9-9-1	0.002239	0.9996	0.01333
LM 9-10-10-1	0.001438	0.9998	0.005502
LM 9-11-11-1	0.001665	0.9998	0.00737
LM 9-12-12-1	0.001266	0.9999	0.004259
LM9-13-13-1	0.001297	0.9999	0.004475
LM 9-14-14-1	0.001633	0.9998	0.007091
LM 9-15-15-1	0.001161	0.9999	0.003585
LM 9-16-16-1	0.001125	0.9999	0.003368
LM 9-17-17-1	0.001045	0.9999	0.002902
LM 9-18-18-1	0.00102	0.9999	0.002765
LM 9-19-19-1	0.001005	0.9999	0.002684

From the data presented in Table 4.4 and Table 4.5, the optimal artificial neural network was with 10 neurons in the two hidden layers (9-10-10-1). The decrease in mean square error during training of the network is shown in Figure 4.2. The regression curve for the validation set is given in Figure 4.3. This data set was not used for ANN training or testing. The correlation obtained in this case is 0.9991, which is very satisfactory.

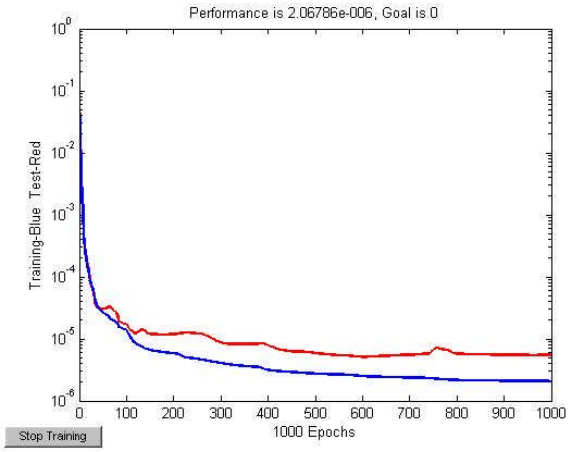

Figure 4.2: Variation of R^2 with training epochs for ANN LM-9-10-10-1

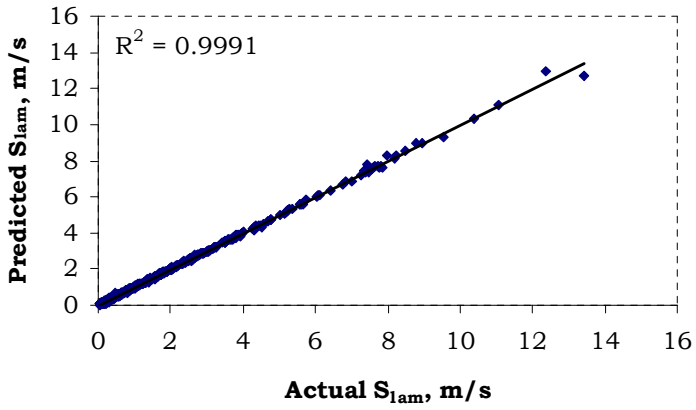

Figure 4.3: Comparison of actual and predicted by ANN values of laminar burning velocities for the validation data set

Network validation

To validate the artificial neural network the computed laminar burning velocity values for a CO/H_2 fuel mixtures were compared to the results presented in the literature [127, 128, 145, 93]. The comparison for fuel mixtures of 50%CO/50%H_2, 75%CO/25%H_2, 95%CO/5%H_2 and 99%CO/1%H_2 are presented in Figure 4.4. From the comparison it can be

seen that the artificial neural network predicts the laminar burning velocities for CO/H_2 mixtures sufficiently well.

The largest discrepancy between ANN and literature values is around 30% in the comparison of laminar burning velocities predicted by ANN. These results were obtained by Sun et al. [127] in a constant pressure bomb. For all the other results the differences are in the range of 10%. There are larger differences for lean mixtures (equivalence ratio below 0.6) and for a mixture with 95%CO/5%H_2 as well. This indicates that in the case of low values of laminar burning velocities the ANN tends to under-predict.

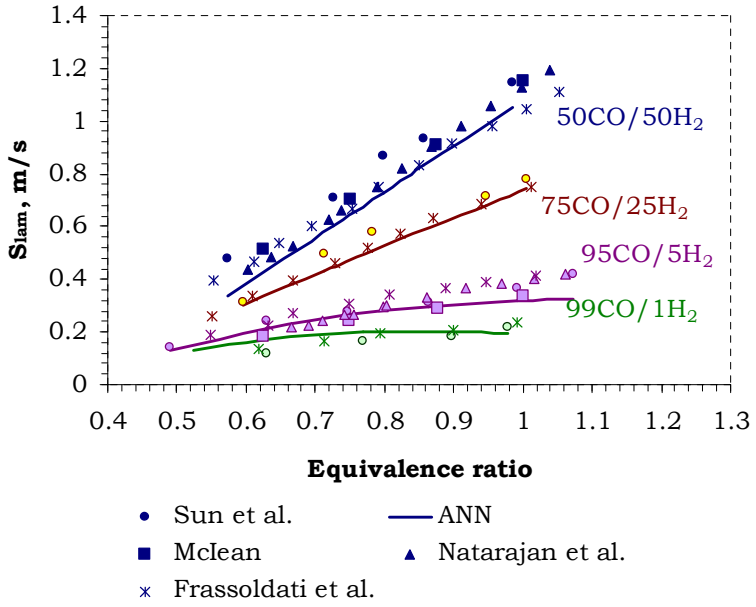

Figure 4.4: Laminar burning velocities for CO/H_2 mixtures: comparison with literature

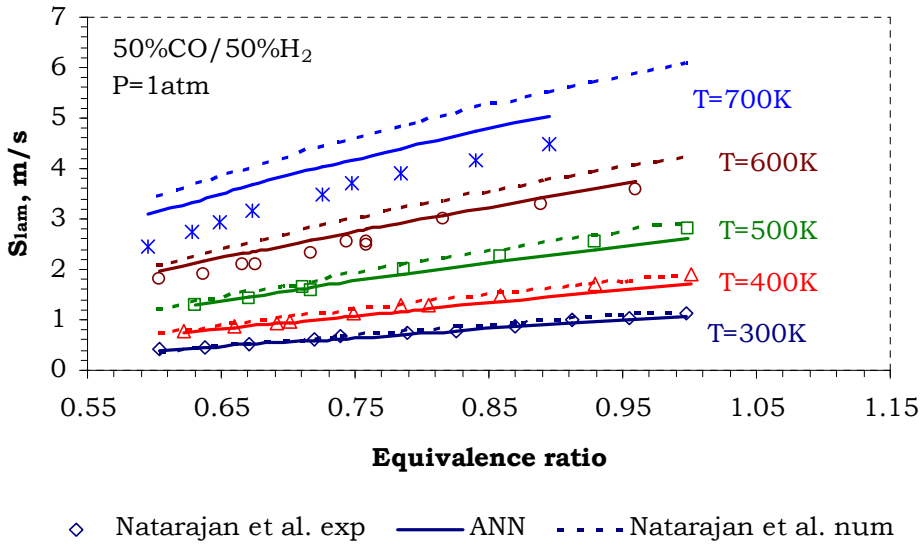

Figure 4.5: Laminar burning velocities for CO/H_2 mixture at high temperatures: comparison with literature [145]

The laminar burning velocity data for CO/H_2 mixtures at high temperatures are limited. In order to validate the ANN, experimental data for a fuel mixture containing 50%CO and 50%H_2, obtained by Natarajan et al. [144], are used. The comparison between these data and the ones computed with ANN shows a good agreement for temperatures up to 600K, see Figure 4.5; the discrepancies are less than 12%, which is acceptable.

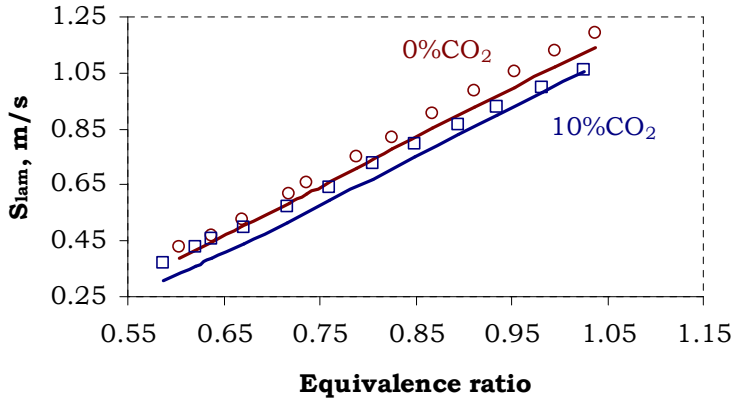

Figure 4.6: Laminar burning velocities for CO/H_2 mixture with CO_2 addition: comparison with literature [145]

Natarajan et al. [144] also presented results of the effect of CO_2 dilution, see Figure 4.6. These values were used to validate the ANN network as well. The comparison between the experimental values and the results from the ANN shows a good agreement, the discrepancies being less than 10% for richer mixtures, but larger for lean mixtures. These authors also indicate that for very lean flames with CO_2 addition, the experimental laminar burning velocities are higher than numerical values.

4.4.2.2 ANN for Critical strain rate to extinction

The artificial neural network for critical strain rate estimation was trained in the same manner. A number of networks with single and two hidden layers (with 6-13 neurons in each layer), with and without early stopping, were tested. From the data presented in Table 4.6 and Table 4.7, the optimal artificial neural network was the one with 8 neurons in a single hidden layer. The decrease of mean square error during training of the network is shown in Figure 4.7.

Table 4.6: Statistical values for ANNs with one hidden layer (critical strain rate to extinction)

Number of Neurons	RMSE	R^2	SSE
LM 6-6-1	0.001494	0.9998	0.001357
LM 6-6-1ES	0.004786	0.9983	0.01392
LM 6-7-1	0.001424	0.9999	0.001232
LM 6-7-1ES	0.002518	0.9995	0.003855
LM 6-8-1	0.001403	0.9999	0.001197
LM 6-8-1ES	0.001585	0.9998	0.001528
LM 6-9-1	0.001225	0.9999	0.0009126
LM 6-9-1ES	0.003505	0.9991	0.007469
LM 6-10-1	0.00097	0.9999	0.0005721
LM 6-10-1ES	0.004696	0.9994	0.004696
LM 6-11-1	0.0009999	0.9999	0.0006079
LM 6-11-1ES	0.003975	0.9989	0.009605
LM 6-12-1	0.001262	0.9999	0.000968
LM 6-12-1ES	0.003121	0.9993	0.005921
LM 6-13-1	0.0007816	1	0.0003714
LM 6-13-1ES	0.002221	0.9996	0.003

Table 4.7: Statistical values for ANNs with two hidden layers (critical strain rate to extinction)

Number of Neurons	RMSE	R^2	SSE
LM 6-6-6-1	0.00113	0.9999	0.0007761
LM 6-6-6-1ES	0.003734	0.999	0.008477
LM 6-7-7-1	0.0008562	0.9999	0.0004457
LM 6-7-7-1ES	0.001732	0.9998	0.001824
LM 6-8-8-1	0.0007186	1	0.000314
LM 6-8-8-1ES	0.003256	0.9992	0.006444
LM 6-9-9-1	0.0005999	1	0.0002188
LM 6-9-9-1ES	0.002118	0.9997	0.002727
LM 6-10-10-1	0.0004478	1	0.0001219
LM 6-10-10-1ES	0.007034	0.9964	0.03008
LM 6-11-11-1	0.0003419	1	7.11E-05
LM 6-11-11-1ES	0.004868	0.9983	0.01441
LM 6-12-12-1	0.0003185	1	6.17E-05
LM 6-12-12-1ES	0.002831	0.9994	0.004872
LM 6-13-13-1	0.0002365	1	3.40E-05
LM 6-13-13-1ES	0.002126	0.9997	0.002748

ES – ANN with early stopping

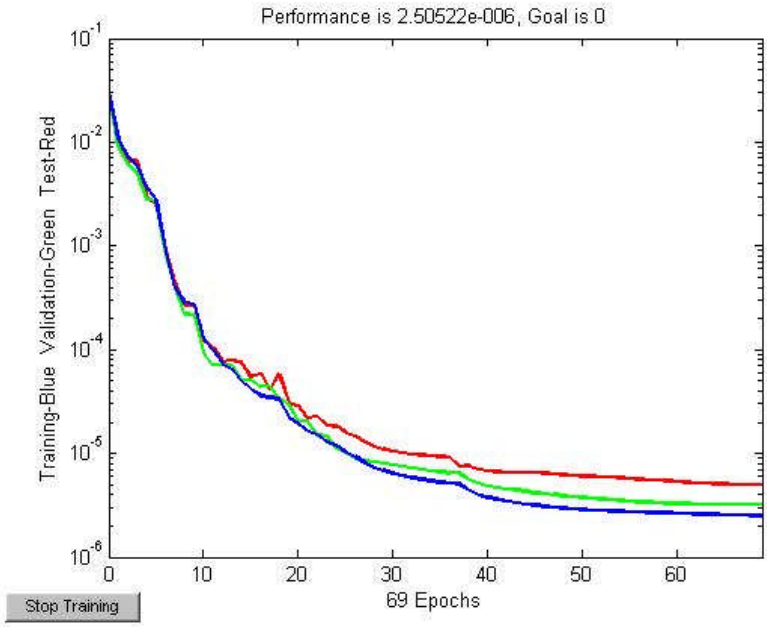

Figure 4.7: Variation of mean square error with training epochs

4.4.2.3 ANNs for Autoignition delays

Several artificial neural networks having pressure, temperature and mixture composition as inputs were trained. Although it had a good training performance and a low testing set error, it failed to predict ignition delay times at high temperatures correctly, see Figure 4.8 and Figure 4.9. For the first network, which was designed to predict autoignition delays for a temperature range of 600-1300K, all the ignition delay data set was normalized by one normalisation factor, which is 5.0E+5s, in order to have all values smaller than 1. Because of this all values of autoignition delay become very small, as low as 1.0E-10. Even though an artificial neural network is able to find relations between inputs and outputs successfully, it fails to predict very low values, which can be even smaller than its accuracy threshold.

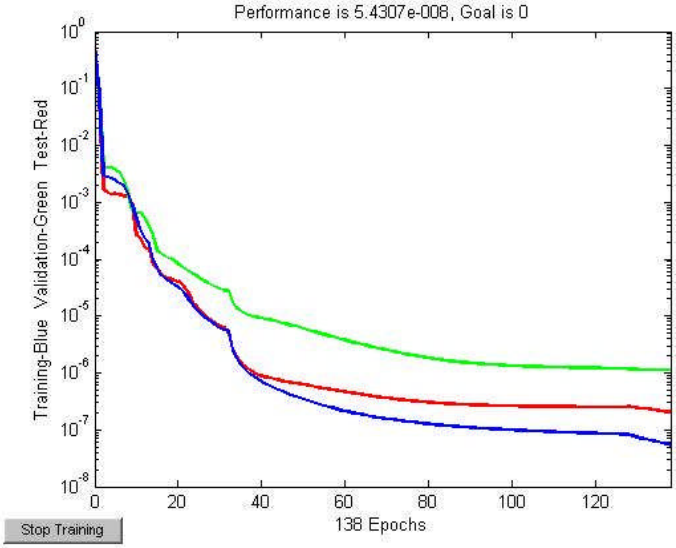

Figure 4.8: Variation of mean square error with training epochs for ANN for autoignition delay prediction

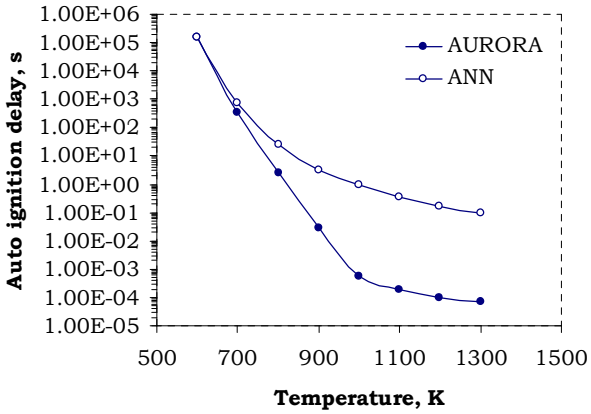

Figure 4.9: The comparison between autoignition delay, obtained with AURORA and ANN for mixture with 70%CO/10%H_2/20%N_2 at ambient pressure

In addition, another artificial neural network for the temperature range between 900K and 1300K was trained. It also had a good training performance and low testing error, but it failed to predict autoignition delay time at high temperatures.

These attempts to train ANNs for ignition delays demonstrated that the ANN has great difficulty when handling a data set where differences between minimum and maximum values are of several orders of magnitude. Therefore this method cannot be used for ignition delay data processing.

4.5 Conclusions

Detailed experimental and computational methodologies adopted in the present study are presented. The validation experiments for the Bunsen burner method with 50%CO/50%H_2 – air mixture show good agreement with the measured laminar burning velocities from the published literature.

The application of artificial neural networks (ANNs) to predict laminar burning velocities, critical strain rates to extinction and autoignition delays was discussed in this chapter as well. ANNs can be successfully employed to predict laminar burning velocities and critical strain rates to extinction, but they failed when applied for the prediction of autoignition delays. The validation simulations for different CO/H_2 – air mixtures show good agreement with the laminar burning velocities predicted by ANNs from the published literature.

Having demonstrated the accuracy of the experimental facility, in the next chapter experimental results obtained from the tests with syngas mixtures will be presented.

5 Experimental results

As was discussed earlier syngas composition varies depending on the gasification process. Normally it is composed of hydrogen and carbon monoxide with some diluents like nitrogen, carbon dioxide and water. The presence of highly diffusive hydrogen complicates the combustion phenomenon through selective diffusion of component gas molecules. Flame stretch at the tip due to the strong curvature effects and preferential diffusion of heat or mass because of non-unity Lewis numbers alters the flame structure as well.

Experiments with several CO/H_2 mixtures burning in air unveiled various flame phenomena such as open tip flames, polyhedral flames with varying number of edges, highly luminous inner cone and smooth cones with uniform luminosity. The objective of the present study was to measure laminar burning velocities of syngas–air mixtures as a function of equivalence ratio, temperature and pressure. The area averaged laminar burning velocity measurements need to be limited to continuous and smooth flame structures. Therefore the range of mixture equivalence ratios is very limited.

Experiments were performed with the following three $CO/H_2/N_2$ mixtures: 67%CO/33%H_2; 1.5%CO/28.5%H_2/70%N_2; 50%CO/50%H_2 and one H_2/N_2 mixture with 57%H_2 and 43%N_2. Laminar burning velocities for these gases were obtained on a straight pipe of 5mm in diameter and 50 diameters in length. This pipe produces fully developed laminar pipe flow.

Earlier experiments with a fuel mixture of 67%CO/33%H_2 were performed on a convergent nozzle with a 10mm exit diameter, machined in

stainless steel and incorporating a 4:1 contraction in order to produce aerodynamic stretch free flames.

5.1 Polyhedral flames

Cellular flame structures with the formation of cells and ridges of characteristic sizes over the flame surface are very beautiful and an intriguing phenomena in flame dynamics [129]. Cellular flame structures in premixed flames are widely discussed phenomena [130, 131]. The basic mechanisms driving cellular flame instabilities and many aspects of the flame dynamics are believed to be explained quite well [132] through preferential diffusion instability, hydrodynamic instability and acceleration instability. Cellular flames on a Bunsen burner are the graphic appearance of polyhedral flames. The flame pattern consists of flame surfaces which have the appearance of petals. These surfaces are separated by extinguished regions of ridges, with the "petals" being convex towards the unburnt mixtures. The number of ridges varies with the mixture strength and the flow velocity. In addition, the polyhedral flames rotate rapidly about a central axis. This rotation is usually accompanied by an increase in the number of ridges [133].

In the present investigation, polyhedral flames at ambient pressure were obtained in the equivalence ratio range of 0.626 to 0.786 for the fuel mixture 1.5%CO/28.5%H_2/70%N_2, one flame at equivalence ratio 0.523 for fuel mixture 50%CO/50%H_2, and 0.499 to 0.541 for fuel mixture 57%H_2/43%N_2. No polyhedral flames were observed for mixture 67%CO/33%H_2. The number of sides of polyhedral structure varied from 3 edges at an equivalence ratio of 0.523 (50%CO/50%H_2) to 10 edges at an equivalence ratio of 0.7433 (1.5%CO/28.5%H_2/70%N_2). All high pressure

flames had polyhedral shapes. Schlieren photographs of all fuel mixtures, Figure 5.1, show the number of edges varied from 4 to 10.

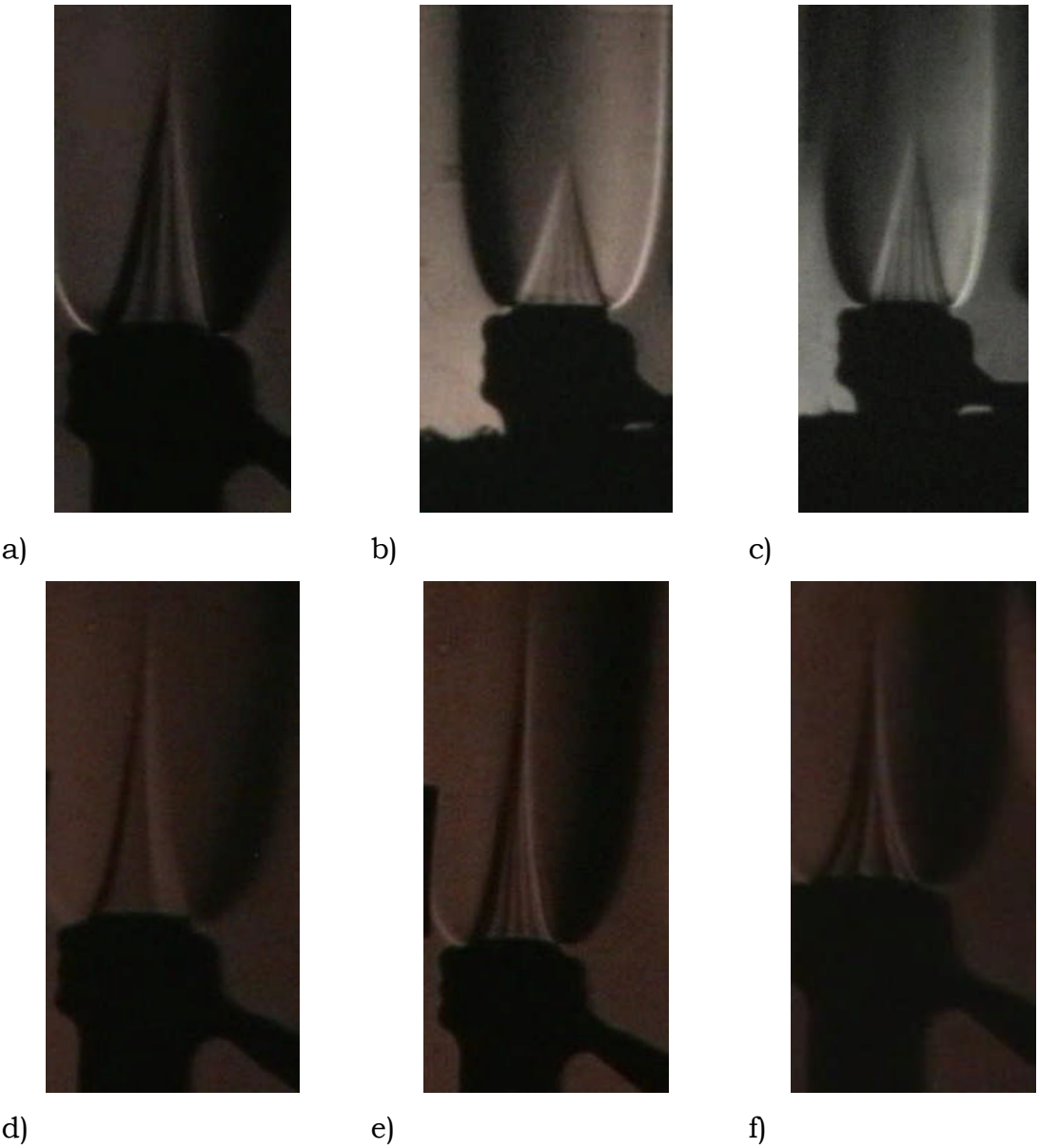

Figure 5.1: Polyhedral flames; a) mixture 67%CO/33%H_2 at ϕ=0.522, T=435K, P=3.05bar; b) mixture 50%CO/50%H_2, at ϕ=0.464, T=517K, P=4.29bar, c) mixture 57%H_2/43%N_2 at ϕ=0.521, T=517K, P=2.9bar; d) mixture 1.5%CO/28.5%H_2/70%N_2 at ϕ=0.786, T=290K, P=1bar; e) at ϕ=0.743, T=290K, P=1bar, f) at ϕ=0.685, T=340K, P=1.99bar

The formation of polyhedral flames is related to the presence of hydrogen in the fuel mixture. Polyhedral flames have been observed in lean mixtures of hydrogen-air and rich mixtures of heavy hydrocarbon-air flames [134].

Behrens [134] observed the formation of polyhedral flames with the addition of small quantities of hydrogen into methane flames. A pure methane-air flame always retains its homogeneous undisturbed surface. A similar phenomenon was observed by Garside et al [133] with premixed carbon monoxide-air and propane-air mixtures. Addition of small quantities of hydrogen produced polyhedral flames for both mixtures. The presence of hydrogen in the "free state" was considered to be a possible reason for such phenomena. Hydrogen is at first released in pre-flame reactions and then the free hydrogen diffuses into specific zones until its concentrations reach the required level for combustion. The zonal combustion creates the polyhedral shape of the flame, since the burning velocity in the hydrogen-rich zones will be greater than anywhere else. Behrens [134] also attributed the flame structure irregularity to the presence of the H radicals. In the case of hydrocarbon flames, intermediate formation and burning of hydrogen is considered to be responsible for the irregularity of the flame surface. However, in methane combustion, no hydrogen was found to be forming intermediately. Therefore the flame has a very stable structure for all concentrations.

When a balance between the supply of hydrogen and its consumption is achieved, the flame becomes very stable and stationary. Hertzberg [135] considers the polyhedral flames to be stable structures. He also proposed a flame perturbation analysis of cellular flames. It is based on the theory that cellular flames in lean mixtures of hydrogen-air and rich mixtures of

heavy hydrocarbon-air flames are formed because of the selective diffusion of oxygen or fuel, depending on their diffusional velocities. The rapid chemical reactions in the flame front, propagating into the homogeneous premixed mixture, will generate large concentration gradients. As a result, both fuel and oxidiser molecules will have large diffusion velocities into the flame front. If either oxidiser or fuel molecule has greater diffusion velocity, it will diffuse selectively (preferentially) into the flame zone. The flame propagation rate will then be influenced and the mixture will become leaner or richer, in comparison to its original composition, depending on whether oxidant or fuel molecule has the greater diffusivity. Any shift in actual composition of the reactant mixture will cause a shift in laminar burning velocity of the mixture relative to its value when there is no selective diffusion.

In the case of hydrogen, the fuel (hydrogen) molecule has much higher diffusivity in comparison to the oxidiser (oxygen); therefore the hydrogen will preferentially diffuse into the flame zone. As a result the reactant mixture will behave as if it is richer, compared to the initial composition [135].

This provides the general notion that cellular structures are formed in a mixture containing a deficient amount of highly diffusive components. Hertzberg's [135] perturbation analysis also shows that cellular flame structures are not instabilities, but rather stable curvilinear flame structures which involve a complex, multidimensional balance between flow velocities, diffusion velocities and flame propagation velocities.

5.2 Weak tip flames

Some weak flames at high pressures with equivalence ratio between 0.548 and 0.97 for fuel mixture 1.5%CO/28.5%H_2/70%N_2 had a tip which was barely luminous or even completely open. This was observed from schlieren images. Bunsen burner flame tip opening/weakening is attributed to the non-equidiffusive mixture (non unity Lewis numbers) along with the presence of a strong stretch at the tip of the flame [136].

Burning intensity of premixed Bunsen flames is affected only in the concurrent presence of stretch effects due to flame curvature and preferential diffusion of heat or mass. Mizomoto et al [137, 138] quantified these effects and showed that lean hydrogen-air mixtures have open tips because of the presence of a strong curvature at the tip. For mixtures with Lewis number less than unity the effect of flame stretch due to flame curvature is significant. They also demonstrated the opposite effect (brightening of the tip) for rich hydrogen-air mixtures. For propane-air mixtures the tip effects are opposite: the tip is more intensive for lean mixtures and open for rich mixtures. In another study, Law et al [139] also examined the combined effect of preferential diffusion of heat or mass and stretch on the flame temperature and burning intensity.

5.3 Smooth cone with uniform luminosity

For mixtures 67%CO/33%H_2, 50%CO/50%H_2 and 57%H_2/43%N_2 at ambient pressure, flames formed smooth inner cones with uniform luminosity. Only a few very lean flames with equivalence ratio below 0.55 attained polyhedral shapes.

For mixture 1.5%CO/28.5%H_2/70%N_2, flame cones at equivalence ratio above 0.78 were smooth. Flames were bright blue in colour. Flames of mixture with 57%H_2/43%N_2 were hardly visible.

Schlieren photography was used to measure the premixed inner cone area to calculate the laminar burning velocities.

5.3.1 Mixture with 67%CO/33%H_2 at ambient conditions

The burning velocities were found to vary from 0.3 m/s to 0.67 m/s for the measured range. Laminar burning velocities at ambient conditions for this mixture were obtained using two arrangements: 10 mm converging nozzle and straight tube. The burning velocity variation with equivalence ratio is shown in Figure 5.2.

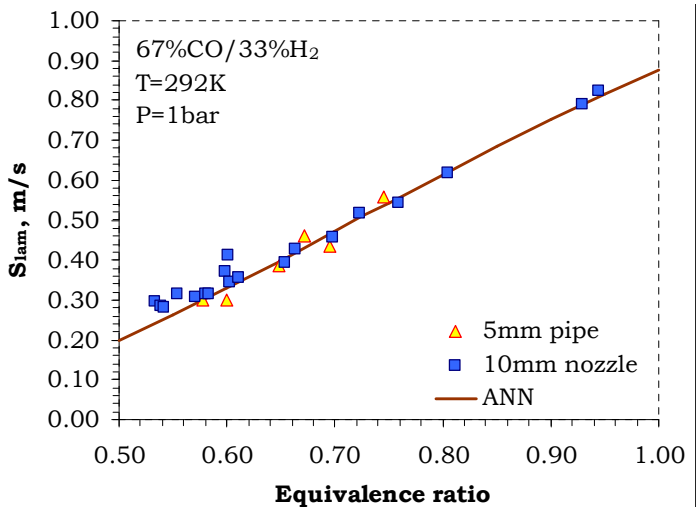

Figure 5.2: Laminar burning velocities for 67%CO/33%H_2 mixture at ambient conditions obtained with 10mm nozzle and 5mm pipe and compared to artificial neural network

From Figure 5.2 it can be seen that there is no large difference between laminar burning velocity values obtained with the two burner arrangements for equivalence ratios between 0.6 up to 0.75. In addition, experimental values compare very well with results obtained from the

Artificial Neural Network (ANN). There is linear relationship between laminar burning velocity and equivalence ratio. The discrepancy between experimental and numerical data is less than ±4%, which is acceptable. The laminar burning velocity values obtained with the 5mm straight tube are more scattered; the discrepancies are less ±10%. For leaner flames, with equivalence ratios of less than 0.6, the experimental laminar burning velocities are higher and more scattered in comparison to the numerical values; the discrepancies between some experimental and numerical values are as high as ±20%.

The reason for changing the nozzle is that flames, at equivalence ratios 0.95 and higher, attain irregular shapes, see Figure 3.3. As was discussed earlier for mixtures with Le<1, increase in stretch created by preferential diffusion increases flame temperature and laminar burning velocity, while negative aerodynamic stretch created by flow velocity gradient will have opposite effects on the flame. It will therefore help to eliminate these irregularities.

In addition to the mentioned effects, flame can be subjected to stretch caused by preferential diffusion.

5.3.1.1 The effect of the burner rim cooling

In addition a water-cooled jacket was also mounted near the rim of the 5mm tube burner in order to stabilise flames at higher pressures and minimise the heat transfer effects from the flame to the burner rim.

Experiments were performed on the 5mm tube with and without burner rim cooling in order to investigate the effect of rim cooling on laminar burning velocity.

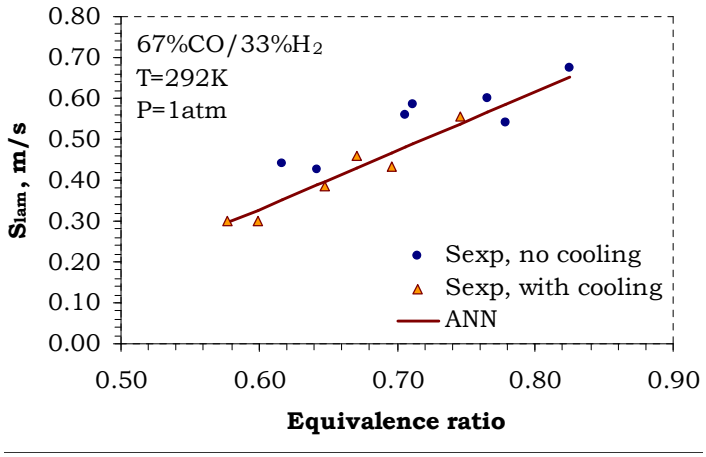

Figure 5.3: Laminar burning velocities for 67%CO/33%H_2 mixture at ambient conditions for experiment with and without mounted water cooling jacket

The results with both configurations (with and without cooling jacket) are presented in Figure 5.3. From the results it can be seen that laminar burning velocities with cooling arrangement are slightly lower in comparison to ones without nozzle rim cooling. The laminar burning velocities for the arrangement without cooling are over-predicted. It can be observed that there is no systematic over-prediction; some differences in experimental laminar burning velocities are larger while some are comparatively close to the numerical values. This can be explained by the flame stabilisation at higher mass flows, which resulted in higher hydrodynamic strains and higher heat transfer from the burner rim to the reactants.

This is non intuitive, as it would have been expected that these effects would be reversed as the residence time of the reactants in contact with the nozzle wall is shorter. The velocity increase in the nozzle tube results in higher heat transfer even though the residence time is shorter.

The experimental arrangement with the cooling jacket was chosen to perform the experimental campaign.

5.3.2 Mixture with 50%CO/50%H_2 at ambient conditions

The burning velocities were found to vary from 0.31 m/s to 1.79 m/s for the measured range, see Figure 5.4. The experimental laminar burning velocities compare well with numerical values; the discrepancy is less than 10%, which is acceptable.

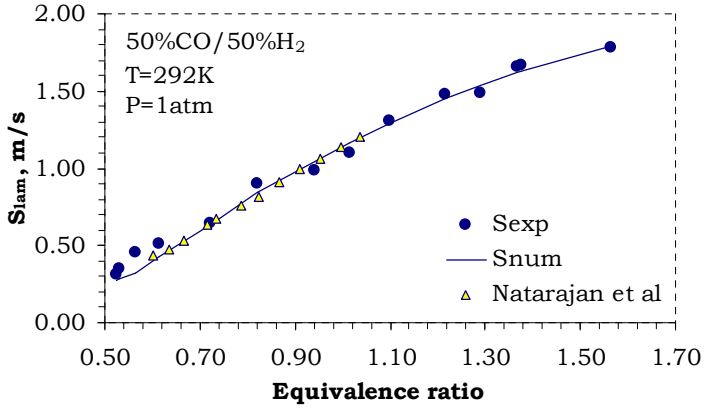

Figure 5.4: Laminar burning velocities for 50%CO/50%H_2 mixture at ambient conditions

In addition, laminar burning velocity values obtained in this study compare well with Bunsen burner experiments performed by Natarajan et al [144].

5.3.3 Mixture with 1.5%CO/28.5%H_2/70.0%N_2 at ambient conditions

The burning velocities were found to vary from 0.23 m/s to 0.50 m/s for the measured range, see Figure 5.5. The experimental laminar burning velocities compare reasonably well with numerical values; the discrepancy is less than 20% (in most data points it is less than 10%), which is acceptable.

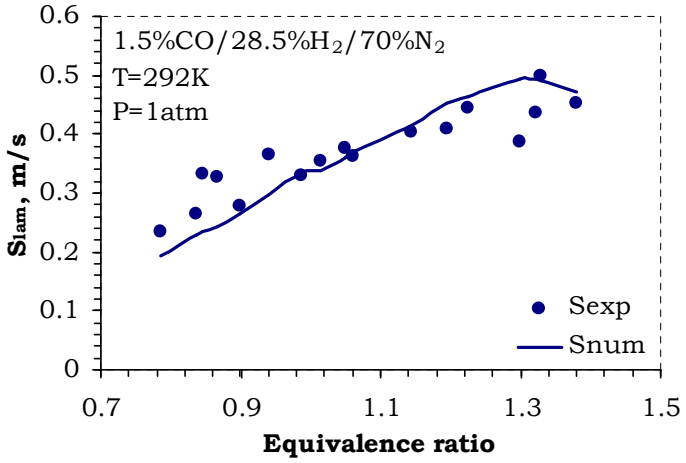

Figure 5.5: Laminar burning velocities for 1.5%CO/28.5%H_2/70%N_2 mixture at ambient conditions

The discrepancies are larger for leaner flames. This is because these flames attained polyhedral shapes for almost the entire range of equivalence ratios. This resulted in higher errors in the flame area calculations. In addition, as was discussed earlier, the actual mixture composition at the flame front is richer in comparison to the initial one, which was 1.5%CO/28.5%H_2/70%N_2.

5.3.4 Mixture with 57%H_2/43%N_2 at ambient conditions

For this mixture the burning velocities vary from 0.28 m/s to 1.22 m/s for the measured range, see Figure 5.6. The experimental laminar burning velocities compare reasonably well with numerical values for equivalence ratios higher than 0.6; the discrepancy is less than 10%, which is acceptable. For flames at lower equivalence ratios, the discrepancy is much larger – around 50%; the experimental laminar burning velocities are considerably larger in comparison to the numerical values.

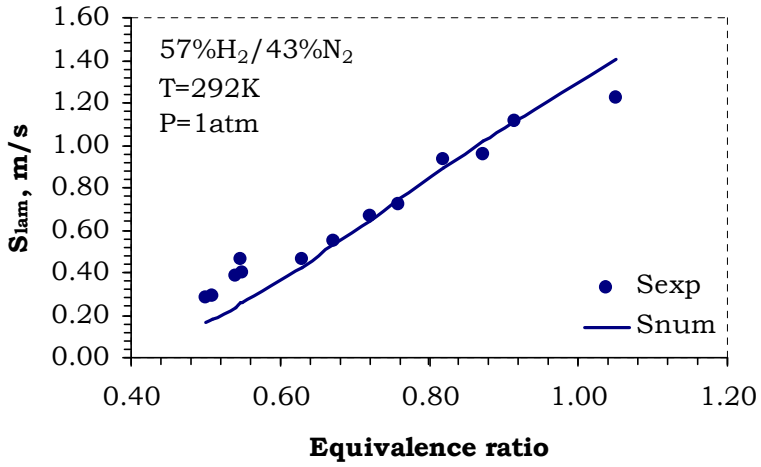

Figure 5.6: Laminar burning velocities for 57%H_2/43%N_2 mixture at ambient conditions

The burning velocity can be seen to peak at an equivalence ratio of 1.6 for 50%CO/50%H_2 and 1.3 for 1.5%CO/28.5%H_2/70%N_2, see Figure 5.4 and Figure 5.5. The experimental results for 67%CO/33%H_2 and 57%H_2/43%N_2 also indicate that maximum laminar burning velocities should be achieved at equivalence ratios higher than unity; see Figure 5.2 and Figure 5.7. This is in disagreement with the laminar burning velocity peaking trends for the other hydrocarbon fuel-air mixtures, where maximum burning velocities are near stoichiometric concentrations. The reason for these differences is that the flame structure of the mixture is governed by the presence of hydrogen. For a pure hydrogen-air mixture laminar burning velocity peaks at an equivalence ratio of 1.8 [62] at ambient temperature and pressure. The reason for such behaviour is that flame zone reactivity depends not only on the chemical reaction rate within the flame front, but also on the rate of back diffusion of heat and free radicals from the burned gases to the unburned mixture. This back diffusion is needed to activate the reactants. Hertzberg [135] showed that although the reaction rate for an hydrogen-air stream reaches a maximum

at stoichiometric conditions, the maximum effective diffusivity is at much higher hydrogen concentrations. Therefore the maximum burning velocity can be found at equivalence ratios greater than unity; it is at equivalence ratios around 1.6 and 1.3 respectively. This is true for all hydrogen containing mixtures, whose behaviour is primarily dictated by the presence of hydrogen.

5.3.5 Effect of reactant mixture preheat

In order to investigate the effects of reactant preheat all the mixtures were tested over the range of temperatures from room temperature to 600K.

As the unburned reactant temperature increases, the laminar burning velocity also rises. The increase in laminar burning velocity requires operating at higher average flow velocities. The flow in the tube remains laminar due to the increase in gas viscosity. 67%CO/33%H_2 tests were performed on the 10mm burner, while for the other three mixtures tests were performed on the 5mm tube burner.

The effect of preheat temperature for the 67%CO/33%H_2 fuel mixture is shown in Figure 5.7. The measured and computed laminar burning velocities compare well up to a preheat temperature of 443K over the entire range of equivalence ratios. As the temperature is increased further, the discrepancy between measured and calculated laminar burning velocities increases, with larger differences for richer mixtures. The computed laminar burning velocities over-predict measured values by as much as 20%.

Similar results were obtained with 50%CO/50%H_2 fuel mixture composition, see Figure 5.8. As in 67%CO/33%H_2 case, the computed and measured laminar burning velocities are in good agreement up to 400K.

Above this temperature, the discrepancy between computed and experimental values increases again. The computed laminar burning velocities are higher than experimental ones; the discrepancy is around 15%. Natarajan et al [144] obtained similar results for this mixture as well.

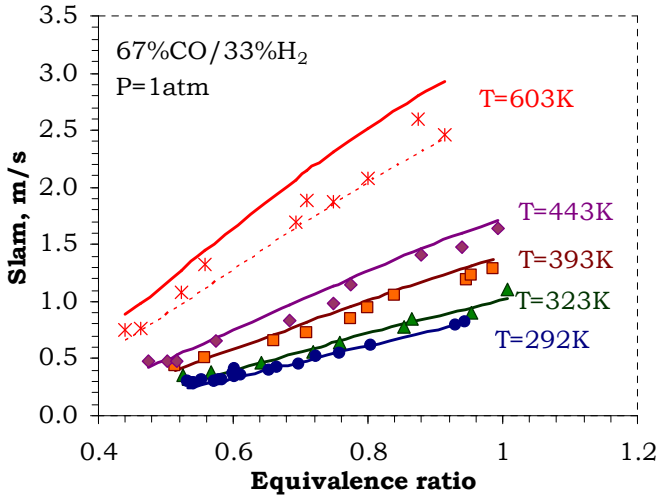

Figure 5.7: Laminar burning velocities for 67%CO/33%H_2 mixture at various preheat temperatures (10mm converging nozzle); points: experimental results, lines: numerical and dotted line: T-50K

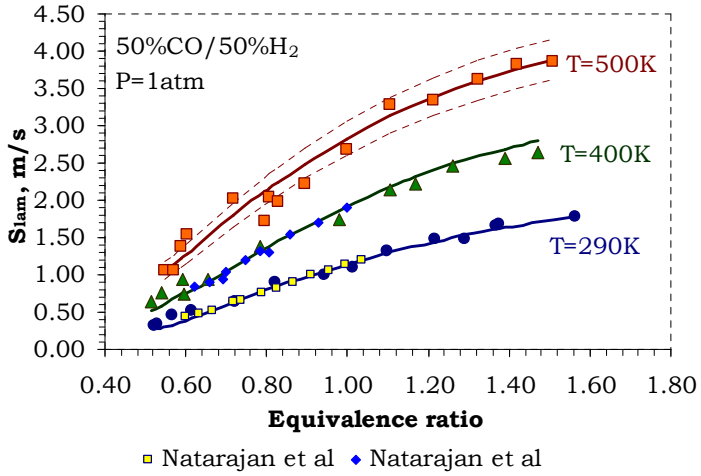

Figure 5.8: Laminar burning velocities for 50%CO/50%H_2 mixture at various reactant temperatures; points: experimental results, lines: numerical and dotted lines: T±20K

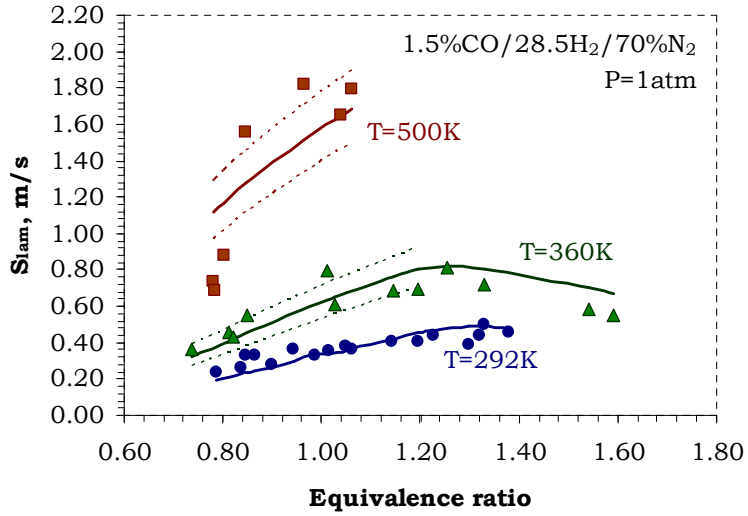

Figure 5.9: Laminar burning velocities for 1.5%CO/28.5%H_2/70%N_2 mixture at various reactant temperatures; points: experimental results, lines: numerical and dotted lines: T±20K

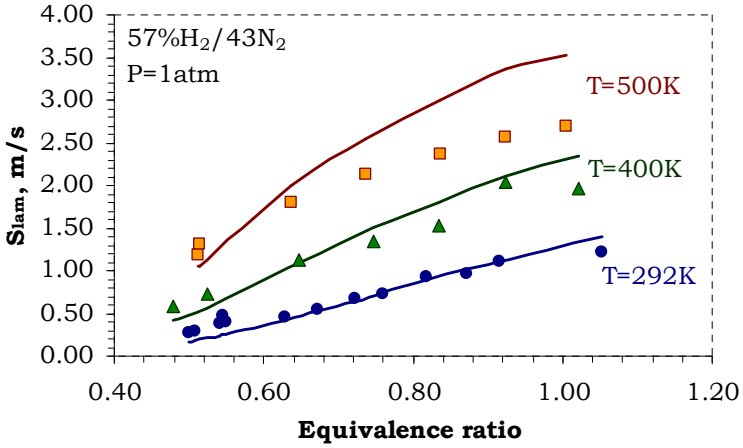

Figure 5.10: Laminar burning velocities for 57%H_2/43N_2 mixture at various reactant temperatures

For fuel mixture with 1.5%CO/28.5%H_2/70%N_2, experimental laminar burning velocities again compare well with numerical values at preheat temperature of 360K; the discrepancy is less than 10%, Figure 5.9. For a

temperature of 500K, the experimental values are more scattered because the reactants' exit temperature was not exactly 500K, but varied between 480K and 525K. The discrepancy between experimental and numerical laminar burning velocities at preheat temperatures of 500K is around 20%.

For fuel mixture with 57%H_2/43%N_2 the discrepancies between experimental and numerical values are less than 30% at preheat temperature of 500K, see Figure 5.10. The numerical laminar burning velocities over predict in comparison to the experimental values. As for other all gases, at preheat temperatures of 400K, the experimental and numerical values compare very well. The discrepancies are less than 10%, which is very acceptable.

The difference between the experimental results and the numerical predictions at higher preheat temperatures indicates either errors in the temperature dependence of the chemical mechanism or gas properties (e.g., diffusivities) used in the computations [144]. The difference may also be due to errors in the current measurements.

The measurements of the reactant preheat temperatures are challenging. This is because thermocouple measurements at the burner exit are impractical and can only be made upstream or in the absence of the flame.

One possible way of measuring reactant temperature is by placing a thermocouple on the burner wall (assuming that gas temperature is close to the burner wall temperature). The thermocouple should be close to the burner rim, as some heat is lost by the heat transfer from the tube to the surrounding. This effect becomes more significant with increase in reactant preheat temperatures. In addition, the temperature cannot be

measured precisely enough due to the heat transfer from the flame to the burner rim. This would result in much higher recorded temperature.

It is not practical to put the thermocouple in the flow stream as well, because it will distort the flow. Laminar flames are very sensitive to the smallest flow distortions.

5.3.6 Effect of pressure

Experiments for all four gases were performed at higher pressures to investigate the pressure effect on laminar burning velocity.

Results for high pressure tests of a gas fuel mixture composed of 33%H_2/67%CO obtained on the 5mm tube are presented in Figure 5.13. For this experimental arrangement stable laminar flames were acquired for pressures up to 5 bar and for very lean mixtures with equivalence ratios below 0.7. Only a very few flames were stabilised at 6 and 7 bars.

In general, it has not proved possible to get data for richer flames because the Re number in the tube approaches 2000 and the flow enters the transitional to turbulent regime. Theoretical computations show that with increase in pressure the limiting equivalence ratio drops; see Figure 5.11 and Figure 5.12. In order to minimise flame curvature effects at the flame tip and base, longer flames need to be stabilised. Therefore the equivalence ratio range for the available data (when the flame is laminar) becomes narrower. In addition, in order to avoid a flashback, higher mass flows are needed to stabilise the flame.

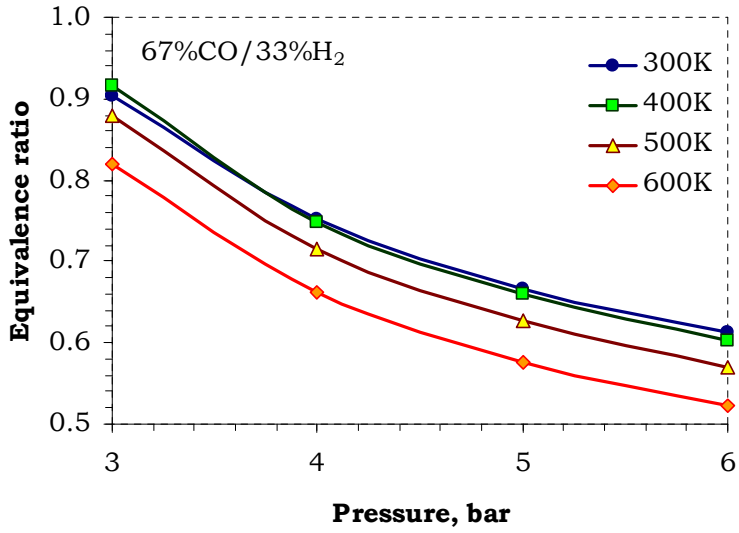

Figure 5.11: Computed conditions for which Re=2000, when assumed reactants velocity is three times higher than laminar burning velocity and laminar burning velocity remains constant with increase in pressure

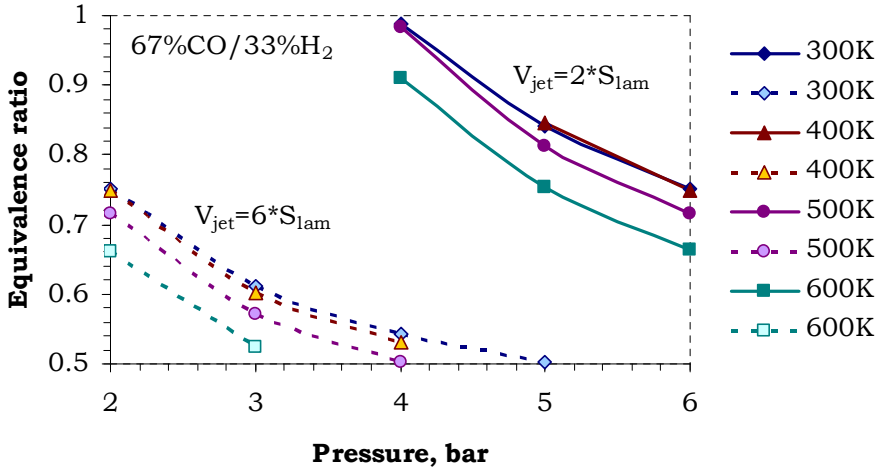

Figure 5.12: Computed conditions for which Re=2000, when laminar burning velocity is two times and six times lower than reactants velocity and laminar burning velocity is assumed to remain constant with increase in pressure

Unlike the numerical simulations, these experiments indicate that pressure has little effect on laminar burning velocities at very lean

equivalence ratios. Numerical simulations show that the laminar burning velocity falls by a factor of 2 with an increase in pressure from 1 to 3 bar.

The results for mixtures with 50%CO/50%H_2, 1.5%CO/28.5%H_2/70%N_2 and 57%H_2/43%N_2 show similar trends. Experimental laminar burning velocities for these mixtures are highly overpredicted in comparison to the numerical values. Even where the data points are scattered, results indicate that laminar burning velocities are little affected by pressure rise.

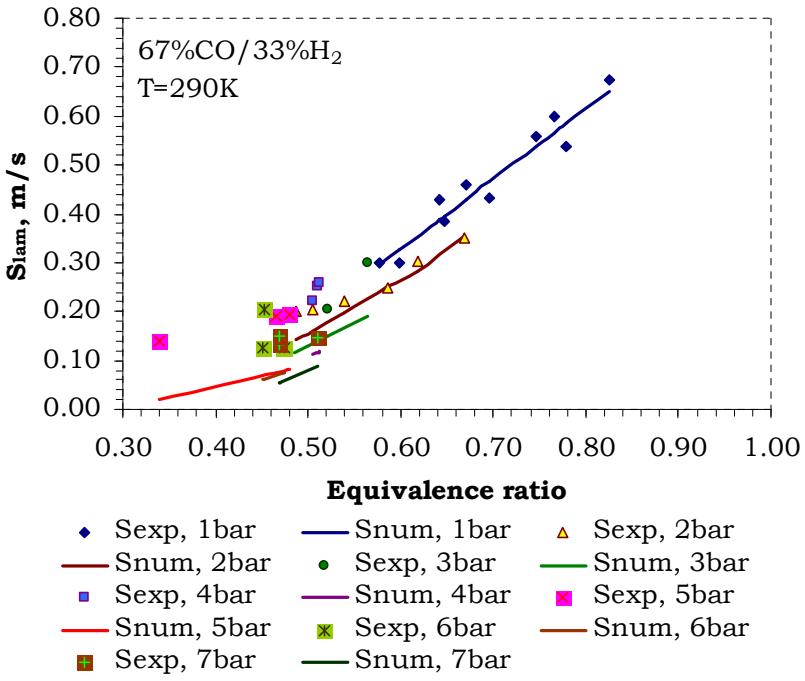

Figure 5.13: Laminar burning velocities of 33%H_2/67%CO fuel mixture at different pressures

For a mixture with composition of 50%CO/50%H_2, laminar burning velocities at 4bar pressure were obtained for lean mixtures with equivalence ratios between 0.43 and 0.48, see Figure 5.14. These equivalence ratios are close to the lean flammability limit. Again it was not possible to obtain laminar flames for richer mixtures, as the flow in the

pipe would enter the transitional to turbulent region. This mixture is more reactive than 67%CO/33%H_2; therefore the laminar burning velocities are greater and require higher mass flows to stabilise flames.

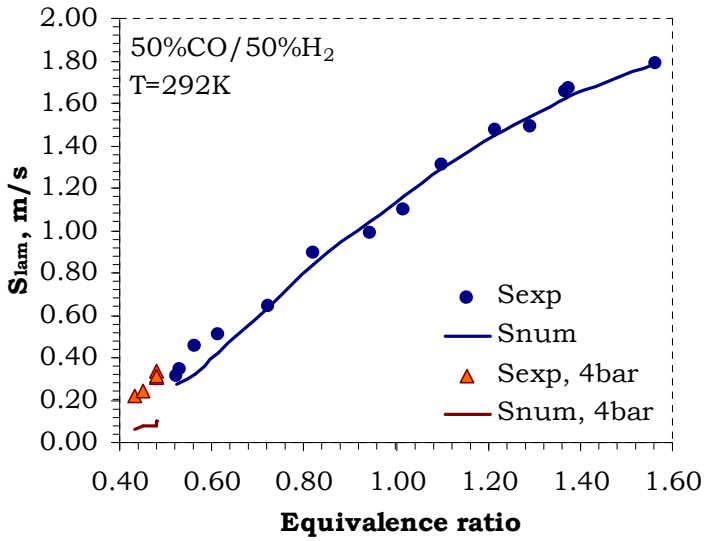

Figure 5.14: Laminar burning velocities for 50%CO/50%H_2 mixture at ambient and 4bar pressures

For a mixture with 1.5%CO/28.5%H_2/70%N_2, it was possible to get laminar burning velocities for flames at equivalence ratios between 0.64 and 0.9 and reactant temperatures of 292K and 400K, see Figure 5.15 and Figure 5.16. From the two figures it can be seen that flames were stabilised over a broader equivalence ratio region for 400K reactant preheat temperature.

In comparison to other investigated fuels, this mixture is greatly diluted with nitrogen. The laminar burning velocities are much lower; consequently laminar burning velocity data were obtained at richer equivalence ratios as lower mass flows are needed to stabilise flames. In addition, the lower flammability limit of this mixture is at richer fuel-air in comparison to other investigated fuels.

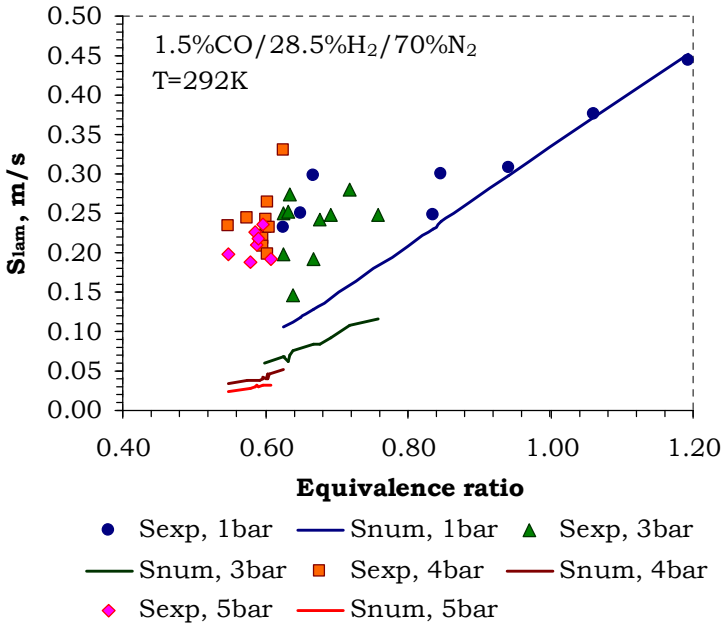

Figure 5.15: Laminar burning velocities for 1.5%CO/28.5%H_2/70%N_2 mixture at different pressures

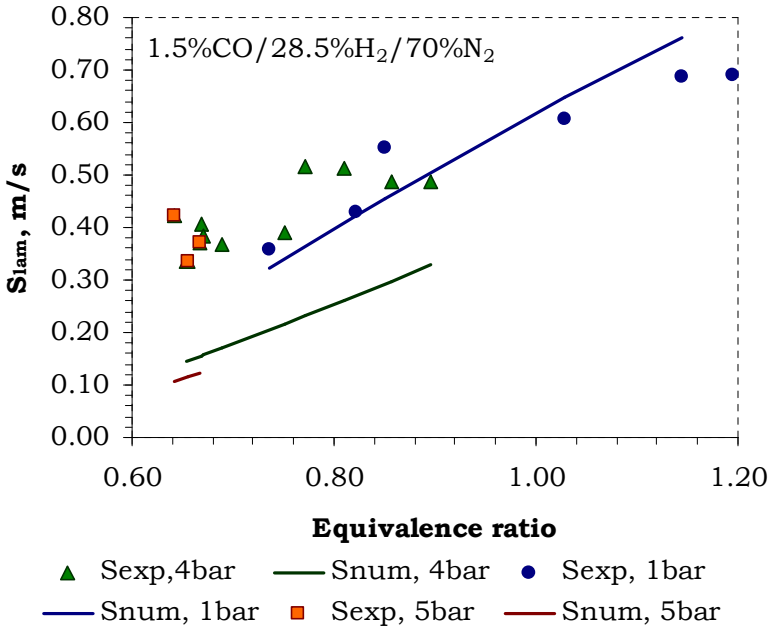

Figure 5.16: Laminar burning velocities for 1.5%CO/28.5%H_2/70%N_2 mixture at different pressures and T=360K (1bar pressure) and T=400K (4bar and 5bar pressure)

For a mixture with a composition of 57%H_2/43%N_2 laminar burning velocities were obtained at 2bar pressure and equivalence ratios between 0.48 and 0.75, see Figure 5.17. These data were obtained at 500K temperature, because it was not possible to stabilise any laminar flames at ambient temperature and higher pressures for this mixture. Laminar burning velocities are high for this mixture. Therefore higher mass flows are needed to avoid flashback and achieve stable flames.

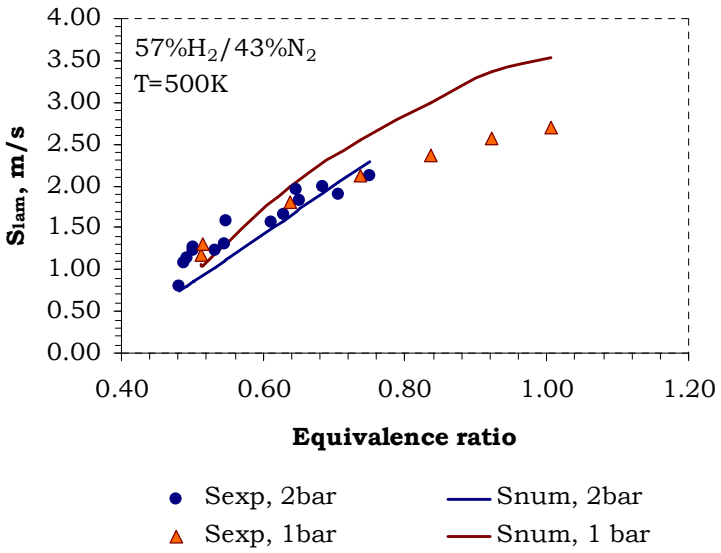

Figure 5.17: Laminar burning velocities for 57%H_2/43%N_2 mixture at different pressures and 500K temperature

A possible explanation for the discrepancies between experimental and numerical values could be that the experimental values are correct and there are shortcomings in the GRI Mech 3.0 mechanism at high pressures for very lean flames, as the mechanism was designed and validated to simulate methane combustion under ambient conditions.

Alternatively, it is possible that the actual flame area is substantially under-estimated from the Schlieren images, resulting in an over-estimate

of laminar burning velocity. Lean flames at higher pressures appear increasingly susceptible to cellular disturbance promoted by preferential diffusion instability.

Another explanation could be that heat is transferred from the flame into the rim of the burner due to conduction upstream. Some heat is then transferred into the reactants' flow raising the gas temperature, while some of it is carried away by cooling water. As the laminar burning velocities are comparatively low, the reactants' flow velocity is lower as well. The reactant heating effects on laminar burning velocity of lean flames at high pressures are significant.

Limits between flame flashback and blowout are very narrow for these flames as well. This limitation makes it difficult to stabilise the flame under the desired conditions.

5.4 Conclusions

Laminar burning velocities for medium and low calorific value gas at different preheat temperatures and pressures were presented as a function of equivalence ratios. Tests were performed on converging nozzle and straight tube experimental setups. Polyhedral flames were seen to form for all fuel mixtures at equivalence ratios close to the lean flammability limit. It was observed that severe stretch at the tip of the premixed cone, along with preferential diffusion due to the presence of hydrogen, can break the tip.

Laminar burning velocity values for mixtures with compositions of 67%CO/33%H_2, 50%CO/50%H_2, 57%H_2/43%N_2 and 1.5%CO/28.5%H_2/70%N_2 were presented. There is good agreement between experimental and numerical values at ambient conditions for all

mixtures; the discrepancies are less than ±10%. Only for flames at equivalence ratios close to the lean flammability limit the errors are larger.

All mixtures were tested over the temperature range from room temperature to 500K (and for 67%CO/33%H_2 up to 600K) in order to evaluate the reactants' preheat effect on laminar burning velocity. For all mixtures, measured laminar burning velocities compare well with computed values for temperatures up to 400K. For higher temperatures the numerical laminar burning velocities over-predict measured values by 20%.

High pressure tests were performed with all mixtures, and pressure effects on laminar burning velocity were evaluated. Data were obtained for very lean flames close to their flammability limit. It was not possible to get data for richer flames, because the Reynolds number in the tube approached 2000 and flow entered the transitional regime. Experimental laminar burning velocities data indicate that the effect of pressure on laminar burning velocity is small, while numerical predictions show that laminar burning velocity falls by a factor of 2 with a pressure rise from 1bar to 3bar.

The next chapter presents the computational results of unstretched laminar burning velocities calculated using a 1D freely propagating flame model of CO/H_2/Diluents–Air mixtures for a range of pressures, preheat temperatures, and an equivalence ratio range between 1 and the lean flammability limit.

6 Numerical simulations results

6.1 Introduction

The background to flame kinetics modelling is presented in Section 4.3. This approach has been employed to investigate laminar burning velocities of $CO/H_2/CH_4$/Diluent – Air flames. The following diluents, added to the $CO/H_2/CH_4$ fuel mixture, are N_2, H_2O and CO_2. A large range of $CO/H_2/CH_4$/Diluent fuel mixture compositions were studied numerically in order to develop a comprehensive laminar burning velocity database. The effects of temperature, pressure and mixture strength on laminar burning velocity were also investigated.

The freely propagating flame model (similar to PREMIX in CHEMKIN) in the open-source code Cantera [140] with the GRI-Mech 3.0 mechanism was used for laminar burning velocity simulations. The GRI-Mech 3.0 mechanism was chosen because it is the most widely researched and employed in the combustion community, especially for methane flames, but it also contains comprehensive H_2 and CO combustion chemistry.

The critical strain rate to extinction for these mixtures was modelled using the opposed-flow, diffusion flame model (OPPDIF) in the commercial code CHEMKIN [141].

Data on ignition delay for $CO/H_2/N_2$ mixtures were also gathered from simulations on the closed, perfectly stirred reactor model (AURORA) in the commercial code CHEMKIN.

6.2 Laminar burning velocities

6.2.1 Effect of CO/H_2 ratio in fuel composition

Although there is growing interest in the combustion properties of CO/H_2 mixtures, there are very few laminar burning velocity data reported in the open literature. In addition, the information on the single component behaviour of CO and H_2 is not sufficient to get CO/H_2 mixture performance characteristics. The chemistry of CO is strongly coupled to H_2 oxidation for example, through the reaction $CO+OH \rightarrow CO_2+H$. This reaction is the dominant one for CO conversion under most conditions [1, 142, 143]. In addition, CO and H_2 have significantly different transport properties (e.g. Lewis numbers) and burning velocities [144].

For hydrogen chemistry the chain branching reaction $H+O_2 \rightarrow O+OH$ is the main reaction for high temperature H_2 and "wet" CO [1, 145] combustion. This reaction consumes one H atom and produces two radical species O and OH. In any combustion system, an increase in H atoms will accelerate the overall combustion rate by raising the net amount of chain branching from the reaction $H+O_2 \rightarrow O+OH$ [1]. On the other hand, reactions which compete with $H+O_2 \rightarrow O+OH$ for H atoms and reduce its concentrations will tend to slow down the combustion process. For this reason, the addition of H_2 to CO flames results in an increase of laminar burning velocities as the H radicals from H_2 lead to raised branching, the OH radical concentrations rise and accelerate the CO oxidation rate [146].

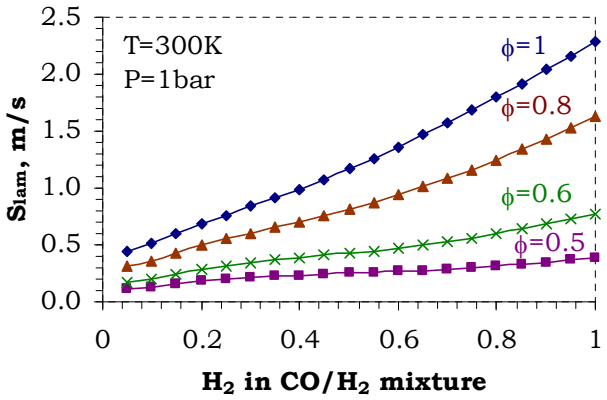

Figure 6.1: Laminar burning velocities for CO/H_2 mixture at different CO/H_2 ratio and equivalence ratio

Results of laminar burning velocities for different CO/H_2 fuel mixture compositions at ambient conditions and several equivalence ratios are given in the Figure 6.1. As expected, the addition of hydrogen to the carbon monoxide flame raises the laminar burning velocities considerably. For a mixture with 95%CO/5%H_2 the laminar burning velocity is 0.44 m/s, while for pure hydrogen the laminar burning velocity is 2.28 m/s. All quoted values are at the stoichiometric equivalence ratio.

The maximal fraction of CO is considered to be 95% in these computations. From Figure 6.1 it can be seen that by extrapolating to pure CO, the laminar burning velocity would be around 0.39 m/s at stoichiometric equivalence ratio. This burning velocity value cannot be reached for pure CO flames in dry air, because "dry" CO is oxidised only by the following chemical steps:

$CO + O_2 \rightarrow CO_2 + O$

$CO + O + M \rightarrow CO_2 + M$

This bone "dry" CO oxidation is practically hardly possible to achieve due to its high activation energy, and slow reaction rates [147]. Rightley et

al [147] reported the numerical laminar burning velocity of CO in dry air to be 0.006m/s. These authors claim as well that with sufficient amounts of hydrogen containing species the reaction OH + CO → H + CO_2 is initiated, which is much more rapid, resulting in a laminar burning velocity rise.

Present sensitivity analyses for hydrogen and carbon monoxide show that the most important reactions are OH + H_2 → H + H_2O and O + H_2 → H + OH which produce O, H and OH radicals, see Figure D 1. These radicals diffuse upstream to meet incoming oxygen and react with it by the lower activation energy cycle via reaction H + O_2 + H_2O→ HO_2 + H_2O.

For the lean flames, where concentrations of O, H, OH and adiabatic flame temperatures are lower, the chain breaking reaction H + O_2 + M → HO_2 + M have a greater contribution to the system reactivity; see Figure D 2, Figure D 3 and Figure D 4. Furthermore, the reaction H + O_2 + H_2O→ HO_2 + H_2O is then followed by reactions:

H + HO_2 → 2OH

H+HO_2 → O_2+H_2

OH+HO_2 → O_2+H_2O

O+HO_2 → OH+O_2

This study demonstrates as well that the reaction OH + CO → H + CO_2 plays a major role in CO chemistry for the CO/H_2 flame. This slow secondary reaction takes place over a more extended region on the hot, burnt gas side of the flame and it is responsible for the oxidation of bulk CO to CO_2, see Appendix D. Since the reaction OH+CO→H+CO_2 consumes the bulk of CO with OH, the CO oxidation rate depends very much on the OH radical concentrations [1].

6.2.2 Effect of Pressure

The effect of pressure on the laminar burning velocity for several CO/H_2 mixtures is shown in Figure 6.2. It is evident that the pressure rise causes a decrease in the laminar burning velocity. The laminar burning velocity drops from 1.17 m/s (at the ambient pressure) to 0.48 m/s at 15bar pressure for a mixture of 50%CO/50%H_2 at equivalence ratio 1.0. For a mixture with 80%CO/20%H_2, the laminar burning velocity drop is from 0.68 m/s at ambient conditions to 0.24 m/s at 15bar pressure. This behaviour is common to all H_2, H_2/CO and hydrocarbon fuel flames.

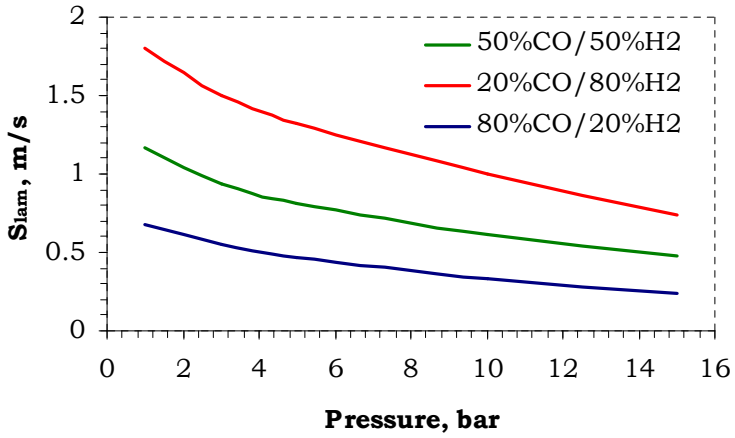

Figure 6.2: Laminar burning velocity variation with pressure for different CO/H_2 mixtures

Sensitivity analysis for high pressure flames shows that the reaction $H+O_2 \rightarrow O+OH$ (R1) competes directly with the reaction $H+O_2+H_2O \rightarrow HO_2+H_2O$ (R2) for H radicals and the reaction $H+O_2+N_2 \rightarrow HO_2+N_2$ consumes all H radicals produced by reaction $O+H_2 \rightarrow H+OH$, see Figure D 5 and Figure D 6.

The third order reaction R2 is much more pressure dependent than R1, therefore it becomes more effective in the H radical competition at

higher pressures and leads to a reduction in laminar burning velocity. This shows the non-linear dependence of the laminar burning velocity on pressures for H_2, H_2/CO and any hydrocarbon fuels [1]. It can also be noted that the temperature sensitivity coefficient curves for reactions $H+O_2 \rightarrow O+OH$ and $OH+CO \rightarrow H+CO_2$ overlap indicting that all OH radicals produced by reaction R1 are consumed for CO oxidation.

6.2.3 Effect of Temperature

The laminar burning velocity rises significantly with an increase in reactant preheat temperatures, see Figure 6.3. As it was mentioned earlier, for a mixture with 50%CO/50%H_2 the laminar burning velocity at ambient conditions is 1.17 m/s. With a temperature rise of 100 degrees, the laminar burning velocity rises to 1.87 m/s, while for T=800K it exceeds 8.32 m/s.

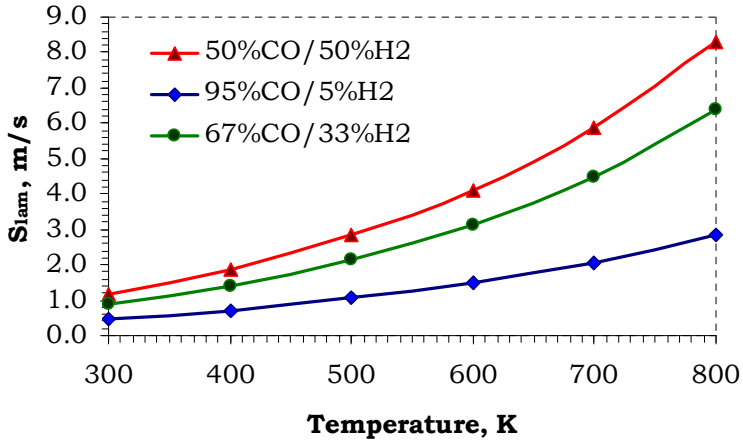

Figure 6.3: Laminar burning velocity change with temperature for different CO/H_2 mixtures

With an increase in the reactant preheat temperature, the reaction rates for nearly all reactions increase to accelerate the fuel consumption, heat release rate and overall combustion process.

The sensitivity analysis based on H_2, shows that with an increase in temperature there is no great difference in the sensitivity coefficients for all important reactions. Although, for temperatures above 800K, the combustion process is completely dominated by the high temperature reactions $O+H_2 \rightarrow H+OH$, $OH+H_2 \rightarrow H+H_2O$ and CO conversion reaction $OH+CO \rightarrow H+CO_2$. The HO_2 formation reaction $H+O_2+H_2O \rightarrow HO_2+H_2O$ becomes more important far downstream in the flame zone, where concentrations of H_2O are considerably high, see Figure D 7.

6.2.4 Effect of N_2 addition

The addition of nitrogen into hydrogen results in a decrease in the laminar burning velocity, since N_2 acts as a passive diluent by reducing the adiabatic flame temperature and combustion system reactivity as concentrations of reactive components (H_2, CO or CH_4) are reduced. For the mixture with a fuel composition of 30%H_2/70%N_2 the laminar burning velocity is 0.42 m/s (at ϕ=1 and ambient conditions), while for pure hydrogen it is 2.28 m/s, see Figure 6.4.

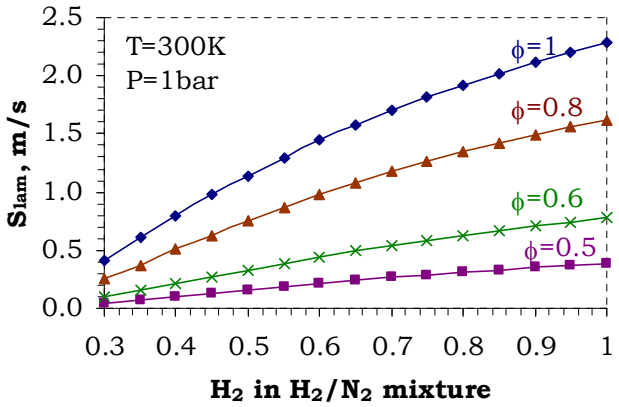

Figure 6.4: Laminar burning velocities for H_2/N_2 mixture at different H_2/N_2 ratio and equivalence ratio

The sensitivity analysis shows that with an increase in the nitrogen concentration in the fuel mixture, the combustion system exhibits a very similar behaviour to the lean flames. Lean flames have low adiabatic flame temperature. For nitrogen diluted mixture flames HO_2 production and consumption reactions, which compete for H radicals with the reaction $H+O_2 \rightarrow O+OH$, become more significant, see Figure D 8. In addition, the dilution with nitrogen reduces available H radical concentrations resulting in a branching reduction.

Figure 6.5 shows a comparison between the effects on the laminar burning velocity of introducing CO and N_2. This comparison is very interesting, as N_2, unlike other diluents like CO_2 or H_2O, does not alter H_2 chemistry. From this figure it can be seen that for fuel mixture compositions between pure hydrogen and fuel mixture of 50%H_2/50%CO (N_2), nitrogen and carbon monoxide act to a certain extent as diluents, since the decrease in laminar burning velocities follows very similar trends.

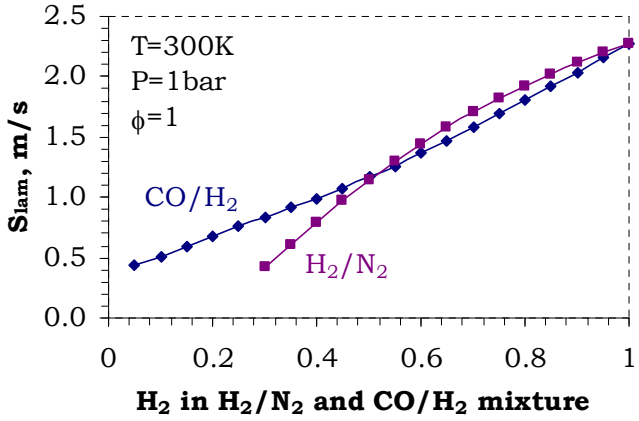

Figure 6.5: The effect of CO replacement with N_2

For mixtures with higher contents of carbon monoxide it is evident that the CO oxidation reaction OH + CO → H + CO_2 becomes more

important and contributes significantly to the laminar burning velocity rise.

6.2.5 Effect of CO_2 addition

As was discussed in Chapter 2, syngas fuels have a large variability in the fuel composition and in the diluents. For example the range of composition of CO_2 is from 2% up to 30% [148]. The presence of CO_2 will impact the flame in several ways, through changes in mixture specific heat and adiabatic flame temperature, chemical kinetics rates and radiative heat transfer [145].

The molar specific heat of CO_2 is larger than CO and H_2. Consequently, the addition of CO_2 will lower the reactant temperatures in the preheat flame region and the adiabatic flame temperature and, thus, the laminar burning velocity. Because of the CO_2 higher molar specific heat, its effect on the adiabatic flame temperature and burning velocity is greater in comparison to air dilution. In addition, the flammability limits and extinction strain rates of the CO_2 diluted mixtures are correspondingly narrower. These aspects of the effects of CO_2 dilution on CH_4 [149-151] and H_2 [152] flames [145] have been discussed in the literature.

CO_2 does not act as a passive diluent in the fuel, but interacts kinetically. The kinetic effects of CO_2 dilution appear primarily through the main CO oxidation reaction $CO + OH \rightarrow CO_2 + H$. Higher CO_2 levels lead to enhanced reverse reaction rates and CO oxidation reduction and enhanced consumption of H atoms. In lean H_2/CO flames, the H atoms are very important because they control the following main branching ($H + O_2 \rightarrow O + OH$) and termination ($H + O_2 + M \rightarrow HO_2 + M$) reactions. Since CO_2 dilution changes the H atom concentration, it has great effects on the flame propagation and laminar burning velocities of CO/H_2 flames. CO_2

effects are more significant at high pressures where the three-body termination reactions become dominating [145].

Another effect of CO_2 dilution is through higher levels of radiation as CO_2 is a more effective absorber and radiator in comparison to O_2 or N_2. Therefore CO_2 dilution can lower adiabatic flame temperature and laminar burning velocity due to radiative losses from the flame [151]. Non-gray radiation must be considered to predict laminar burning velocity and flammability limits of flames with CO_2 dilution [145, 153]. Furthermore, flame radiation effects are more significant at elevated pressures.

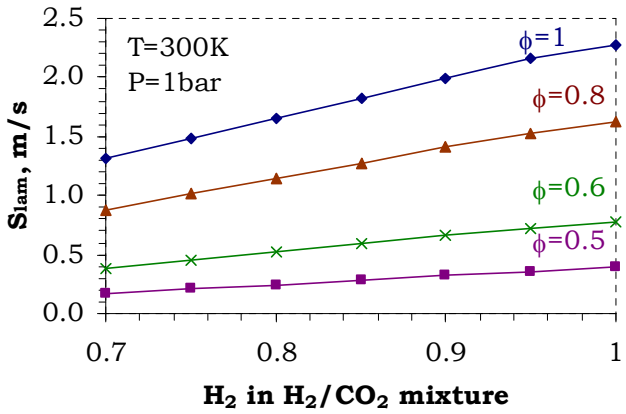

Figure 6.6: Laminar burning velocities for H_2/CO_2 mixture at different H_2/CO_2 ratio and equivalence ratios

The effects of CO_2 dilution on laminar burning velocity are shown in Figure 6.6 and Figure 6.7. For the H_2/CO_2 mixture at ambient conditions and equivalence ratio equal to 1, the laminar burning velocity drops by 43% from 2.28 m/s for pure hydrogen down to 1.31m/s for a mixture with 30% CO_2 dilution. It is evident that the presence of CO_2 has a considerable impact on combustion system reactivity. It needs to be noted that in all chemical kinetics simulations of flames with CO_2, radiation effects were not taken into account.

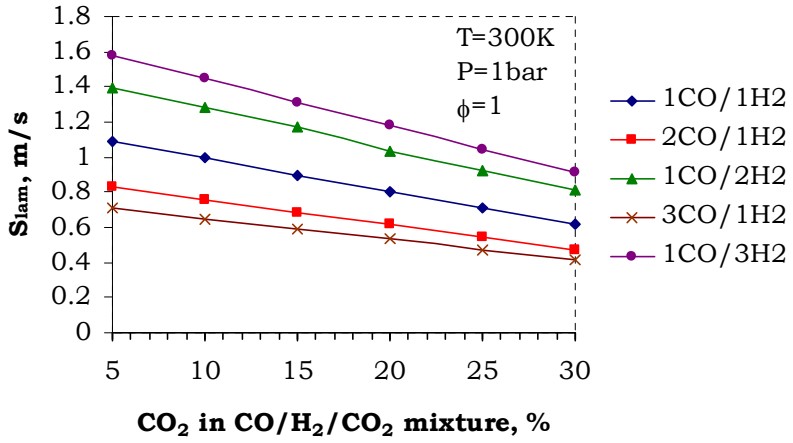

Figure 6.7: Laminar burning velocities for $CO/H_2/CO_2$ mixture at different H_2/CO_2 ratio, where $1CO/1H_2$ refers to one part of CO and one part of H_2 (50%CO/50%H_2)

Temperature sensitivity analysis reveals that for H_2/CO_2 mixtures with carbon dioxide concentrations up to 30%, CO_2 doesn't alter hydrogen chemistry significantly; only the following hydrogen chemistry reactions are involved, see Figure D 9:

$OH+H_2 \rightarrow H+H_2O$

$O+H_2 \rightarrow H+OH$

$H+O_2 \rightarrow O+OH$

In addition, the HO_2 production and consumption reactions become more significant for fuel mixture 70%H_2/30%CO_2 due to the reduced adiabatic flame temperature:

$H+O_2+H_2O \rightarrow HO_2+H_2O$

$H+HO_2 \rightarrow 2OH$

$H+HO_2 \rightarrow O_2+H_2$

It is evident that the presence of CO_2 in small concentrations has only thermal effects. As was discussed earlier, CO_2 lowers the reactant temperatures in the preheat flame region due to its larger specific heat.

For $CO/H_2/CO_2$ mixtures with several CO/H_2 ratios, sensitivity analysis indicates that CO oxidation reaction to CO_2 contributes significantly to a temperature rise, see Figure D 10 to Figure D 12. It is also evident that for mixtures with higher CO or CO_2 concentrations, the CO conversion to CO_2 takes place over an extended length. The reason is that the adiabatic flame temperatures are lower for higher CO or CO_2 concentrations. Therefore it takes longer for the $OH+CO \rightarrow H+CO_2$ reaction to oxidise CO.

6.2.6 Effect of H_2O addition

As previously mentioned, the syngas composition and diluent contents can vary significantly depending on the gasification process. H_2O is also present and for some gases its content can be as high as 19% [165, 154].

The presence of H_2O will impact the flame in several ways, through changes in mixture specific heat and adiabatic flame temperature and chemical kinetics rates because H_2O interacts kinetically with other components.

The effect of H_2O addition on the laminar burning velocity of H_2 is given in Figure 6.8. For the H_2/H_2O mixture at ambient conditions and equivalence ratio equal to 1 the laminar burning velocity drops by 29% from 2.28 m/s (for pure hydrogen) to 1.63m/s for a mixture composition $70\%H_2/30\%H_2O$.

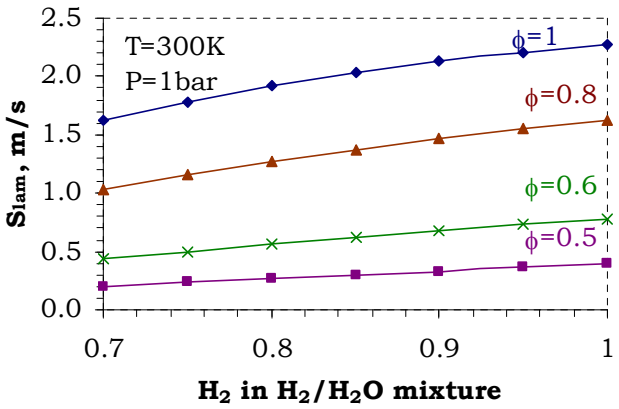

Figure 6.8: Laminar burning velocities for H_2/H_2O mixture at different H_2/H_2O ratio and equivalence ratio

The sensitivity analysis shows that H_2O acts in a similar way to other diluents, if it is present in small amounts; it slightly lowers adiabatic flame temperature, but does not alter H_2 chemistry significantly, see Figure D 13.

For H_2/H_2O mixtures with large amounts of H_2O, it also acts as a diluent and lowers the adiabatic flame temperature, but it also interacts kinetically as a third body in the chemical reaction like $H+O_2+H_2O \rightarrow HO_2+H_2O$, see Figure D 14.

The temperature sensitivity analysis also shows that for these mixtures there are large concentrations of HO_2 present, since some of the HO_2 consumption reactions have significant impact on the temperature:

$H+HO_2 \rightarrow O_2+H_2$ (R1)

$H+HO_2 \rightarrow 2OH$ (R2)

It is evident that the reaction R1 consumes all H radicals produced by the reaction $O+H_2 \rightarrow H+OH$. The reaction R2 (which is very exothermic) has a similar temperature sensitivity coefficient to the chain propagation

reactions $O+H_2 \rightarrow H+OH$, $OH+H_2 \rightarrow H+H_2O$ and $H+O_2 \rightarrow O+OH$, signifying that there are large concentrations of HO_2 radicals produced in the flame.

In the H_2/H_2O flame H_2 is consumed, whereas H_2O persists, being converted into free radicals and converted into H_2O again through HO_2 chemistry or acting as a third body.

The addition of CO and CO_2 into the H_2 flame results in a higher laminar burning velocity drop, whereas effects of N_2 and H_2O are very similar, see Figure 6.9. This indicates that N_2 and H_2O present in small quantities do not contribute significantly to reactions; they act rather like a passive diluent or third body in the recombination reactions.

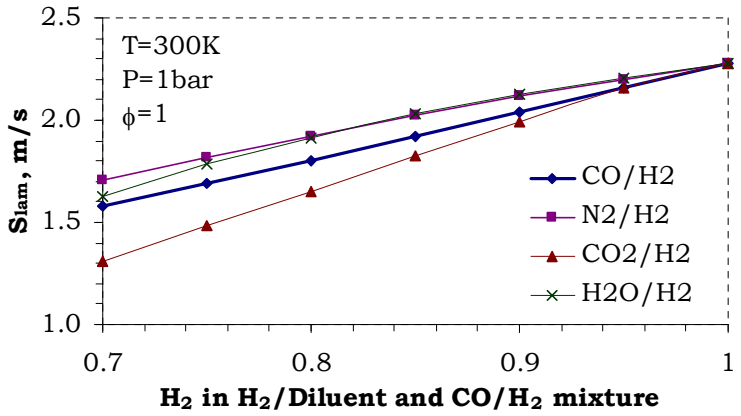

Figure 6.9: The effect of addition of CO and diluents into H_2 on laminar burning velocity

As previously discussed for H_2/CO and H_2/CO_2 flames, the following CO oxidation reaction $CO + OH \rightarrow CO_2 + H$ is the most important. If CO_2 concentrations are higher, H radicals are consumed more effectively through the reverse reaction $CO_2 + H \rightarrow CO + OH$. This results in a reduction of system reactivity as the main chain branching reaction $H+O_2 \rightarrow O+OH$ has to compete for H radicals.

6.2.7 The effect of CH_4 addition

6.2.7.1 Methane combustion

Methane is also present in the syngas in small quantities for most gasification processes. But some gasification processes, like the Lurgi Dry Ash Process (10% CH_4) and the E-Gas Process (16%CH_4) [155] produce large amounts of methane. Therefore the methane effect on CO/H_2 combustion needs to be also considered.

Methane has unique combustion characteristics because of its tetrahedral molecular structure. For example it has a low laminar burning velocity and high autoignition temperature.

Methane kinetics are well researched and most well understood, because of extensive kinetic modelling [156]. The earliest methane oxidation mechanism was proposed by Smoot et al. [157] and Tsatsaronis [158]. This mechanism involved 14 species and 30 reactions. Both authors compared their numerical predictions with experiments for lean methane-air flames. Westbrook [159] introduced a more complex mechanism with 24 species and 74 reactions. He claimed, along with Egolfopoulous et al [160], that C2 species were important for stoichiometric and rich flames. During the oxidation of methane, radical recombination reactions produce significant amounts of C2 hydrocarbons. The subsequent consumption reactions of these C2 species must be included in a complete methane mechanism for rich flames [1].

The major chemical pathway for methane conversion to carbon dioxide can be represented in the following way: $CH_4 \rightarrow CH_3 \rightarrow CH_2O \rightarrow HCO \rightarrow CO \rightarrow CO_2$.

At first, the CH_4 molecule is attacked by OH, O and H radicals to produce the methyl (CH_3) radical though reactions:

$O+CH_4 \rightarrow OH+CH_3$

$H+CH_4 \rightarrow CH_3+H_2$

$OH+CH_4 \rightarrow CH_3+H_2O$

Then CH_3 combines with the oxygen atom to form formaldehyde (CH_2O) through the reaction $O+CH_3 \rightarrow H+CH_2O$. The formaldehyde then reacts with OH, H and O radicals to produce a formyl radical (HCO):

$O+CH_2O \rightarrow HCO+OH$

$H+CH_2O \rightarrow HCO+H_2$

$OH+CH_2O \rightarrow HCO+H_2O$

The formyl radical is then converted into CO:

$OH+HCO \rightarrow H_2O+CO$

$HCO+M \rightarrow H+CO+M$

$HCO+H_2O \rightarrow H+CO+H_2O$

which is finally converted into CO_2, primarily though reactions $CO+OH \rightarrow CO_2+H$ and $O+CO+M \rightarrow CO_2+M$.

In addition to the major pathway from methyl (CH_3) to formaldehyde (CH_2O), CH_3 radicals also react to form CH_2 in two possible electronic configurations. The singlet CH_2 state is designated as $CH_2(S)$ (not a solid). In another side loop CH_3 is converted into CH_2OH, which is converted into CH_2O. Other less important paths complete the methane oxidation mechanism [2].

Sensitivity analysis of pure methane in this study shows that the above mentioned reactions have large CH_4 sensitivity coefficients; see Figure D 15. In addition, the reaction $H+O_2 \rightarrow O+OH$ has the highest CH_4 sensitivity coefficient indicating that it is the major chain propagation reaction in the system, providing necessary radicals for the CH_4 conversion to CH_3.

6.2.7.2 CH_4/H_2 mixture

With the increase in the hydrogen concentration in the fuel mixture, the laminar burning velocity rises exponentially, see Figure 6.10. For pure methane the laminar burning velocity is 0.39 m/s, while for pure hydrogen it is 2.28 m/s

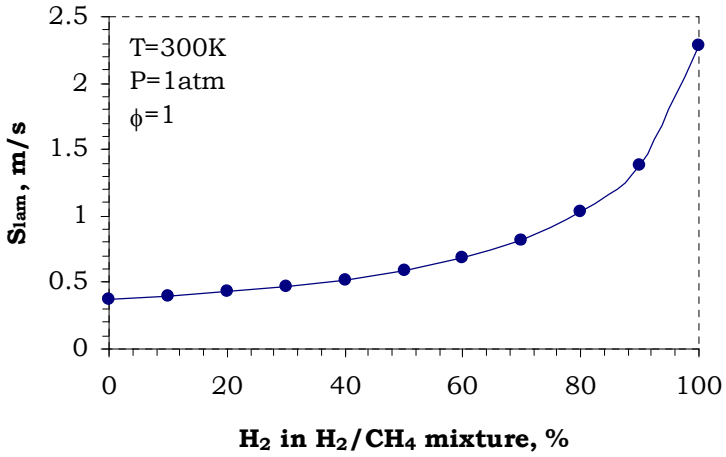

Figure 6.10: Laminar burning velocities for H_2/CH_4 mixture at different H_2/CH_4 compositions

The addition of hydrogen promotes the high temperature branching reactions and increases the reactivity of the combustion system. Actually H_2 reacts mainly with O_2 and produces the H radical needed for the reaction $H+O_2 \rightarrow OH+O$ to proceed. This reaction produces the OH and O radicals needed for methane oxidation, which are involved in $CH_4 \rightarrow CH_3$ conversion. In such a way, the methane oxidation pathways can be initialized and accelerated by the greater amount of radicals present in the system due to increased concentrations of the hydrogen. The same findings are reported by Dagaut et al. [161] and Sabia et al. [162].

6.2.7.3 CH_4/CO mixture

The effect of CO addition to a CH_4 flame is shown in Figure 6.11. The laminar burning velocity of the carbon monoxide flame in dry air is close to zero m/s. With small amounts of methane addition to carbon monoxide, the laminar burning velocity of the CH_4/CO mixture rises rapidly up to 0.57 m/s (for 20%CH_4/80%CO). If more CH_4 is added, the laminar burning velocity slowly decreases and reaches 0.39 m/s for pure methane.

The reason for such behaviour is that the presence of hydrocarbon fuel (methane) will inhibit CO oxidation until all of the fuel has disappeared. At this point the OH concentration rises rapidly and the OH+CO→H+CO_2 reaction which consumes CO to produce CO_2 is accelerated [1].

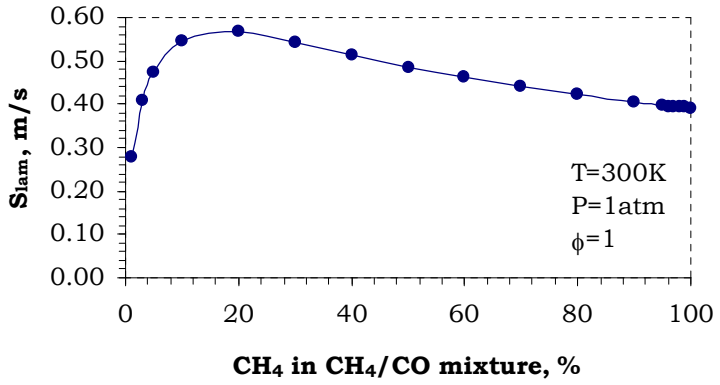

Figure 6.11: Laminar burning velocities for CH_4/CO mixture at different CH_4/CO compositions

Sensitivity analysis for pure methane shows that the H+O_2→O+OH reaction has the highest positive temperature sensitivity making it a main source of OH radical production. Other important reactions are HO_2+CH_3→OH+CH_3O and OH+CO→H+CO_2. Two chain termination reactions H+CH_3(+M)→CH_4(+M) and OH+CH_3→CH_2(S)+H_2O have the

largest negative sensitivities because they consume H and OH radicals, see Figure D 15. For a fuel mixture composition of 20%CH_4 and 80%CO, the reaction OH+CO→H+CO_2 becomes much more significant due to increased amounts of CO. It has a very similar sensitivity coefficient to H+O_2→O+OH, which is a source for OH radicals for CO oxidation, see Figure D 16. This shows that almost all OH radicals are consumed by reaction OH+CO→H+CO_2. For fuel mixtures with very small amounts of CH_4 (97%CO/3%H2), the most important reaction for a temperature rise is OH+CO→H+CO_2. Even the effect of the reaction H+O_2→O+OH on the temperature rise is considerably smaller, this reaction is a source for OH radicals, which are needed for CO oxidation, see Figure D 17.

6.2.8 CO/H_2/CH_4/Diluents mixtures

Three syngas mixtures were investigated in order to examine the chemistry of practical mixtures, which contain CO, H_2, some diluents and small amounts of methane. The compositions of these mixtures are given in Table 6.1.

The first gas (Mix1) was produced in "The Wabash River Coal Gasification Repowering Project". The design of Wabash River coal gasifier was based on Destec's Louisiana Gasification Technology Inc. (LGTI) gasifier. It is an oxygen-blown, entrained-flow, refractory-lined gasifier with continuous slag removal [163]. This coal syngas has mainly H_2 and CO; it also contains high amounts of CO_2.

Table 6.1: Mixture compositions of syngas

	H_2	CO	CO_2	CH_4	H_2O	N_2	AR	HHV, MJ/m^3
Mix1	0.344	0.453	0.158	0.019	-	0.019	0.006	10.32
Mix2	0.27	0.356	0.126	0.001	0.186	0.058	-	7.98
Mix3	0.22	0.22	0.1	0.04	-	0.42	-	7.18

The second gas (Mix2) is similar to the first one, but has considerable amounts of H_2O (18.6%). This gas was produced in "The Tampa Electric Integrated Gasification Combined-Cycle Project". It has the single-stage, downdraft-firing, entrained flow coal gasifier used in the Texaco coal gasification technology. Here coal/water slurry with 60-70% of coal and oxygen (95% pure) are fed to a gasifier. The coal reacts with oxygen and produces raw coal gas (syngas) and molten ash at a temperature of about 1480°C [164].

The third gas is a producer gas. It is heavily diluted with nitrogen. This mixture composition was taken from K. Murthy's thesis [165].

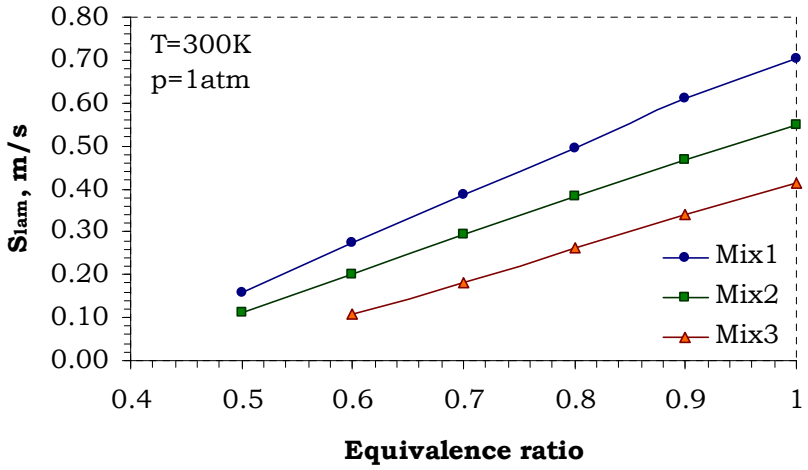

Figure 6.12: Laminar burning velocities for gas, produced by gasifiers, at different equivalence ratios

The laminar burning velocities for lean flames of all these mixtures are given in the Figure 6.12. As expected, Mix1 has the highest laminar burning velocity ranging from 0.70 m/s at equivalence ratio 1 down to 0.16 m/s at equivalence ratio 0.5. This mixture has higher hydrogen content in comparison to Mix2 and Mix3. For Mix2, the laminar burning velocity changes from 0.55 m/s at the stoichiometric equivalence ratio to

0.11 m/s at equivalence ratio 0.5. As mentioned above, this mixture contains large amounts of H_2O, which lowers the laminar burning velocity. Mix3 is heavily diluted with N_2 (42%); therefore it has the lowest laminar burning velocity. For this mixture the laminar burning velocity ranges from 0.41 m/s at the stoichiometric equivalence ratio to 0.11 m/s at equivalence ratio 0.6.

The temperature sensitivity analysis for the first mixture shows that for the stoichiometric equivalence ratio, the CO oxidation reaction is the main contributor to the temperature rise, see Figure D 18. The reason that the CO oxidation reaction takes over hydrogen chemistry is that this fuel mixture contains large amounts of CO and CO_2. It needs to be noted that for lean mixtures (with equivalence ratio 0.6), where the adiabatic flame temperature is lower, hydrogen chemistry reactions of HO_2 production and consumption become important, while CO conversion to CO_2 takes place over longer region. Similar trends are observed for the Mix2, containing considerable amounts of CO_2 and H_2O. For Mix3 the CO oxidation reaction has a similar sensitivity coefficient to $H+O_2 \rightarrow O+OH$. Because this reaction is endothermic, it does not contribute directly to the temperature rise, but it is a source of OH radicals for the CO oxidation. As this mixture is diluted with N_2, its adiabatic temperature is lowered; therefore again HO_2 production and consumption reactions become important due to larger concentrations of HO_2 radical.

6.3 Artificial neural network for laminar burning velocities

As was mentioned in Section 4.4.2, the artificial neural network (ANN) was trained to find the correlation of laminar burning velocity with mixture composition, temperature, pressure and equivalence ratio. The ANN in the

form of a number of linear equations and number of transfer functions is given in Appendix E.

The data for ANN with the 9 input neurons (P, T, CO, H_2, N_2, CO_2, H_2O, CH_4 and O_2) were supplied in the form of pressure, temperature and air/fuel mixture composition and for output neurons – laminar burning velocity. However, the more convenient way to present input data is in the form of a fuel mixture composition and equivalence ratio rather than in air/fuel mixture composition. The mixture composition + equivalence ratio can be related to the air/fuel mixture composition (number of moles) in the following way:

$$N_{CO} = CO_{mix} \quad \textbf{(6.1)}$$

$$N_{H_2} = H_{2,mix} \quad \textbf{(6.2)}$$

$$N_{N_2} = N_{2,mix} + 3.76\left(\frac{CO_{mix} + 2.5 \cdot CH_{4,mix} + H_{2,mix}}{2}\right)\frac{1}{\phi} \quad \textbf{(6.3)}$$

$$N_{CO_2} = CO_{2,mix} \quad \textbf{(6.4)}$$

$$N_{H_2O} = H_2O_{mix} \quad \textbf{(6.5)}$$

$$N_{CH_4} = CH_{4,mix} \quad \textbf{(6.6)}$$

$$N_{O_2} = \left(\frac{CO_{mix} + 2.5 \cdot CH_{4,mix} + H_{2,mix}}{2}\right)\frac{1}{\phi} \quad \textbf{(6.7)}$$

Here the subscript “mix” refers to the volume fraction of the component in the fuel mixture composition, ϕ is the equivalence ratio; N is the number of moles.

The mixture composition needs to be normalized in the form of mole fractions. Then the mole fraction of each component is calculated using the following equation (CO mole fraction):

$$V_{CO} = \frac{N_{CO}}{N_{CO} + N_{H_2} + N_{N_2} + N_{CO_2} + N_{H_2O} + N_{CH_4} + N_{O_2}} \quad \textbf{(6.8)}$$

The same relation is used to compute mole fractions of H_2, N_2, CO_2, H_2O, CH_4 and O_2).

The ANN presented in this study can accurately predict the laminar burning velocities for various $CO/H_2/CH_4$/Diluents fuel mixtures (here diluents are N_2, CO_2 and H_2O) for a temperature range from 300K up to 900K and a pressure range from 1bar up to 50bar. This network can handle any CO/H_2 ratio in fuel mixture, CO_2, H_2O addition up to 10% and N_2 addition up to 70% and CH_4 addition up to 30%.

6.4 Critical strain rate to extinction

In addition to its dependence on state properties – composition, temperature and pressure – the burning velocity is also influenced by the hydrodynamic field in which combustion takes place. Whilst the open laminar Bunsen flame imposes a fairly benign strain field, the practical application in the gas turbine involves both high levels of flow velocity and intense turbulent fluctuations, which can lead to local flame extinction. Thus, data at strain rates up to flame extinction are needed for the more accurate simulations of turbulent premixed burning.

6.4.1 Effect of CO/H_2 and N_2/H_2 ratio in fuel composition

Results of critical strain rate to extinction for different CO/H_2 fuel mixture compositions at ambient conditions and stoichiometric equivalence ratio are presented in the Figure 6.13. It can be seen that with an increase in hydrogen concentration in the fuel mixture the extinction strain rate of the CO/H_2 and N_2/H_2 flames increases linearly from 2890 1/s for 90%CO/10%H_2 (890 1/s for 90%N_2/10%H_2) up to 32500 1/s for

pure hydrogen. Only for mixtures with 50%CO/50%H_2 and 40%CO/60%H_2 is the critical strain rate to extinction slightly lower and not following exactly the linear change. This indicates that the combined effects of CO and H_2 oxidation results in a slight decrease in the critical strain rate to extinction.

The temperature sensitivity analysis shows that for a pure hydrogen chain propagation reaction $O+H_2 \rightarrow H+OH$ competes mainly with the chain termination reaction $H+HO_2 \rightarrow O_2+H_2$. Other reactions which contribute considerably to the temperature rise are $OH+H_2 \rightarrow H+H_2O$, $H+HO_2 \rightarrow 2OH$ and $O+H_2 \rightarrow H+OH$.

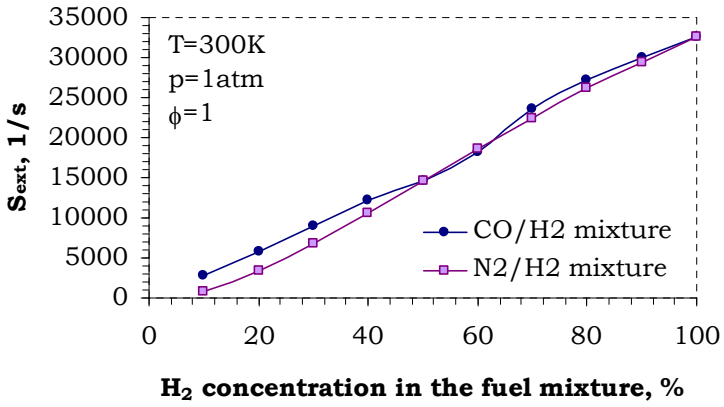

Figure 6.13: The effect of H_2 concentration on critical strain rates to extinction for CO/H_2 and H_2/N_2 mixtures

With an increase in the CO concentration in the CO/H_2 fuel mixture the CO oxidation has a great effect. The temperature sensitivity analysis for the fuel mixture 50%CO/50%H_2 shows that the CO oxidation reaction $OH+CO \rightarrow H+CO_2$ has the highest positive temperature sensitivity. Other important hydrogen oxidation reactions e.g. $O+H_2 \rightarrow H+OH$, $H+HO_2 \rightarrow 2OH$ and $H+O_2 \rightarrow O+OH$ have a two times lower sensitivity coefficient. Furthermore for a fuel mixture 80%CO/20%H_2, the CO oxidation reaction

is the dominant one. The contribution to the temperature rise from the hydrogen oxidation reactions becomes small. Additionally, for CO/H_2 mixtures the main chain termination reaction is $H+HO_2 \rightarrow O_2+H_2$, which has the highest negative temperature sensitivity.

From Figure 6.13 it can also be observed that for H_2 rich mixtures down to 50%H_2 in the fuel mixture, the effects of CO and N_2 are very similar indicating that CO for these mixtures acts as a diluent, but its oxidation reaction becomes more important for CO rich CO/H_2 fuel mixtures.

6.4.2 Effect of equivalence ratio

The results of the equivalence ratio effect on extinction strain rate for several CO/H_2/air and N_2/H_2/air mixtures are presented in Figure 6.14. It is evident that for lean flames with increase in the equivalence ratio the extinction strain rate rises considerably. For example, for a mixture with 50%CO/50%H_2, the critical strain rate to extinction is 202 s^{-1} (for equivalence ratio 0.3), while for the stoichiometric equivalence ratio it can rise up to 14630 s^{-1}.

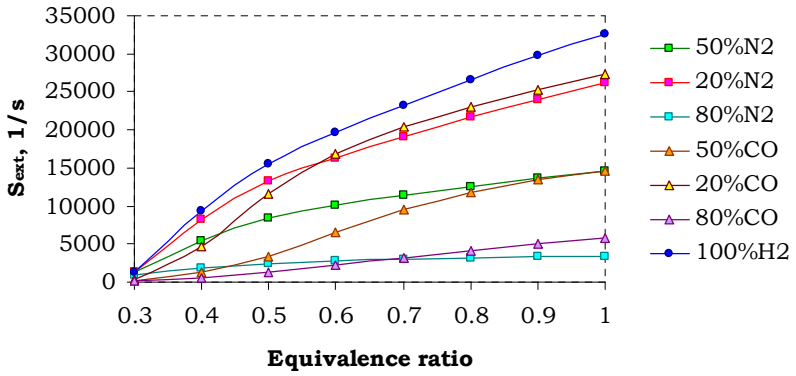

Figure 6.14: the effect of equivalence ratio on critical strain rate to extinction for CO/H_2 and N_2/H_2 fuel mixtures

Additionally, it can be noted that for CO/H_2 mixtures for lean flames with equivalence ratios below 0.6, the critical strain rate to extinction is much lower in comparison to the corresponding N_2/H_2 mixtures. These differences indicated that CO oxidation has a large effect on flame kinetics for very lean flames under extreme strain conditions.

Sensitivity analysis for CO/H_2/air and N_2/H_2/air flames at equivalence ratio 0.5 shows that for the CO/H_2/air flame the CO oxidation reaction $OH+CO \rightarrow H+CO_2$ contributes most to the adiabatic flame temperature rise, while for the N_2/H_2/air flame the main reaction is the chain propagation reaction $OH+H_2 \rightarrow H+H_2O$. These reactions compete for H radicals with the chain termination reaction $H+HO_2 \rightarrow O_2+H_2$, which has its highest negative temperature sensitivity coefficient. The main reason that CO/H_2/air flames cannot be sustained in the flow with higher strain rates is that the CO oxidation reaction is much slower in comparison to $OH+H_2 \rightarrow H+H_2O$, which becomes far less significant for CO/H_2 flames, see Figure D 21 and Figure D 22.

6.4.3 Effect of temperature

With increase in temperature the critical strain rate to extinction rises. At higher temperatures the reaction rates increase leading to the fuel consumption acceleration, the heat release rate increase and acceleration of overall combustion process. In addition, a flame can be sustained in the higher strain fields as the main chain propagation reactions can be initiated faster due to higher reaction rates, where it would not have sufficient time at lower temperatures.

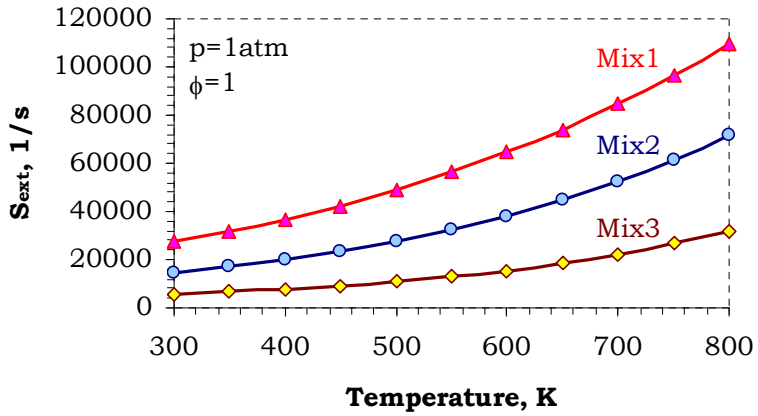

Figure 6.15: Temperature effect on critical strain rate to extinction; Mix1 is 20%CO/80%H_2, Mix2 is 50%CO/50%H_2 and Mix3 is 80%CO/20%H_2

For the mixture with a composition of 50% CO/50% H_2, the critical strain rate is 14630s^{-1} at temperature of 300K, while at 800K temperature it reaches 71900s^{-1}; see Figure 6.15. For a mixture with composition of 20%CO/80%H_2 the critical strain rate rises from 27300s^{-1} (300K) up to 109950s^{-1} (800K). The same behaviour is observed for a mixture with 80%CO/20%H_2: the critical strain rate rises from 5720s^{-1} (300K) up to 32000s^{-1} (800K).

6.4.4 Effect of pressure

For fuel mixtures containing large amounts of hydrogen (for CO/H_2 fuel mixtures with CO concentration of up to 30%), the critical strain rate to extinction rises with an increase in pressure up to 15 bars and then starts decreasing with a further pressure rise, see Figure 6.16.

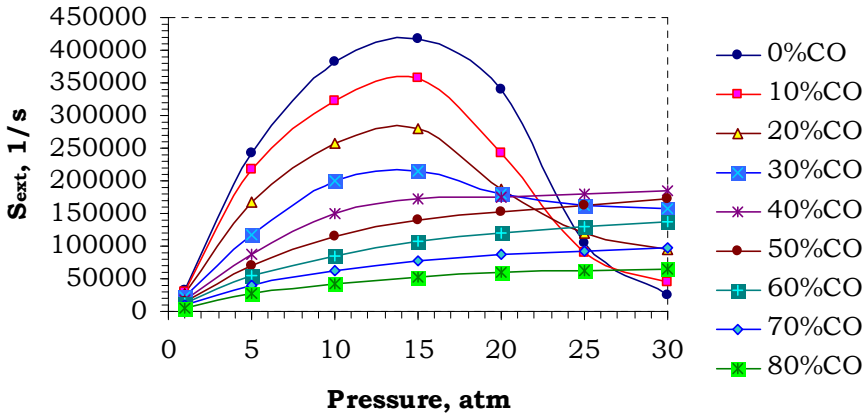

Figure 6.16: Pressure effect on critical strain rate to extinction for various CO/H_2 fuel mixtures

The hydrogen is released at first in pre-flame reactions and then this "free hydrogen" diffuses into the combustion zone. As a consequence the flame temperature is raised and the flame becomes more resistant to extinction. Therefore for fuel mixtures with higher hydrogen content, the critical strain rate to extinction is considerably higher. Additionally, H_2 is able to be sustained in much thinner flame zones by providing faster rates of OH production, resulting in less sensitivity in flame temperature with respect to strain. Therefore the flame is able to sustain higher strain rates [166].

For CO richer mixtures, with CO concentration in CO/H_2 fuel mixture higher than 40%, the critical strain rate to extinction increases for the entire pressure range from 1 up to 30 bars. The pressure effect on critical strain rate to extinction is most significant for pressures up to 10 bars.

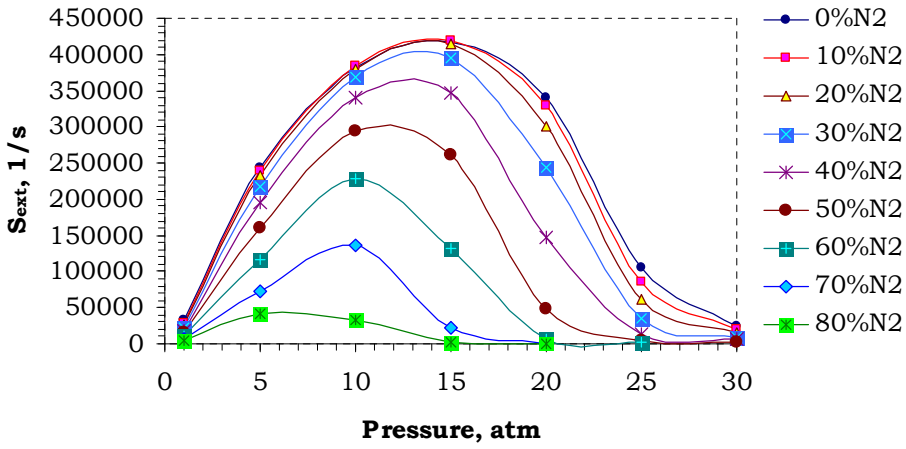

Figure 6.17: Pressure effect on critical strain rate to extinction for various N_2/H_2 fuel mixtures

For N_2/H_2 fuel mixtures the pressure effects on critical strain rate to extinction are similar to hydrogen mixtures: it increases at lower pressures and starts decreasing for higher pressures. For mixtures with small amounts of nitrogen, the peak value of critical strain rates to extinction is 15 bars and for a mixture with $80\%N_2/20\%H_2$, it is at 5 bars, see Figure 6.17.

This behaviour indicates that mass diffusivity of the reactants (especially H_2) has a significant effect on the flame's ability to sustain itself in highly strained flows.

6.5 Artificial neural network for critical strain rate to extinction

The data for the artificial neural network, trained to predict critical strain rate to extinction as a function of mixture composition, equivalence ratio, pressure and temperature, were presented in a similar manner as for ANN for laminar burning velocities. This ANN, presented in the form of a

number of linear equations and a number of transfer functions, is given in Appendix E as well.

The data for ANN with 6 input neurons (P, T, CO, H_2, N_2 and O_2) were supplied in the form of pressure, temperature and air/fuel mixture composition and for output neuron – critical strain rate to extinction. The mixture composition + equivalence ratio can be related to the air/fuel mixture composition (number of moles) in a following way:

$$N_{CO} = CO_{mix} \quad \textbf{(6.9)}$$

$$N_{H_2} = H_{2,mix} \quad \textbf{(6.10)}$$

$$N_{N_2} = N_{2,mix} + 3.76\left(\frac{CO_{mix} + H_{2,mix}}{2}\right)\frac{1}{\phi} \quad \textbf{(6.11)}$$

$$N_{O_2} = \left(\frac{CO_{mix} + H_{2,mix}}{2}\right)\frac{1}{\phi} \quad \textbf{(6.12)}$$

Here subscript "mix" refers to the volume fraction of the component in the fuel mixture composition, ϕ is the equivalence ratio and N is the number of moles.

The mixture composition was also normalized in the form of mole fractions. Then the mole fraction of each component was calculated using the following equation (CO mole fraction):

$$V_{CO} = \frac{N_{CO}}{N_{CO} + N_{H_2} + N_{N_2} + N_{O_2}} \quad \textbf{(6.13)}$$

The same relation is used to compute mole fractions for H_2, N_2 and O_2.

This ANN can predict strain rate to extinction for various $CO/H_2/N_2$ fuel mixtures in an operating pressure range from 1 to 50 bars, with temperatures ranging from 300K up to 900K.

6.6 Ignition delay

The emphasis on low emissions, particularly of NO_X, from the industrial gas turbine has focussed primarily on the development of lean-burning premixed combustion systems. The presence of a premixing chamber upstream of the combustor, in turn, emphasises the importance of preventing flashback and autoignition. Whilst the former is largely a matter of aero-thermal design, the latter is strongly influenced by fuel composition and chemical kinetics. Simulations of ignition delays have therefore been performed for the gas mixtures also examined in respect of burning velocity.

The ignition delay time, used to quantify the ignition of a combustible mixture, is defined as the time interval required for the mixture to spontaneously ignite under prescribed conditions of temperature, pressure and equivalence ratio. The definition of an ignition criterion from conditions in a homogeneous reactor is open to interpretation. We here adopt the convention that the delay is the time elapsed before the reactants in a perfectly-stirred reactor show a 5% temperature rise with respect to the initial conditions. The calculations were performed using the GRI-Mech 3.0 mechanism in the AURORA model.

6.6.1 Ignition chemistry

This section presents the chemistry of hydrogen and carbon monoxide ignition. At first the chemistry of the H_2/O_2 system is discussed, followed by the CO to CO_2 conversion chemistry in the presence of hydrogen.

Similar chemical reactions are involved in $CO/H_2/N_2$ – Air mixture ignition as in premixed flame propagation.

From shock tube experiments, which can be modelled accurately, the most probable reaction initiation step for ignition is proposed to be [167]:

$H_2+O_2 \rightarrow HO_2+H$ R1

This reaction produces one H radical and one relatively unreactive HO_2 radical. The main feature of this reaction is to supply an H radical for the chain propagation system. It does not contribute significantly to the ignition itself, but it provides necessary radicals that develop a radical pool of OH, H and O by the following reactions:

$H+O_2 \rightarrow O+OH$ R2

$O+H_2 \rightarrow H+OH$ R3

$H_2+OH \rightarrow H_2O+H$ R4

$O+H_2O \rightarrow OH+OH$ R5

Because the H radical is regenerated from the chain propagation system there is no chemical barrier to prevent ignition. This chain propagation sequence is very important not only for hydrogen ignition, but also for oxidation mechanisms of any hydrocarbon, because it provides fast chain branching and propagation steps, together with a radical pool for fast reactions [169].

In a constant volume reactor, when the system moves from lower to higher pressures, the fast chain propagation reaction R2 is competing with a third-order reaction:

$H+O_2+M \rightarrow HO_2+H+M$ R6

Here M is the usual third body that removes the energy needed to stabilize the combination of H and O_2. At higher pressures this reaction becomes more competitive with reaction R2 [140].

At higher temperatures the HO_2 radical can react in the following way:

$HO_2+H_2 \rightarrow H_2O_2+H$ R7a

$H_2O_2 \rightarrow 2OH$ R7b

Since reaction R6 requires a third body its rate decreases with an increase in temperature, while the rate of reaction R2 increases with temperature rise. The reaction R2 is the dominating one at higher temperatures, while reaction R6 is more effective at higher pressures and lower temperatures.

If HO_2 concentrations build up in the system it will react in the following way:

$HO_2+H \rightarrow H_2+O_2$ R8

$HO_2+H \rightarrow OH+OH$ R9

$HO_2+H \rightarrow H_2O+O$ R10

$HO_2+O \rightarrow O_2+OH$ R11

HO_2 can also recombine, which yields hydrogen peroxide formation:

$HO_2+HO_2 \rightarrow H_2O_2+O_2$ R12

Then H_2O_2 is consumed by radicals H and OH through the following steps:

$H_2O_2+OH \rightarrow H_2O+HO_2$ R13

$H_2O_2+H \rightarrow H_2O+OH$ R14

$H_2O_2+H \rightarrow HO_2+H_2$ R15

$H_2O_2+M \rightarrow 2OH+M$ R16

It is evident that at some conditions, reaction R6 will terminate the chain, while under some conditions it is a part of a chain propagating path. In addition, the following sequences are very exothermic:

$H+O_2+M \rightarrow HO_2+M$

$HO_2+H \rightarrow 2OH$

and

$H+O_2+M \rightarrow HO_2+M$

$HO_2+HO_2 \rightarrow H_2O_2+O_2$

$H_2O_2+M \rightarrow 2OH+M$

Because these reactions are very exothermic they significantly contribute to the temperature rise and initiate ignition [169].

It also needs to be noted that for many hydrocarbon species the rates of reactions that consume H radicals are larger than the rate of reaction R2, so these reactions compete effectively for H radicals and reduce the chain branching rate. For this reason hydrocarbons act as inhibitors for the hydrogen reaction system. As was mentioned, at high pressures (P≥20 atm) and relatively low temperatures (T = 1000K), reaction R6 will dominate reaction R2 and reactions R6, R12 and R16 will provide the chain propagation. Therefore the fuel will accelerate the overall reaction and will act as an inhibitor at lower pressures due to competition with reaction R2 [45].

If CO is added into the H_2 fuel, it will react most effectively with OH through the following reaction:

$CO+OH \rightarrow CO_2+H$ R17

As was discussed before, the reaction R6 will supply HO_2, which will provide another root for CO conversion to CO_2 by:

$CO+HO_2 \rightarrow CO_2+OH$ (18)

The reaction R18 can become competitive to reaction R17 only at high pressures or in initial stages of the hydrocarbon oxidation, when high concentrations of HO_2 are produced. The reaction R18 is rarely important in most combustion situations, but it contributes significantly to ignition at high pressures.

As discussed before, the fate of H radicals is critical in determining the rate of the H_2/O_2 reaction sequence in any hydrogen containing mixture, while the concentration of hydroxyl radicals is important in the

rate of CO oxidation. Because reaction R17 is relatively slow in comparison to other hydrocarbon oxidation reactions it comes later in the reaction scheme. The conversion of CO to CO_2 is delayed until all the original fuel and intermediate hydrocarbon fragments have been consumed [45]. When these species have disappeared, the HO_2 concentrations rise to high levels and converts CO to CO_2. Because the rate of reaction R17 starts rising sharply only at temperatures above 1100K, at lower temperatures than 1100K the CO will not be converted completely [169].

6.6.2 Effect of reactants initial temperature and pressure

The ignition delay times for representative fuel mixture with composition 50%CO/50%H_2 are given in Figure 6.18. From this figure it can be seen that with an increase in the reactants' preheat temperature, the ignition delay time drops exponentially.

As mentioned earlier, the main reaction for OH generation and ignition initiation is $H+O_2 \rightarrow OH+O$ (R2). This reaction is strongly endothermic; therefore it will not proceed rapidly at low temperatures. Consequently, at low temperatures, the H atom can survive much more collisions and can find its way to a surface, where it is destroyed [168] or consumed by other reactions.

Compared to the effect of temperature, the effect of pressure on ignition delay is small, see Figure 6.19. Performed simulations show that for a 50%CO/50%H_2 mixture for an initial temperature of 800K the ignition delay drops with an increase in pressure, while at a temperature of 900K, it rises with an increase in pressure and reaches a peak at 5 atm and then starts decreasing with a further increase in pressure. For a temperature of 1100K, the longest ignition delay is at 15bar. For temperatures of 1200K and 1300K, the ignition delay drops with an

increase in pressure reaching a minimum value at about 5 atm pressure and then starts rising again with a further increase in pressure. A very similar behaviour of ignition delay was observed for a 50%H_2/50%N_2 mixture, see Figure 6.20.

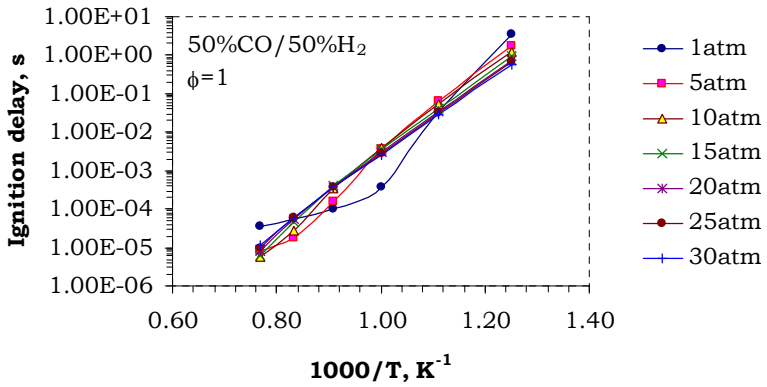

Figure 6.18: Ignition delays for 50%CO/50%H_2 fuel mixtures at different temperatures and pressures

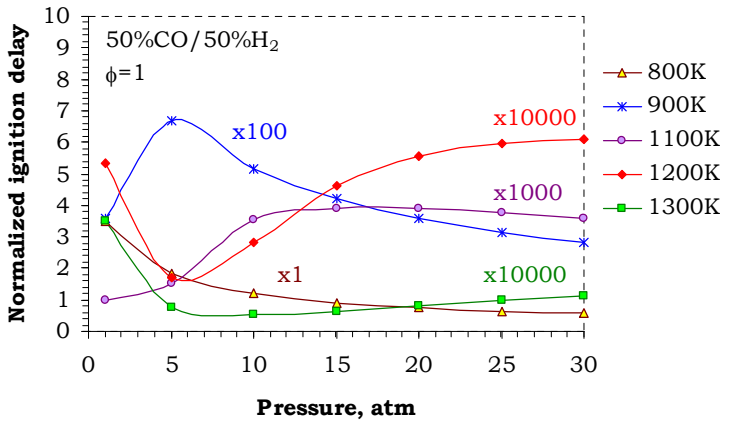

Figure 6.19: Ignition delays change for 50%CO/50%H_2 fuel mixtures at different temperatures and pressures (given normalized values)

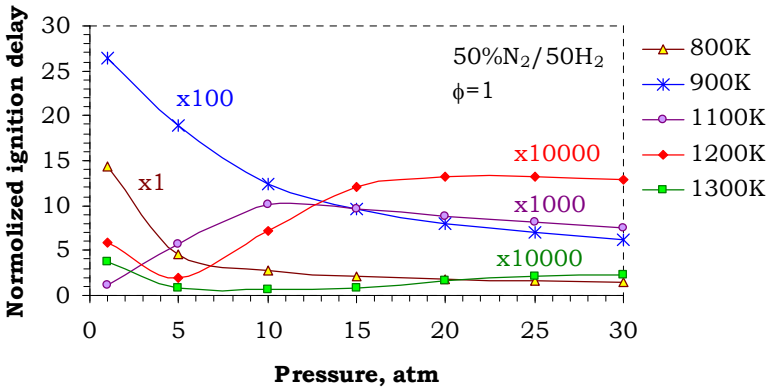

Figure 6.20: Ignition delays change for 50%H_2/50%N_2 fuel mixtures at different temperatures and pressures (given normalized values)

As was discussed in the previous section, at higher pressures the chain initiation reaction R2 and chain termination reaction R6 compete for H radicals and even HO_2 radicals. OH sensitivity analysis for mixture composition 50%CO/50%H_2 at initial reactants' temperature 1100K shows that the main reaction for all pressures ranging from 1 to 30 atm is R2. It mainly competes for H radicals with two reactions:

$H+O_2+N_2 \rightarrow HO_2+N_2$ R19

$H+O_2+M \rightarrow HO_2+M$ R6

The sensitivity coefficients for reactions R19 and R6 rise dramatically for pressures up to 10 bar and then drop with further pressure rise, see Figure D 24. Because reactions R6 and R19 become more significant at higher pressures, they reduce system reactivity resulting in longer ignition delays. In addition, the CO to CO_2 conversion reaction R18 becomes more important at higher pressures, indicating that there are enough HO_2 radicals, produced by reactions R6 and R19, for it to proceed.

The OH sensitivity analysis at atmospheric pressure shows that reaction R2 is the main one which supplies OH radicals and contributes

most to the system reactivity, while the effects of reactions R6 and R19 are considerably smaller, see Figure D 23.

6.6.3 Effect of mixture composition

The effect of the CO/H_2 mixture composition on the ignition delay is shown in Figure 6.21. From this figure it can be seen that for temperatures lower than 1000K, with an increase in H_2 concentration in the fuel mixture, ignition delay time becomes longer, while for temperatures higher than 1000K, the addition of H_2 results in ignition delay shortening.

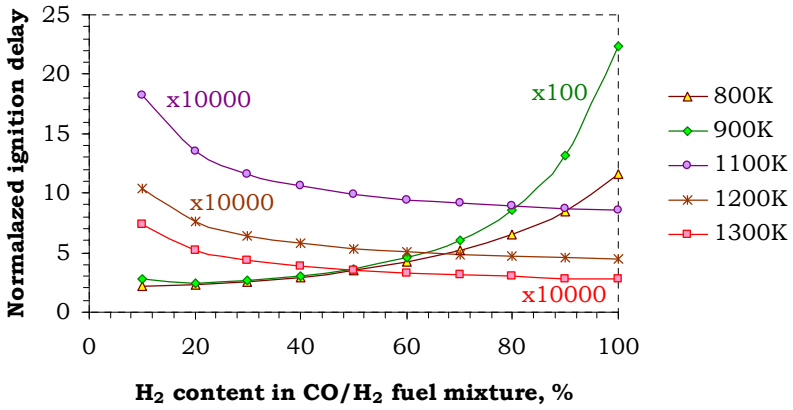

Figure 6.21: Mixture composition effect on ignition delay for various CO/H_2 fuel mixtures at different temperatures

The sensitivity analysis based on OH at 1100K and 1atm pressure for fuel mixtures with different CO/H_2 compositions shows that the major reaction contributing to a highly reactive OH production for all mixtures is R2, which is competing for radicals with the HO_2 production reactions R19 and R6 for the entire range of mixture compositions, see Figure D 25. With increase in CO concentration, the sensitivity coefficient for reaction R2 drops significantly indicating that the system is becoming less reactive due to smaller concentrations of H_2 and H radical. In addition, for mixture

compositions with higher CO concentrations the CO oxidation is proceeding only through reaction R17. The reaction R18 is not taking place effectively due to lack of HO_2 radicals.

For systems at lower temperatures than 1000K with addition of CO the ignition delay gets shorter. This behaviour indicates that CO is contributing more significantly through the HO_2 radical consumption reaction R18. With a decrease in temperature the reaction R2 proceeds more slowly, and reactions R6 and R19, which produce HO_2 radicals, become more important to the system reactivity. In addition, they proceed to further chain propagation though HO_2 and H_2O_2 reactions, because at lower temperatures HO_2 concentrations are expected to be sufficiently higher.

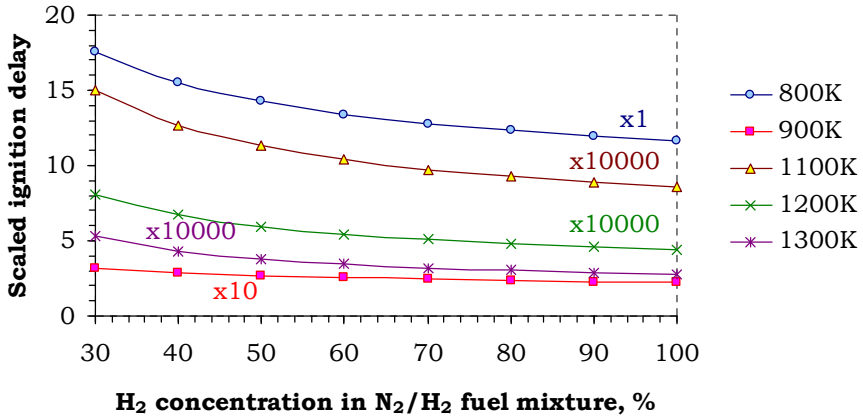

Figure 6.22: Mixture composition effect on ignition delay for various H_2/N_2 fuel mixtures at different temperatures

For N_2/H_2 fuel mixtures with an increase in N_2 concentration, the ignition delay gets longer, see Figure 6.22. Nitrogen dilutes the fuel/air mixture resulting in a decrease of H radical concentrations, which are crucial for the reaction R2, see Figure D 26. From the sensitivity analysis it is evident that for N_2/H_2 fuel the change in N_2 composition affects only the

value of the OH sensitivity coefficients of the main chemical reactions, which are the same for different N_2/H_2 compositions

6.7 Conclusions

Values of laminar burning velocities, critical strain rates to extinction and ignition delays for various syngas mixtures were computed using 1D flames and 0D reactor models. The computations of laminar burning velocities were particularly extensive in order to build a comprehensive database for lean flames covering a wide variety of fuel mixture compositions involving CO, H_2, CH_4, N_2, CO_2 and H_2O and a broad range of operating conditions (temperatures from 300K up to 900K and pressures from 1 up to 50 bars). The databases of critical strain rates to extinction and ignition delays were limited to $CO/H_2/N_2$ fuel mixtures under a range of operating temperatures (from 300K up to 900K) and pressures (from 1 up to 50 bars).

From the laminar burning velocity computations and reaction rate sensitivity analyses it was concluded:

◊ That the addition of CO to the H_2 flame lowers the laminar burning velocity, but CO does not act as a passive diluent, it has a very low burning velocity in the "dry" air, but it interacts kinetically through its main oxidation reaction: $CO+OH \rightarrow CO_2+H$. This reaction is slow when compared to hydrogen reactions and mainly takes place in the extended post-flame region, where temperatures are sufficiently high.

◊ The pressure rise results in a laminar burning velocity decrease in CO/H_2 flames due to an increase in the effectiveness of the third order reactions $H+O_2+H_2O \rightarrow HO_2+H_2O$ and $H+O_2+N_2 \rightarrow HO_2+N_2$, which become more efficient with pressure rise. These H radical consuming

reactions are chain terminating reactions; therefore their increased effectiveness results in a laminar burning velocity drop.

◊ The temperature rise results in a rapid laminar burning velocity rise due to an increase in reaction rates of nearly all reactions and acceleration of the fuel consumption, heat release rate and overall combustion process.

◊ The addition of N_2 results in a laminar burning velocity drop, because N_2 acts mainly as a passive diluent, resulting in a decrease of the adiabatic temperature drop and promotion of HO_2 production and consumption reactions. N_2 also acts as a third body in the recombination reaction.

◊ The presence of CO_2 in the fuel mixture will impact the flame and its laminar burning velocity in several ways through changes in mixture specific heat and adiabatic flame temperature, chemical kinetic rates and radiative heat transfer. The presence of CO_2 results in the decrease in laminar burning velocity due to the enhanced reverse reaction $CO + OH \rightarrow CO_2 + H$ rates and H radical consumption. The effects of CO_2 are more significant at high pressures as well because it participates as a third body in the recombination reactions.

◊ The effect of H_2O is similar to N_2 if it is present in small quantities, but if its concentrations are increased it starts to interact kinetically as a third body in chain termination reactions, it accelerates H consumption though enhanced reverse reaction rates of $OH+H_2 \rightarrow H+H_2O$ and converts into radicals and into H_2O through HO_2 chemistry.

◊ The increase in concentration of H_2 in the H_2/CH_4 fuel mixture results in the exponential laminar burning velocity rise due to the promotion

of high temperature branching reactions and increase in system reactivity. H_2 reacts mainly with O_2 and produces the H radical needed for the reaction $H+O_2 \rightarrow OH+O$ to proceed. This reaction produces OH and O radicals needed for $CH_4 \rightarrow CH_3$ conversion.

◊ The laminar burning velocities for pure methane (0.39 m/s) and for CO flames in "wet" air are similar, but for CO/CH_4 fuel mixtures it is higher reaching a peak value of 0.57 m/s at a fuel mixture composition of 80%CO/20%CH_4. The reason for such behaviour is that the presence of hydrocarbon fuel (methane) will inhibit CO oxidation until all of the fuel has disappeared, but at this point the OH concentration rises rapidly and the reaction $OH+CO \rightarrow H+CO_2$ which consumes CO to produce CO_2 is accelerated, resulting in the laminar burning velocity rise.

◊ This study also demonstrates that thermal ignition kinetics for the CO/H_2 fuel mixtures at different pressures, temperature and fuel mixture composition are driven by several reactions: $H+O_2 \rightarrow O+OH$, $H+O_2+M \rightarrow HO_2+M$, $H+O_2+N_2 \rightarrow HO_2+N_2$, $CO+HO_2 \rightarrow CO_2+OH$

While for the N_2/H_2 system, the main reactions are $H+O_2 \rightarrow O+OH$, $H+O_2+M \rightarrow HO_2+M$ and $H+O_2+N_2 \rightarrow HO_2+N_2$.

7 Gas turbine combustor modelling

In premixed combustion, where oxidiser and fuel are mixed prior to ignition, combustion takes place as a flame that is propagating into the unburned reactants.

The modelling of premixed combustion is generally more difficult in comparison to that in non-premixed flames because combustion occurs as a thin propagating flame that is more closely coupled to the velocity and pressure fields and more strongly affected by turbulence. For subsonic flows, the overall rate of the flame propagation is determined by both the laminar burning velocity and the turbulent eddies in the unburned reactant mixture. To capture the laminar burning velocity the internal flame structure needs to be resolved and hence detailed chemical kinetics and molecular diffusion processes. Since practical laminar flame thicknesses are of the order of millimetres or smaller, the required computational resolution is not affordable.

The turbulence wrinkles and stretches the propagating flame sheet resulting in an increase in the sheet area and the effective burning velocity. These effects are created by the larger turbulent eddies, while the small turbulent eddies, if they are smaller than the laminar flame thickness, penetrate the flame sheet and modify the flame structure.

While non-premixed combustion can be greatly simplified to that of a mixing problem, premixed combustion modelling is based on capturing the turbulent burning velocity.

7.1 Turbulent flame speed closure (TFC) model

A combustion model, based on a turbulent flame speed closure, has become popular within the gas turbine community due to its computational efficiency. The idea of the TFC model was first proposed by Zimont [169] in the late 70s but only recently applied practically. The original TFC model was only capable of handling homogeneously premixed combustion; however in the last couple of years it has been extended to partially premixed combustion problems [170-173].

The TFC model is based on the solution of the transport equation for the density weighted progress variable, whose closure is based on the turbulent burning velocity:

$$\frac{\partial}{\partial t}(\rho c) + \nabla \cdot (\rho \vec{v} c) = \nabla \cdot \left(\frac{\mu_t}{Sc_t} \nabla c \right) + \rho S_c \qquad \textbf{(7.1)}$$

where c is mean reaction progress variable, Sc_t is a turbulent Schmidt number and S_c – reaction progress source term (s^{-1}).

Here progress variable is defined in terms of normalized combustion products in the following way:

$$c = \frac{\sum_{i=1}^{n} Y_i}{\sum_{i=1}^{n} Y_{i,eq}} \qquad \textbf{(7.2)}$$

Here n is the number of products, Y_i is the mass fraction of product species i, whilst $Y_{i,eq}$ is the equilibrium mass fraction of product species i. Based on this definition, for unburned mixture c=0 and for fully burned mixture c=1.

The transient and convective terms on the left side of equation 7.1 can be calculated directly from the iterative solver, but it is necessary to model

the turbulence parameters and the reaction source term on the right. The modelling of these terms introduces some problems. The accurate representation of the turbulent diffusion term (first term) and the source term of mean reaction rate depends on both chemical and turbulent processes.

The problem with the diffusion term is that it cannot be represented accurately by a gradient expression, analogous to Fick's law, because of the existence of counter gradient diffusion.

The differential effect of a pressure gradient on the cold and heavy reactants and the hot and light products gives rise to the transport process usually described as counter gradient diffusion. The light products will accelerate more than the heavy reactants and diffuse towards the burnt side of the flame, where their concentrations are already high, while the reactants will remain close to the unburnt side, where their concentrations are still elevated.

As counter gradient diffusion is caused by the density change during combustion, its influence will depend on the heat release, for high heat release the counter gradient diffusion will be greater and vice versa [174].

Another problem is the modelling of the chemical source term, which varies sensibly with chemical and turbulence time scales. Various approaches have been adopted to develop a model for the reaction progress source term, ranging from the assumption that reaction rate is only controlled by the turbulent mixing to models based on the structure of unstrained laminar flames. The advantage of using turbulent burning velocity is that the effects of chemical kinetics are included but not explicitly calculated within the turbulent flow.

The mean reaction rate is modelled as:

$$\rho S_c = \rho_u S_t |\nabla c| \quad \textbf{(7.3)}$$

where ρ_u is unburned mixture density and S_t is turbulent burning velocity. Turbulent burning velocity is then computed using the following expression:

$$S_t = A(u')^{3/4} S_{lam}^{1/2} \alpha^{-1/4} l_t^{1/4} = Au' \left(\frac{\tau_t}{\tau_c} \right)^{1/4} \quad \textbf{(7.4)}$$

where A is a model constant and the value of 0.52 was shown by Zimont et al. [175] to give accurate results over a wide range of operating conditions and hydrocarbon fuels, u' is the root-mean-square turbulence velocity (m/s), S_{lam} – laminar burning velocity (m/s), α – thermal diffusivity of the unburnt reactants (m^2/s), l_t – turbulence length scale (m); τ_t – turbulence time scale (s), τ_c – chemical time scale (s)

The values of S_{lam} and α depend on the fuel and operating conditions. The value of S_t will be altered as the chemistry of the combustion process is changed. The other terms are influenced by the turbulence, so the source term will also respond to changes in the turbulence field.

7.1.1 The partially premixed TFC model

The original TFC model was only applicable for cases where reactants were homogeneously premixed. This assumption was used to perform analysis of commercial premixed gas turbine combustors, but the effects of the mixture inhomogeneity are also very important as they have considerable influence on flame stability, pollution formation and thermo-acoustic effects. Therefore, the model has been extended to partially premixed combustion.

The partially premixed model solves three transport equations for the progress variable, mean mixture fraction ($\tilde{\xi}$) and mixture fraction variance ($\tilde{\xi}^2$). Using these variables and assuming a pdf (probability density function) for the mixture fraction distribution it is possible to calculate an average value for the variables required for the following equation:

$$S_t\left(\tilde{\xi}\right) = A(u')^{3/4} S\left(\tilde{\xi}\right)_{lam}^{1/2} \alpha\left(\tilde{\xi}\right)^{-1/4} l_t^{1/4} \quad \textbf{(7.5)}$$

In this model mixture fraction distribution is described by a beta function. The disadvantage of this method is that significant complexity is introduced to the model. The beta function cannot be readily integrated in "real time"; therefore lookup tables need to be produced. But the use of lookup tables ensures that the values of all variables that depend on the mixture fraction can be estimated accurately.

7.1.2 Flame stretch effect

Since industrial low-emission combustors typically operate near the blow-off limit, flame stretching has a significant effect on the heat release intensity. To take this effect into account the source term of mean reaction rate for progress variable (ρS_c) is multiplied by a stretch factor, which represents the probability that the flame will not be quenched by the stretching. If there is no stretching (G=1), the probability that the flame will be unquenched is 100%.

The stretch factor is found by integrating the log-distribution of the turbulence dissipation rate ε:

$$G = \frac{1}{2}\,\mathrm{erfc}\left\{-\sqrt{\frac{1}{2\sigma}}\left[\ln\left(\frac{\varepsilon_{cr}}{\varepsilon}\right) + \frac{\sigma}{2}\right]\right\} \quad \textbf{(7.6)}$$

Here erfc is the complementary error function.

$\sigma^2 = \mu_{str} \ln(l_t/\eta)$ is the variance of the log-normal distribution (where μ_{str} is a constant equal to 0.26, measured in turbulent non-reacting flows, but is considered suitable for most premixed flames) and ε_{cr} is the turbulence dissipation rate at the critical strain rate:

$$\varepsilon_{cr} = 15\nu g_{cr}^2 \quad \textbf{(7.7)}$$

where g_{cr} is the critical strain rate to extinction, which can be obtained experimentally or from chemical kinetics simulations.

7.2 Simulations – PRECCINSTA Project

7.2.1 Introduction

The **PRE**diction and **C**ontrol of **C**ombustion **INS**tabilities in **T**ubular and **A**nnular GT Combustion Systems Project (PRECCINSTA) was a recent European project which investigated combustion instability phenomena.

One of the project partners DLR (German Aerospace Centre) performed experimental work and provided a significant amount of validation data to support the future development of combustion models and to assess the level of existing modelling. They undertook an extensive measurement programme covering aerodynamics, temperatures and species on an atmospheric premixed gas turbine type combustion rig [205].

Although this project focussed on combustion instability phenomena; it provided experimental data for model validation and allows us to examine the combustion of syngas in a gas turbine combustor.

7.2.2 Experimental facility

The brief background provided here is intended to simply establish the context for the numerical simulations reported.

All experimental investigations were performed on premixed swirling CH_4/air flames at atmospheric pressure in a gas turbine like combustor, which has optical access.

The experimental combustor has three major geometry components: the air plenum, the swirling burner and the square combustion chamber, which is completely transparent, enabling experiments by Laser Doppler Velocimetry, Raman spectroscopy and Laser Induced Fluorescence to be performed [176].

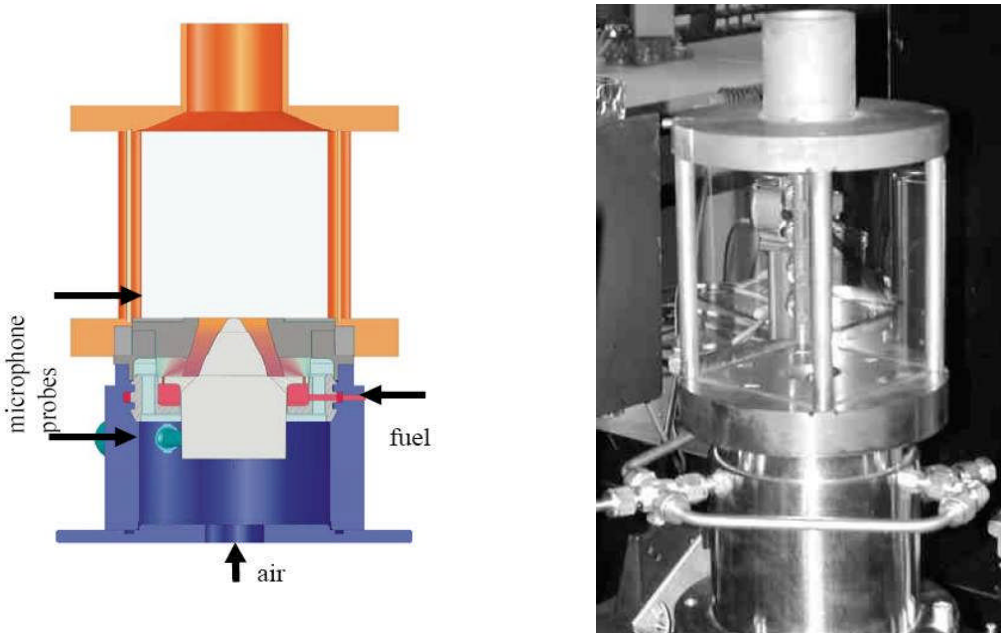

a) b)

Figure 7.1: a) Complete experimental rig layout; b) Detail of DLR's combustion chamber [177]

The structures holding the four quartz windows and swirling burner are made out of metal; see Figure 7.1 and Figure 7.2.

All experiments were performed under ambient operating conditions (pressure and temperature). The choice of these conditions is clearly far from real gas turbine combustor operating conditions, where air from the

compressor is typically supplied at approximately 15bar pressure and 600K temperature. This experimental setup is easy to put in operation however and simple to maintain, whilst the risks associated with high pressures and temperatures are eliminated.

The test rig is setup vertically with flow moving from the bottom upwards. The air is supplied by an electronically controlled compressor.

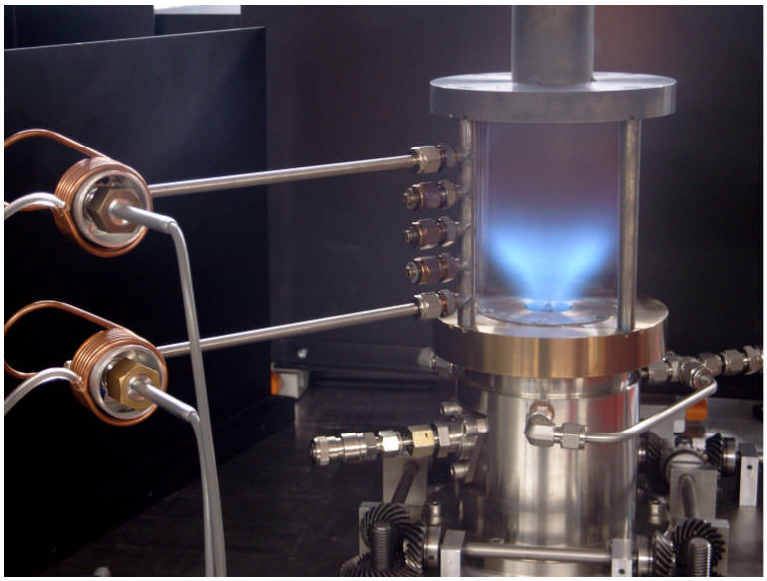

Figure 7.2: Operating experimental equipment with the measurement instrumentation [177]

The injector consists of an experimental swirler with simple gimlets, which have twelve valves. Fuel is injected by twelve orifices connected directly to the swirler's arms and at the same time directs the flow so it moves rotationally inside the chamber.

Figure 7.3: Backside view of the swirler with the three air inlets and twelve fuel injectors [177]

Figure 7.4: Front side view of the swirler and detail of the twelve arms which gathers in one exit [177]

The fuel was injected through small holes of 1mm diameter in each of the swirler slots with very high momentum to ensure very good air and fuel premixing. The fuel injection orifices with diameter of approximately 1mm were used; therefore the fuel was injected with very high speed (about 100 m/s for methane) [177]. The exit diameter of the nozzle is about 30mm, see Figure 7.3 and Figure 7.4.

The respective flows of air and fuel (methane) can be controlled completely independently, but they are limited by the structural resistance of the combustion chamber windows. In this configuration 35 kW was not exceeded in order to ensure the reasonable lifespan of the chamber walls [177].

7.2.3 Combustor geometry

As was mentioned before, the PRECCINSTA combustor rig has a very complex geometry consisting of air plenum, the swirling burner and the

square combustor. Because the air was fed from the burner plenum and mixed within the swirler and the central part of the burner in this way, none of the geometrical details can be neglected or the combustor geometry simplified.

Some elements, like connections of the measurement instrumentation, were neglected due to their small size.

Due to complexity of the combustor geometry, a hybrid grid, containing trihedral non-structured and quadrilateral structured elements was employed. The grid contains approximately 700000 modes and 1600000 cells. This grid was taken from the project partners.

The density of the mesh varies in different part of the domain; in the swirler it is highly refined due to the complex geometry, while in the combustion chamber it was optimized to sustain the best possible compromise between grid density and desired solution quality.

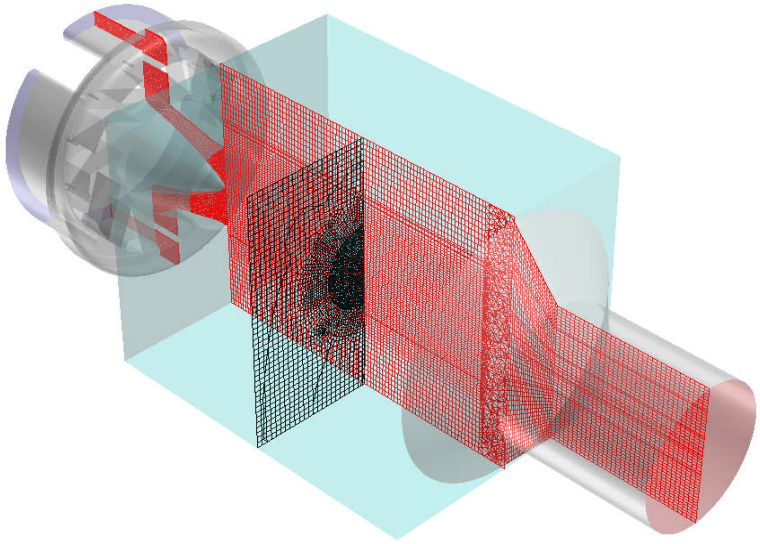

Figure 7.5: Computational domain section

A section of the computational domain is given in Figure 7.5. The domain zone along the chamber centreline is discretised with greater

density to accommodate the large gradients which appears with the presence of the flame. A more refined grid in the combustion chamber would be desired as well, but in order to reduce computational effort, it was created to be coarser.

7.2.4 Modelling background

The numerical model used in this study was developed using the commercial Computational Fluid Dynamics (CFD) software, Fluent. To determine the compressible reacting flow and heat transfer in the computational domain, Fluent solves the fundamental equations of mass, momentum (i.e. the continuity, Navier-Stokes equations), energy conservation and gas species mass fraction conservation on an unstructured 3-D finite-volume grid. The models and methods applied in this work are summarised.

Fluent provides several different turbulence closure models ranging from the simple two-equation k-ε model to the Reynolds stress model (RSM). Although two-equation turbulence models give reliable results in many applications, they are known to be inaccurate for buoyant or highly-swirling flows where the structure of the turbulence is clearly no longer isotropic. Therefore the Reynolds stress model is expected to perform better in this situation. RSM closes the RANS equations by solving transport equations for the Reynolds stresses, together with equation for the dissipation rate. Seven additional transport equations are solved for 3D flow. More information on this model is given in Fluent's user guide [206].

Fluent solves the complete set of transport equations by first discretising them on a finite-volume mesh and then solving for the velocity, pressure, temperature and conserved scalars in an iterative way until the equations are satisfied to a given numerical accuracy. Here Pressure-

Based Segregated algorithm is employed. This algorithm extracts pressure field by solving a pressure equation, which is obtained from continuity and momentum equations. The pressure interpolation is performed using PRESTO! scheme, which is considered to be most suitable for flows with high swirl numbers [206].

A second order upwind differencing scheme is used for the convection terms to ensure good resolution of the high gradients of species and velocity expected in the regions of strong mixing.

Transient simulations were performed, because due to highly swirling flow the steady solutions failed to converge.

7.2.5 Boundary conditions

The boundary conditions for the benchmark case with methane were adopted from DLR combustion experiments, which they had considered. For cases with CO/H_2 mixtures, air and fuel boundary conditions were calculated based on fuel gas stoichiometric air fuel ratio by keeping the total mass flow (air + fuel) the same as for methane case.

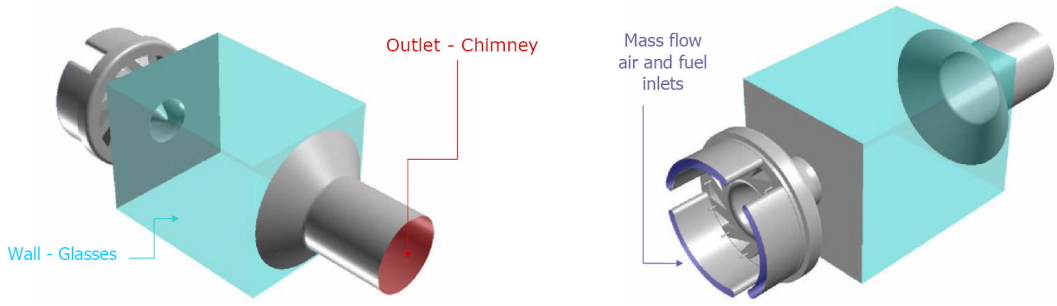

Figure 7.6: Description of the nature of the boundary conditions

7.2.6 Benchmark case - methane

Stable combustion with methane fuel at an equivalence ratio of 0.84 has been investigated computationally here. DLR performed experiments

for lean flames with equivalence ratios of 0.84 and 0.7. The experimental campaign at equivalence ratio 0.7 was performed in order to study combustion instabilities. This case was not considered in the present study. The boundary conditions are given in Table 7.1.

Table 7.1: Boundary conditions for the simulation with methane

Variable	**Air Inlets**	**Fuel Inlets**
Mass flow	0.00407 kg/s	$4.96 \cdot 10^{-5}$ kg/s
Turbulence intensity	2 %	2 %
Hydraulic diameter	0.05 m	0.000987 m
Inlet Temperature	300 K	300 K
Equivalence Ratio	0.84	
Fuel	Methane	

In order to examine the effect of methane replacement with syngas, methane fuel was replaced with $CO/H_2/N_2$ mixtures.

7.2.7 First gas – high calorific value syngas

In order to provide a demonstration of the modelling similar to that with methane, a comparatively high H_2-content gas has been introduced comprising of 88%H_2/12%CO. This gas has a similar heating value (HHV=55.76 MJ/kg, LHV=48.00 MJ/kg) to methane and its stoichiometric air fuel ratio (AFR_{st}=13.41) is similar too. The values for methane are HHV=55.5MJ/kg and LHV=50.16MJ/kg; with an AFR_{st}=17.16.

The choice of a syngas, to replace methane, is limited by several other factors. The air/fuel ratio needs to be kept similar, so that the mass flows of air and fuel fed through the air plenum and fuel injectors will be also similar. The hydrogen rich gas will have much lower density, however, and therefore the fuel inlet velocities are expected to be significantly higher. Another factor is that this gas should have a similar heat release rate given

the similar heating values and mass flows. The boundary conditions for the fuel mixture with 12%CO/88%H_2 are given in the Table 7.2.

Table 7.2: Boundary conditions for the simulation with 12%CO/88%H_2 fuel mixture

Variable	**Air Inlets**	**Fuel Inlets**
Mass flow	0.00407 kg/s	$6.37 \cdot 10^{-5}$ kg/s
Turbulence intensity	2 %	2 %
Hydraulic diameter	0.05 m	0.000987 m
Inlet Temperature	300 K	300 K
Equivalence Ratio	0.84	
Fuel	12%CO/88%H_2	

7.2.8 Second gas – low calorific value syngas

Another gas has also been considered, which has very different properties in comparison to methane and the fuel mixture with 12%CO/88%H_2. This fuel mixture is highly diluted with nitrogen (1.5%CO/28.5%H_2/70%N_2) and has therefore a low calorific value of 3.6 MJ/kgK and a stoichiometric air fuel ratio of 1. In order to maintain the total mass flow, the air mass flow rate needs to be minimised (due to the increase in fuel mass flow) in order to retain the desired equivalence ratio. This is clearly not the strategy to be adopted in practice but the intention here is simply to retain the same basic combustor geometry.

The boundary conditions for this fuel gas mixture are given in Table 7.3.

Table 7.3: Boundary conditions for the simulation with 1.5%CO/28.5%H_2/70%N_2 fuel mixture

Variable	Air Inlets	Fuel Inlets
Mass flow	0.002134 kg/s	0.002134 kg/s
Turbulence intensity	2 %	2 %
Hydraulic diameter	0.05 m	0.000987 m
Inlet Temperature	300 K	300 K
Equivalence Ratio	1	
Fuel	1.5%CO/28.5%H_2/70%N_2	

7.2.9 Third gas – medium calorific value gas

Another fuel mixture of 50%CO/50%H_2 was employed. It has a medium calorific value (HHV=17.5 MJ/kg) and a stoichiometric air fuel ratio of 4.576. For this case, the air mass flow was kept the same, but the fuel mass flow needed to be increased due to the difference in air to fuel ratio, in comparison to methane. The power output in the combustor is expected to be similar to the methane. Boundary conditions are given in the Table 7.4.

In order to observe greater effects of flame straining and flame behaviour, air mass flow was increased by 50%. In order to preserve equivalence ratio, fuel mass flow was increased as well, see

Table 7.5.

Table 7.4: Boundary conditions for the simulation with 50%CO/50%H_2 fuel mixture

Variable	Air Inlets	Fuel Inlets
Mass flow	0.00407 kg/s	0.000178 kg/s
Turbulence intensity	2 %	2 %
Hydraulic diameter	0.05 m	0.000987 m
Inlet Temperature	300 K	300 K
Equivalence Ratio	0.84	
Fuel	50%CO/50%H_2	

Table 7.5: Boundary conditions for the simulation with 50%CO/50%H_2 fuel mixture with increased air mass flow by 50%

Variable	Air Inlets	Fuel Inlets
Mass flow	0.006105 kg/s	0.0002802 kg/s
Turbulence intensity	2 %	2 %
Hydraulic diameter	0.05 m	0.000987 m
Inlet Temperature	300 K	300 K
Equivalence Ratio	0.84	
Fuel	50%CO/50%H_2	

For all four cases the combustor outlet is modelled with a zero gradient outflow boundary, placed sufficiently far away from the burner to ensure that combustion is completed.

The walls of the combustor are considered to be adiabatic.

7.2.10 Laminar burning velocities and critical strain rate to extinction data

As mentioned earlier, the source term in the equation is a function of turbulence properties and turbulent burning velocity, which in turn is a function of laminar burning velocity. The laminar burning velocity is not computed directly by the CFD code, but it is included as information in the probability density function (PDF) along with mixture fraction and mixture fraction variance. Combustion is detected by the mathematical model where the laminar burning velocity appears in the domain and the production term of progress variable becomes positive.

The laminar burning velocity data for methane are already available in Fluent, but need to be provided for $CO/H_2/N_2$ mixtures.

For fuel mixtures with 12%CO/88%H_2, 1.5%CO/28.5%H_2/70%N_2 and 50%CO/50%H_2 laminar burning velocities as a function of mixture fraction were provided in the form of 6th or 5th degree polynomials.

For fuel mixture with 12%CO/88%H_2:

$$S_{lam} = 289372 \cdot m_{fr}^6 - 318596 \cdot m_{fr}^5 + 135880 \cdot m_{fr}^4 - 27492 \cdot m_{fr}^3 + \\ + 2462.6 \cdot m_{fr}^2 - 54.762 \cdot m_{fr} + 0.163 \quad \textbf{(7.8)}$$

For fuel mixture with 1.5%CO/28.5%H_2/70%N_2:

$$S_{lam} = -5948.3 \cdot m_{fr}^6 + 21268 \cdot m_{fr}^5 - 31024 \cdot m_{fr}^4 + 23546 \cdot m_{fr}^3 - \\ - 9779.5 \cdot m_{fr}^2 + 2106.5 \cdot m_{fr} - 183.99 \quad \textbf{(7.9)}$$

For fuel mixture with 50%CO/50%H_2:

$$S_{lam} = -473.83 \cdot m_{fr}^5 + 1029.1 \cdot m_{fr}^4 - 791.97 \cdot m_{fr}^3 + \\ + 238.29 \cdot m_{fr}^2 - 19.627 \cdot m_{fr} + 0.5127 \quad \textbf{(7.10)}$$

User Defined Functions (UDFs) were then used to provide laminar burning velocity data in Fluent.

In practical premixed combustion the flame is continuously wrinkled and stretched by the turbulence, which can even quench the flame locally.

Flame stretching effects can be taken into account by multiplying the reaction source term (ρS_c) by the stretch factor G. In order to calculate the turbulence dissipation at the critical strain rate to extinction, the values of critical strain rate need to be provided, because they are not computed directly by the solver.

By default in Fluent a large value of critical strain rate to extinction (1.0e+08) is given. Therefore the flame stretch factor is most likely to be equal 1 (100% probability that flame will not extinguish) for the entire flow field. In order to take flame stretching into account the strain rate to

extinction as a function of mean mixture fraction must also be provided through a UDF.

For fuel mixture with 12%CO/88%H_2:

$$g_{cr} = 98370000 \cdot m_{fr}^3 - 22510000 \cdot m_{fr}^2 + 1995000 \cdot m_{fr} - 33630 \quad \textbf{(7.11)}$$

For fuel mixture with 1.5%CO/28.5%H_2/70%N_2:

$$g_{cr} = 5789 \cdot m_{fr}^3 - 53075 \cdot m_{fr}^2 + 56897 \cdot m_{fr} - 9125.2 \quad \textbf{(7.12)}$$

For fuel mixture with 50%CO/50%H_2:

$$g_{cr} = -15760000 \cdot m_{fr}^3 + 5718000 \cdot m_{fr}^2 - 515836 \cdot m_{fr} + 13925 \quad \textbf{(7.13)}$$

For methane the critical strain rate to extinction was defined using the following equation:

$$g_{cr} = C \frac{S_{lam}^2}{\chi(T_{at})} \quad \textbf{(7.14)}$$

where C is a constant, S_{lam} is the laminar burning velocity and $\chi(T_{at})$ is the molecular diffusivity evaluated at adiabatic flame temperature. The constant C was taken to be equal 8.4. This value was determined by Polifke et al. [174] and is valid for atmospheric flames.

7.3 Simulations results

7.3.1 Methane flames

The purpose of these simulations is to demonstrate the application of laminar burning velocity and critical strain rate to extinction data in computational fluid dynamics (CFD) modelling. As a first step the evaluation of the TFC model performance was carried out. The computations were performed using methane fuel. The results from these

simulations were compared with experimental values, reported by DLR [177].

The comparison of predicted axial velocities for strained and unstrained flames show a good agreement with experimental values, see Figure 7.7. However, the experimental values indicate that there is stronger recirculation zone than predicted by computations. Tangential velocity results support the analysis as tangential velocity, predicted numerically, is lower in comparison to experimental values, see Figure 7.8. In addition, the axial velocities further downstream of the burner are considerably lower for the strained flame in comparison to experimental values and computations for the unstrained flame, see Figure 7.7. The more detailed comparisons of experimental and numerical values of axial and tangential velocities are given in Appendix F, see Figure F 11 to Figure F 20.

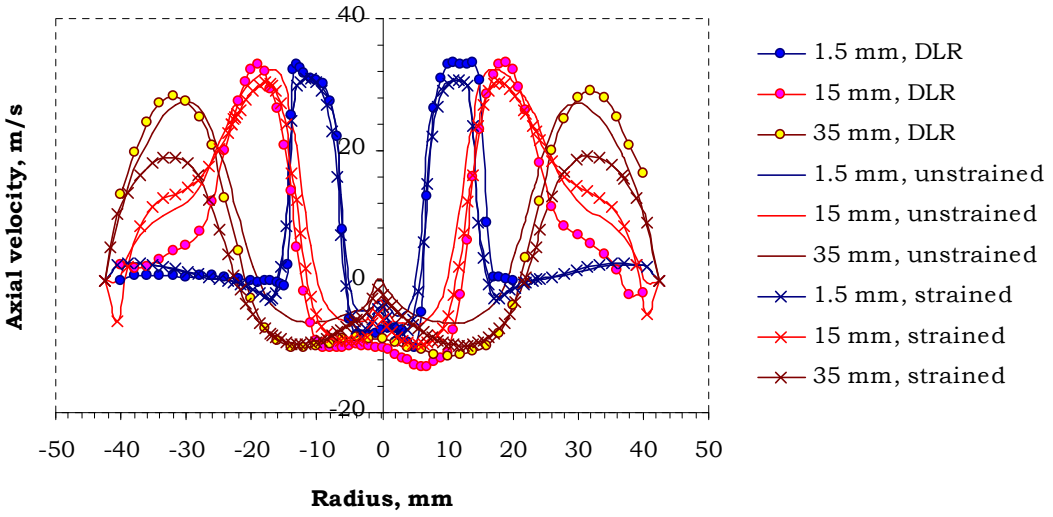

Figure 7.7: Predicted axial velocities compared with experimental measurements for methane

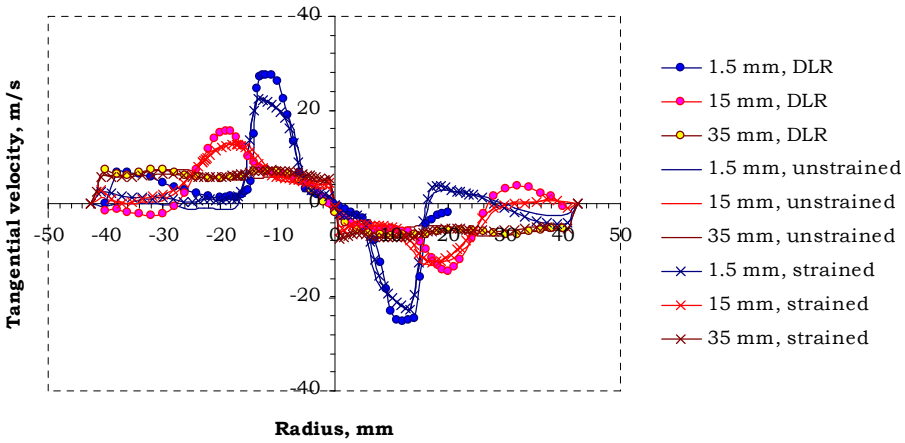

Figure 7.8: Predicted tangential velocities compared with experimental measurements for methane

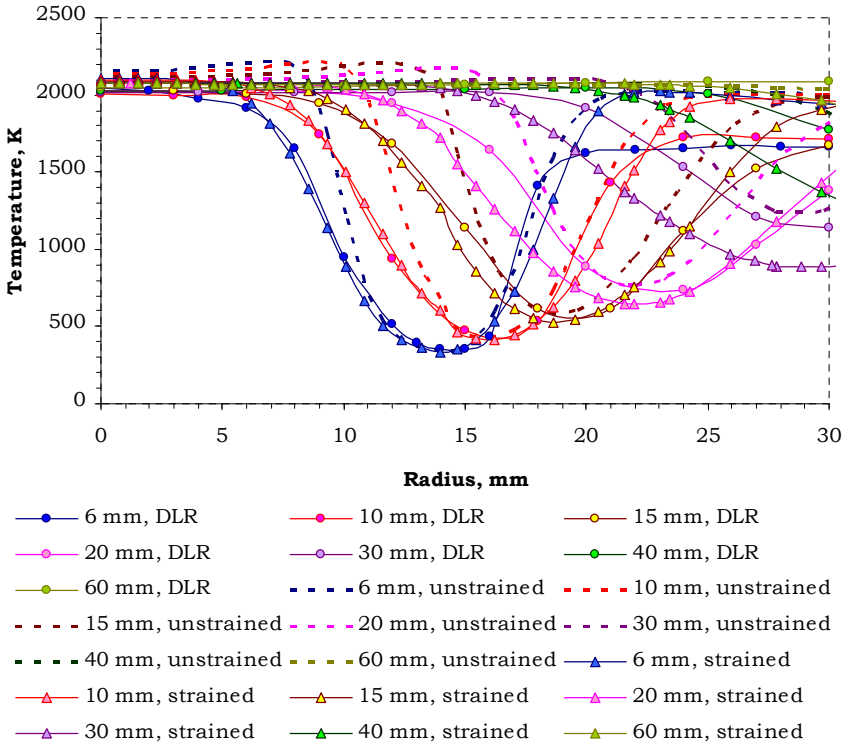

Figure 7.9: Predicted temperatures compared with experimental measurements for methane

Temperature field analysis shows that the flame straining has an impact on heat release and the flame temperature. The comparison between experimental and numerical simulations shows that the unstrained flame model over-predicts temperature at the inner flame cone region, where heat release is expected to highest, see Figure 7.9 and Figure F 3 to Figure F 10. From these figures it is evident that the flame cone, predicted by the unstrained flame model, is narrower and shorter in comparison with experiment, with the strained flame model indicating more intense combustion. Although the strained flame model predicts very well the flame profile in the inner region of the flame cone, it overestimates flame temperatures in the regions outside the flame cone and close to the combustor walls. The same temperature levels in this region are achieved from simulations with the unstrained flame model as well, showing that in this region the flame stretching has little impact on the temperature, except in regions several millimetres away from the combustor wall. These discrepancies appear because both numerical simulations assume that there is no heat loss though the combustor wall. Considerable heat transfer by convection and radiation takes place due to high temperatures in the combustion chamber. This heat loss is not taken into account in the numerical simulations.

7.3.2 $CO/H_2/N_2$ mixtures

7.3.2.1 Fuel mixture with composition 12%CO/88%H_2

Methane was replaced with a fuel mixture composed of 12%CO/88%H_2. This mixture has a similar stoichiometric air to fuel ratio and calorific value to methane, but its laminar burning velocity (1.73 m/s for 12%CO/88%H_2 compared with 0.42 m/s for CH_4 at ϕ=1) and critical

strain rate to extinction (29475 1/s for 12%CO/88%H_2 compared with 8000 m/s for CH_4 at ϕ=1) are much higher. These differences are expected to affect the combustion process and resulting flow.

The comparison between computations of strained and unstrained flame models show that flame of this fuel mixture is weakly strained as flame stretching has negligible impact on the temperature and velocities, see Figure F 21 to Figure F 28. The stretch factor contour plot supports this finding as the stretch factor is close to unity for almost the entire flow field, except in the region close to the flame front, where turbulence is more intense due to flow recirculation, and higher shear stresses result in an increase in hydrodynamic strain; see Figure 7.10.

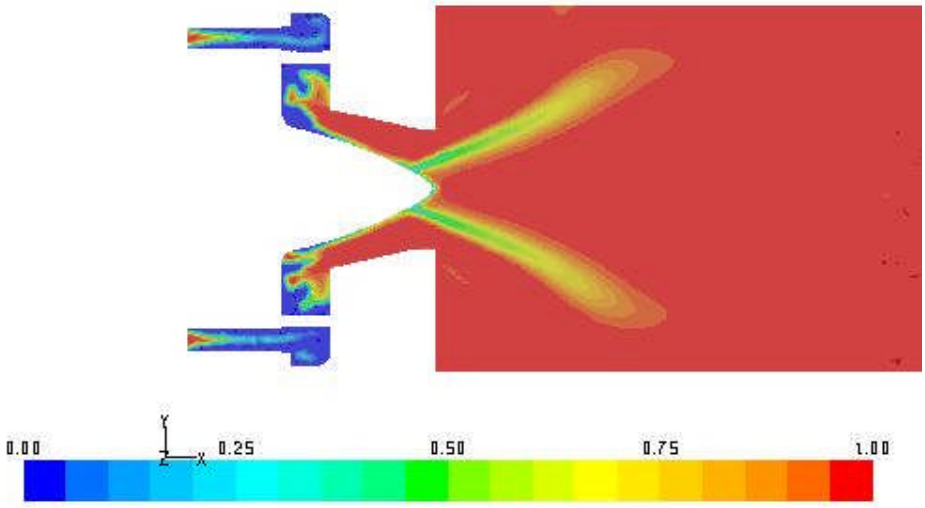

Figure 7.10: Contours of the stretch factor for combustion with 12%CO/88%H_2 fuel mixture

The temperature and velocity profiles (Figure F 21 to Figure F 28) show that the replacement of the fuel results in a shorter flame cone, as this fuel burns more intensively due to the high content of hydrogen. Due

to lower density and higher adiabatic flame temperature, axial and tangential velocities in the device are higher in comparison to methane burning.

7.3.2.2 Fuel mixture with composition 1.5%CO/28.5%H_2/70%N_2

This fuel mixture has similar laminar burning velocities to methane and its critical strain rates to extinction are considerably lower (7000 1/s at ϕ=1) in comparison to the fuel mixture with 12%CO/88%H_2. It is expected to exhibit greater effects of flame straining on the overall combustion process. This fuel mixture has a stoichiometric air fuel ratio of unity and a calorific value of 3.6 MJ/kgK. Therefore the fuel mass flow rate would need to be 17.2 times greater in comparison to methane to keep the same power output. This way of scaling proved to be impractical without major changes in the combustor sizing in particular. For this case the total air/fuel mass flow was preserved, so the air mass flow needed to be reduced.

Simulation results for strained and unstrained flames show that this gas flame is much shorter in comparison to methane, see Figure F 29 to Figure F 34. Due to reduced mass flows the power output is considerably lower resulting in a very short flame. For this gas the strain has an effect on flame shape and length. The heat release rate is much lower in comparison to unstrained flame, so combustion takes place over an extended length of flame.

7.3.2.3 Fuel mixture with composition 50%CO/50%H_2

The reason for choosing this fuel mixture was that the fuel mixtures with 12%CO/88%H_2 and 1.5%CO/28.5%H_2/70%N_2 did not provide sufficient information about flame stretching effects on the turbulent

flame. The first gas has a similar calorific value and stoichiometric AFR to methane, but its critical strain rates to extinction are much larger due to the presence of H_2. The comparison between strained and unstrained flames shows negligible strain effect on the flame shape. The second gas has similar laminar burning velocities to the methane, but its calorific value and stoichiometric AFR is an order of magnitude lower. Due to combustor size restrictions, the air and fuel mass flows were adjusted to preserve the overall mass flow passing through the combustion chamber. The temperature field analysis for this gas shows that there is a very small flame occurring in the combustor and flame straining has an impact on the flame.

The fuel mixture with 50%CO/50%H_2 is expected to produce reasonable results, because it is possible to keep the same power output in the combustion chamber without great alterations in the combustion device geometry. Although, it needs to be pointed out that due to great differences in the densities of methane and hydrogen rich fuels, the combustor geometry would be needed to be modified anyway. This study is limited to the demonstration of laminar burning velocity and the application of critical strain rate to extinction data. Therefore the combustor sizing issues are not considered here.

Two cases for the gas with composition of 50%CO/50%H_2 were investigated. For the first case the air mass flow is the same as for the methane case, only the fuel mass flow was recalculated to preserve the equivalence ratio of 0.84. For the second case the air mass flow was increased by 50% (and the corresponding fuel mass flow to keep ϕ=0.84). Even though the power output of the device is raised, it is expected to see

greater effects of flame straining due to increased velocities and turbulence.

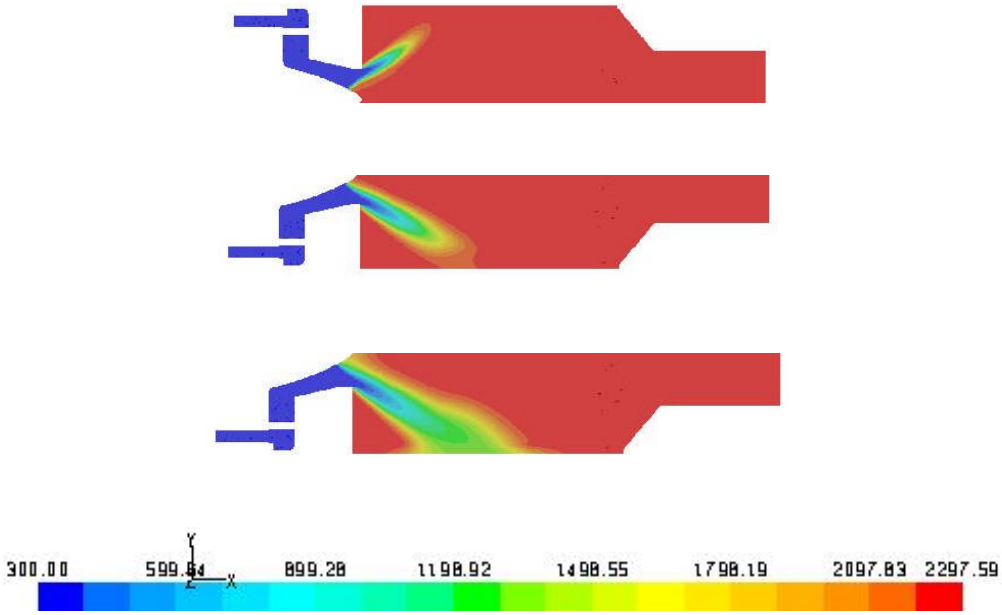

Figure 7.11: Temperature contours for simulations with fuel mixture 50%CO/50%H_2: a) unstrained flame; b) strained flame; c) strained flame with larger air and fuel mass flows.

Simulation results for unstrained flames for both cases show no effect of velocity increase on flame shape; see Figure F 35 to Figure F 40. For strained flames, the increase in mass flow and turbulence results in a peak temperature decrease by 170K (at 6 mm downstream of the burner nozzle). The flame also became wider and longer, see Figure 7.11.

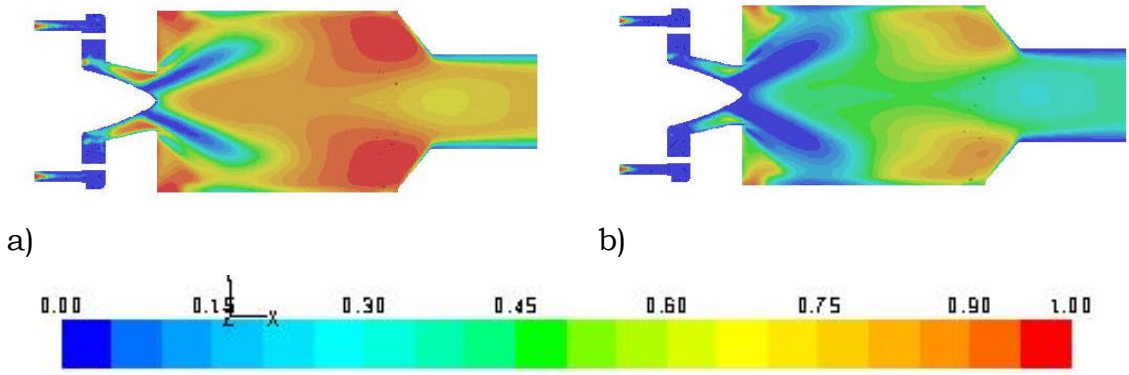

Figure 7.12: Contours of stretch factor for simulation with 50%CO/50%H_2 fuel mixture: a) case with similar mass flows to methane, b) case with increased air and fuel mass flows

The stretch factor contours show that the flame is stretched more severely for the second case due to increased flow velocities and shear stress levels in the areas of the recirculating flow, see Figure 7.12.

7.4 Conclusions

CFD simulations were performed on a practical combustor geometry fuelled by methane and several $CO/H_2/N_2$ mixtures. The purpose of these simulations is to evaluate the turbulent flame speed closure (TFC) model for partially premixed flames burning syngas and assess flame straining effects. Another aim is simply to demonstrate the application of syngas laminar burning velocity and critical strain rate to extinction data for turbulent flame modelling.

This study demonstrated good agreement between experiments and numerical simulations for strained methane flames, showing that flame straining affects both product formation rate and overall flame behaviour. Implementation of an adiabatic model resulted in temperatures close to the combustor wall being overpredicted.

The replacement of methane with $CO/H_2/N_2$ fuel mixtures led to the following findings:

- For fuel mixture with 12%CO/88%H_2, which has similar calorific value and stoichiometric air fuel ratio as methane, but much lower density, inlet velocities for the fuel were much greater. These differences in the fuel density need to be accommodated in the combustor design. For this gas the flame stretching had negligible effect on the temperature field and flame shape due to much greater critical strain rates to extinction.
- Another gas is heavily diluted with nitrogen (1.5%CO/28.5%H_2/70%N_2). This gas has similar laminar burning velocities and critical strain rates to extinction values as methane, but its calorific value and stoichiometric air to fuel ratio is much lower. The mass flows of air and fuel were set to preserve the same total mass flow as for methane. This resulted in lower power output from the combustor. For this mixture the flame was very short and flame straining had a considerable impact on the combustion process.
- The simulations with medium calorific value gas (50%CO/50%H_2) showed greater effects of flame straining on the peak flame temperature and the flame shape.

This study demonstrated that accurate determination of laminar burning velocities and critical strain rates to extinction is very important for the accuracy of the TFC model.

8 Conclusions

Syngas mixtures, which are the gasification products of various feedstocks, like coal, petroleum coke, heavy oil, biomass and waste materials, are employed as a fuel in low-emission power generation applications. Unlike natural gas or methane, which was widely used and researched for many years, these mixtures have not been widely investigated. Thus the aim of this study was to provide data on the combustion properties of the syngas mixtures.

The main focus of this research was to create a comprehensive database of laminar burning velocities and critical strain rates to extinction of various syngas mixtures. These combustion properties data are essential for gas turbine combustor modelling using turbulent burning velocity closure models.

The establishment of such a database in this study mainly relied on numerical computations, as performing laminar burning velocity experiments can be very expensive and time consuming. Therefore, the experimental campaign was limited to investigation of only four fuel mixtures ($CO/H_2/N_2$) at different equivalence ratios and operating conditions. The laminar burning velocity values obtained from the experimental campaign were used mainly for validation of the chemical kinetics model and reaction mechanism. To measure laminar burning velocities, an experimental facility for the Bunsen burner method was adopted and was set up within an existing high pressure experimental rig. Although this is a relatively inexpensive and straightforward technique, which provides laminar burning velocity data with acceptable accuracy, it has some limitations. During the experiments polyhedral flame structures

were observed for the lean (close to lean flammability limit) and for all high pressure flames. This phenomenon is a characteristic of hydrogen, which is a major constituent in the fuel mixture. Other flame phenomena observed on the Bunsen burner included weak tip flames, smooth cones with uniform luminosity and cellular flames. While the polyhedral flames represent fuel characteristics, other flame phenomena developed due to the combined effects of severe flame stretch at the tip of the premixed cone, and preferential diffusion. Since only perfect conical flames with uniform luminosity are expected to provide accurate laminar burning velocity values, only a limited amount of data could be obtained using this method.

Three medium calorific value fuel mixtures (67%CO/33%H_2, 50%CO/50%H_2, 57%H_2/43%N_2) and one low calorific value mixture (1.5%CO/28.5%H_2/70%N_2) were investigated experimentally. The experimental data obtained at ambient conditions compared well with the numerical computations.

From the results from high temperature tests it was observed that the laminar burning velocity rises with increase in the unburned reactant temperature. The measured and computed laminar burning velocities compared well up to a preheat temperature of 450K over the entire range of equivalence ratios for all gases. As the temperature is increased further, the discrepancy between measured and calculated laminar burning velocities increases. These differences at higher preheat temperatures indicates either errors in the temperature dependence of the chemical mechanism or gas properties (e.g., diffusivities) used in the computations, or errors in the reactant preheat temperature in the current measurements.

The experiments at higher pressures presented a number of complications. For the experimental arrangement with a Bunsen burner, only very lean flames were stabilised for pressures up to 5 bars. Very few flames were obtained at 6 and 7 bars, because flames at these pressures were generally very unstable. It was attempted to stabilise these very lean flames at conditions where stability limits between flashback and blowout are very narrow. It proved impossible to stabilise richer laminar flames at high pressures because the flow in the tube enters the transitional regime as the Re number approaches 2000. Therefore this technique cannot be used for laminar burning velocity determination at gas turbine operating pressures.

Various $CO/H_2/CH_4$/Diluent fuel mixture compositions were investigated numerically to determine laminar burning velocities and to investigate the effects of each constituent. The sensitivity analysis for a number of fuel mixture compositions and operating conditions showed that the combustion processes for the lean flames are governed by only a few main reactions.

Critical strain rates to extinction were determined numerically for various $CO/H_2/N_2$ fuel mixtures at different pressures, temperatures and equivalence ratios. The effects of temperature, equivalence ratio and CO or N_2 addition on critical strain rates to extinction are similar to the effects on laminar burning velocities.

The generated laminar burning velocity and critical strain rate to extinction data patterns were used to train artificial neural networks. Two separate networks were trained: one for laminar burning velocities, another for critical strain rates to extinction. The first ANN was able to predict laminar burning velocities for various $CO/H_2/CH_4$/Diluents

mixtures at different fuel mixture compositions, pressures, temperatures and equivalence ratios. Another ANN predicted critical strain rates to extinction for various $CO/H_2/N_2$ fuel mixtures at different fuel mixture compositions, pressures, temperatures and equivalence ratios.

Low emission combustor development for industrial gas turbines focuses primarily on lean-burning premixed combustion systems. The presence of the premixing chamber upstream of the combustor emphasises the importance of preventing flashback and autoignition. While flashback can be resolved with proper aero-thermal design, autoignition is strongly influenced by fuel composition and chemical kinetics. Therefore, autoignition delay simulations for various stoichiometric $CO/H_2/N_2$ fuel mixtures were carried out with a constant volume reactor model. Results from these simulations indicate that auto-ignition delay is strongly influenced by the initial reactant temperature. With increase in reactant initial temperature, the ignition delay time drops exponentially. For CO/H_2 fuel mixtures at initial reactant temperatures higher than 1000K, with increase in CO concentration in the fuel mixture, ignition is delayed. For lower temperatures the effect is opposite.

For H_2/N_2 fuel mixtures with increase in N_2 concentrations in the fuel, ignition delay gets longer due to reduced concentrations of the H radical needed for the main chain branching reaction to proceed.

Practical combustor simulations were performed to assess the accuracy of the turbulent flame speed closure model and to demonstrate the use of laminar burning velocity and critical strain rate to extinction data for turbulent combustion modelling. The data from CFD simulations of strained flames on methane were compared with experiments performed by the DLR. The comparison between computations and experiments

showed good agreement, indicating that this model is robust and can be applied for design of industrial applications.

The replacement of methane with $CO/H_2/N_2$ fuel mixtures presented several issues. First, gas ($12\%CO/88\%H_2$), which has similar calorific value and AFR_{st} to methane, was tested. The main issue with this fuel is that its density is very low due to the high quantities of hydrogen, resulting in unrealistically high fuel injection velocity. This issue needs to be addressed in the combustion device design.

The comparison between cases of strained and unstrained flames for this gas shows that flame stretching has little effect due to very high critical strain rates to extinction for this fuel mixture.

The simulation with low calorific value gas, which has a high content of nitrogen ($1.5\%CO/28.5\%H_2/70\%N_2$), shows that flame was affected by the flame straining. The difference between methane and this gas is that a very small flame was stabilised in the combustor. The main issue with this mixture is that in order to keep the same power output in the combustion device the mass flows need to be increased considerably. To accommodate these mass flows the burner needs to be redesigned.

The simulations with medium calorific value gas ($50\%CO/50\%H_2$) showed greater effects of flame straining on peak flame temperatures and flame shape.

From this study, it is evident that for medium and low calorific value gases the flame straining needs to be taken into account in order to predict turbulent flame behaviour accurately. These simulations also demonstrated that precise determination of laminar burning velocities and critical strain rates to extinction is very important for the accuracy of the turbulent combustion solution with the TFC model.

8.1 Future Work

This study focused primarily on lean $CO/H_2/N_2$ mixtures, but practical syngas contains trace amounts of CH_4, C_2H_6 and C_3H_8. The effects of these components on fuel combustion properties needs to be investigated experimentally and numerically. The combustion properties database needs to be expanded to include laminar burning velocities and critical strain rates to extinction for these mixtures for the entire combustible range from lean to rich flammability limits.

Some improvements to the present experimental and computational techniques need to be considered:

- ◊ The accuracy of laminar burning velocity data, obtained experimentally from the Bunsen burner, suffered from several factors. It is evident that flame stretch is not uniform over the surface of the flame cone due to curvature. An adiabatic flat flame burner with very accurate flow meters would help to obtain unstretched laminar burning velocities more accurately. The accurate determination of the flame front is very important for flame area estimation as well. The flame front estimated from Schlieren images is slightly larger than the true one; therefore alternative more accurate flame imaging techniques, like PLIF, need to be considered.
- ◊ Since the Bunsen burner flame technique is limited to pressures up to 5 bars, alternative laminar burning velocity determination techniques like the constant pressure bomb need to be evaluated.
- ◊ The validation of present chemical kinetics schemes like GRI-Mech 3.0 is limited to ambient conditions. However computations at high pressures and temperatures, with suitable corrections in the

reaction rate parameters in the chemical kinetics scheme, need to be performed.

- ◊ The turbulent flame closure model requires experimental and further computational validation.

Regardless of the limited time and resources available during the period of this study, all efforts were made to obtain the best possible results. The theoretical and experimental studies enabled the better understanding of the combustion of syngas. The developed databases of laminar burning velocities and critical strain rates to extinction would be helpful for researchers working on gas turbine combustion for IGCC applications.

9 References

[1] El-Mahallawy F., El-Din Habik S., (2002), *Fundamentals and Technology of Combustion*, 1st Edition, ELSEVIER SCIENCE Ltd, UK

[2] Turns S.R., (2000) *"An Introduction to Combustion – Concepts and Applications"*, 2nd Edition, McGraw-Hill International Editions, Mechanical Engineering Series, United States,

[3] Law C.K., Faeth G.M., (1994) *"Opportunities and challenges of combustion in micro-gravity"*, Progress in Energy and Combustion Science 20, p. 65-113,

[4] Wu C.K., Law C.K. (1984) *"On the determination of laminar flame speeds from stretched flames"*, 20th Symposium on Combustion, The Combustion Institute, p. 1941-1949

[5] Karlovitz B., Denniston Jr. D.W., Knapschaefer D.H., Wells F.E. (1953) *"Studies on turbulent fames"*, In 4th Symposium (International) on Combustion, The Combustion Institute, p. 613-619

[6] Law C.K. (1988) *"Dynamics of stretched flames"*, In Twenty-Second Symposium (International) on Combustion, The Combustion Institute, p. 1381-1402

[7] Chelliah H.K., Law C.K., Ueda T., Smooke M.D., Williams F.A. (1990), "*An Experimental and Theoretical Investigation of the Dilution, Pressure and Flow-Field Effects on the Extinction Condition of Methane-Air-Nitrogen Diffusion Flames*", 23rd Symposium (International) on Combustion, the Combustion Institute, Pittsburgh, p. 503-511

[8] Wang Ching-Hua, Ueng Gwo-Jiun, Tsay Mei-Shyong (1998) *"An Experimental Determination of the Laminar Burning Velocities and Extinction Stretch Rates of Benzene/Air Flames"*, Combustion and Flame 113, the Combustion Institute, Published by Elsevier Science Inc, p. 242-248

[9] Arzu Sencan, Soteris A. Kalogirou (2005), *"A new approach using artificial neural networks for determination of the thermodynamic*

properties of fluid couples", Energy Conversion and Management 46, p. 2405–2418

[10] Yao H.M., Vuthaluru H.B., Tade M.O., Djukanovic, D. (2005), *"Artificial neural network-based prediction of hydrogen content of coal in power station boilers"*, Fuel 84, p. 1535–1542

[11] *MATLAB 7.0.4, Help File; Neural Networks Toolbox,* 1994-2006 by The MathWorks, Inc

[12] Choi Chun W., Puri Ishwar K., (2000) *"Flame stretch effects on partially premixed flames"*, Combustion and Flame 123, p. 119-139

[13] Choi Chun W., Puri Ishwar K., (2001) *"Contribution of curvature to flame-stretch effects on premixed flames"*, Combustion and Flame 126, p. 1640-1654,

[14] Choi Chun W., Puri Ishwar K., (2003), *"Response of flame speed to positively and negatively curved premixed flames"*, Combustion Theory Modelling 7, p. 205-220,

[15] Sohrab S.H., Law C.K., (1985) *"Influence of burner rim aerodynamics on polyhedral flames and flame stabilization"*, Combustion and Flame 62, p. 243-254

[16] Durox D., Prud'homme R., (1987) *"Polyhedral flames of propane at low pressure"*, Combustion and Flame 70, p. 243-249

[17] Echekki T., Mungal M. G., (1990) *"Flame speed measurements at the tip of a slot burner: effects of flame curvature and hydrodynamic stretch"*, Proceedings of the 23rd International Symposium on Combustion, The Combustion Institute, Pittsburgh, pp. 455–461

[18] Durox D., (1992) *"Effects of gravity on polyhedral flames"*, In 24th Symposium (International) on Combustion, The Combustion Institute, p. 197-204

[19] Gutman S., Axelbaum R.L., Sivashinsky G.I., (1994) *"On bunsen burner polyhedral flames"*, Combustion Science and Technology 98, p. 57-70

[20] Sung C.J., Yu K.M., Law C.K., (1994) *"On the geometry and burning intensity of bunsen flames"*, Combustion Science and Technology 100, p. 245-270

[21] Rosen L.J., Axelbaum R.L., (2001) *"Suppression of cellular structure in slot-burner flames"*, Combustion and Flame 126, p. 1433-1444

[22] Law C.K., Ishizuka, Cho P., (1982) *"On the opening of premixed bunsen flame tips"*, Combustion Science and Technology 28, p. 89-96,

[23] Mishra D.P., (2007) *"Experimental studies of flame stability limits of CNG–air premixed flame"*, Energy Conversion and Management 48, p. 1208–1211

[24] De Goey L.P.H., Van Maaren A., Quax R.M., (1993) *"Stabilization of adiabatic premixed laminar flames on a at flame burner"*, Combustion Science and Technology 92(1-3), p. 201-207

[25] Van Maaren A., de Goey L.P.H., (1994) *"Laser doppler thermometry in at flames"*, Combustion Science and Technology 99, p. 105-118

[26] Van Maaren A., De Goey L.P.H., (1994) *"Stretch and the adiabatic burning velocity of methane-and propane-air flames"*, Combustion Science and Technology 102, p. 309-314

[27] Lewis Bernard, von Elbe Guenther, (1934) *"Determination of the speed of flames and the temperature distribution in a spherical bomb from time-pressure explosion records"*, Journal of Chemical Physics 2, p. 283-290

[28] Fiock Ernest F., Marvin Charles F., Caldwell Jr. Frank R., Roeder Carl H., (1939) *"Flame speeds and energy considerations for explosions in a spherical bomb"*, Technical Report 682, National Advisory Committee for Aeronautics

[29] Stone R., Clarke A., Beckwith P., (1998) *"Correlations for the laminar burning velocity of methane/diluent/air mixtures obtained in free-fall experiments"*, Combustion and Flame 114, p. 546-555

[30] Price T.W., Potter J.H., (1952) *"Factors affecting flame velocity in stoichiometric carbon monoxide oxygen mixtures"*, In 4th Symposium of Combustion (International), The Combustion Institute, p. 363-369

[31] Vagelopoulos Christina M., (1999) *"An Experimental and Numerical Study on the Stability and Propagation of Laminar Premixed Flames"*, PhD thesis, Faculty of the Graduate School, University of Southern California

[32] Yu G., Law C.K., Wu C.K., (1986) *"Laminar flame speeds of hydrocarbon + air mixtures with hydrogen addition"*, Combustion and Flame 63, p. 339-347

[33] Zhu D.L., Egolfopoulos F.N., Law C.K., (1988) *"Experimental and numerical determination of laminar flame speeds of methane/(ar, n2, co2) - air mixtures as function of stoichiometry, pressure and flame temperature"*, In 22nd Symposium (International) on Combustion, The Combustion Institute, p. 1537-1545

[34] Egolfopoulos F.N., Law C.K., (1990) *"An experimental and computational study of the burning rates of ultra-lean to moderately-rich hydrogen/oxygen/nitrogen laminar flames with pressure variations"*, In 23rd Symposium (International) on Combustion, The Combustion Institute, p. 333-340

[35] Vagelopoulos C.M., Egolfopoulos F.N., (1994) *"Laminar flame speeds and extinction strain rates of mixtures of carbon monoxide with hydrogen, methane and air"*, In 25th Symposium (International) on Combustion, The Combustion Institute, p. 1317-1323

[36] Vagelopoulos C.M., Egolfopoulos F.N., Law C.K., (1994) *"Further considerations on the determination of laminar burning velocities with the counterflow twin-flame technique"*, In 25th Symposium (International) on Combustion, The Combustion Institute, p. 1341-1347

[37] Vagelopoulos C.M., Egolfopoulos F.N., (1998) *"Direct experimental determination of laminar flame speeds"*, In 27th Symposium (International) on Combustion, The Combustion Institute, p. 513-519

[38] Hirasawa T., Sung C.J., Joshi A., Yang Z., Wang H., Law C.K., (2002) *"Determination of laminar flame speeds using digital particle image velocimetry: Binary fuel blends of ethylene, n-butane, and toluene"*, In Proceedings of the Combustion Institute, vol. 29, The Combustion Institute, p. 1427-1434

[39] Kee R.J., Miller J.A., Evans G. H., (1988) *"A computational model of the structure and extinction of strained, opposed flow, premixed methane-air flow"*, Proceedings of the 22nd Symposium (International) on Combustion, The Combustion Institute, Pittsburgh, Pennsylvania, p. 1479-1494

[40] Grcar J.F., (1992) "*Technical Report SAND91-8230*", Sandia National Laboratories

[41] Rogg B., Wang W., (1995) *"RUN-1DL: The Laminar Flame and Flamelet Code"*, Cambridge University, June 1995 edition

[42] Dixon-Lewis G., (1986) *"Towards a Quantitative Consistent Scheme for the Oxidation of Hydrogen, Carbon Monoxide, Formaldehyde and Methane in Flames"*, vol. Complex Chemical Reaction Systems, Mathematical Modelling and Simulation, Springer-Verlag, J. Warnatz and W. Jager edition, p. 265-280

[43] Konnov, A.A., (1998) *"Detailed reaction mechanism for small hydrocarbons combustion"*, Release 0.4 http://homepages.vub.ac.be/~akonnov/

[44] Smith Gregory P., Golden David M., Frenklach Michael, Moriarty Nigel W., Eiteneer Boris, Goldenberg Mikhail, Bowman C. Thomas, Hanson Ronald K., Song Soonho, Gardiner Jr. William C., Lissianski Vitali V., Qin Zhiwei http://www.me.berkeley.edu/gri_mech/

[45] Westbrook C.K., Dryer F.L., (1984) *"Chemical kinetic modelling of hydrocarbon combustion"*, Progress in Energy Combustion Science 10, p. 1-57

[46] Law C.K., Sung C.J., Wang H., Lu T.F., (2003) *"Development of comprehensive detailed and reduced reaction mechanisms for combustion modelling"*, AIAA Journal 41(9), p. 1629-1646

[47] Mueller M.A., Kim T.J., Yetter R.A., Dryer F.L., (1999) *"Flow reactor studies and kinetic modelling of the hydrogen-oxygen reaction"*, International Journal of Chemical Kinetics 31, p. 113-125

[48] Tse S.D., Zhu D.L., Law C.K., (2000) *"Morphology and burning rates of expanding spherical flames in hydrogen/oxygen/inert mixtures up to 60 atmospheres"*, In Proceedings of the Combustion Institute 28, p. 1793-1800

[49] Al-Himyary T.J., Karim G.A., (1987) *"A correlation for the burning velocity of methane-air mixtures at high pressures and temperatures"*, Journal of Engineering for Gas Turbines and Power 109, p. 439-442

[50] Ulinski Matthew, Moore Patrice, Elia Mimmo, Metgalchi Mohamad, (1998) *"Laminar burning velocity of methane-air diluent mixtures"*, In Proceedings of the ASME Internal Combustion Engine Division, volume ICE-Vol 30-2

[51] Elia Mimmo, Moore Patrice, Ulinski Matthew, Metghalchi Mohamad, (1999) *"Laminar burning velocity of methane-oxygen-argon mixtures"*, In Proceedings of the ASME Internal Combustion Engine Division, volume ICE-Vol 32-3

[52] Ulinski Matthew, Li Zhouyun, Elia Mimmo, Fletcher Cedric, Metghalchi Mohamad, (1999) *"Burning velocity measurements in micro-gravity conditions"*, In Proceedings of the 1999 Eastern Section of the Combustion Institute Meeting, North Carolina State University, October 11-13

[53] Rahim Faranak, Ulinski Matthew, Metghalchi Hameed, (2001) *"Burning velocity measurements in spherical and cylindrical vessels"*, In Proceedings of the ISME

[54] Elia M., Ulinski M., Metghalchi M., (2001) *"Laminar burning velocity of methane-air-diluent mixtures"*, In *Transactions of the ASME,* vol. 123, p. 190-196

[55]. Hassan M.I, Aung K.T., Faeth G.M., (1998) *"Measured and predicted properties of laminar premixed methane/air flames at various pressures"*, Combustion and Flame 115, p. 539-550

[56] Gu X.J., Haq M.Z., Lawes M., Woolley R., (2000) *"Laminar burning velocity and markstein lengths of methane-air mixtures"*, Combustion and Flame 121, p. 41-58

[57] Dahoe A.E., de Goey L.P.H., (2003) *"On the determination of the laminar burning velocity from closed vessel gas explosions"*, Journal of Loss Prevention in the Process Industries 16, p. 457-478

[58] Bosschaart Karel Joop, (2002) *"Analysis of the Heat Flux Method for Measuring Burning Velocities"*, PhD thesis, Technische Universiteit Eindhoven

[59] Liu D.D.S., Farlane R. Mac, (1983) *"Laminar burning velocities of hydrogen-air and hydrogen-air-steam fames"*, Combustion and Flame 49, p. 59-71

[60] Milton B.E., Keck J.C., (1984) *"Laminar burning velocities in stoichiometric hydrogen and hydrogen-hydrocarbon gas mixtures"*, Combustion and Flame 58, p. 13-22

[61] Aung K.T., Hassan M.I., Faeth G.M., (1997) *"Flame stretch interactions of laminar premixed hydrogen/air fames at normal temperature and pressure"*, Combustion and Flame 109, p. 1-24

[62] Aung K.T., Hassan M.I., Faeth G.M., (1998) *"Effects of pressure and nitrogen dilution on flame/stretch interactions of laminar premixed h2/o2/n2 fames"*, Combustion and Flame 112, p. 1-15

[63] Hermanns R.T.E., Bastiaans R.J.M., de Goey L.P.H., (2003) *"Laminar burning velocities of hydrogen-oxygen-nitrogen mixtures"*, Proceedings of the European Combustion Meeting, p. 121

[64] Tse S.D., Zhu D.L., Law C.K., (2000) *"Morphology and burning rates of expanding spherical fames in hydrogen/oxygen/inert mixtures up to 60 atmospheres"*, Proceedings of the Combustion Institute 28, p. 1793-1800

[65] Sharma S.P., Gupta C.P., (1971) *"Burning velocities and explosion pressures of acetylene-freon12-air mixtures in spherical bombs"*, Combustion and Flame 16, p. 213-222

[66] Gulder Omer L., (1984) *"Burning velocities of ethanol-isooctane blends"*, Combustion and Flame 56, p. 261-268

[67] Shebeko Yu. N., Tsarichenko S. G., Korolchenko A. Ya., Trunev A. V., Navzenya V. Yu., Papkov S. N., Zaitzev A. A., (1995) *"Burning velocities and flammability limits of gaseous mixtures at elevated temperatures and pressures"*, Combustion and Flame 102, p. 427-437

[68] Rightley M.L., Williams F.A., (1997) *"Burning velocities of co flames"*, Combustion and Flame 110, p. 285-297

[69] Vagelopoulos C.M., Egolfopoulos F.N., (1994) *"Laminar flame speeds and extinction strain rates of mixtures of carbon monoxide with hydrogen, methane and air"*, In 25th Symposium (International) on Combustion, The Combustion Institute, p. 1317-1323

[70] Scholte, T. G., Vaags, P. B., (1959) *"Burning velocities of mixtures of hydrogen, carbon monoxide, and methane with air"*, Combustion and Flame 3, p. 511-524

[71] Brown Martin J., McLean Ian C., Smith David B., Taylor Simon C., (1996) *"Markstein lengths of CO/H2/air flames, using expanding spherical flames"*, In 26th Symposium (International) on Combustion, The Combustion Institute, p. 875-881

[72] Yumlu, V. S., (1967) *"Prediction of burning velocities of carbon monoxide-hydrogen-air flames"*, Combustion and Flame 11, p. 190-194

[73] Hermanns R.T.E., Kortendijk J.A., Bastiaans R.J.M., de Goey L.P.H., (2003) *"Laminar burning velocities of methane-hydrogen-air mixtures"*, In 3rd European Conference on Small Burner Technology and Heating Equipment, p. 240-247

[74] Chomiak J., Longwell J.P., Sarofim A.F., (1989) *"Combustion of low calorific value gases; problems and prospects"*, Progress in Energy and Combustion Science, p. 109-129

[75] Cho Sunghwan, Marlow David, Niksa Stehen, (1995) *"Burning velocities of multicomponent organic fuel mixtures derived from various coals"*, Combustion and Flame 101, p. 399-410

[76] Davis, S. G., Joshi, A. V., Wang, H., and Egolfopoulos, F. (2004) *"An optimized kinetic model of H2/CO combustion"*, Proceedings of the Combustion Institute 30, p. 1283-1292

[77] Bradley D., Hicks R.A., Lawes M., Sheppard C.G.W., Woolley R., (1998) *"The measurement of laminar burning velocities and Markstein numbers for iso-octane-air and iso-octane-n-heptane-air mixtures at elevated temperatures and pressures in an explosion bomb"*, Combustion and Flame 115, p. 126-144

[78] Qin W., Ren J.Y., Egolfopoulos F.N., Wu S., Zhang H., Tsotsis T.T., (2000) *"Oxygen composition modulation effects on flame propagation and NOx formation in methane/air premixed flames"*, In Proceedings of the Combustion Institute 28, p. 1825-1831

[79] Ren J.-Y., Egolfopoulos F.N., Tsotsis T.T., (2001) *"Reactive membrane separations for power-generation applications: Pollutant emission aspects"*, Industrial Engineering Chemistry Research 40, p. 5155-5161

[80] Zhou X., Mahalingam S., (2001) *"Evaluation of reduced mechanism for modelling combustion of pyrolysis gas in wildland fire"*, Combustion Science and Technology 171, p. 39-70

[81] Aung K.T., Hassan M.I., Kwon S., Tseng L.K., Kwon O.C., Faeth G.M., (2002) *"Flame/stretch interactions in laminar and turbulent premixed flames"*, Combustion Science and Technology 174, p. 61-99

[82] Huang Y., Sung C.J., Eng J.A., (2004) *"Laminar flame speeds of primary reference fuels and reformer gas mixtures"*, Combustion and Flame 139, p. 239-251

[83] Ishizuka S., Law C.K., (1982) *"An Experimental Study on Extinction and Stability of Stretched Premixed Flames"*, 19th Symposium (International) on Combustion, The Combustion Institute, p. 327-335

[84] Tsuji Hiroshi, Yamaoka Ichiro, (1982) *"Structure and Extinction of Near-Limit Flames in a Stagnation Flow"*, 19th Symposium (International) on Combustion, The Combustion Institute, p. 1533-1540

[85] Law C.K., Zhu D.L., Yu G., (1986) *"Propagation and Extinction of Stretched Premixed Flames"*, 21st Symposium (International) on Combustion, The Combustion Institute, p. 1419-1426

[86] Guo Hongsheng, Ju Yiguang, Maruta Kaoru, Niioka Takashi, (1997) *"Radiation Extinction Limit of Counterflow Premixed Lean Methane-Air Flames"*, Combustion and Flame 109, p. 639-646

[87] Jackson Gregory S., Sai Roxanne, Plaia Joseph M., Boggs Christopher M., Kiger Kenneth T., (2003) *"Influence of H2 on the response of lean premixed CH4 flames to high strained flows"*, Combustion and Flame 132, p. 503–511

[88] Humer S., Seiser R., Seshadri K., (2002) *"Non-Premixed and Premixed Extinction and Autoignition of C2H4, C2H6, C3H6, and C3H8"*, Proceedings of the Combustion Institute 29, p. 1597–1604

[89] Wang Ching-Hua, Ueng Gwo-Jiun, Tsay Mei-Shyong, (1998) *"An experimental Determination of the Laminar Burning Velocities and Extinction Stretch Rates of Benzene/Air flames"*, Combustion and Flame 113, p. 242-248

[90] Kumar Kamal, Sung Chih-Jen, (2007) *"Laminar flame speeds and extinction limits of preheated n-decane/O2/N2 and n-dodecane/O2/N2 mixtures"*, Combustion and Flame 151, p. 209–224

[91] He X., Donovan M.T., Zigler B.T., Palmer T.R., Walton S.M., Wooldridge M.S., Atreya A., (2005) *"An experimental and modeling study of iso-octane ignition delay times under homogeneous charge compression ignition conditions"*, Combustion and Flame 142, p. 266–275

[92] Qin Zhiwei, Yang Huixing, Gardiner, Jr. William C., (2001) *"Measurement and Modeling of Shock-Tube Ignition Delay for Propene"*, Combustion and Flame 124, p. 246–254

[93] Frassoldati A., Faravelli T., Ranzi E., (2007) *"The ignition, combustion and flame structure of carbon monoxide/hydrogen mixtures", Note 1: Detailed kinetic modeling of syngas combustion also in presence of*

nitrogen compounds", International Journal of Hydrogen Energy 32 p. 3471 – 3485

[94] Petersen Eric L., Kalitan Danielle M., Simmons Stefanie, Bourque Gilles, Curran Henry J., Simmie John M., (2007) *"Methane/propane oxidation at high pressures: Experimental and detailed chemical kinetic modelling"*, Proceedings of the Combustion Institute 31 p. 447–454

[95] Mittal G., Sung C.J., Fairweather M., Tomlin A.S., Griffiths J.F., Hughes K.J., (2007) *"Significance of the HO2 + CO reaction during the combustion of CO + H2 mixtures at high pressures"*, Proceedings of the Combustion Institute 31, p. 419–427

[96] Wang B.L., Olivier H., Grönig H., (2003) *"Ignition of shock-heated H2-air-steam mixtures"*, Combustion and Flame 133, p. 93-106

[97] Walton S.M., He X., Zigler B.T., Wooldridge M.S., (2007) *"An experimental investigation of the ignition properties of hydrogen and carbon monoxide mixtures for syngas turbine applications"*, Proceedings of the Combustion Institute 31, p. 3147–3154

[98] Petersen Eric L., Kalitan Danielle M., Barrett Alexander B., Reehal Shatra C., Mertens John D., Beerer David J., Hack Richard L., McDonell Vincent G., (2007) *"New syngas/air ignition data at lower temperature and elevated pressure and comparison to current kinetics models"*, Combustion and Flame 149, p. 244–247

[99] Coward H.F., Jones G.W., (1938) *"Technical Report Bulletin No. 279"*, U.S. Bureau of Mines

[100] *"Standard Test Method for Concentration Limits of Flammability of Chemicals (Vapors and Gases) E 681-98"*, American Society for Testing and Materials, 1998

[101] Guenoche H., (1964) *"Non-Steady Flame Propagation (Ed. G.H. Markstein)"* AGARD, Pergamon, Oxford

[102] Egerton Sir Alfred C., (1952) *"Limits of Inflammability"*, In 4th Symposium (International) on Combustion, The Combustion Institute, p. 4-13,

[103] Armitage J.W., Gray P., (1965) *"Flame speeds and flammability limits in the combustion of ammonia: Ternary mixtures with hydrogen, nitric oxide, nitrous oxide or oxygen"* Combustion and Flame 9, p. 173-184

[104] Craven, Foster, (1966) *"The limits of flammability of ethylene in oxygen, air and air-nitrogen mixtures at elevated temperatures and pressures"*, Combustion and Flame 10, p. 95-100

[105] Goethals M., Vanderstraeten B., Berghmans J., De Smedt G., Vliegen S., Van't Oost E., (1999) *"Experimental study of the flammability limits of toluene–air mixtures at elevated pressure and temperature"*, Journal of Hazardous Materials A70, p. 93–104

[106] Ciccarelli G., Jackson D., Verreault J., (2006) *"Flammability limits of NH3–H2–N2–air mixtures at elevated initial temperatures"*, Combustion and Flame 144, p. 53–63

[107] Van den Schoor F., Verplaetsen F., (2007) *"The upper flammability limit of methane/hydrogen/air mixtures at elevated pressures and temperatures"*, International Journal of Hydrogen Energy 32, p. 2548 – 2552

[108] McHale E.T., Geary R.W., von Elbe G., Huggett C., (1971) *"Flammability limits of h2-o2-hydrocarbon mixtures"*, Combustion and Flame 16, p. 167-175

[109] Holland S., Jones D.T., Gray P., (1971) *"Combustion supported by nitrous oxide: Flame speeds and flammability limits in the hydrogen+ethane+nitrous oxide system"*, Combustion and Flame 17, p. 31-35

[110] Holmstedt Goran S., (1971) *"The upper limit of flammability of hydrogen in air, oxygen, and oxygen-inert mixtures at elevated pressures"*, Combustion and Flame 17, p. 295-301

[111] Lovachev L.A., Babkin V.S., Bunev V.A., V'yun A.V., Krivulin V.N., Baratov A.N., (1973) *"Flammability limits: An invited review"*, Combustion and Flame 20, p. 259-289

[112] Halstead M.P., Pye D.B., Quinn C.P., (1974) *"Laminar burning velocities and weak flammability limits under engine-like conditions"*, Combustion and Flame 22, p. 89-97

[113] Yu, Shebeko N., Tsarichenko S.G., Ya A., Korolchenko, Trunev A.V., Yu, Navzenya V., Papkov S.N., and Zaitzev A.A., (1995) *"Burning velocities and flammability limits of gaseous mixtures at elevated temperatures and pressures"*, Combustion and Flame 102, p. 427-437

[114] Heffington Warren M., Gaines William R., Renfroe David A., (1984) *"Flammability limits of coal-derived low-btu gas mixtures containing large amounts of inert gases"*, Combustion Science and Technology 36, p. 191-197

[115] Zabetakis M.G., (1965) *"Flammability characteristics of combustible gases and vapors"*, Technical Report Bulletin No. 627, U.S. Bureau of Mines

[116] Law C.K., Egolfopoulos F.N., (1990) *"A Kinetic Criterion of Flammability Limits: The C-H-O-Inert System"*, In 23rd Symposium (International) on Combustion, The Combustion Institute, p. 413-421

[117] Wierzba I., Kilchyk V., (2001) *"Flammability limits of hydrogen–carbon monoxide mixtures at moderately elevated temperatures"*, International Journal of Hydrogen Energy 26, p. 639–643

[118] Wierzba I., Wang Q., (2006) *"The flammability limits of H2–CO–CH4 mixtures in air at elevated temperatures"*, International Journal of Hydrogen Energy 31, p. 485 – 489

[119] Liao S.Y., Jiang D.M., Huang Z.H., Cheng Q., Gao J., Hu Y., (2005) *"Approximation of flammability region for natural gas–air–diluent mixture"*, Journal of Hazardous Materials A125, p. 23–28

[120] Settles G.S., (2001) *"Schlieren and Shadowgraph Techniques: Visualizing Phenomena in Transparent Media"*, Ed. Springer-Verlag, Germany,

[121] Weinberg, F.J. (1963) *"Optics of Flames: Including Methods for the Study of Refractive Index Fields in Combustion and Aerodynamics"*, Butterworths, London

[122] Speak, G. S. Walters, D. J. (1950) *"Optical Considerations and Limitations of the Schlieren Method"*, ARC R&M 2859, British Aero, Research Council

[123] Shafer, H. J. (1949) *"Physical Optic Analysis of Image Quality in Schlieren Photography"*, Journal of the SMPE 53(11), p. 524-544

[124] Danon Y., (2000) Digitize-Pro 4.1, http://www.nuceng.com/Digitizepro.htm, (accessed September 2005)

[125] Kline S.J., McClintock F.A., (1953) *"Describing Uncertainties in Single-Sample Experiments"*, Mechanical Engineering 1, p. 3-8

[126] Kee R.J., Rupley F.M., Miller J.A., Coltrin M.E., Grcar J.F., Meeks E., Moffat H.K., Lutz A.E., Dixon-Lewis G., Smooke M.D., Warnatz J., Evans G.H., Larson R.S., Mitchell R.E., Petzold L.R., Reynolds W.C., Caracotsios M., Stewart W.E., Glarborg P., Wang C., Adigun O., Houf W.G., Chou C.P., Miller S.F., Ho P., Young D.J., (2006) *"A Software Package for the Analysis of Gas-Phase Chemical and Plasma Kinetics"*, CHEMKIN collection release 4.2 edition

[127] Sun H., Yang S.I, Jomaas G., Law C.K., (2007) *"High-pressure laminar flame speeds and kinetic modeling of carbon monoxide/hydrogen combustion"*, Proceedings of the Combustion Institute 31, p. 439–446

[128] McLean, I. C., Smith, D. B., Taylor, S. C., (1994) *"The use of carbon monoxide/hydrogen burning velocities to examine the rate of the CO + OH reaction"* Proceedings of the Combustion Institute 25, p. 749-757

[129] Law C.K., Sung C.J., (2000) *"Structure, aerodynamics and geometry of premixed flamelets"*, Progress in Energy and Combustion Science 26, p. 459-505

[130] Markstein G.H., Somers L.M., (1952) *"Cellular fame structure and vibratory fame movement in n-butane-methane mixtures"*, 4th Symposium (International) on Combustion, The Combustion Institute, p. 527-535,

[131] Durox D., (1992) *"Effects of gravity on polyhedral fames"*, 24th Symposium (International) on Combustion, The Combustion Institute, p. 197-204

[132] Gutman S., Axelbaum R.L., Sivashinsky G.I., (1994) *"On Bunsen burner polyhedral flames"*, Combustion Science and Technology 98, p. 57-70

[133] Garside J.E., Jackson B., (1952) *"The formation and some properties of polyhedral burner flames"*, In 4th Symposium (International) on Combustion, The Combustion Institute, p. 527-535,

[134] Behrens H., (1952) *"Flame instabilities and combustion mechanism"*, In 4th Symposium (International) on Combustion, The Combustion Institute, p. 527-535

[135] Hertzberg Martin, (1989) *"Selective diffusional demixing: Occurrence and size of cellular flames"*, Progress in Energy and Combustion Science 15, p. 203-239

[136] Law C.K., Sung C.J., (2000) *"Structure, aerodynamics and geometry of premixed flamelets"* Progress in Energy and Combustion Science 26, p. 459-505

[137] Mizomoto M., Asaka Y., Ikai S., Law C.K., (1984) *"Effects of preferential diffusion on the burning intensity of curved flames"*, In 20th Symposium (International) on Combustion, The Combustion Institute, p. 1933-1939

[138] Mizomoto M., Yoshida H., (1987) *"Effects of Lewis number on the burning intensity of Bunsen flames"*, Combustion and Flame 70, p. 47-60

[139] Law C.K., Cho P., Mizomoto M., Yoshida H., (1986) *"Flame curvature and preferential diffusion in the burning intensity of Bunsen flames"*, In 21st Symposium (International) on Combustion, The Combustion Institute, p. 1803-1809

[140] Goodwin, D.G. (2003) *"Cantera: An open-source, extensible software suite for CVD process simulation"*, Vol. 1.6

[141] Kee RJ, Grcar JF, Smooke MD, Miller JA, (1985) *"A Fortran program for modelling steady laminar 1-D premixed flames"*, Sandia National Laboratories Report, SAND85-8240

[142] McLean, I. C., Smith, D. B., and Taylor, S. C., (1994) *"The use of carbon monoxide/hydrogen burning velocities to examine the rate of the CO + OH reaction"*, Proceedings of the Combustion Institute 25, p. 749-757

[143] Hassan, M. I., Aung, K. T., and Faeth, G. M., (1997) *"Properties of laminar premixed CO/H2/air flames at various pressures"*, Journal of Propulsion and Power 13(2), p. 239-245

[144] Natarajan J., Nandula S., Lieuwen T., Seitzman J., (2005) *"Laminar Flame Speeds Of Synthetic Gas Fuel Mixtures"*, Proceedings of GT2005, ASME Turbo Expo 2005: Power for Land, Sea and Air, June 6-9, 2005, Reno-Tahoe, Nevada, USA, GT2005-68917

[145] Kim, T. J., Yetter, R. A., Dryer, F. L. (1994), *"New results on moist CO oxidation: High pressure, high temperature experiments and comprehensive modelling"*, Proceedings of the Combustion Institute 25, p. 759-766

[146] Rightley M.L., Williams F.A., (1997) *"Burning Velocities of CO Flames"*, Combustion and Flame 110, p. 285-297

[147] Sivaramakrishnan R., Comandini A., Tranter R.S., Brezinsky K., Davis S.G., Wang H., (2007) *"Combustion of CO/H2 mixtures at elevated pressures"*, Proceedings of the Combustion Institute 31, p. 429–437

[148] Moliere, M., (2002) *"Benefiting from the wide fuel capability of gas turbines: A review of application opportunities"*, ASME Paper GT-2002-30017

[149] Ren J.-Y., Qin W., Egolfopoulos F. N., Mak H., Tsotsis T.T. (2001) *"Methane reforming and its potential effect on the efficiency and pollutant emissions of lean methane-air combustion"*, Chemical Engineering Science 56, p. 1541-1549

[150] Qin W., Egolfopoulos F. N., Tsotsis T.T. (2001) *"Fundamental and environmental aspects of landfill gas utilization for power generation"*, Chemical Engineering Journal 82, p. 157-172

[151] Zhu D.L., Egolfopoulos F.N., Law C.K., (1988) *"Experimental and numerical determination of laminar flame speeds of methane/(Ar, N2, CO2) – air mixtures as function of stoichiometry, pressure, and flame temperature"*, Proceedings of the Combustion Institute 22, p. 1537-1545

[152] Lamoureux N., Djebaili-Chaumeix N., Paillard C.E. (2003) *"Laminar flame velocity determination for H2-air-He-CO2 mixtures using the spherical bomb method"*, Experimental Thermal and Fluid Science 27, p. 385-393

[153] Ju Y., Masuya G., Ronney P.D., (1998) *"Effects of radiative emission and absorption on the propagation and extinction of premixed gas flames"*, Proceedings of the Combustion Institute 27, p. 2619-2626

[154] Hanneman F., Schiffers U., Karg J., Kanaar M., (2002) *"V94.2 Buggenum Experience and Improved Concepts for Syngas Applications"*, 2002 Gasification Technologies Conference, San Francisco, California, USA 28 Oct. 2002 (conference presentation), available at: http://www.gasification.org/

[155] Schilling H.D., Bonn B., Krauss U., Peters W., "Coal Gasification", *Graham & Trotman Limited, Bond Street House, 14 Clifford Street, London W1X 1RD,* 1981

[156] Dixon-Lewis G., Williams A**.**, (1967), *"Some observations on the combustion of methane in premixed flames",* 11th (International) on Combustion, The Combustion Institute, Pittsburgh, p. 951-958

[157] Smoot L. Douglas, Hecker William C., Williams Gerald A., (1976) *"Prediction of propagating methane-air flames"*, Combustion and Flame 26, p. 323-342

[158] Tsatsaronis Georgios, (1978) *"Prediction of propagating laminar flames in methane, oxygen, nitrogen mixtures"*, Combustion and Flame 33, p. 217-239

[159] Westbrook C. K., Dryer F. L., Schug K. P., (1982) *"A comprehensive mechanism for the pyrolysis and oxidation of ethylene"*, 19th Symposium (International) on Combustion, The Combustion Institute, Pittsburgh, p. 153-166

[160] Egolfopoulos F.N., Cho P., Law C.K., (1989) *"Laminar flame speeds of methane-air mixtures under reduced and elevated pressures"*, Combustion and Flame 76, p. 375-391

[161] Dagaut Philippe, Dayma Guillaume, (2006) *"Hydrogen-enriched natural gas blend oxidation under high-pressure conditions: Experimental and detailed chemical kinetic modelling"*, International Journal of Hydrogen Energy 31, p. 505–515

[162] Sabia P., de Joannon M., Fierro S., Tregrossi A., Cavaliere A., (2007) *"Hydrogen-enriched methane Mild Combustion in a well stirred reactor"*, Experimental Thermal and Fluid Science 31, p. 469–475

[163] Topical Report #20: *"The Wabash River Coal Gasification Repowering Project"*, Sept. 2000, available at: http://www.netl.doe.gov/cctc/topicalreports/documents/topical20.pdf (access November 2004)

[164] Topical Report #6: *"The Tampa Electric Integrated Gasification Combined-Cycle Project"*, Oct. 1996, available at: http://www.netl.doe.gov/cctc/topicalreports/documents/topical6.pdf (access November 2004)

[165] Keshava Murthy T.V., (2005) *"Combustion Characteristics of Multicomponent Fuel-Air Mixtures"*, Department of Mechanical Engineering, Indian Institute of Technology, Delhi

[166] Jackson Gregory S., Sai Roxanne, Plaia Joseph M., Boggs Christopher M., Kiger Kenneth T., (2003) *"Influence of H2 on the response of lean premixed CH4 flames to high strained flows"*, Combustion and Flame 132, p. 503–511

[167] Westbrook Charles K., (1982) *"Hydrogen Oxidation Kinetics in Gaseous Detonations"*, Combustion Science and Technology 29, p. 67-81

[168] Glassman I., (1996) *"Combustion"*, 3rd Edition, Academic Press, USA,

[169] Zimont V.L., (1979) *"Theory of turbulent combustion of a homogeneous fuel mixture at high Reynolds numbers"*, Combustion, Explosion and Shock Waves 15, p. 305-311

[170] Zimont V.L, Biagioli F, Syed K., (2001) *"Modelling turbulent premixed combustion in the intermediate steady propagation regime"*, Progress in Computational Fluid Dynamics 1, p. 14-28

[171] Biagioli F, Zimont V.L, Syed K.J. (2001) *"Modelling and numerical simulation of gas combustion in DLE burners based on a turbulent flame speed closure approach"* International Joint Power Generation Conference and Exposition, New Orleans, Lousiana, USA, June 4-7

[172] Zimont V.L., Biagioli F. (2002) *"Gradient, counter-gradient transport and their transition in turbulent premixed flames"*, Combustion Theory and Modelling 6, p. 79-101

[173] Polifke W., Flohr P., Brandt M., (2002) *"Modelling inhomogeneously premixed combustion with an extended TFC model"*, Journal of Engineering for Gas Turbines and Power 124, p. 58-65

[174] Libby P.A., Bray K.N.C., (1981) *"Countergradient diffusion in premixed turbulent flames"*, AIAA Journal 19, p. 205-213

[175] Zimont V.L. and Lipatnikov A.N., (1995) *"A numerical model of premixed turbulent combustion of gases"*, Chemical Physics Reports 14, p. 993-1025

[176] Sanderson Victoria, (1999) *"Final report for EU-PRECCINSTA project"*, SIEMENS, Project No NNE5-1999-20185

[177] Higman C., van der Burgt M., (2003) *"Gasification"*, Elsevier Science, 200 Wheeler Road, Burlington, MA 01803

[178] Schilling H.D., Bonn B., Krauss U., Peters W., (1981) *"Coal Gasification"*, Graham & Trotman Limited, Bond Street House, 14 Clifford Street, London W1X 1RD

[179] Gardner T.H., Berry D.A., Lyons K.D., Beer S.K., Freed A.D., (2002) *"Fuel processor integrated H2S catalytic partial oxidation technology for sulfur removal in fuel cell power plants"*, Fuel 81, p. 2157-2166

[180] Jazbec M., Sendt K., Haynes B.S., (2004) *"Kinetic and thermodynamic analysis of the fate of sulphur compounds in gasification products"*, Fuel 83, p. 2133-2138

[181] Clean Coal Technology Compendium: *"Demo Project Fact Sheets By Technology Type"*, available at: http://www.netl.doe.gov/cctc/factsheets/fs_techaepg.html (accessed November 2004)

[182] Clean Coal Technology Compendium: *"Tampa Electric Integrated Gasification Combined-Cycle Project, available at"*: http://www.netl.doe.gov/cctc/factsheets/tampa/tampaedemo.html (accessed November 2004)

[183] Topical Report #8: *"The Piñon Pine Power Project"*, Dec. 1996, available at: http://www.netl.doe.gov/cctc/topicalreports/documents/topical8.pdf (accessed November 2004)

[184] Clean Coal Technology Compendium: *"Kentucky Pioneer IGCC Demonstration Project, available at"*: http://www.netl.doe.gov/cctc/factsheets/clnen/cleanedemo.html (accessed November 2004)

[185] Steinfeld G., (2003) *"Kentucky Pioneer Energy IGCC CCT Fuel Cell Demonstration: Basis of Design"* FuelCell Energy Inc., 3 Great Pasture Road, Danbury, CT 06813, May 22, , Available at: http://www.netl.doe.gov/cctc/resources/pdfs/clnen/Basis.pdf (accessed November 2004)

[186] Cohen H., Rogers G.F.C, Saravanamutto H.I.H, (1996) *"Gas Turbine Theory"*, 4th Edition, Longman Group Limited, Longman House, Burnt Mill, Harlow, Essex CM20 2JE, England

[187] Brdar R.D., Jones R.M., (2000) *"GE IGCC Technology and Experience with Advanced Gas Turbines"*, GE Power Systems, Report GER-4207, 10/2000

[188] Hannemann F., Koestlin B., Zimmermann G., (2003) *"Pushing Forward IGCC Technology at Siemens"*, Gasification Technologies Conference, San Francisco, California, USA 12-15 Oct. 2003, available at: http://www.gasification.org/

[189] Coca M. Treviño, Méndez-Vigo I., Elias F. Azcoitia, (1998) *"Coal Gasification, Conception, Implementation and Operation of the Elcogas IGCC Power Plant"*, ELCOGAS, S.A. Madrid, Spain, 1998, available at: http://www.worldenergy.org/wec-geis/publications/default/tech_papers/tech_papers.asp (accessed November 2004)

[190] The Website for the Power Industry, ISAB Energy IGCC Plant, Italy, available at: http://www.power-technology.com/projects/isab (accessed November 2004)

[191] NPRC Negishi IGCC Startup and Operation, *2003 Gasification Technologies Conference, San Francisco, California, USA 12-15 Oct. 2003, available at:* http://www.gasification.org/Docs/2003_Papers/05ONO_paper.pdf (accessed November 2004)

[192] Tsukagoshi K., Shiozaki S., (2004) *"Latest Operating Experiences and Technologies of Large Industrial Gas Turbine"*, Mitsubishi Heavy Industries, Ltd., Japan, Apr. 29, 2004, available at; http://www.came-gt.com/2InternatConf/Tech%20Session%201/KTsukagoshi.ppt (accessed November 2004)

[193] Nippon Petroleum Refining Co., Ltd. (2003) *"Negishi Refinery Integrated Gasification Combined Cycle Electric Power Plant Begins Commercial Operation"*, July 2003, available at: http://www.mhi.co.jp/power/e_power/topics/2003/jul_06.html accessed November 2004)

[194] Callan Robert, (1999) *"The Essence of Neural Networks"*, Prentice Hall Europe, United Kingdom

[195] Hassan Md. Rafiul, Nath Baikunth, Kirley Michael, (2007), *"A fusion model of HMM, ANN and GA for stock market forecasting"*, Expert Systems with Applications 33, p. 171–180

[196] Cao Qing, Leggio Karyl B., Schniederjans Marc J., (2005), *"A comparison between Fama and French's model and artificial neural networks in predicting the Chinese stock market"*, Computers & Operations Research 32, p. 2499–2512

[197] Tsai Chih-Fong, Wu Jhen-Wei, (2007), *"Using neural network ensembles for bankruptcy prediction and credit scoring"*, Expert Systems with Applications, Available online 17 May 2007

[198] Lee Tian-Shyug, Chen I-Fei, (2005) *"A two-stage hybrid credit scoring model using artificial neural networks and multivariate adaptive regression splines"*, Expert Systems with Applications 28, p. 743–752

[199] Sencan Arzu, (2007) *"Performance of ammonia–water refrigeration systems using artificial neural networks"*, Renewable Energy 32, p. 314–328

[200] Choi Y., Chen J.-Y., (2005) *"Fast prediction of start-of-combustion in HCCI with combined artificial neural networks and ignition delay model"*, Proceedings of the Combustion Institute 30, p. 2711–2718

[201] Inal Fikret, Tayfur Gokmen, Melton Tyler R., Senkan Selim M., (2003) *"Experimental and artificial neural network modeling study on soot formation in premixed hydrocarbon flames"*, Fuel 82, p. 1477–1490

[202] MATLAB 7.0.4, *"Help File; Neural Networks Toolbox"*, 1994-2006 by The MathWorks, Inc

[203] Haykin S., (1999) *"Neural Network, a comprehensive foundation"*, *Ed.* Prentice Hall, London

[204] Holman J.P., (2001) *"Experimental Methods for Engineers"*, 7th Edition, McGraw-Hill International Edition, Mechanical Engineering Series, Singapore

[205] Weigand P., Duan X.R., Meier W., Meier U., Aigner M., Berat C., (2005) *"Experimental investigations of an oscillating lean premixed CH4/air swirl flame in a gas turbine model combustor"*, Proceedings of the European Combustion Meeting 2005

[206] Fluent 6.3 User Guide, ANSYS

Appendix A – Gas Compositions from Gasifiers

Gasifiers are classified into three main categories depending on their characteristics: moving-bed, fluid-bed and entrained-flow.

Moving-bed (fixed bed) gasifiers are characterized by the bed, in which coal moves slowly downwards under gravity and is gasified by a counter-current blast. In such arrangements hot synthetic gas, flowing from the gasification zone on the bottom, preheats and pyrolizes the coal. In this process the oxygen requirement is comparatively low, but syngases contain some pyrolysis products. The temperature of product gases is generally low. This process is the oldest one. The atmospheric producer gas and water gas processes were the most important in the early production of syngas from coal and coke [177].

The moving-bed gasification processes (including theoretical ones) and typical gas compositions are as follows:

- *Producer Gas (Wellmann-Galusha Process***)** with dry gas composition of 15.0% H_2, 28.6% CO, 3.4% CO_2, 2.7% CH_4, 50.3% N_2 by volume and calorific value of 6.587 MJ/m^3 [178].
- *Gasification with Oxygen and Steam under Atmospheric Pressure* with dry gas compositions for coal: 41.0% H_2, 40.0% CO, 16.5% CO_2, 0.9% CH_4, 1.5% N_2 and 0.1% O_2; for coke as feedstock: 31.0% H_2, 54.1% CO, 11.3% CO_2, 0.4% CH_4, 2.6% N_2 and 0.6% O_2. The calorific values of the gases are 10.6 MJ/m^3 and 10.1 MJ/m^3 respectively [179].
- *The Lurgi Dry Ash Process* (pressurized; 25-30bar). The dry syngas composition from this process is following: 38.0-42.2% H_2, 15.2-24.0% CO, 28.0-31.0% CO_2, 8.6-10.0% CH_4, 0.68% N_2 by volume,

some H_2S+COS and NH_3. Calorific value of the gas is from 11.2 to 11.8 MJ/m^3 [178, 179].

- *British Gas/Lurgi (BGL) Slagging Gasifier* (pressurized) The dry syngas composition from BGL process is typically: 27.3-31.5% H_2, 55.0-70.4% CO, 1.9-3.5% CO_2, 0.5-6.7% CH_4, 3.4% N_2 by volume, 1.3% H_2S+COS and 0.4%NH_3. Calorific value of the gas is from 12.5 to 14.6 MJ/m^3 [178, 179].
- *Ruhr 100 Gasifier* (very high pressure of 90-100bar). The dry gas composition from this process is following: 39.1% H_2, 17.2% CO, 35.5% CO_2, 7.9% CH_4, and 0.2% N_2 [178].
- *Water Gas*; No gas composition data are available.

The Lurgi Dry Ash and BGL Slagging Gasifier are commercialized processes.

Fluid-bed gasifiers provide a very good mixing between feedstock and oxidant. This feature ensures an even distribution of reaction material in the bed. But fluid bed gasifiers have some limitations. The operation of this gasifier is restricted to temperatures lower than the ash softening point, because slagging of the ash in the bed will disturb fluidization. Sizing of the particles is essential, because if a particle is too fine, it will be carried out from the bed with the flowing synthesis gas. Some of these particles are captured by cyclone filter and returned to the bed. The fluid-bed gasification processes are more suitable for gasifying reactive feedstock, like low-rank coals and biomass, due to lower operation temperatures in the reactor [178].

There are several fluid-bed gasification processes. Some of them and their gas compositions are listed below:

- *The Winkler Process* (historic, too expensive) [178].

- *The High Temperature Winkler (HTW) Process*; Gas composition from this process varies depending on the feedstock and reaction conditions chosen: 35.0-46.0% H_2, 30.0-50.0% CO, 13.0-25.0% CO_2, 1.0-1.8% CH_4 and 0.5-1.5% N_2 by volume. Calorific value of the gas varies from 9.2 to 13.0 MJ/m^3 [179].
- *Circulating Fluid-Bed (CFB) Process*; No gas composition data are available for this process.
- *The Kellog Brown and Root (KBR) Transport Gasifier*; No gas composition data are available.
- *Cogas Process (COED);* Clean gas composition from this gasification process is as follows: 57.9% H_2, 31.2% CO, 6.6% CO_2, 4.0% CH4 and 0.3% N_2 by volume. Calorific value of the gas is about 12.9 MJ/m^3 [179].
- *CO_2 Acceptor Process*; the gas from this process contains considerable amount of hydrogen: 56.0% H_2, 15.5% CO, 10.9% CO_2, 14.1% CH_4, and 3.0% N_2 by volume. Gas also contains some NH_3 and H_2S. Calorific value of the synthetic gas is about 14.7 MJ/m^3 [179].
- *Synthane Process***;** the raw gas composition is as follows: 27.8% H_2, 16.7% CO, 29.0% CO_2, 24.5% CH_4, 0.8% N_2, 0.8% C_2H_6 and 0.5% H_2S by volume. Calorific value of the gas is approximately 15.9 MJ/m^3 [179].
- *Agglomerating Fluid-bed Processes:*
  - *U-Gas (Utility Gas) Technology* (pressurized, working pressure 25bar); gas composition from this process varies depending on reaction agent used. For gasification with steam and air, gas contains considerable amounts of nitrogen: 9.8-15.5% H_2, 12.0-

16.6% CO, 10.3-14.7% CO_2, up to 0.5% CH_4, 59.9-62.7% N_2. The calorific value of this gas is very low, only about 2.8 to 3.6 MJ/m^3. If steam and oxygen is used for gasification, gas contains higher amounts of hydrogen and carbon monoxide: 34.9-36.9% H_2, 21.3-29.8% CO, 34.5-42.7% CO_2 and 0.5-1.1% CH_4; no N_2 present in the gas. Due to large amounts of carbon dioxide, gas calorific value is only 7.4-8.5 MJ/m^3 [179].

- *Kellog Rust Westinghouse (KRW) Process* (pressurized, working pressure 10 to 20bar); raw gas composition from this gasifier is as follows: 14.4% H_2, 19.2% CO, 9.4% CO_2, 2.8% CH_4 and 54.2% H_2 by volume. Calorific value of the synthesis gas is 5.2 MJ/m^3 [179].

Entrained flow gasifiers operate with feedstock and oxidant in co-current flow. The main features of this process are that the residence time is very short (only a few seconds) and feedstock size is kept very small (less than 100μm) to promote mass transfer. Due to the short residence time, high temperatures are required to ensure good carbon conversion. For this reason, all entrained flow gasifiers are operating in the slagging regime. This high temperature operation demands high oxygen levels for the gasification process. These gasifiers can operate on any type of coal, but high moisture or ash content feedstocks may require such high oxygen levels that it ceases to be economically feasible [178].

Some entrained-flow gasification processes and gas compositions are listed below:

- *The Koppers-Totzek Atmospheric Process*; the raw gas composition from this process is following: 21.0-32.0% H_2, 55.0-66.0% CO, 7.0-

12.0% CO_2, 0.1% CH_4, 1.0% N_2 and 0.5-1.0% H_2S by volume. Calorific value of the gas is from 10.6 to 11.8 MJ/m^3 [179].

- *Shell Coal Gasification Process (SCGP) and Prenflo Process*
- *The Noell Process*; (no gas composition data are available).
- *The Texaco Process* (pressurized, working pressure for chemical processes can exceed 70-80bar, for IGCC plants – 30bar); dry raw gas composition from this process is following: 38.7-37.9% H_2, 45.7-46.6% CO, 11.5-13.2% CO_2, 0.7-0.9% CH_4, 1.7-2.0% N_2 and 0.6-0.7% H_2S by volume. Calorific value of the gas is 11.1 MJ/m^3 [179]. Some literature sources report that water content present in the gas from Texaco gasifier can be as much as 18.0% [179, 180].
- *The E-Gas Process (Bi-Gas Process);* gas from this process contains a large amount of methane: 32.1% H_2, 21.5% CO, 29.3% CO_2, 15.6% CH_4, 0.7% N_2 and 0.8% H_2S. Calorific value of the gas is around 13.7 MJ/m^3 [179].
- *The Clean Coal Power R&D Company (CCP) Gasifier*; (no gas composition data are available for the gasifier).
- *The EAGLE Gasifier*; (no gas composition data are available for this gasifier).
- *Ruhrgas Vortex Chamber Process* (atmospheric process); the gas composition depends on the oxidant employed. It operates on air/steam and on oxygen/steam. If air and steam is used, gas composition is following: 8.0% H_2, 22.0% CO, 5.1% CO_2 and 64.1% N_2 by volume. Calorific value of this gas is low, only 3.9 MJ/m^3. Syngas composition from gasification process with oxygen and steam: 33.2% H_2, 48.5% CO, 16.8% CO_2, 0.5% CH_4 and 1.0% N_2 by

volume; and calorific value of the gas is considerably higher – 10.5 MJ/m^3 [179].

- *Combustion Engineering Process* (atmospheric); this process is operating with air. Gas from this process contains high amounts of nitrogen: 10.7% H_2, 24.4% CO, 4.1% CO_2, 60.2% N_2 and 0.4% H_2S+COS by volume. Gas calorific value is 4.6 MJ/m^3 [179].

Existing IGCC Projects

United States of America

Four coal Integrated Gasification Combine Cycle (IGCC) demonstration projects were started in the US under the Clean Coal Technology Program (CCT Program). The CCT Program is managed by the National Energy Technology Laboratory in cooperation with industry.

Three projects are completed: (1) the Wabash River Coal Gasification Repowering Project (09/91-09/00), (2) the Tampa Electric Integrated Gasification Combined-Cycle Project (12/89-12/02) and (3) the Piñon Pine IGCC Power Project (09/91-01/01). The fourth project: Kentucky Pioneer Energy Project is still under development (planned timeline is 05/93-12/07) [181].

The Wabash River Coal Gasification Repowering Project

The design of Wabash River coal gasifier was based on Destec's Louisiana Gasification Technology, Inc. (LGTI) gasifier. Both gasifiers are of similar size and operating characteristics.

The E-GAS™ two-stage coal gasification technology is based on an oxygen-blown, entrained-flow, refractory-lined gasifier with continuous slag removal.

The main elements of the combined cycle power plant are the high-temperature gas turbine/generator (General Electric MS 7001FA), the heat recovery steam generator and the re-powered steam turbine. The gas turbine is a dual-fuel machine (syngas for operations and oil fuel No. 2 for start-up) and produces 192 MWe power. The gas turbine was converted to use natural gas as a start-up fuel instead of oil. The steam turbine output is 104 MWe. The auxiliary equipment electric consumption is 34 MWe, consisting of power to operate the air separation unit, pumps, motors, etc. Total net power production of the combined cycle power plant is 262 MWe [164].

The main components of synthesis gas from coal and petroleum coke from Wabash River IGCC Power Plant are CO_2, CO and H_2, which comprise more than 95% of gas composition. Gas composition from typical coal was: 34.4% H_2, 45.3% CO, 15.8% CO_2, 1.9% CH_4, 1.9% N_2 and 0.6% Ar by volume. The higher heating value of the gas was 10.32 MJ/m^3. Gas composition from petroleum coke was similar: 33.2% H_2, 48.6% CO, 15.4% CO_2, 0.5% CH_4, 1.9% N_2 and 0.6% Ar. Heating value of the gas was 9.99 MJ/m^3 [164].

The Wabash River IGCC Power Plant is designed to use a range of coals with a maximum sulfur content of 5.9% (dry basis). The selected coal for initial operation was high-sulfur Midwestern bituminous from the No. 6 seam of a mine in Indiana (Peabody Hawthorn). Alternative feedstocks, like petroleum coke and blends of coal and coke, were tested as well during the three-year demonstration period [164].

The Tampa Electric Integrated Gasification Combined-Cycle Project

A single-stage, downdraft-firing, entrained flow coal gasifier is used in Texaco coal gasification technology. Coal/water slurry with 60-70% of coal

and oxygen (95% pure) are fed to a gasifier. The coal reacts with oxygen and produces raw coal gas (syngas) and molten ash at a temperature of about 1480°C. The gas flows downward into a cooler where high-pressure steam is produced [165].

The gas turbine employed in the Tampa EIGCC power plant is a low-NO_X emission, dual-fuel (operating on syngas and using low sulfur fuel oil for startup and backup) machine (General Electric model MS 7001F). The power output from the gas turbine was 192 MWe. Nitrogen was used as syngas diluent to reduce NO_X formation. The steam turbine power output was 121 MWe. Power consumption for auxiliary equipment was 63 MWe, resulting in a net power output of 250 MWe [165].

The main components in cleaned syngas were CO, H_2 and CO_2. The gas after hot-gas cleanup also contained quite high quantities of water. Gas composition after hot-gas cleanup: 27.0% H_2, 35.6% CO, 12.6% CO_2, 0.1% CH_4, 18.6% H_2O and 5.8% N_2 by volume; after cold-gas cleanup: 33.8% H_2, 48.3% CO, 10.0% CO_2, 0.2% CH_4, 0.5% H_2O, 6.1% N_2 and 1.1% Ar by volume, gas also contained some carbonyl sulphide [165].

The Tampa IGCC Power Plant was able to operate on a range of fuels. The coals used were Illinois #5 and #6, Pittsburgh #8, West Kentucky #11, and Kentucky #9; Indiana #5 & #6 (2.5–3.5% sulfur); petcoke, it was possible to employ petcoke/coal blends and biomass as well [182].

The Piñon Pine Power Project

The KRW gasifier, licensed by the M.W. Kellogg Technology Company, was employed in this project. The gasifier working principle is based on a fluidized bed in which coal and limestone particles are suspended in a stream of flowing gases. The particle size and weight are adjusted to

prevent them from blowing out and remain within the bed until most of the carbon is gasified.

The gasifier operates at about 982°C temperature, which is low enough to avoid extensive gas cooling prior to cleaning and high enough for reactions to proceed rapidly, and prevent formation of tars and oils [183].

The cleaned syngas was delivered at 540°C temperature to General Electric model MS 6001 FA gas turbine. The gas turbine produced about 61 MWe power. Gas turbine exhaust produces steam in the HRSG that contributes 46 MWe power from the steam turbine. Power requirement for auxiliary equipment is around 7 MWe. The power consumption by auxiliary equipment is comparatively low due to the absence of oxygen production plant. The net power of the Piñon Pine power plant was about 100 MWe [184].

The main components in the gas from KRW gasifier were N_2, CO and H_2: 14.5% H_2, 23.9% CO, 5.5% CO_2, 1.4% CH_4, 48.6% N_2, 5.5% H_2 and 0.6% Ar by volume. Lower heating value of the gas was 4.81 MJ/m^3 [184].

Kentucky Pioneer IGCC Demonstration Project

In this project the utility-scale IGCC system, which uses a high-sulphur bituminous coal and refuse-derived fuel (RDF), was combined with a molten carbonate fuel cell (MCFC) fuelled by coal gas [184]. The British Gas/Lurgi gasifier is supplied with coal and pelletized RDF, limestone, oxygen, and steam. Oxygen and steam react with coal and limestone during the gasification process. Produced syngas is rich in H_2 and CO. Raw gas from the gasifier is washed and cooled; gas is also cleaned from H_2S and other sulfur compounds. Remaining particles, tars and oils are recycled to the gasifier for further gasification [185].

Some part of the syngas is supplied to the gas turbine. The remaining gas is utilized in the fuel cell plant. The MCFC is composed of a molten carbonate electrolyte placed between porous anode and cathode plates. Cleaned fuel (syngas) and steam are fed continuously into the anode; CO_2-enriched air is supplied into the cathode [185].

The gross power from Kentucky Pioneer Energy IGCC power plant is 580 MWe; the net power is 540 MWe. Around 2.0 MWe power is generated in the MCFC plant [185].

Syngas composition depends on the feedstock; for coal operation: 34.4% H_2, 45.3% CO, 15.8% CO_2, 1.9% CH_4, 1.9% N_2 and 0.6% Ar, higher heating value of the gas is 10.32 MJ/m^3; for 33.2% H_2, 48.6% CO, 15.4% CO_2, 0.5% CH_4, 1.9% N_2 and 0.6% Ar by volume, HHV=9.99 MJ/m^3 [185].

Cool Water IGCC Power Plant Demonstration Project

Texaco gasifier, which has 1100 tonne/day gasification capacity, was installed in Cool Water power plant. The plant was operated from 1984 to 1989 and completed 27000 hours of operation. Four different coal types were tested in the plant [186].

The gross power output in the Cool Water IGCC power plant is 120 MWe, [187] 80 MWe power [187] is generated by General Electric 107E [188] model gas turbine.

Gas composition is as follows: 30.0% H_2, 65.0% CO, 1.0% CO_2, 3.0% N_2+Ar and 1.0% H_2O [187].

Europe

Buggenum IGCC Power Plant Nuon Demonstration Project (Netherlands)

A Shell gasifier was built in the Buggenum IGCC Power plant [155]. The gasifier capacity is 2000 t/d using internationally traded coal as a feedstock [178] (Drayton coal from Australia) [155].

The gross power output in the Buggenum IGCC power plant is 284 MWe, 156MWe power is generated by Siemens V94.2 model gas turbine and 128 MWe by Siemens KN model steam turbine. Auxiliary equipment consumes 31 MWe power. The net power output is 253 MWe [155].

Syngas from this process contains considerable amount of nitrogen. Gas composition is following: 12.3% H_2, 24.8% CO, 0.8% CO_2, 42.0% N_2, 0.6% Ar, 19.1% H_2O and 0.4% O_2 by volume; lower heating value of the gas is equal to 4.3 MJ/kg [155].

Elcogas Puertollano IGCC Power Plant Demonstration Project (Spain)

Prenflo [188,189] gasifier unit was installed in 1997 for Puertollano IGCC power plant with capacity of 3000 t/d using a blend of high-ash coal and petcoke as feedstock [189].

The gross power output in the Buggenum IGCC power plant is 335 MWe, 200 MWe power is generated by Siemens V94.3 model gas turbine and 135 MWe by steam turbine. Auxiliary equipment consumes 35 MWe power. The net power output is 300 MWe [189].

The wet syngas composition from the gasification process is following: 10.7% H_2, 29.2% CO, 1.9% CO_2, 53.1% N_2, 0.01% CH_4, 0.6% Ar, 4.2% H_2O and 0.3% O_2; Lower heating value of the gas is 4.3 MJ/kg [189].

ISAB Energy Priolo Gargallo IGCC Power Plant Demonstration Project (Italy)

The Texaco gasifier unit is installed for ISAB IGCC power plant. The plant is adjacent to Italy's second largest refinery, which provides the feedstock (usually asphalt from the plant) [190].

The gross power output in the ISAB IGCC power plant is 540 MWe, 2×156 MWe power is generated by Siemens V94.2 model gas turbines and 2×114 MWe by steam turbines. Auxiliary equipment consumes 28 MWe power. The net power output is 512 MWe [191].

Syngas consists of the following components: 31.3% H2, 28.5% CO, 3.2% CO2, 36.9% H2O; lower heating value of the gas is 9.1 MJ/kg [189].

Asia

Negishi IGCC Power Plant (Japan)

Negishi IGCC power plant is the first plant in Japan using residual oil (asphalt) as fuel for an IGCC system [191].

A Chevron Texaco Direct Quench Type gasifier unit is installed for the Negishi IGCC power plant [192].

The gross power output in the Negishi IGCC power plant is 430 MWe, 295 MWe power is generated by Mitsubishi M701F model gas turbine and 135 MWe by steam turbine [192]. Auxiliary equipment consumes 88 MWe power. The net power output is 342 MWe [193].

Appendix B – Artificial neural networks (theory)

Introduction

Artificial neural networks (ANNs) are parallel computing devices, which consist of many simple interconnected processors. Each processor in a network only knows signals, which it receives and sends to other processors. Yet the large network of such connected processors is able to perform complicated tasks.

The development of ANNs started in the early 20th century, but only during the 90s, after breaking some theoretical barriers and benefiting from the growth in computing power did ANNs become useful tools. The word "artificial" is used to describe artificial devices rather than the biological neural networks found in the brain. ANNs are often referred to as a connectionist networks when emphasis is put on computing ability rather than on biological fidelity: ANNs aim to solve specific tasks rather than attempt to mimic some part of a biological process.

The main difference between ANNs and ordinary computer software is that most neural solutions are "learned" not programmed: ANNs learns to perform tasks rather than being directly programmed. Certainly, many network solutions have been developed because it is not possible to write a suitable program or the "learnt solution" provides better performance [194].

ANNs have been applied successfully in various fields of aerospace, business, automotive, banking, industrial, manufacturing, robotics, telecommunications and many others.

The application base for ANNs is massive: stock market forecasting [195, 196], credit scoring [197, 198] credit card fraud detection, optical

character recognition, machine health monitoring, human health monitoring and diagnostics, road vehicle autopilots, coal composition prediction [10], thermodynamic properties of refrigerants prediction [9,199], ignition delay prediction [200], pollutant formation prediction [201] and others.

Neuron model

The model of a single neuron is given in Figure B 1. It can also be called perceptron [202]. As mentioned earlier, "neuron" is used for analogy only and does not describe the biological neuron.

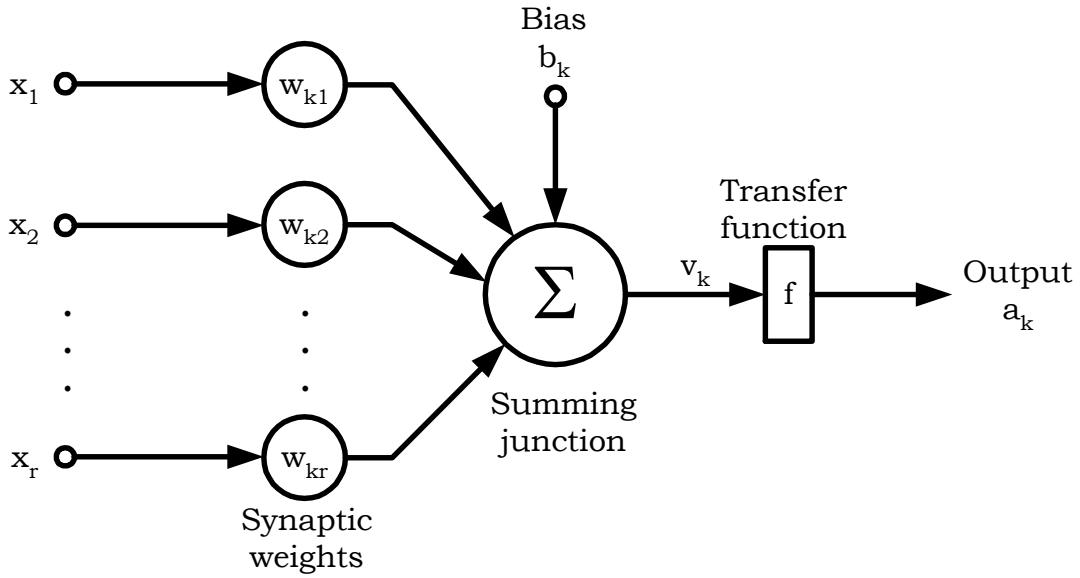

Figure B 1: The neuron model [202]

Each scalar input x is transmitted through a connection that multiplies it by the scalar weight w (connection strength), to form the product w_x (scalar). All the scalars w_x are fed to summing junction, where:

$$v_k = x_1 \cdot w_{k1} + x_2 w_{k2} + \ldots + x_r \cdot w_{kr} + b_k \quad \textbf{(B.1)}$$

and v_k, the sum of weighted inputs, is the only argument of the transfer function f, which produces the scalar output a_k. The neuron usually has a scalar bias b_k which has a raising or lowering effect on the weighted input sum.

The transfer function F is typically a step function or a sigmoid function. This function introduces non-linearity in the network (sigmoid function) and limits the amplitude range of the output signal. A typical range of the output a_k is between -1 and 1 [203].

In mathematical notations such neurons can be described as [204]:

$$v_k = \sum_{j=1}^{r} w_{kj} \cdot x_j + b_k \quad \textbf{(B.2)}$$

$$a_k = F(v_k) \quad \textbf{(B.3)}$$

w_{kj} and b_k are adjustable scalar parameters of the neuron. The working principle of the ANNs is such that parameters can be adjusted so the network behaves in a certain manner. Thus the network can be trained to do a particular job by adjusting the weight and bias parameters [203].

Transfer functions

There are a number of transfer functions used in artificial neural networks. ANNs with a back-propagation training algorithm mainly uses log-sigmoid, tan-sigmoid and linear transfer functions [203]:

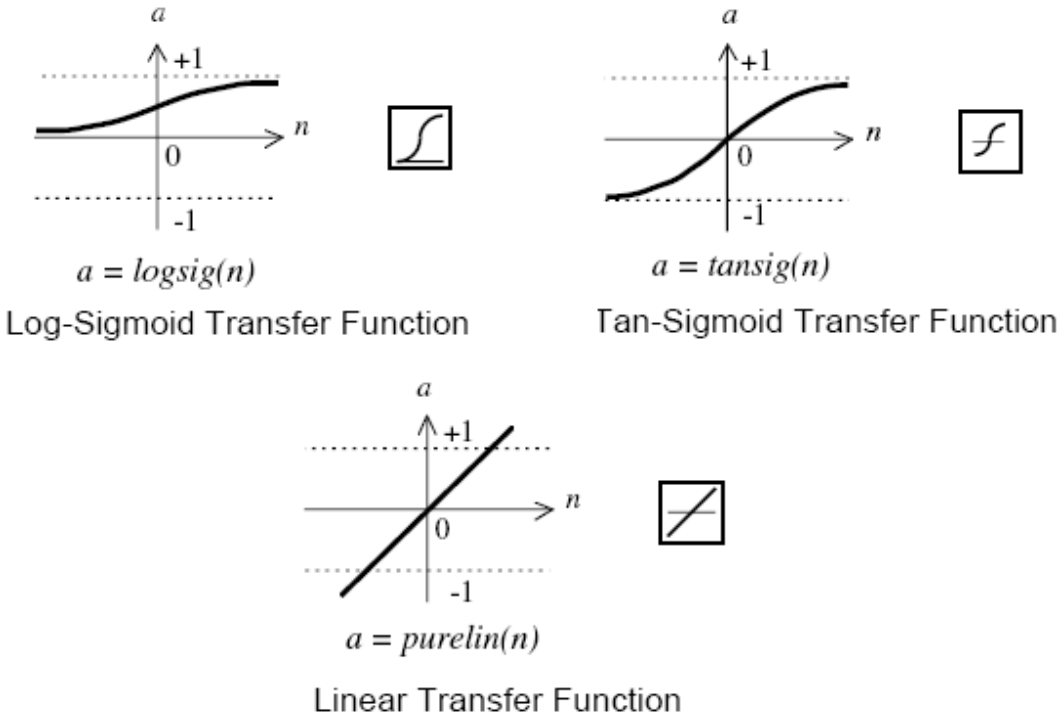

Figure B 2: Common transfer functions [203]

Artificial neural network architecture

The simplest form of the artificial processor consists of a single perceptron, see Figure B 1. As it has an input layer, a processing unit and an output, it can be considered as an operational structure.

Actually, it is evident, that such a simple structure cannot cope with complex problems. This is the reason why neurons are linked together, hence mimicking the brain configuration to a certain extent.

There are different ways to link neurons in the network. The most common way to design networks is to link neurons in the form of layers. Some ANN architectures can be widely employed, while others are used only for specific applications [203]. Layered networks can have a single layer or multiple layers.

Single-layer feedforward networks

This network is the basic form of ANN. In this ANN the input layer source nodes project onto an output layer of neurons, but output neurons do not project on input nodes. For this reason this network is called a feedforward ANN. A single-layer ANN with 3 input and output neurons is given in Figure B 3.

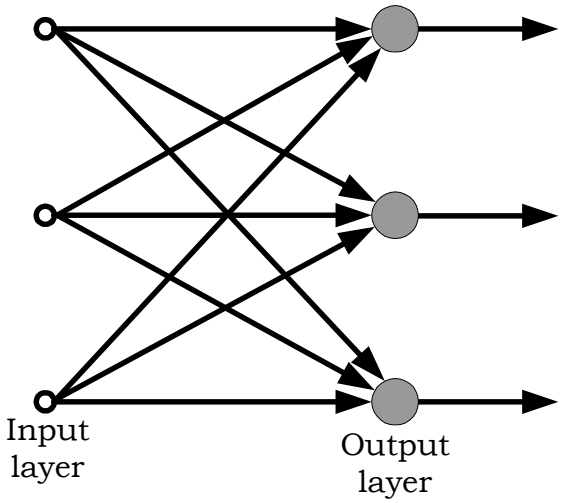

Figure B 3: A simple single-layer ANN [203]

This network is called "single-layer" because computations are performed only in the output layer of neurons. In general, the input layer of neurons is not viewed as a layer [204].

Multilayer Feedforward Networks

The presence of hidden layer(s) of neurons, located between input nodes and the output neuron layer, characterises multilayer networks. There can be one or several hidden layers in ANNs.

In this network the set of input nodes is presented to the first hidden layer. The computed signal from the first hidden layer is the input for the

following layer and so on until the output layer is reached. In this network activation travels in a direction from input to output [195, 204].

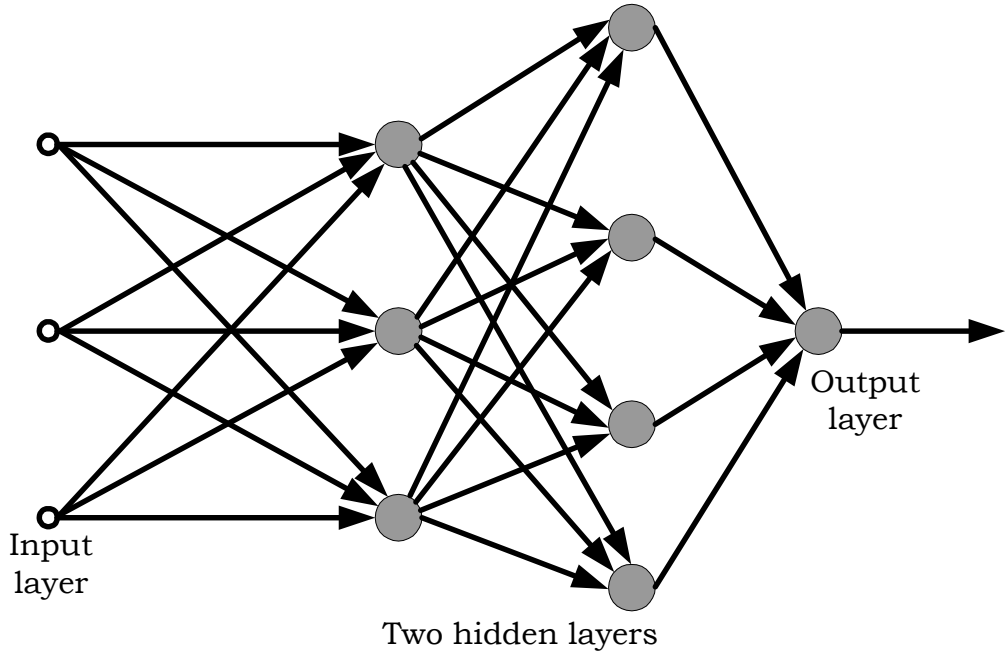

Figure B 4: A multilayer ANN [204]

The multilayer ANN with 3 input nodes, two hidden layers (one with 3 neurons and another with 4 neurons) and a 1 neuron output layer is given in Figure B 4. It can be presented as a 3-3-4-1 network.

Most multilayer ANNs are fully connected: each neuron is connected to each neuron in the previous and the next layer. Sometimes they can be partially connected; thus some interconnections can be missing in the network.

For the ANN with hidden layers its ability to extract higher order statistics increases and therefore to handle complex and non-linear problems. Hidden layers are especially important when there are many input nodes [204].

ANN training

The training rule is applied to train networks to perform some particular tasks. The ANN training rule is defined as a procedure (training algorithm) for modifying network weights and biases.

Training rules can be divided into two main categories: supervised training and unsupervised training [203, 204].

In supervised training the ANN is provided with a training set. As the inputs are presented to the network, the network outputs are compared to the targets, see Figure B 5. The learning rule is then used to adjust the weights and biases of the network in order to bring the network outputs closer to the targets.

In unsupervised training the weights and biases are modified in response to network inputs only; there are no targets available. The unsupervised training algorithms are employed to perform clustering operations, because they categorize the input patterns into a finite number of classes [203].

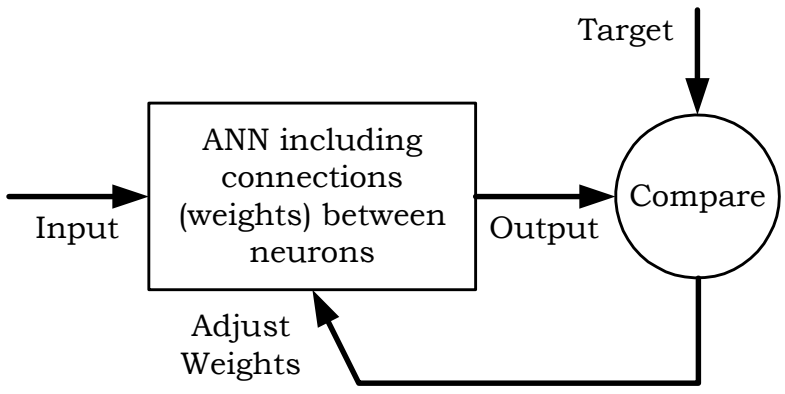

Figure B 5: Supervised training principle [203]

Backpropagation learning

This algorithm is employed to train multilayer networks with nonlinear transfer functions. In the backpropagation algorithm input vectors and the corresponding target vectors are used to train the ANN until it can relate input vectors with specific output vectors, approximate a function, or classify input vectors in a defined way. ANNs with biases, sigmoid layer and a linear output layer can approximate any function with a finite number of discontinuities [203].

The backpropagation algorithm defines two sweeps of the network: first the forward sweep from the input to the output layer and second the backward sweep from the output to the input layer. Both steps are similar, except that error values are propagated back through the network to determine how weights are to be changed during the training [195].

The backpropagation employs a generalisation of the delta or Widrow-Hoff rule.

The generalized version of the delta rule

Consider an output unit having a transfer (output) of y and target output of t, see Figure B 6.

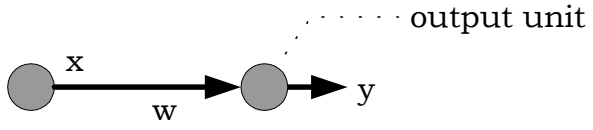

Figure B 6: A single weight connecting two units. The signal x is multiplied by w (weight) and passed through transfer function which means that output y is the same as weighted input [195]

The error δ is equal to:

$$\delta = t - y \qquad \textbf{(B.4)}$$

The signal coming into the output unit is x. the delta rule states that the needed adjustment Δw is equal to:

$$\Delta w = \psi \delta x \quad \textbf{(B.5)}$$

where ψ is the learning rate (real number). The new weight value is adjusted by:

$$w = x + \Delta w \quad \textbf{(B.6)}$$

The generalised version of the delta rule can be expressed as:

$$\Delta w_{ij} = \psi \delta_j x_i \quad \delta_j = (t_j - o_j) \quad \textbf{(B.7)}$$

where t_j is the target value of the unit j, o_j is the actual output, x_i is the signal coming from unit i, ψ is the learning rate (how much to adapt the weight) and Δw_{ij} – the change in weight of connection between units i and j. The error derivative is expressed as:

$$\frac{\partial E}{\partial w_{ij}} = \frac{\partial E}{\partial o_j} \frac{\partial o_j}{\partial net_j} \frac{\partial net_j}{\partial w_{ij}} \quad \textbf{(B.8)}$$

δj can be defined as:

$$\delta_j = -\frac{\partial E}{\partial net_j} \quad \textbf{(B.9)}$$

The delta rule for linear units, where output is the same as input is:

$$\delta_j = -\frac{\partial E}{\partial o_j} \frac{\partial o_j}{\partial net_j} \quad \textbf{(B.10)}$$

Since $E_p = \frac{1}{2} \Sigma_j (t_j - o_j)^2$, we have:

$$\frac{\partial E}{\partial o_j} = -(t_j - o_j) \quad \textbf{(B. 11)}$$

For transfer function f, which typically is a logistic function, the output can be expressed as:

$$o_j = f(net_j) \quad \textbf{(B.12)}$$

The derivative of f' is given by:

$$\frac{\partial o_j}{\partial net_j} = f'(net_j) \quad \textbf{(B.13)}$$

so

$$\delta_j = (t_j - o_j) f'(net_j) \quad \textbf{(B.14)}$$

The standard summation of products is used to find the net total input:

$$net_j = \sum_{i=0} x_i w_{ij} \quad \textbf{(B.15)}$$

and so

$$\frac{\partial net_j}{\partial w_{ij}} = x_i \quad \textbf{(B.16)}$$

So taking the product of each derivative and substituting into equation (B.8) gives:

$$\frac{\partial E}{\partial w_{ij}} = -(t_j - o_j) f'(net_j) x_i \quad \textbf{(B.17)}$$

For the neuron in the hidden layer, the error is given by:

$$\delta_j = f'(net_j) \sum_k \delta_k w_{kj} \quad \textbf{(B.18)}$$

Here k is the index of layer which sends back the error (output layer for a network with single hidden layer).

The suitable transfer function is the logistic sigmoid function:

$$f(net_j) = \frac{1}{1 + \exp(-net_j)} \quad \textbf{(B.19)}$$

The derivative of this transfer function is:

$$f'(net_j) = \frac{\exp(-net_j)}{(1+\exp(-net_j))^2} = \frac{1}{1+\exp(-net_j)}\left(1-\frac{1}{1+\exp(-net_j)}\right) = f(net_j)[1-f(net_j)] \quad \textbf{(B.20)}$$

The backpropagation algorithm

The procedure of the backpropagation algorithm is as follows:

1. At first all weights need to be initialised with small random values: for example between -0.3 and 0.3.
2. The training is provided by supplying input and associated output patterns. Training continues until the change of absolute value of the averaged squared error falls to within some value between two epochs. For example, if the tolerance is equal to 0.001, the squared error cannot change more than ±0.001 between epochs. If ANN meets the tolerance, it has converged. Alternatively, the measure of convergence can be the tolerance between the output and target values.
3. In addition, in order to reduce the oscillation of weight changes, a momentum term is introduced. It adds an allowed proportion of weight change:

   $$\Delta w_{ij}(n+1) = \eta(\delta_j o_i) + \alpha \Delta w_{ij}(n) \quad \textbf{(B.21)}$$

   Thus weight change for epoch n+1 is dependent on the weight change for epoch n [195].

Properly trained backpropagation ANNs can give reasonable answers when the new inputs, which networks have never seen, are presented. Usually, a new input leads to a similar output to the target output for inputs used in training that are close to the new input being introduced. This property to generalise allows training an ANN on a representative set

of input/target pairs and to get reasonable results without using all possible input/output pairs for network training [203].

Some practical considerations

There are some practical points that need to be considered when using backpropagation networks:

1. The successful application of ANN usually requires a lot of experimentation. There are a number of parameters that need to be considered in order to obtain an acceptable solution:
    a. The number of hidden layers in the network or number of neurons in the hidden layer can vary.
    b. The training data set needs to be selected in a way that the correct generalisation of the ANN will be achieved on the data, it have not seen.

There is no clearly defined way of finding a solution for a new application. Some problems appear to be intractable to neural solution, but it does not mean that the problem cannot be solved by ANN. Although the trial and error approach is used in applying ANN, the requirement of knowledge of ANNs and knowledge of the application domain should not be underrated [195].

ANN generalisation

In backpropagation learning as many training examples as possible are used to compute ANN weights and biases. It is expected that the neural network so designed will be able to generalize. The ANN has the ability to generalize well, when it computes correctly (or nearly so) the test data set it hasen't seen during its training. It is assumed that the data are drawn from the same population used to generate the training data.

The training process of the ANN can be viewed as a curve fitting problem. The network itself can be considered to act as a non-linear input-output mapping. Therefore the generalisation of the network can be considered as a good linear interpolation of the input data. The ANN performs useful interpolation primarily because multilayer perceptrons with continuous transfer functions lead to continuous output functions.

A neural network that is designed to generalise will produce a correct input-output mapping even with the data slightly different from the data used for training. When, however, the ANN is presented with too many input-output data sets, it will memorise the training data set. It will find the feature which is in a data set (noise for example) but not a true fundamental function that is to be modelled. Such a phenomenon is called overtraining (overfitting). When the network is overtrained it will loose its ability to generalise and interpolate between similar input-output data patterns.

The essence of the ANN with a good ability to generalise is its capability to produce the smoothest (simplest) function for input-output data patterns [195, 204].

Comprehensive information about ANN architectures, their mathematical formulation, and network validation can be found in S. Haykin's textbook [204].

Appendix C – Uncertainty analysis

The uncertainty of the laminar burning velocity measurement is estimated based on the uncertainties in the primary measurements. If the result R is a given function of the independent variables x_1, x_2, x_3.....x_n, it can be expressed as:

$$R = R(x_1, x_2, x_3, \ldots\ldots x_n) \quad \textbf{(C.1)}$$

If ω_R is the uncertainty in the result and ω_1, ω_2, ... ω_n are the uncertainties in the independent variables of all given with the same odds, then the uncertainty is given by:

$$\omega_R = \left[\left(\frac{\partial R}{\partial x_1}\omega_1\right)^2 + \left(\frac{\partial R}{\partial x_2}\omega_2\right)^2 + \ldots\ldots + \left(\frac{\partial R}{\partial x_n}\omega_n\right)^2\right]^{1/2} \quad \textbf{(C.2)}$$

This equation is used for the calculation of uncertainty in the air-fuel ratio and laminar burning velocity [204].

Uncertainty in air-fuel ratio

The air-fuel ratio (AFR) is:

$$AFR = \frac{\dot{m}_A}{\dot{m}_F} \quad \textbf{(C.3)}$$

The uncertainty in the measured individual flow rates for air ($\dot{m}_A$) and fuel ($\dot{m}_F$) is calculated as follows:

$$\dot{m} = \frac{pQ}{RT} \quad \textbf{(C.4)}$$

$$\frac{\partial \dot{m}}{\partial p} = \frac{Q}{RT} \quad \textbf{(C.5)}$$

$$\frac{\partial \dot{m}}{\partial Q} = \frac{p}{RT} \quad \textbf{(C.6)}$$

$$\frac{\partial \dot{m}}{\partial T} = \frac{pQ}{RT^2} \quad \textbf{(C.7)}$$

$$\omega_{\dot{m}} = \left[\left(\frac{\partial \dot{m}}{\partial p} \right)^2 \omega_p^2 + \left(\frac{\partial \dot{m}}{\partial Q} \right)^2 \omega_Q^2 + \left(\frac{\partial \dot{m}}{\partial T} \right)^2 \omega_T^2 \right]^{1/2} \quad \textbf{(C.8)}$$

$$\omega_{\dot{m}} = \left[\left(\frac{Q}{RT} \right)^2 \omega_p^2 + \left(\frac{p}{RT} \right)^2 \omega_Q^2 + \left(\frac{pQ}{RT^2} \right)^2 \omega_T^2 \right]^{1/2} \quad \textbf{(C.9)}$$

The uncertainty in the AFR:

$$\frac{\partial AFR}{\partial \dot{m}_A} = \frac{1}{m_F} \quad \textbf{(C.10)}$$

$$\frac{\partial AFR}{\partial \dot{m}_F} = \frac{\dot{m}_A}{\dot{m}_F^2} \quad \textbf{(C.11)}$$

$$\omega_{AFR} = \left[\left(\frac{\partial AFR}{\dot{m}_A} \right)^2 \omega_{\dot{m}_A}^2 + \left(\frac{\partial AFR}{\dot{m}_F} \right)^2 \omega_{\dot{m}_F}^2 \right]^{1/2} \quad \textbf{(C.12)}$$

$$\omega_{AFR} = \left[\left(\frac{1}{\dot{m}_F} \right)^2 \omega_{\dot{m}_A}^2 + \left(\frac{\dot{m}_A}{\dot{m}_F^2} \right)^2 \omega_{\dot{m}_F}^2 \right]^{1/2} \quad \textbf{(C.13)}$$

Corresponding uncertainties in equivalence ratio can be expressed as:

$$\frac{\partial \phi}{\partial \dot{m}_A} = AFR_{st} \frac{\dot{m}_F}{\dot{m}_A^2} \quad \textbf{(C.14)}$$

$$\frac{\partial \phi}{\partial \dot{m}_F} = AFR_{st} \frac{1}{\dot{m}_A} \quad \textbf{(C.15)}$$

$$\omega_\phi = AFR_{st} \left[\left(\frac{\dot{m}_F}{\dot{m}_A^2} \right)^2 \omega_{\dot{m}_A}^2 + \left(\frac{1}{\dot{m}_A} \right)^2 \omega_{\dot{m}_F}^2 \right]^{1/2} \quad \textbf{(C.16)}$$

The uncertainty in laminar burning velocity:

$$S_{lam} = \frac{\dot{m}_{tot}}{\rho_{mix} \cdot A_{Flame}} \quad \textbf{(C.17)}$$

The uncertainty in density:

$$\rho_{mix} = \frac{p}{RT} \quad \textbf{(C.18)}$$

$$\frac{\partial \rho_{mix}}{\partial p} = \frac{1}{RT} \quad \textbf{(C.19)}$$

$$\frac{\partial \rho_{mix}}{\partial T} = \frac{p}{RT^2} \quad \textbf{(C.20)}$$

$$\omega_\rho = \left[\left(\frac{1}{RT} \right)^2 \omega_p^2 + \left(\frac{p}{RT^2} \right)^2 \omega_T^2 \right]^{1/2} \quad \textbf{(C.21)}$$

The uncertainty in laminar burning velocity:

$$\frac{\partial S_{lam}}{\partial \dot{m}_{tot}} = \frac{1}{\rho_{mix} \cdot A_{Flame}} \quad \textbf{(C.22)}$$

$$\frac{\partial S_{lam}}{\partial \rho_{mix}} = \frac{\dot{m}_{tot}}{\rho_{mix}^2 \cdot A_{Flame}} \quad \textbf{(C.23)}$$

$$\frac{\partial S_{lam}}{\partial A_{Flame}} = \frac{\dot{m}_{tot}}{\rho_{mix} \cdot A_{Flame}^2} \quad \textbf{(C.24)}$$

$$\omega_{S_{lam}} = \left[\left(\frac{1}{\rho_{mix} A_{Flame}} \right)^2 \omega_m^2 + \left(\frac{\dot{m}_{tot}}{\rho_{mix}^2 \cdot A_{Flame}} \right)^2 \omega_\rho^2 + \left(\frac{\dot{m}_{tot}}{\rho_{mix} \cdot A_{Flame}^2} \right)^2 \omega_A^2 \right]^{1/2} \quad \textbf{(C.25)}$$

Piezo-resistive transducers were used to measure gauge pressures in the rotameters. Instrument accuracies were obtained from the calibration experiment. Transducer accuracies are ± 0.41-0.13%p_{gauge} (for air meter) and ± 0.56-0.09%p_{gauge} (for fuel meter).

The temperature of the air/fuel stream was measured using a type K (Cromel) thermocouple. Thermocouple accuracy is ± 5% (±2.5°C thermocouple and ±2.5°C cables).

Volume flow rate is measured in the rotameter tube with accuracy of 2% FS; here FS – full scale.

Representative example of uncertainty calculation procedure:

67%CO/33%H_2/Air mixture, ambient conditions, ϕ=0.6

Readings:

Barometer pressure: p_{bar}=0.988bar

Air stream: p_{gauge}=1.237bar, T=17°C, Reading=10.0

Fuel stream: p_{gauge}=0.336bar, T=17°C, Reading=6.25

Uncertainties in the individual mass flow rates:

Air:

Q=14.0 cm^3/s=14.0*$10^{-6}m^3/s$

$$\dot{m}_A = \frac{pQ}{RT} = \frac{(p_{bar} + p_{gauge})Q}{(R/MW_{air})T}$$

$$\dot{m}_A = \frac{(1.237 + 0.988)14.0 \cdot 10^{-6}}{(8314.472/28.964) \cdot 290} = 3.742 \cdot 10^{-5}\,kg/s = 0.03742g/s$$

Instrument accuracies for air:

Pressure transducer: $\omega_p = 0.41\%p_{gauge} = 0.005072bar$

Rotameter: $\omega_Q = 0.28cm^3/s$

Thermocouple: $\omega_T = 5\,deg\,C$

Uncertainty in air mass flow:

$\omega_{\dot{m}_A} = 0.000645g/s$

% Uncertainty in air mass flow:

$(\omega_{\dot{m}_A}/\dot{m}_A) \cdot 100\% = (0.000645/0.03742) \cdot 100\% = 1.72\%$

Fuel:

Q=6.0cm^3/s=6.0*$10^{-6}m^3/s$

$MW_F = 0.67 \cdot 28 + 0.33 \cdot 2 = 19.42g/mol$

$$\dot{m}_F = \frac{(0.336+0.988)6.0\cdot 10^{-6}}{(8314.472/19.42)\cdot 290} = 0.6398\cdot 10^{5}\,\mathrm{kg/s} = 0.006398\,\mathrm{g/s}$$

Instrument accuracies:

Pressure transducer: $\omega_p = 0.56\% p_{gauge} = 0.0018816\,\mathrm{bar}$

Rotameter: $\omega_Q = 0.12\,\mathrm{cm}^3/\mathrm{s}$

Thermocouple: $\omega_T = 5\,\mathrm{deg\,C}$

Uncertainty in fuel mass flow:

$\omega_{\dot{m}_F} = 0.0001103\,\mathrm{g/s}$

% Uncertainty in fuel mass flow:

$(\omega_{\dot{m}_F}/\dot{m}_F)\cdot 100\% = (0.0001103/0.006398)\cdot 100\% = 1.72\%$

Uncertainty in AFR:

$\omega_{AFR} = 0.102$

% Uncertainty in AFR:

$(\omega_{AFR}/AFR)\cdot 100\% = (0.102/5.85)\cdot 100\% = 1.75\%$

Uncertainty in equivalence ratio:

$\omega_\phi = 0.0147$

% Uncertainty in equivalence ratio:

$(\omega_\phi/\phi)\cdot 100\% = (0.0147/0.604)\cdot 100\% = 2.44\%$

*% Uncertainty in equivalence ratio is **2.44**%*

Uncertainty in laminar burning velocity

First the uncertainty in the density of fuel/air mixture needs to be evaluated:

$$\omega_\rho = \left[\left(\frac{1}{RT}\right)^2 \omega_p^2 + \left(\frac{p}{RT^2}\right)^2 \omega_T^2\right]^{1/2} \qquad \textbf{(C.26)}$$

Measurement was performed under atmospheric pressure; therefore density of the fuel/air mixture is defined based on atmospheric pressure, which is measured with a barometer:

Barometer accuracy: $\omega_p = 0.5\% p_{barometric} = 0.00494 bar$

Thermocouple accuracy: $\omega_T = 5^{\circ}C$

Gas constant for fuel/air mixture at ϕ=0.604 is 308.71 J/kg/K

Uncertainty in density: $\omega_\rho = 0.0198 kg/m^3$ or **1.80%**

Nominal value of laminar burning velocity:

$$S_{lam} = \frac{\dot{m}_{tot}}{\rho_{mix} \cdot A_{Flame}} = \frac{(0.03742 + 0.006398) \cdot 10^{-3}}{1.1036 \cdot 117.68 \cdot 10^{-6}} = 0.3374 m/s = 33.74 cm/s$$

Uncertainty in the mass flow rate:

$$\omega_{m_{tot}} = \left[\left(\dot{m}_F \cdot \omega_{\dot{m}A} \right)^2 + \left(\dot{m}_A \cdot \omega_{\dot{m}F} \right)^2 \right]^{1/2}$$

$$\omega_{m_{tot}} = 5.84 \cdot 10^{-6} g/s = 5.84 \cdot 10^{-9} kg/s$$

Uncertainty in flame surface area:

The uncertainty in the flame surface area was found to fall within ±5% of an average value of 117.68mm² (85% of data points), see Figure C 1, therefore it is assumed to be 5% of the total surface area. The analysis is based on flame surface areas, obtained from 20 images.

$\omega_A = 0.05 * 117.68 = 5.884 mm^2$

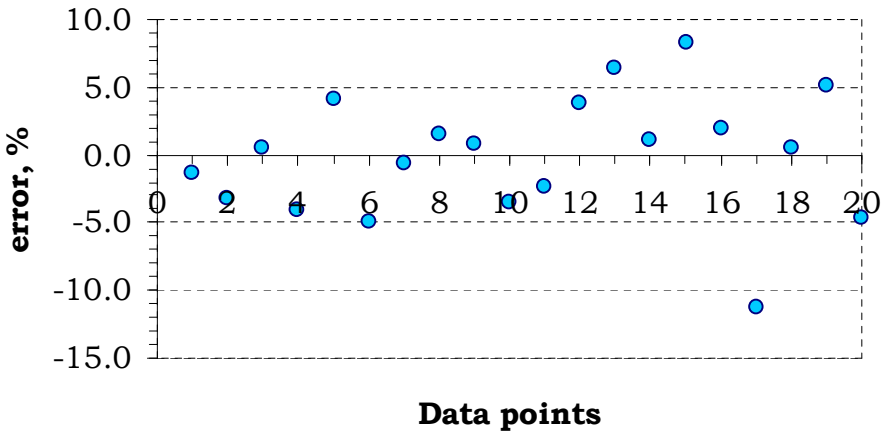

Figure C 1: Discrepancies for flame areas in comparison to the mean value, obtained from 20 images.

Uncertainty in laminar burning velocity:

$$\omega_{S_{lam}} = \left[\left(\frac{1}{1.1036 \cdot 117.68 \cdot 10^{-6}} \right)^2 \left(5.84 \cdot 10^{-9}\right)^2 + \left(\frac{0.043818 \cdot 10^{-3}}{1.1036^2 \cdot 117.68 \cdot 10^{-6}} \right)^2 \cdot 0.0198^2 + \left(\frac{0.043818 \cdot 10^{-3}}{1.1036 \cdot \left(117.68 \cdot 10^{-6}\right)^2} \right)^2 \left(5.884 \cdot 10^{-6}\right)^2 \right]^{1/2}$$

$$\omega_{S_{lam}} = 0.0179 \mathrm{m/s} = 1.79 \mathrm{cm/s}$$

$$\left(\omega_{S_{lam}} / S_{lam}\right) \cdot 100\% = \left(0.0179/0.3374\right) \cdot 100\% = 5.31\%$$

*% Uncertainty in laminar burning velocity is **5.31**%*

Appendix D – Sensitivity analysis graphs

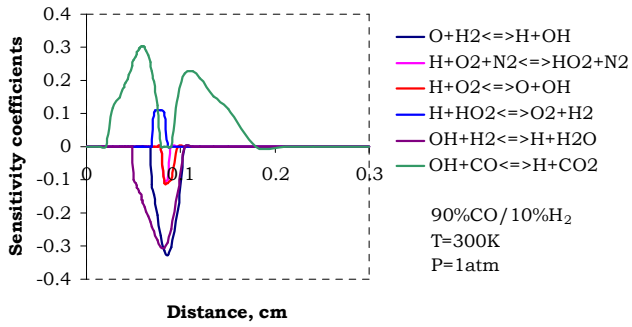

a)

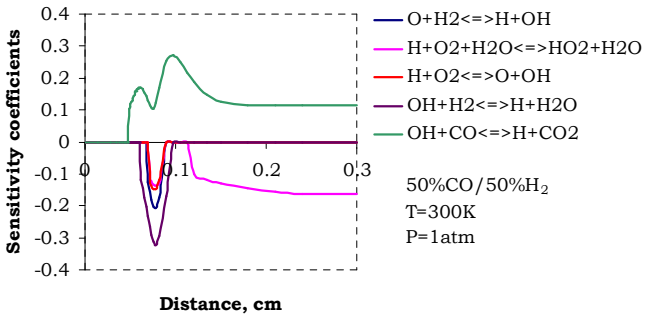

b)

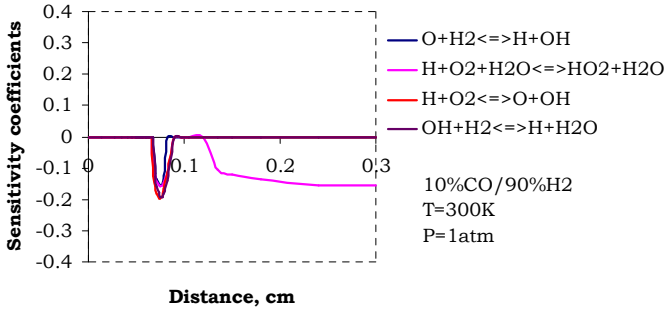

c)

Figure D 1: Sensitivity analysis for CO/H_2 mixture, H2 sensitivity at different CO/H_2 fuel compositions

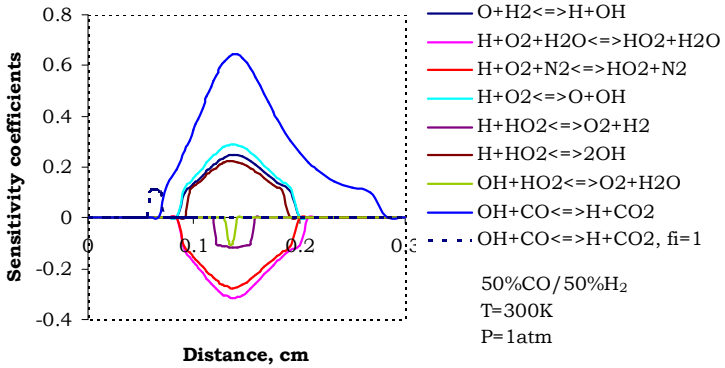

Figure D 2: Temperature Sensitivity analysis at different equivalence ratios

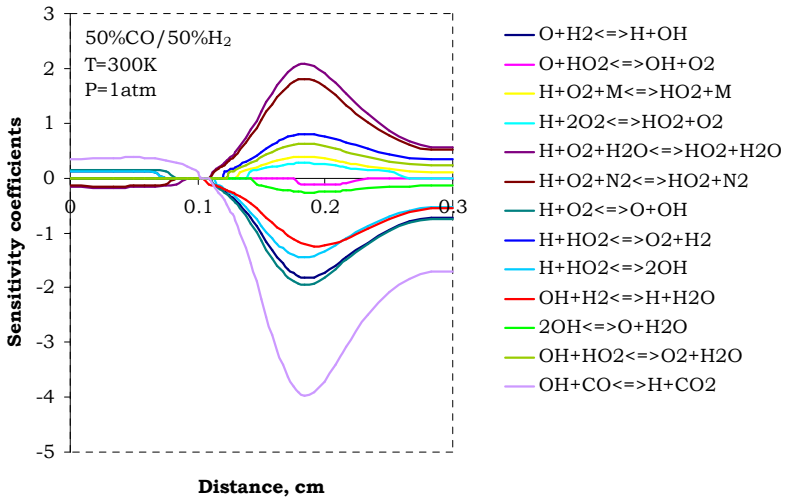

Figure D 3: H_2 Sensitivity analysis at equivalence ratio 0.4

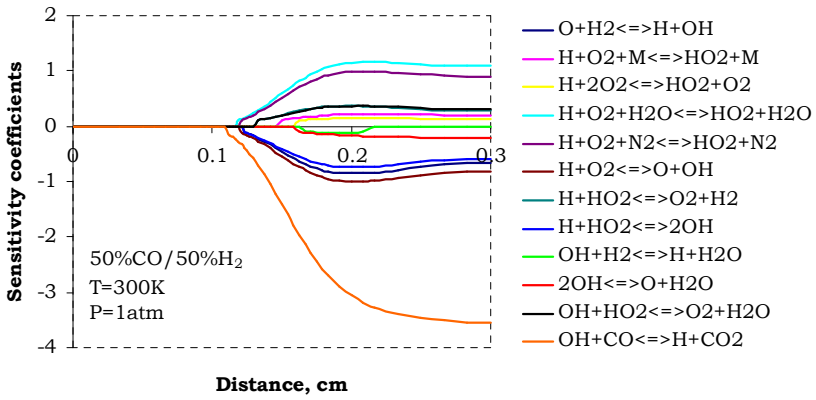

Figure D 4: CO Sensitivity analysis at equivalence ratio 0.4

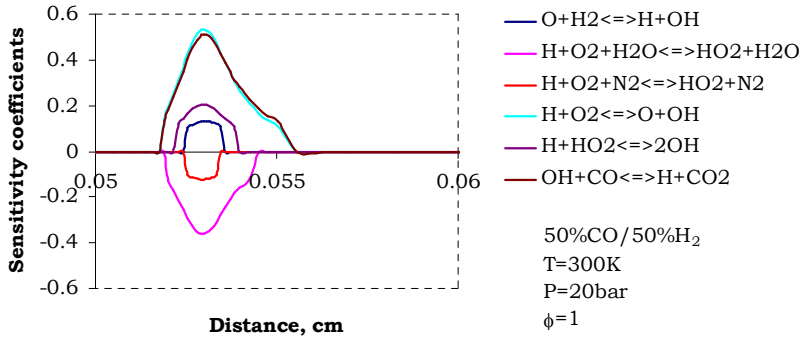

Figure D 5: Temperature Sensitivity analysis at 20bar pressure

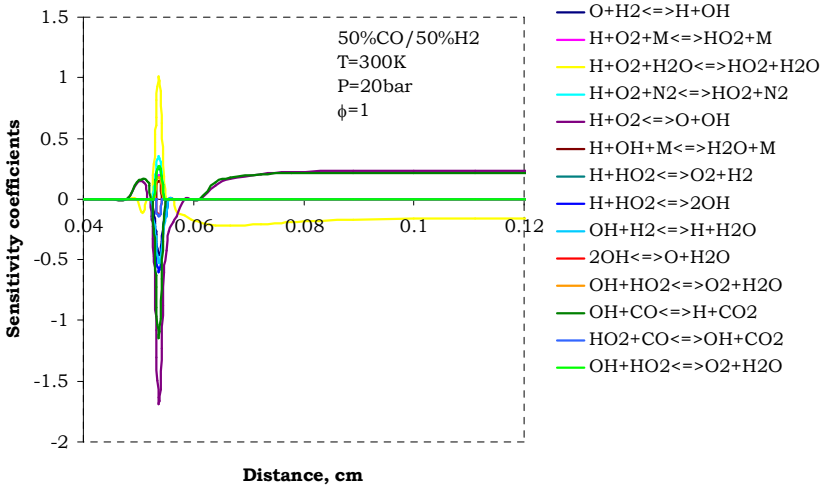

Figure D 6: H_2 Sensitivity analysis at 20bar pressure

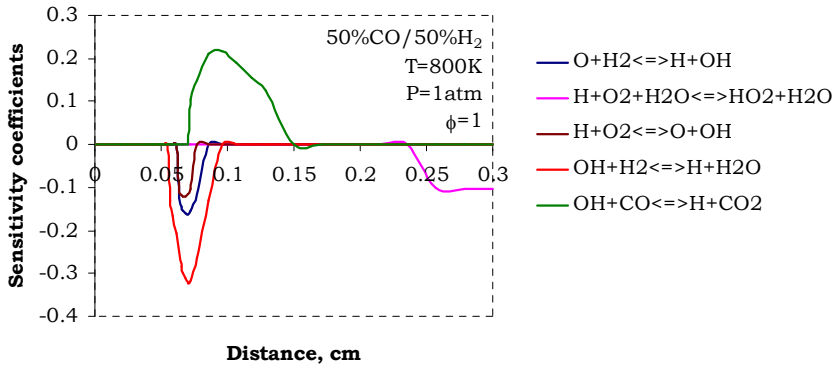

Figure D 7: H_2 Sensitivity coefficients at 800K preheat temperature

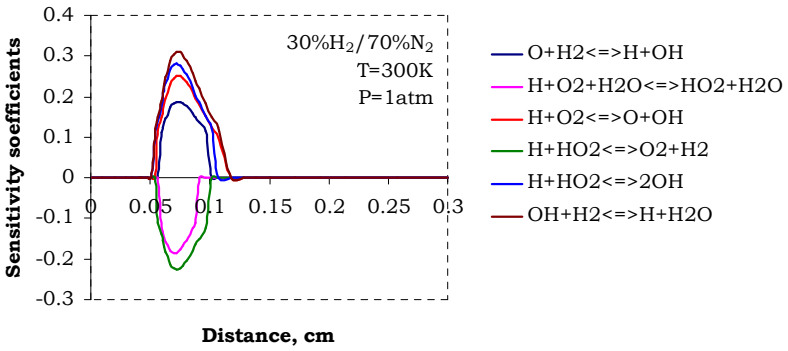

Figure D 8: H_2 Sensitivity analysis for mixture with 30%H_2/70%N_2

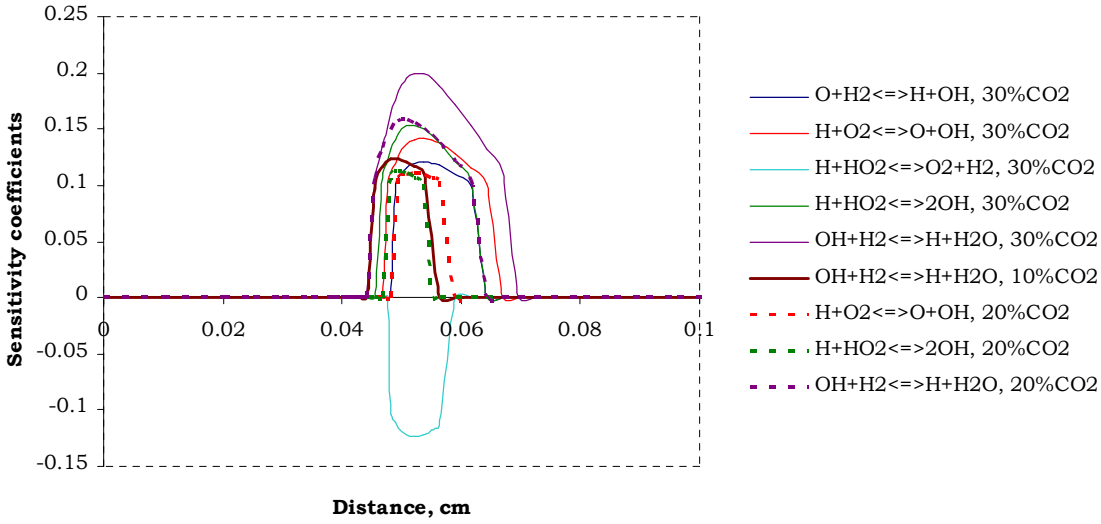

Figure D 9: Temperature sensitivity analysis at different H_2/CO_2 fuel mixture compositions

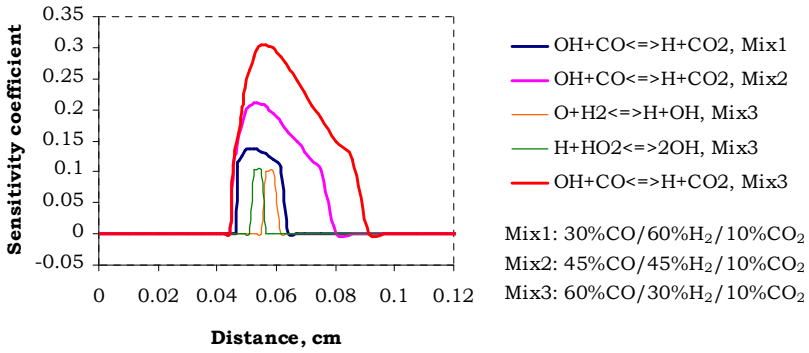

Figure D 10: Temperature Sensitivity analysis at different $CO/H_2/CO_2$ fuel mixture compositions

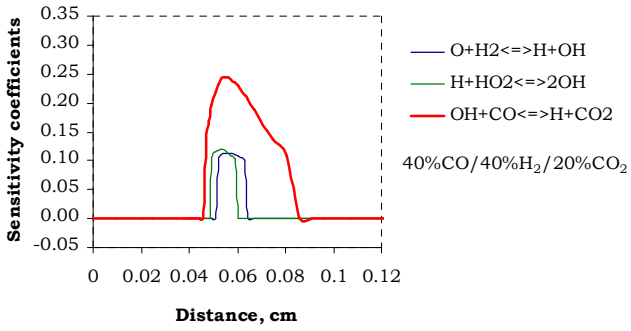

Figure D 11: Temperature sensitivity analysis for $40\%CO/40\%H_2/20\%CO_2$ fuel mixture compositions

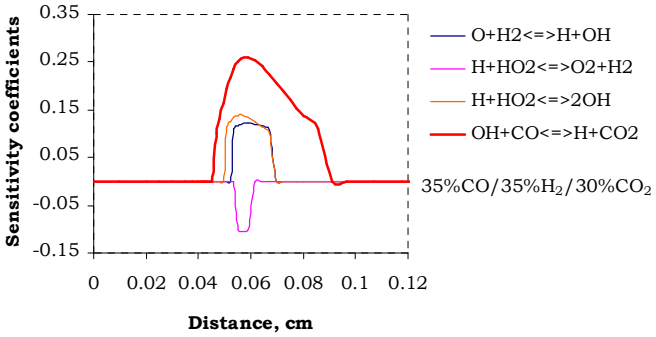

Figure D 12: Temperature sensitivity analysis for $35\%CO/35\%H_2/30\%CO_2$ fuel mixture compositions

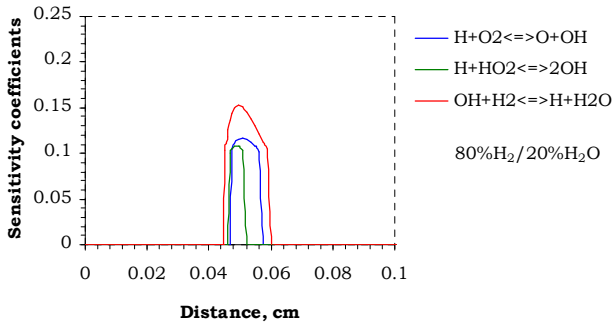

Figure D 13: Temperature sensitivity analysis for stoichiometric 80%H_2/20%H_2O fuel mixture at ambient conditions

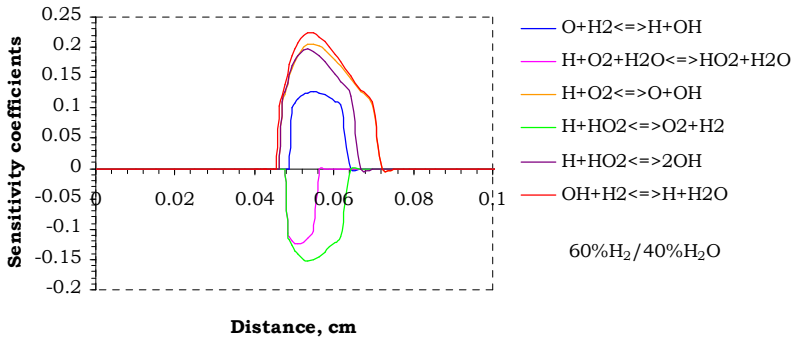

Figure D 14: Temperature sensitivity analysis for stoichiometric 60%H_2/40%H_2O fuel mixture at ambient conditions

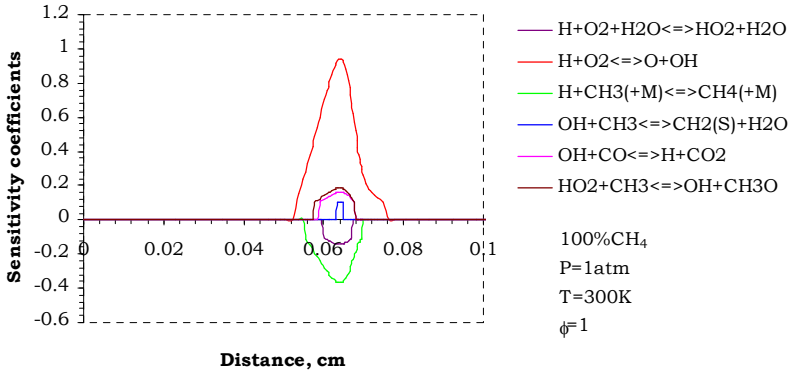

Figure D 15: Temperature sensitivity analysis for 100% CH_4 fuel at equivalence ratio 1 and ambient conditions

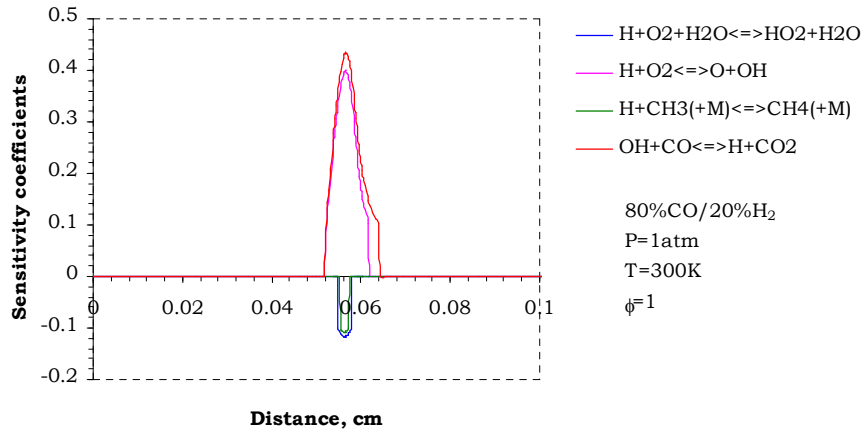

Figure D 16: Temperature sensitivity analysis for 80%CO/20%CH_4 fuel mixture at equivalence ratio 1 and ambient conditions

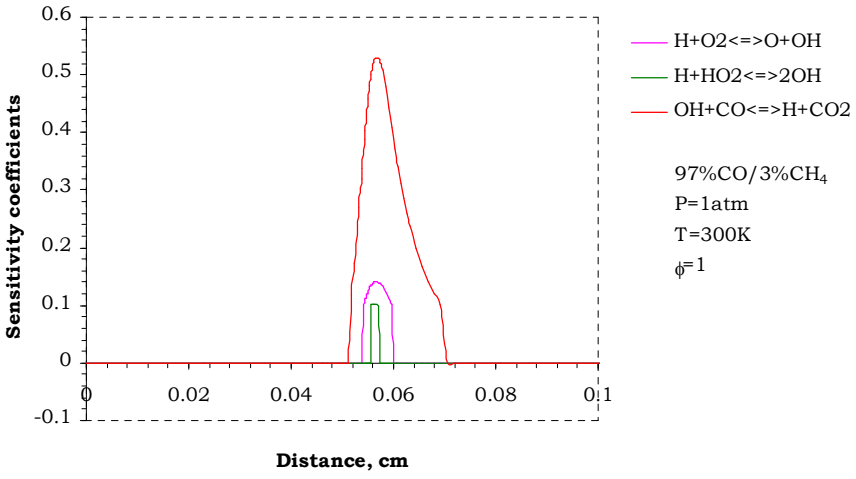

Figure D 17: Temperature sensitivity analysis for 97%CO/3%CH_4 fuel mixture at equivalence ratio 1 and ambient conditions

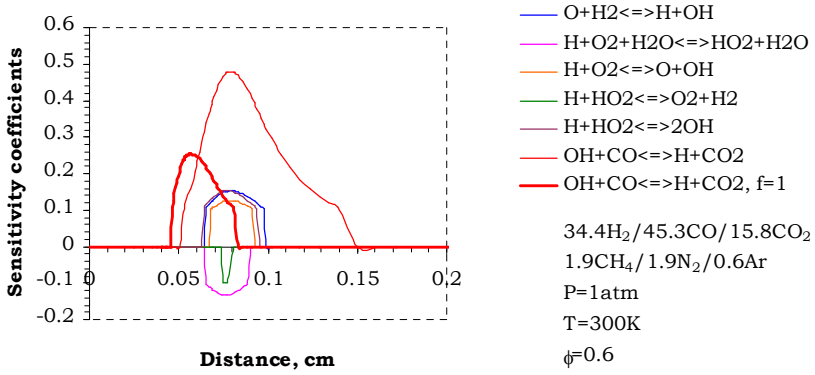

Figure D 18: Temperature sensitivity analysis for Mix1

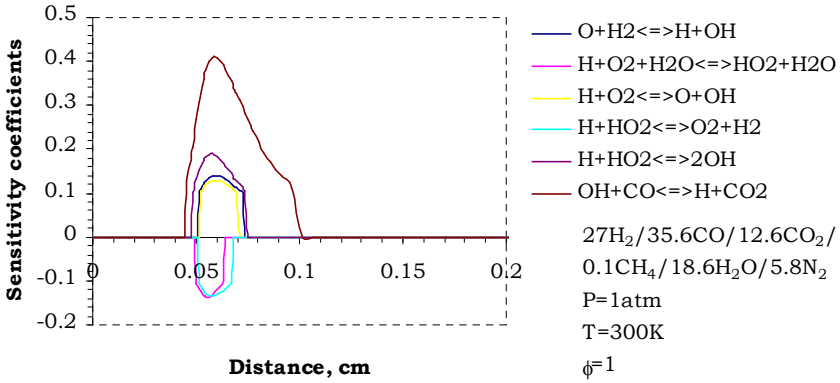

Figure D 19: Temperature sensitivity analysis for Mix2

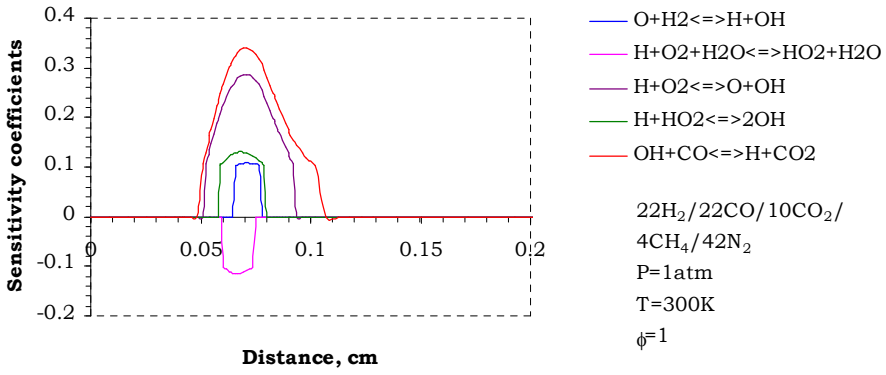

Figure D 20: Temperature sensitivity analysis for Mix3

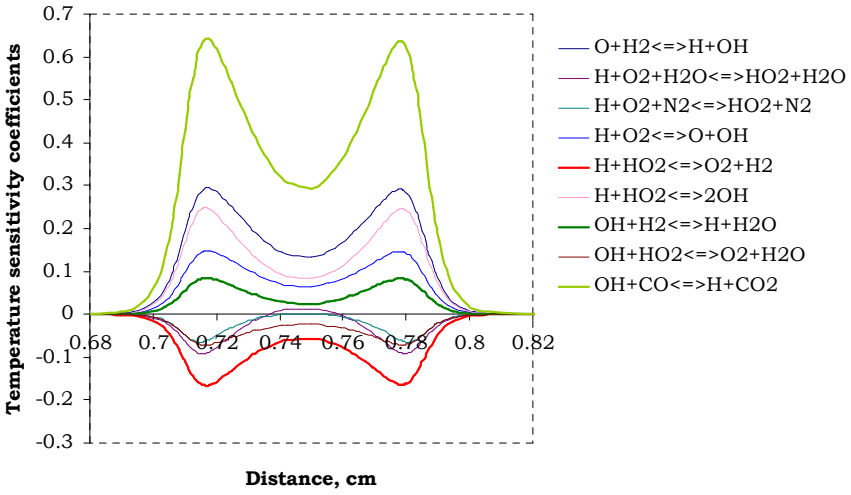

Figure D 21: Temperature sensitivity coefficients for 50%CO/50%H_2 at ϕ=0.5 and critical strain rate

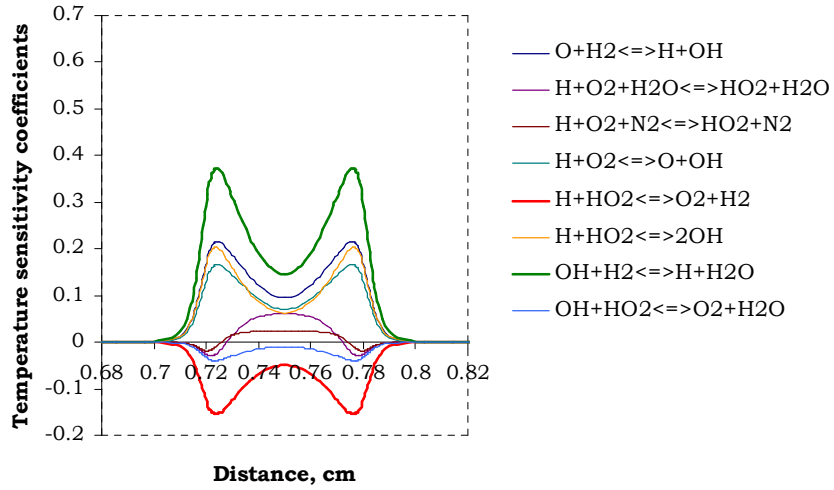

Figure D 22: Temperature sensitivity coefficients for 50%N_2/50%H_2 at ϕ=0.5 and critical strain rate

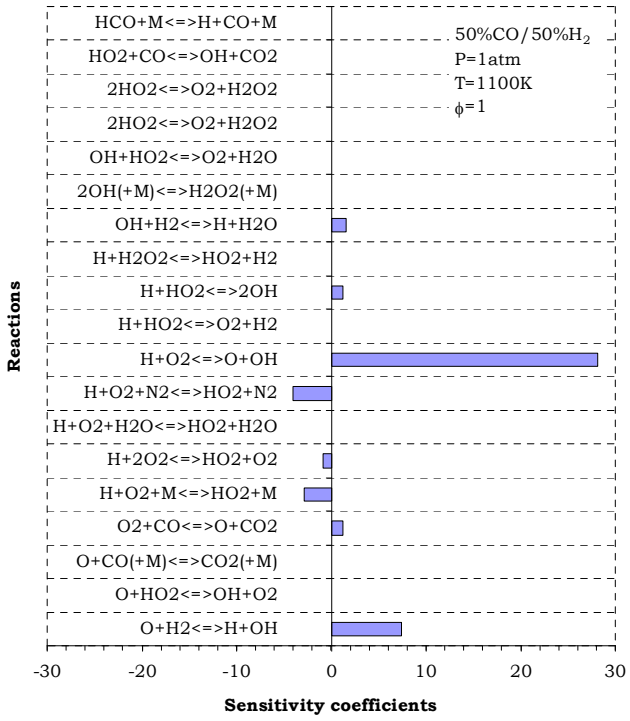

Figure D 23: OH sensitivity coefficients for stoichiometric 50%CO/50%H_2 at atmospheric pressure and 1100K temperature at ignition time

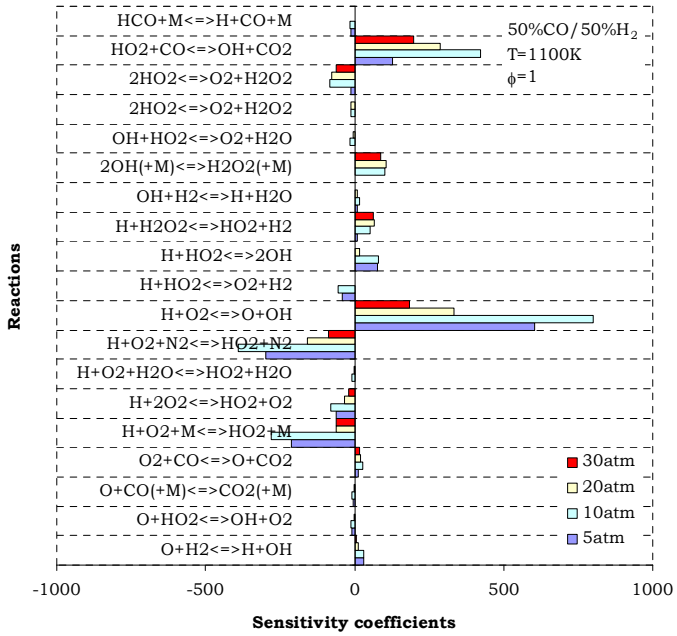

Figure D 24: OH sensitivity coefficients for stoichiometric 50%CO/50%H_2 at different pressures and 1100K temperature at ignition time

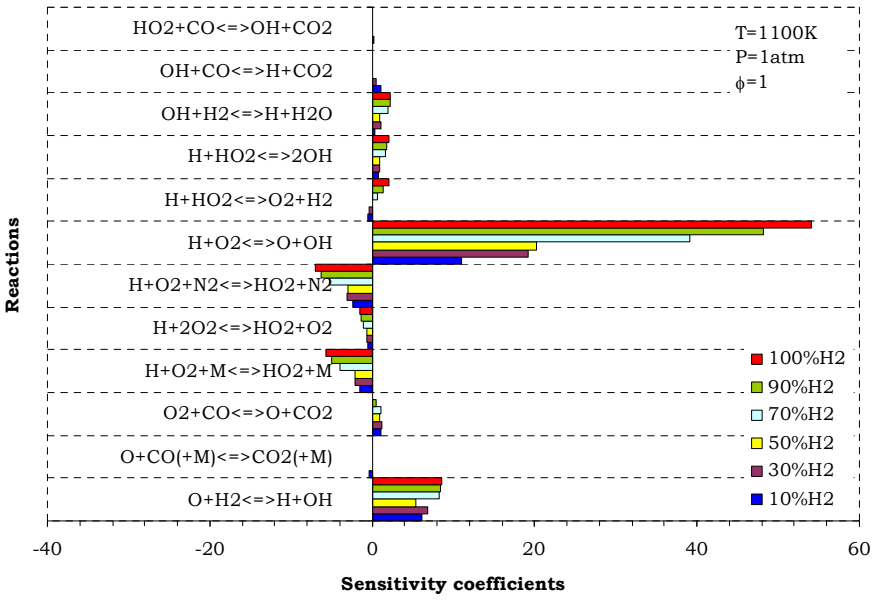

Figure D 25: OH sensitivity coefficients for stoichiometric CO/H_2 mixtures at atmospheric pressure and 1100K temperature at ignition time

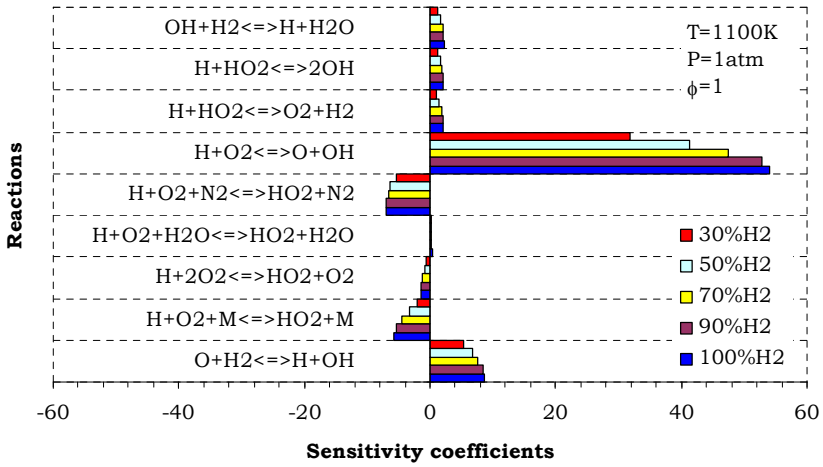

Figure D 26: OH sensitivity coefficients for stoichiometric N_2/H_2 mixtures at atmospheric pressure and 1100K temperature at ignition time

Appendix E - Artificial neural networks (equations)

Artificial neural network for laminar burning velocity

Here the coefficients of the input parameters are used to evaluate the summation function Z_i and activation function F_i for ANNs. These coefficients represent the weights of the summation function of each neuron belonging to the input, hidden and output layers of the trained network. For this purpose nine pairs of equations for the input layer, ten pairs for first and second hidden layers and one pair for the output layer are required. In order to calculate laminar burning velocities for $CO/H_2/CH_4$/Diluents fuel mixture the following equations are derived:

Normalized inputs:

$$P = p/50;\ T = T/1000$$

For CO, H_2, N_2, CO_2 H_2O, CH_4 and O_2 inputs are the fuel/air mixture composition in mole fractions.

Input layer:

$$Z_{11} = 1.8915 \cdot P + 0.60198 \cdot T - 6.0997 \cdot CO - 2.5076 \cdot H_2 + 4.8766 \cdot N_2 - \\ - 44.6437 \cdot CO_2 + 38.0523 \cdot H_2O + 39.3644 \cdot CH_4 - 6.0032 \cdot O_2 - 3.805$$

$$F_{11} = 1/\left(1 + e^{-Z_{11}}\right)$$

$$Z_{12} = 0.10341 \cdot P - 0.75815 \cdot T + 13.4441 \cdot CO + 13.0036 \cdot H_2 + 6.948 \cdot N_2 + \\ + 10.9643 \cdot CO_2 + 9.911 \cdot H_2O + 19.5264 \cdot CH_4 + 11.2811 \cdot O_2 - 5.8346$$

$$F_{12} = 1/\left(1 + e^{-Z_{12}}\right)$$

$$Z_{13} = -3.7784 \cdot P - 16.9954 \cdot T - 6.1149 \cdot CO - 20.2145 \cdot H_2 - 7.4581 \cdot N_2 + \\ + 4.855 \cdot CO_2 - 1.3524 \cdot H_2O + 26.386 \cdot CH_4 + 9.3468 \cdot O_2 + 22.7087$$

$$F_{13} = 1/\left(1 + e^{-Z_{13}}\right)$$

$$Z_{14} = -0.26215 \cdot P - 0.73619 \cdot T - 11.2778 \cdot CO - 10.1139 \cdot H_2 - 12.4451 \cdot N_2 - \\ - 4.8783 \cdot CO_2 - 12.5968 \cdot H_2O - 8.4061 \cdot CH_4 - 8.4093 \cdot O_2 + 12.1527$$

$$F_{14} = 1/\left(1 + e^{-Z_{14}}\right)$$

$$Z_{15} = 14.3571 \cdot P - 0.92365 \cdot T + 2.3515 \cdot CO + 0.5059 \cdot H_2 + 0.037128 \cdot N_2 - \\ - 0.19708 \cdot CO_2 - 0.86457 \cdot H_2O + 6.0866 \cdot CH_4 + 4.5082 \cdot O_2 + 1.1532$$

$$F_{15} = 1/\left(1 + e^{-Z_{15}}\right)$$

$$Z_{16} = 1.3048 \cdot P + 0.18846 \cdot T + 41.2233 \cdot CO - 1.6769 \cdot H_2 + 6.3459 \cdot N_2 - \\ - 31.7577 \cdot CO_2 - 24.8684 \cdot H_2O - 5.6037 \cdot CH_4 + 45.2653 \cdot O_2 - 14.0069$$

$$F_{16} = 1/\left(1 + e^{-Z_{16}}\right)$$

$$Z_{17} = -0.20589 \cdot P - 0.1699 \cdot T - 6.6527 \cdot CO - 2.1905 \cdot H_2 - 6.6696 \cdot N_2 - \\ - 16.4289 \cdot CO_2 + 7.1428 \cdot H_2O + 4.8419 \cdot CH_4 - 9.5816 \cdot O_2 + 8.2622$$

$$F_{17} = 1/\left(1 + e^{-Z_{17}}\right)$$

$$Z_{18} = -0.87081 \cdot P + 1.5729 \cdot T + 1.7226 \cdot CO + 1.9675 \cdot H_2 + 0.21575 \cdot N_2 + \\ + 18.9471 \cdot CO_2 - 18.2463 \cdot H_2O - 7.6645 \cdot CH_4 + 8.9964 \cdot O_2 - 4.9247$$

$$F_{18} = 1/\left(1 + e^{-Z_{18}}\right)$$

$$Z_{19} = 0.3366 \cdot P - 0.30168 \cdot T + 10.0692 \cdot CO + 6.7111 \cdot H_2 + 4.4017 \cdot N_2 - \\ - 16.0028 \cdot CO_2 - 1.9045 \cdot H_2O - 21.4476 \cdot CH_4 + 3.0552 \cdot O_2 - 3.0339$$

$$F_{19} = 1/\left(1 + e^{-Z_{19}}\right)$$

First hidden layer:

$$Z_{21} = 9.0274 \cdot F_{11} + 39.1159 \cdot F_{12} - 9.7984 \cdot F_{13} + 51.9059 \cdot F_{14} + 5.3129 \cdot F_{15} + \\ + 1.2508 \cdot F_{16} - 69.6329 \cdot F_{17} + 79.5175 \cdot F_{18} + 3.4459 \cdot F_{19} - 24.1281$$

$$F_{21} = 1/\left(1 + e^{-Z_{21}}\right)$$

$$Z_{22} = 4.8406 \cdot F_{11} + 8.6325 \cdot F_{12} - 0.27342 \cdot F_{13} + 3.7292 \cdot F_{14} - 18.0973 \cdot F_{15} - \\ - 2.2351 \cdot F_{16} - 8.158 \cdot F_{17} + 3.6693 \cdot F_{18} + 8.9216 \cdot F_{19} + 7.4745$$

$$F_{22} = 1/\left(1 + e^{-Z_{22}}\right)$$

$$Z_{23} = 16.1906 \cdot F_{11} + 58.3675 \cdot F_{12} + 0.1798 \cdot F_{13} + 8.9102 \cdot F_{14} - 19.7549 \cdot F_{15} - \\ - 5.7409 \cdot F_{16} - 12.9759 \cdot F_{17} - 0.419 \cdot F_{18} - 16.3825 \cdot F_{19} - 18.6427$$

$$F_{23} = 1/\left(1 + e^{-Z_{23}}\right)$$

$$Z_{24} = -1.8895 \cdot F_{11} - 7.6632 \cdot F_{12} + 2.3324 \cdot F_{13} - 21.7202 \cdot F_{14} + 25.3932 \cdot F_{15} + \\ + 0.19085 \cdot F_{16} + 38.762 \cdot F_{17} - 2.0613 \cdot F_{18} - 10.0604 \cdot F_{19} - 27.1852$$

$$F_{24} = 1/\left(1 + e^{-Z_{24}}\right)$$

$$Z_{25} = 1.2106 \cdot F_{11} + 26.5801 \cdot F_{12} + 0.14537 \cdot F_{13} + 5.2479 \cdot F_{14} + 7.9515 \cdot F_{15} + \\ + 0.43557 \cdot F_{16} - 25.2893 \cdot F_{17} - 4.7009 \cdot F_{18} - 2.204 \cdot F_{19} - 10.3276$$

$$F_{25} = 1/\left(1 + e^{-Z_{25}}\right)$$

$$Z_{26} = -9.8424 \cdot F_{11} - 14.001 \cdot F_{12} + 2.2526 \cdot F_{13} - 13.3892 \cdot F_{14} + 19.2791 \cdot F_{15} - \\ - 4.6622 \cdot F_{16} - 4.4406 \cdot F_{17} - 6.1767 \cdot F_{18} - 10.6231 \cdot F_{19} + 23.6035$$

$$F_{26} = 1/\left(1 + e^{-Z_{26}}\right)$$

$$Z_{27} = 0.75393 \cdot F_{11} - 43.8315 \cdot F_{12} + 3.3562 \cdot F_{13} + 7.7845 \cdot F_{14} + 14.6597 \cdot F_{15} + \\ + 2.6171 \cdot F_{16} + 17.4157 \cdot F_{17} - 25.2241 \cdot F_{18} - 0.091616 \cdot F_{19} + 1.1125$$

$$F_{27} = 1/\left(1 + e^{-Z_{27}}\right)$$

$$Z_{28} = -15.5749 \cdot F_{11} - 55.3921 \cdot F_{12} + 0.14251 \cdot F_{13} - 32.4948 \cdot F_{14} + 85.484 \cdot F_{15} - \\ - 0.43418 \cdot F_{16} + 35.5534 \cdot F_{17} + 9.5628 \cdot F_{18} - 7.4684 \cdot F_{19} - 27.3844$$

$$F_{28} = 1/\left(1 + e^{-Z_{28}}\right)$$

$$Z_{29} = 1.9694 \cdot F_{11} + 11.9661 \cdot F_{12} - 0.066629 \cdot F_{13} - 0.95919 \cdot F_{14} - 7.6984 \cdot F_{15} - \\ - 0.62486 \cdot F_{16} - 0.47969 \cdot F_{17} + 6.0202 \cdot F_{18} + 3.0712 \cdot F_{19} - 6.2522$$

$$F_{29} = 1/\left(1 + e^{-Z_{29}}\right)$$

$$Z_{210} = -5.9731 \cdot F_{11} + 0.94745 \cdot F_{12} - 0.40737 \cdot F_{13} - 6.6443 \cdot F_{14} + 24.3398 \cdot F_{15} + \\ + 2.8027 \cdot F_{16} + 6.1685 \cdot F_{17} - 1.185 \cdot F_{18} - 12.0251 \cdot F_{19} - 12.5646$$

$$F_{210} = 1/\left(1 + e^{-Z_{210}}\right)$$

Second hidden layer:

$$Z_{31} = -5.7005 \cdot F_{21} - 5.7376 \cdot F_{22} - 0.02455 \cdot F_{23} + 1.5388 \cdot F_{24} - 4.4685 \cdot F_{25} - \\ - 13.6266 \cdot F_{26} - 16.4908 \cdot F_{27} - 0.65503 \cdot F_{28} - 3.1434 \cdot F_{29} + 3.7243 \cdot F_{210} + \\ + 23.6134$$

$$F_{31} = 1/\left(1 + e^{-Z_{31}}\right)$$

$$Z_{32} = 3.1909 \cdot F_{21} - 2.219 \cdot F_{22} + 0.30191 \cdot F_{23} - 0.58642 \cdot F_{24} - 1.8455 \cdot F_{25} + \\ + 4.6298 \cdot F_{26} + 21.4905 \cdot F_{27} - 0.2601 \cdot F_{28} + 1.7854 \cdot F_{29} + 0.26983 \cdot F_{210} - \\ - 6.2842$$

$$F_{32} = 1/\left(1 + e^{-Z_{32}}\right)$$

$$Z_{33} = -0.55424 \cdot F_{21} - 0.42522 \cdot F_{22} - 0.47336 \cdot F_{23} + 1.7986 \cdot F_{24} - 2.6955 \cdot F_{25} + \\ + 0.12941 \cdot F_{26} - 7.517 \cdot F_{27} - 0.89339 \cdot F_{28} + 0.41728 \cdot F_{29} + 1.6746 \cdot F_{210} + \\ + 2.987$$

$$F_{33} = 1/\left(1 + e^{-Z_{33}}\right)$$

$$Z_{34} = 6.8111 \cdot F_{21} - 2.7808 \cdot F_{22} - 19.3346 \cdot F_{23} + 2.2342 \cdot F_{24} - 6.2317 \cdot F_{25} + \\ + 15.3172 \cdot F_{26} - 22.4353 \cdot F_{27} + 3.8699 \cdot F_{28} - 6.1726 \cdot F_{29} + 7.0299 \cdot F_{210} + \\ + 10.9976$$

$$F_{34} = 1/\left(1 + e^{-Z_{34}}\right)$$

$$Z_{35} = 0.18626 \cdot F_{21} + 2.4331 \cdot F_{22} + 1.8362 \cdot F_{23} + 2.9927 \cdot F_{24} - 1.224 \cdot F_{25} - \\ - 3.5608 \cdot F_{26} + 11.6982 \cdot F_{27} - 0.70468 \cdot F_{28} - 8.9199 \cdot F_{29} - 1.4543 \cdot F_{210} + \\ + 4.14$$

$$F_{35} = 1/\left(1 + e^{-Z_{35}}\right)$$

$$Z_{36} = 0.10069 \cdot F_{21} + 5.2725 \cdot F_{22} - 4.1123 \cdot F_{23} - 4.4945 \cdot F_{24} + 5.4578 \cdot F_{25} - \\ - 6.9483 \cdot F_{26} + 16.4311 \cdot F_{27} - 4.4028 \cdot F_{28} + 2.2437 \cdot F_{29} - 8.9676 \cdot F_{210} + \\ + 10.1589$$

$$F_{36} = 1/\left(1 + e^{-Z_{36}}\right)$$

$$Z_{37} = -4.6564 \cdot F_{21} + 2.452 \cdot F_{22} - 13.6011 \cdot F_{23} + 2.1421 \cdot F_{24} - 1.862 \cdot F_{25} - \\ - 7.6864 \cdot F_{26} - 24.3106 \cdot F_{27} + 0.30682 \cdot F_{28} - 4.2854 \cdot F_{29} + 3.6781 \cdot F_{210} + \\ + 21.7968$$

$$F_{37} = 1/\left(1 + e^{-Z_{37}}\right)$$

$$Z_{38} = 1.4633 \cdot F_{21} + 0.082206 \cdot F_{22} + 4.5089 \cdot F_{23} - 3.7015 \cdot F_{24} + 2.1491 \cdot F_{25} - \\ - 0.84113 \cdot F_{26} + 16.1341 \cdot F_{27} + 1.953 \cdot F_{28} + 2.7276 \cdot F_{29} + 3.2894 \cdot F_{210} - \\ - 9.8708$$

$$F_{38} = 1/\left(1 + e^{-Z_{38}}\right)$$

$$Z_{39} = -6.7497 \cdot F_{21} + 5.4342 \cdot F_{22} - 3.6881 \cdot F_{23} - 3.7469 \cdot F_{24} + 8.9082 \cdot F_{25} - \\ - 20.0373 \cdot F_{26} + 33.6807 \cdot F_{27} - 6.2684 \cdot F_{28} + 5.0071 \cdot F_{29} - 11.1967 \cdot F_{210} + \\ + 19.2659$$

$$F_{39} = 1/\left(1 + e^{-Z_{39}}\right)$$

$$Z_{310} = 0.51003 \cdot F_{21} + 6.2525 \cdot F_{22} - 0.545 \cdot F_{23} + 1.4441 \cdot F_{24} + 1.1664 \cdot F_{25} + \\ + 4.5345 \cdot F_{26} + 8.2508 \cdot F_{27} - 1.3402 \cdot F_{28} - 22.6198 \cdot F_{29} - 5.0161 \cdot F_{210} + \\ + 0.80222$$

$$F_{310} = 1/\left(1 + e^{-Z_{310}}\right)$$

Output layer:

$$Z_{41} = -24.1055 \cdot F_{31} + 46.5796 \cdot F_{32} + 54.4497 \cdot F_{33} - 27.6914 \cdot F_{34} - \\ - 3.6506 \cdot F_{35} + 8.5321 \cdot F_{36} + 38.6827 \cdot F_{37} + 8.849 \cdot F_{38} - 10.0473 \cdot F_{39} - \\ - 15.9827 \cdot F_{310} - 40.1347$$

$$F_{41} = 1/\left(1 + e^{-Z_{41}}\right)$$

Laminar burning velocity, dependant on pressure, temperature, mixture composition and equivalence ratio, can be calculated from:

$$S_o = F_{41} \times 20$$

The coefficient 20 is used to convert from normalized value to the actual value of the laminar burning velocity.

Artificial neural network for critical strain rate to extinction

In order to evaluate the summation function Z_i and activation function F_i six pairs of equations for the input layer, eight pairs for the hidden layer and one pair for the output layer are extracted from the trained ANN. In order to calculate critical strain rates to extinction for the $CO/H_2/N_2$ fuel mixture the following equations are derived:

Normalized inputs:

$$P = p/50;\ T = T/1000$$

For CO, H_2, N_2 and O_2, inputs are the fuel/air mixture composition in mole fractions.

Input layer:

$$Z_{11} = -1.2176 \cdot P + 2.9926 \cdot T + 9.0724 \cdot CO + 3.6177 \cdot H_2 - 14.2218 \cdot N_2 - \\ - 16.0576 \cdot O_2 + 10.5752$$

$$F_{11} = 1/\left(1 + e^{-Z_{11}}\right)$$

$$Z_{12} = 0.35449 \cdot P + 0.44734 \cdot T - 11.48 \cdot CO - 18.9454 \cdot H_2 - 8.1392 \cdot N_2 - \\ - 3.6938 \cdot O_2 + 10.0063$$

$$F_{12} = 1/\left(1 + e^{-Z_{12}}\right)$$

$$Z_{13} = -0.35132 \cdot P - 2.6508 \cdot T + 11.4932 \cdot CO - 4.968 \cdot H_2 + 18.0945 \cdot N_2 + \\ + 15.3406 \cdot O_2 - 12.0536$$

$$F_{13} = 1/\left(1 + e^{-Z_{13}}\right)$$

$$Z_{14} = 11.3376 \cdot P - 4.9125 \cdot T + 9.3814 \cdot CO - 25.2602 \cdot H_2 - 5.7187 \cdot N_2 + \\ + 26.9966 \cdot O_2 + 3.5696$$

$$F_{14} = 1/\left(1 + e^{-Z_{14}}\right)$$

$$Z_{15} = 7.9256 \cdot P - 0.56108 \cdot T - 12.2421 \cdot CO + 12.8138 \cdot H_2 - 1.0518 \cdot N_2 + \\ + 25.2317 \cdot O_2 + 2.9542$$

$$F_{15} = 1/\left(1 + e^{-Z_{15}}\right)$$

$$Z_{16} = 13.3033 \cdot P + 0.73407 \cdot T - 7.5024 \cdot CO - 5.995 \cdot H_2 - 8.3459 \cdot N_2 - \\ - 6.4862 \cdot O_2 + 6.5405$$

$$F_{16} = 1/\left(1 + e^{-Z_{16}}\right)$$

Hidden layer

$$Z_{21} = 1.3634 \cdot F_{11} - 3.9336 \cdot F_{12} + 2.8116 \cdot F_{13} - 3.1818 \cdot F_{14} + 2.9992 \cdot F_{15} - \\ - 1.1753 \cdot F_{16} - 8.8558$$

$$F_{21} = 1/\left(1 + e^{-Z_{21}}\right)$$

$$Z_{22} = 0.48874 \cdot F_{11} - 2.3982 \cdot F_{12} + 2.0671 \cdot F_{13} + 0.090671 \cdot F_{14} - 3.5954 \cdot F_{15} - \\ - 1.7321 \cdot F_{16} + 4.6872$$

$$F_{22} = 1/\left(1 + e^{-Z_{22}}\right)$$

$$Z_{23} = -4.4292 \cdot F_{11} - 6.6425 \cdot F_{12} + 3.7628 \cdot F_{13} - 5.5859 \cdot F_{14} - 1.5567 \cdot F_{15} - \\ - 4.2679 \cdot F_{16} + 11.1597$$

$$F_{23} = 1/\left(1 + e^{-Z_{23}}\right)$$

$$Z_{24} = -0.19004 \cdot F_{11} + 2.1588 \cdot F_{12} - 2.257 \cdot F_{13} - 0.74757 \cdot F_{14} - 4.2829 \cdot F_{15} - \\ - 10.4344 \cdot F_{16} + 7.4584$$

$$F_{24} = 1/\left(1 + e^{-Z_{24}}\right)$$

$$Z_{25} = -2.7717 \cdot F_{11} + 1.5099 \cdot F_{12} - 2.3662 \cdot F_{13} - 0.29642 \cdot F_{14} + 1.5872 \cdot F_{15} + \\ + 4.1459 \cdot F_{16} - 0.75864$$

$$F_{25} = 1/\left(1 + e^{-Z_{25}}\right)$$

$$Z_{26} = -8.1572 \cdot F_{11} + 15.2637 \cdot F_{12} - 13.326 \cdot F_{13} + 0.20961 \cdot F_{14} - 2.8439 \cdot F_{15} + \\ + 6.1313 \cdot F_{16} - 5.4975$$

$$F_{26} = 1/\left(1 + e^{-Z_{26}}\right)$$

$$Z_{27} = 15.2493 \cdot F_{11} + 7.5342 \cdot F_{12} + 0.755 \cdot F_{13} - 6.2245 \cdot F_{14} - 3.5782 \cdot F_{15} - \\ - 8.2858 \cdot F_{16} + 1.3606$$

$$F_{27} = 1/\left(1 + e^{-Z_{27}}\right)$$

$$Z_{28} = -1.9782 \cdot F_{11} + 8.7824 \cdot F_{12} + 5.2277 \cdot F_{13} + 2.3156 \cdot F_{14} - 3.2883 \cdot F_{15} + \\ + 0.51978 \cdot F_{16} - 10.6396$$

$$F_{28} = 1/\left(1 + e^{-Z_{28}}\right)$$

Output layer

$$Z_{31} = 1.0873 \cdot F_{21} - 12.6847 \cdot F_{22} + 1.317 \cdot F_{23} - 6.6047 \cdot F_{24} - 3.9306 \cdot F_{25} + \\ + 16.0756 \cdot F_{26} + 6.0596 \cdot F_{27} - 4.1311 \cdot F_{28} + 0.2355$$

$$F_{31} = 1/\left(1 + e^{-Z_{31}}\right)$$

Critical strain rate to extinction, dependant on pressure, temperature, mixture composition and equivalence ratio, can be calculated from:

$$S_{ext} = F_{31} \times 1500000$$

The coefficient 1500000 is used to convert from the normalized value to the actual value of the critical strain rate to extinction.

Appendix F – CFD Results

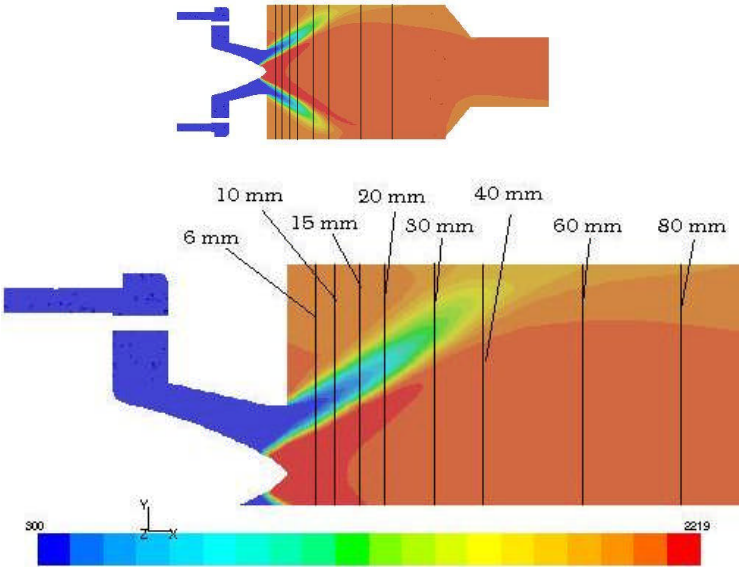

Figure F 1: Positions downstream the burner nozzle for the DLR temperature measurements (drawn on temperature contours for methane)

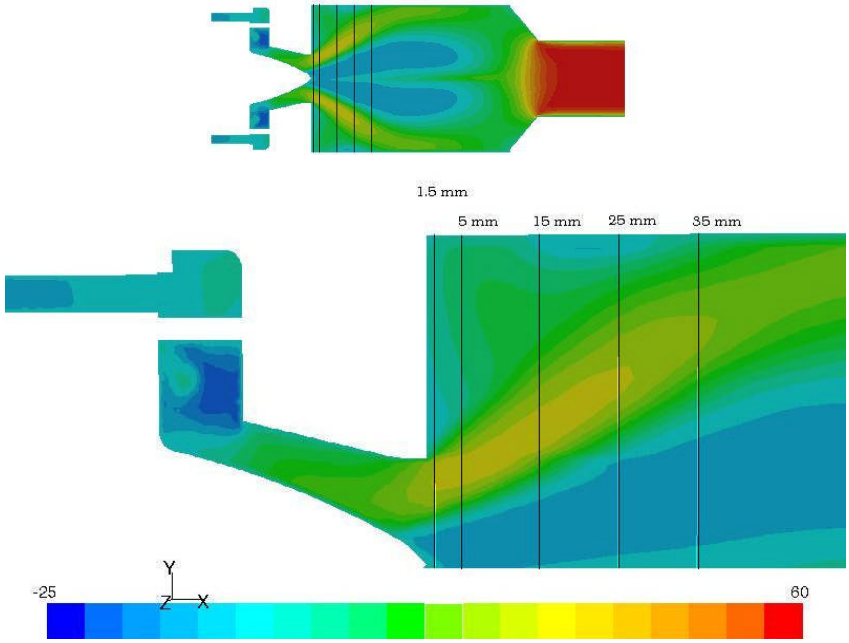

Figure F 2: Positions downstream the burner nozzle for the DLR velocity measurements (drawn on axial velocity contours for methane)

Methane – benchmark case

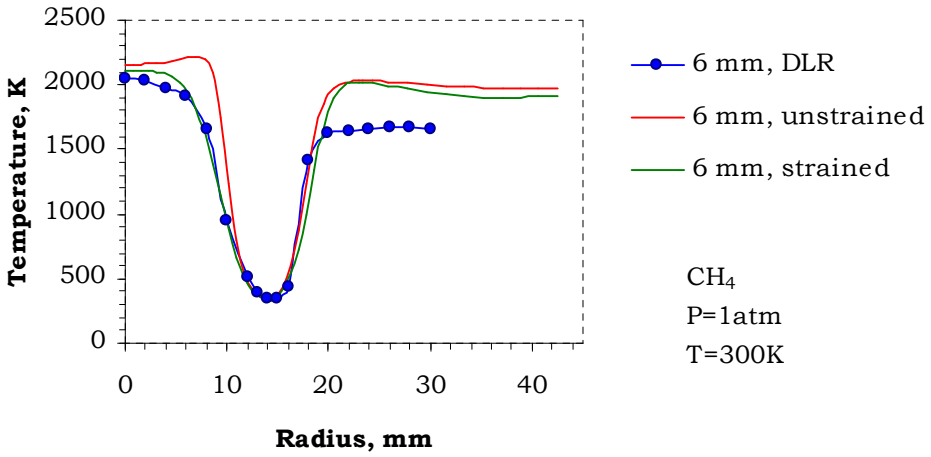

Figure F 3: Predicted temperature profiles for methane compared to experimental measurements at 6 mm downstream the burner nozzle

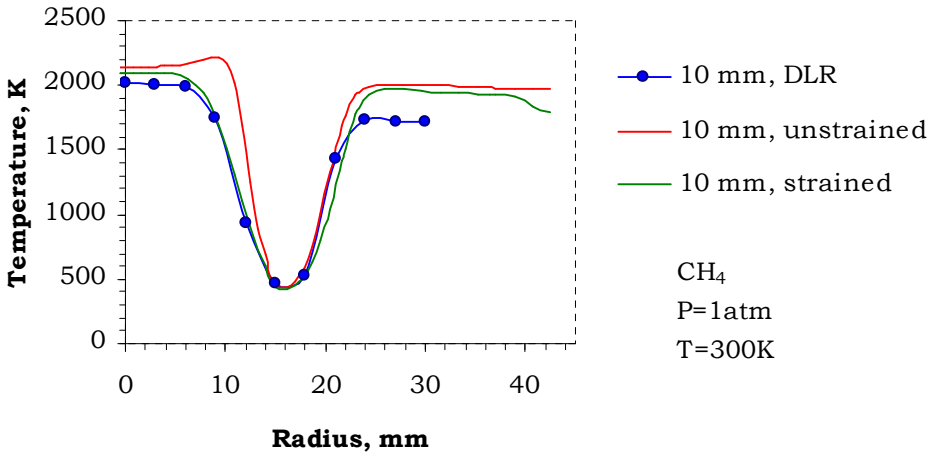

Figure F 4: Predicted temperature profiles for methane compared to experimental measurements at 10 mm downstream of the burner nozzle

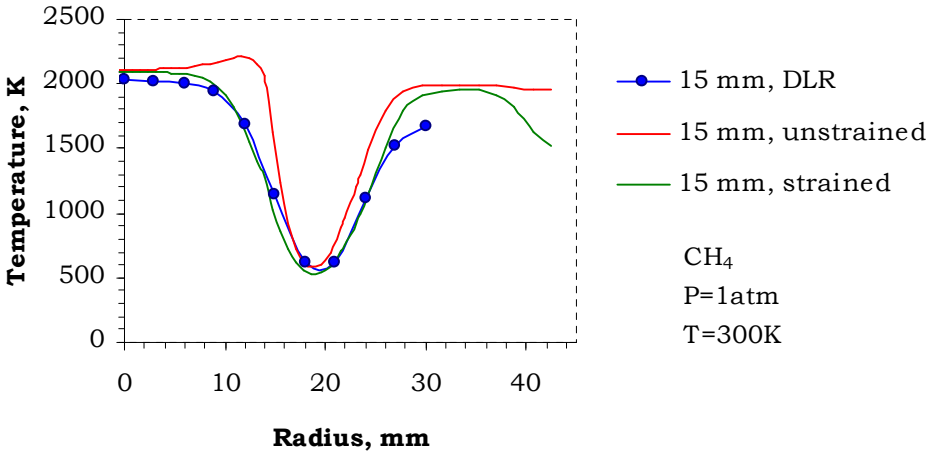

Figure F 5: Predicted temperature profiles for methane compared to experimental measurements at 15 mm downstream of the burner nozzle

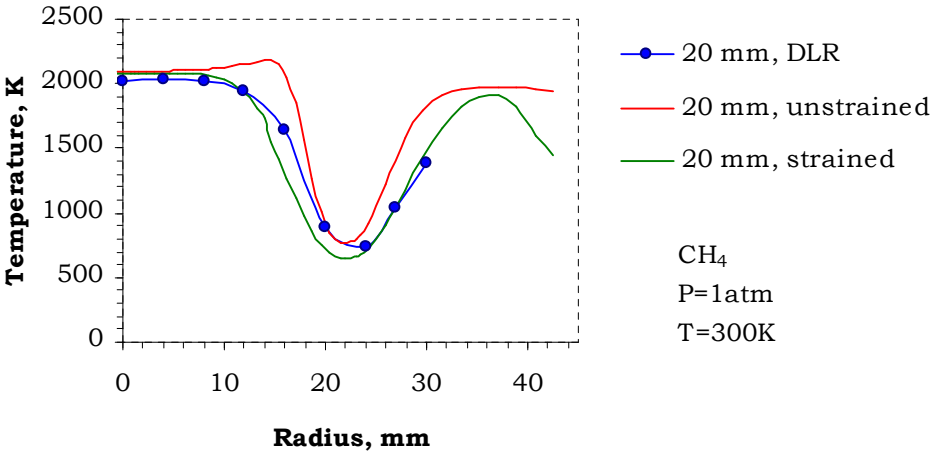

Figure F 6: Predicted temperature profiles for methane compared to experimental measurements at 20 mm downstream of the burner nozzle

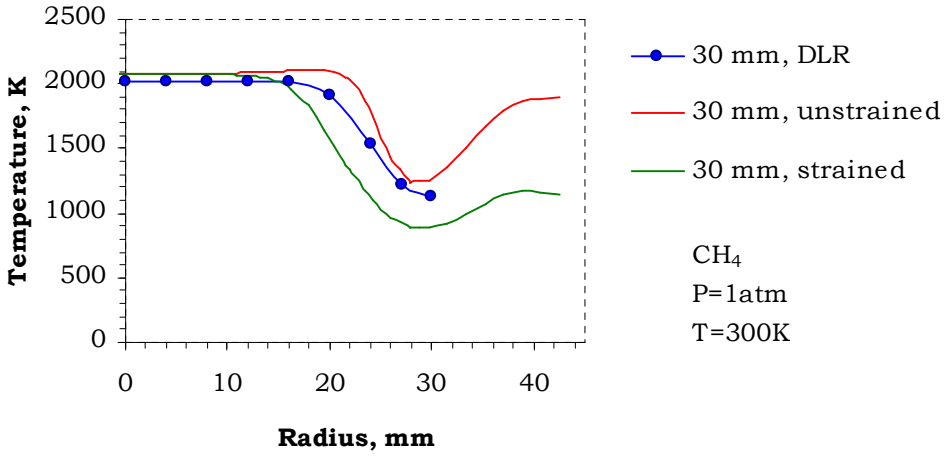

Figure F 7: Predicted temperature profiles for methane compared to experimental measurements at 30 mm downstream of the burner nozzle

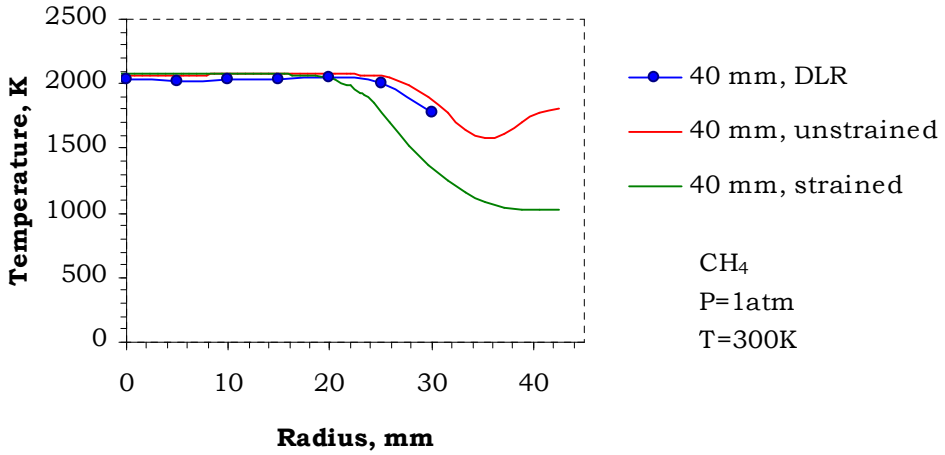

Figure F 8: Predicted temperature profiles for methane compared to experimental measurements at 40 mm downstream of the burner nozzle

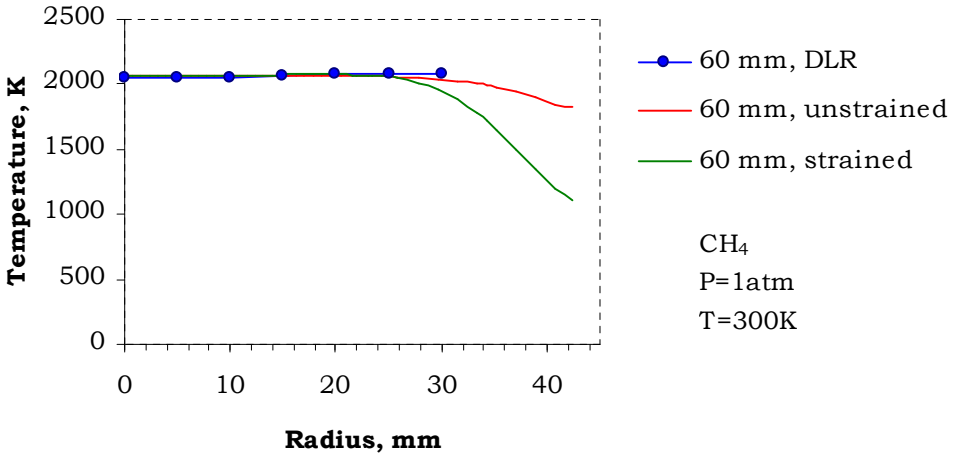

Figure F 9: Predicted temperature profiles for methane compared to experimental measurements at 60 mm downstream of the burner nozzle

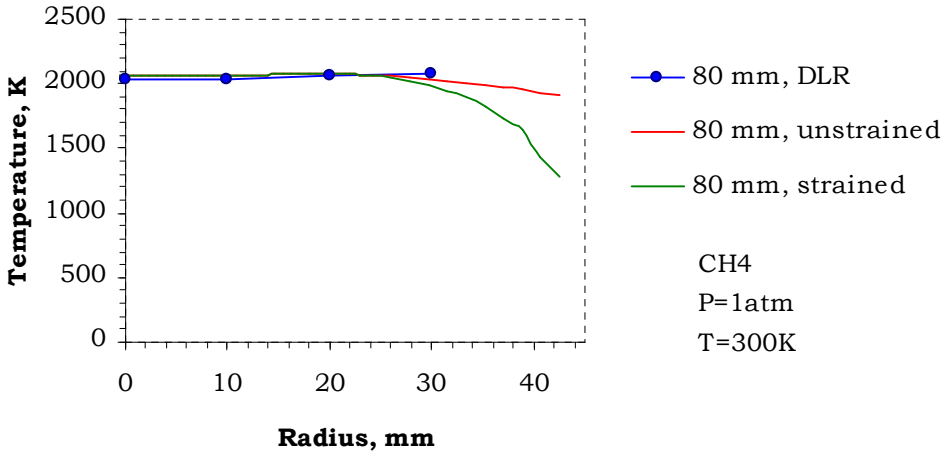

Figure F 10: Predicted temperature profiles for methane compared to experimental measurements at 80 mm downstream of the burner nozzle

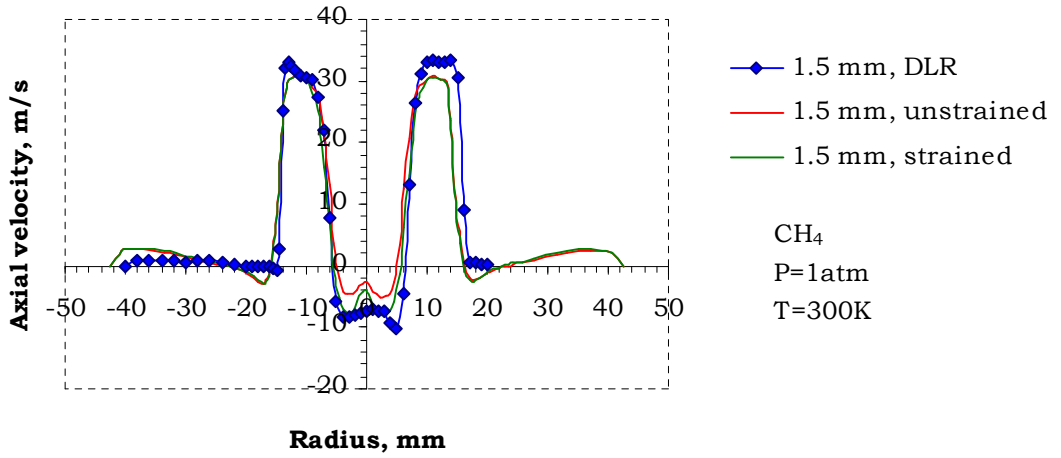

Figure F 11: Predicted axial velocity profiles for methane compared to experimental measurements at 1.5 mm downstream of the burner nozzle

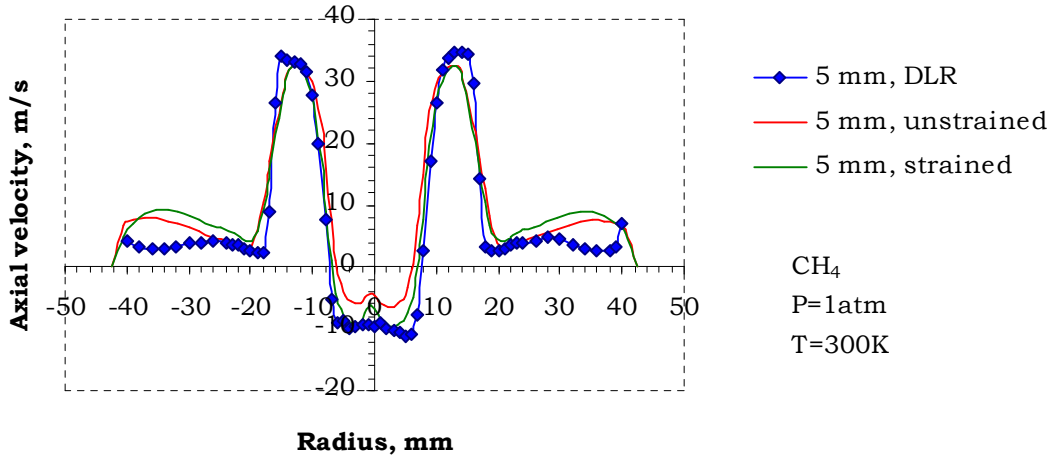

Figure F 12: Predicted axial velocity profiles for methane compared to experimental measurements at 5 mm downstream of the burner nozzle

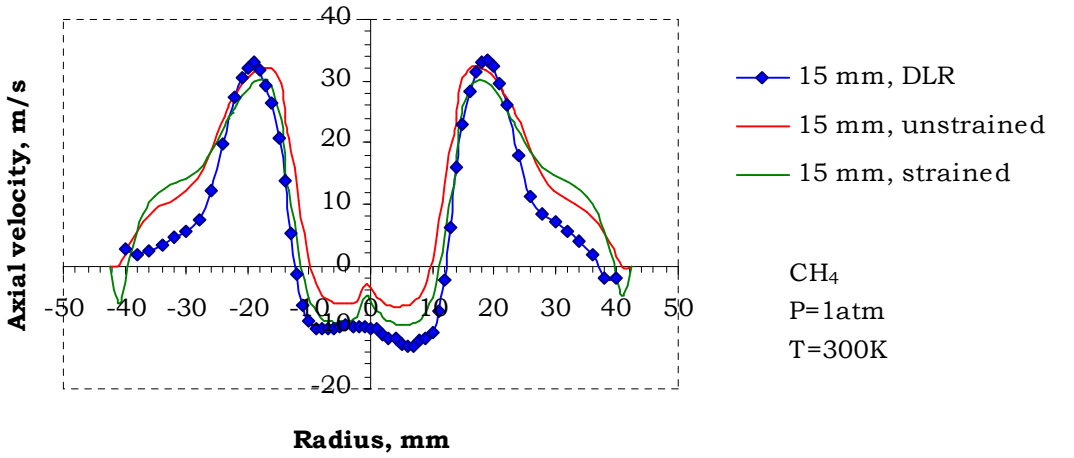

Figure F 13: Predicted axial velocity profiles for methane compared to experimental measurements at 15 mm downstream of the burner nozzle

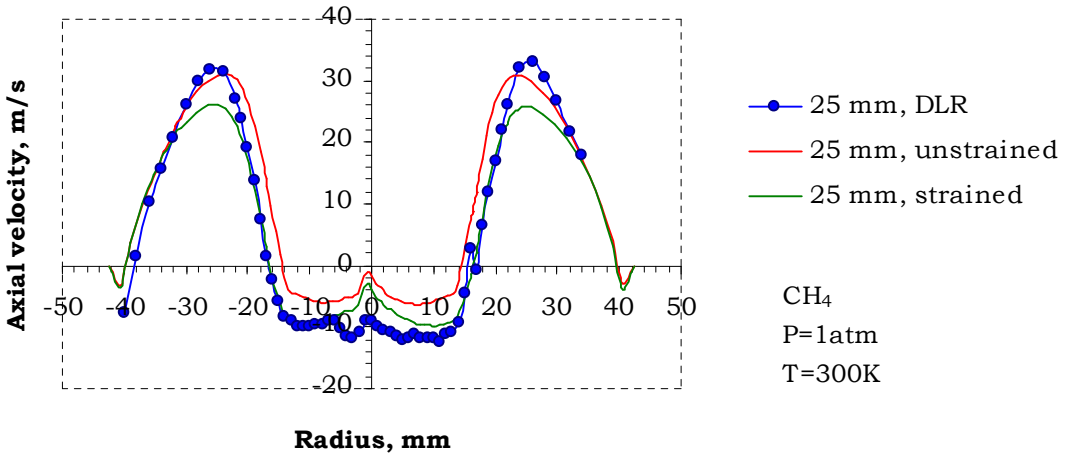

Figure F 14: Predicted axial velocity profiles for methane compared to experimental measurements at 25 mm downstream of the burner nozzle

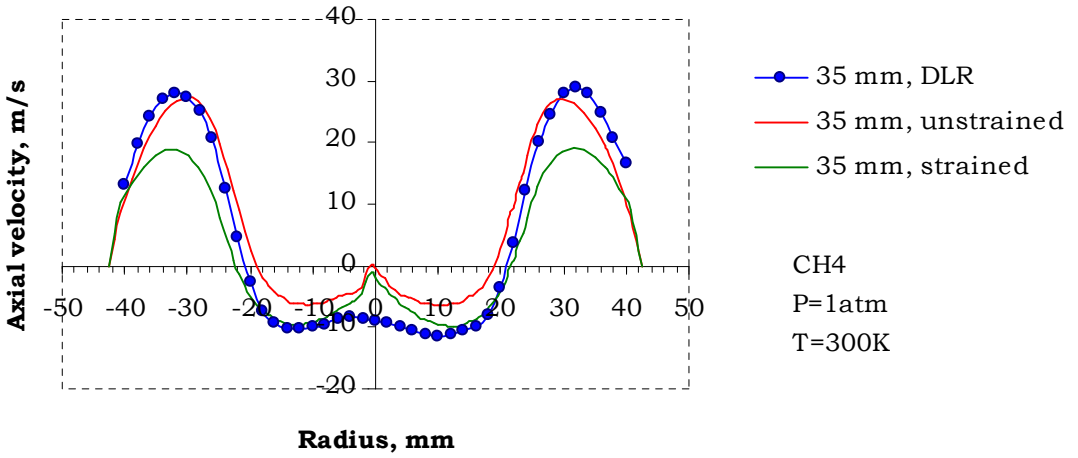

Figure F 15: Predicted axial velocity profiles for methane compared to experimental measurements at 35 mm downstream of the burner nozzle

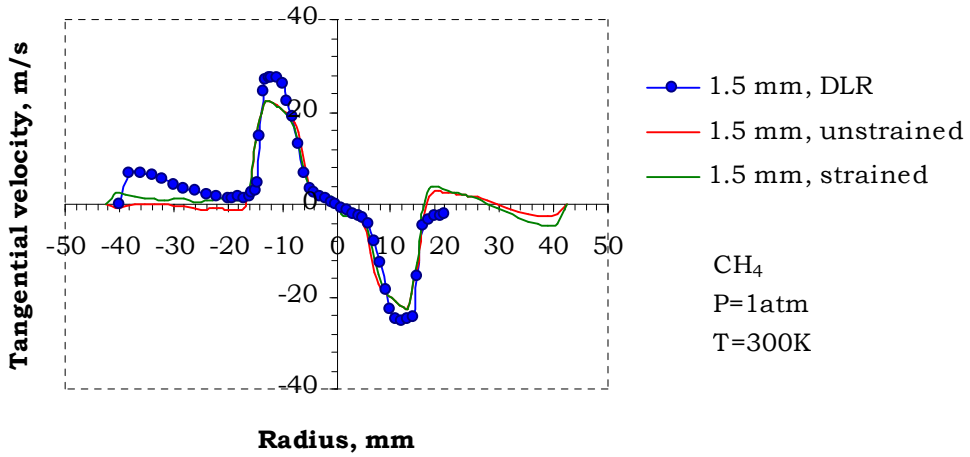

Figure F 16: Predicted tangential velocity profiles for methane compared to experimental measurements at 1.5 mm downstream of the burner nozzle

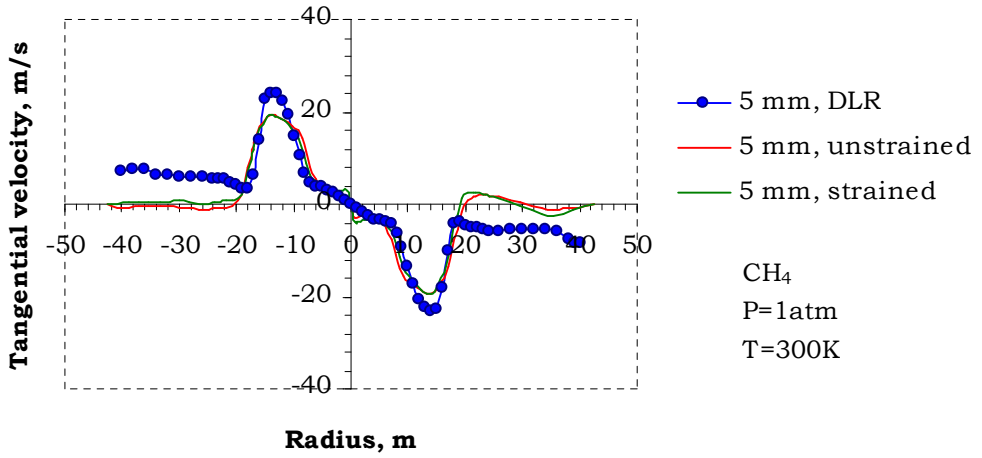

Figure F 17: Predicted tangential velocity profiles for methane compared to experimental measurements at 5 mm downstream of the burner nozzle

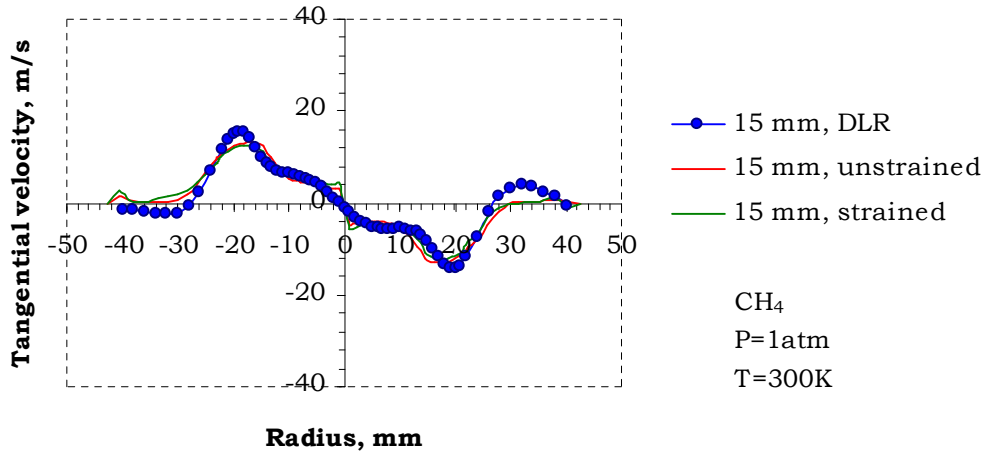

Figure F 18: Predicted tangential velocity profiles for methane compared to experimental measurements at 15 mm downstream of the burner nozzle

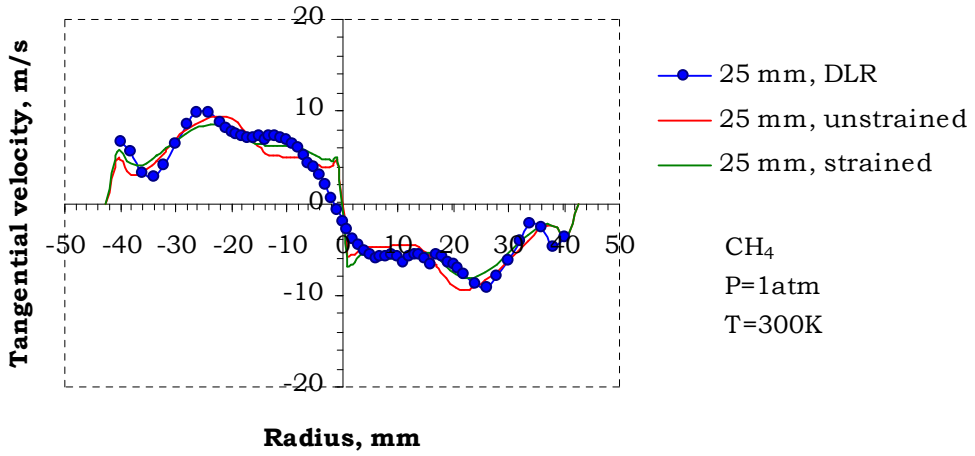

Figure F 19: Predicted tangential velocity profiles for methane compared to experimental measurements at 25 mm downstream of the burner nozzle

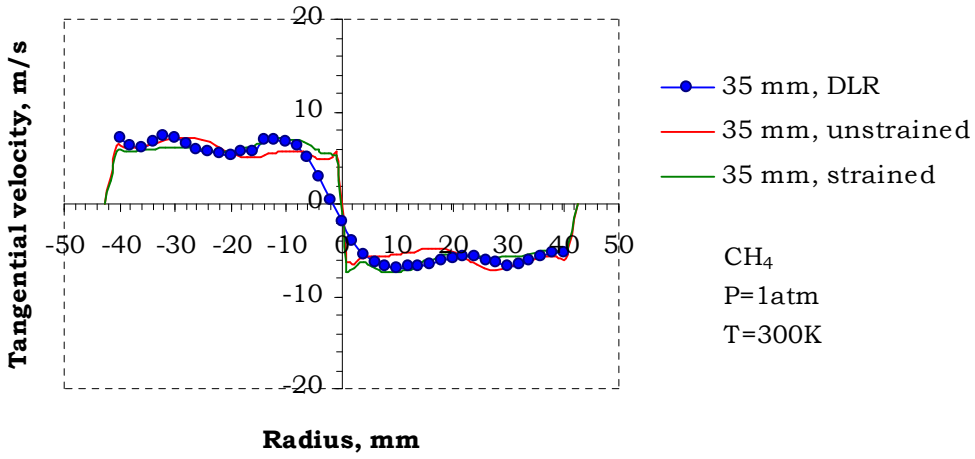

Figure F 20: Predicted tangential velocity profiles for methane compared to experimental measurements at 35 mm downstream of the burner nozzle

12%CO/88%H_2 – first fuel mixture

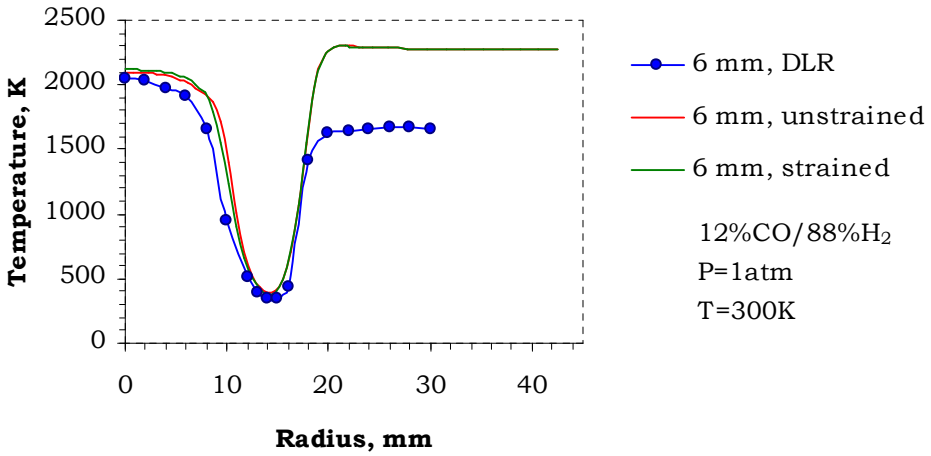

Figure F 21: Predicted temperature profiles for fuel mixture 12%CO/88%H_2 for strained and unstrained flames at 6 mm downstream of the burner nozzle; experimental measurements of methane flame plotted as a reference

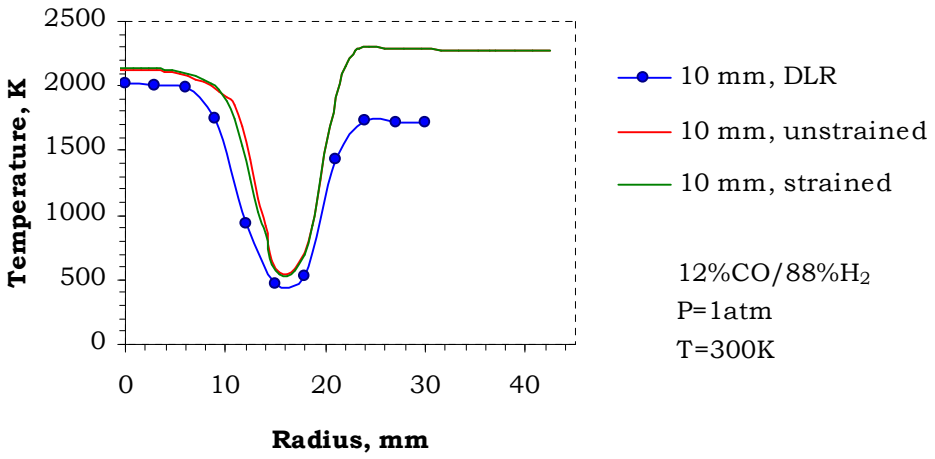

Figure F 22: Predicted temperature profiles for fuel mixture 12%CO/88%H_2 for strained and unstrained flames at 10 mm downstream of the burner nozzle; experimental measurements of methane flame plotted as a reference

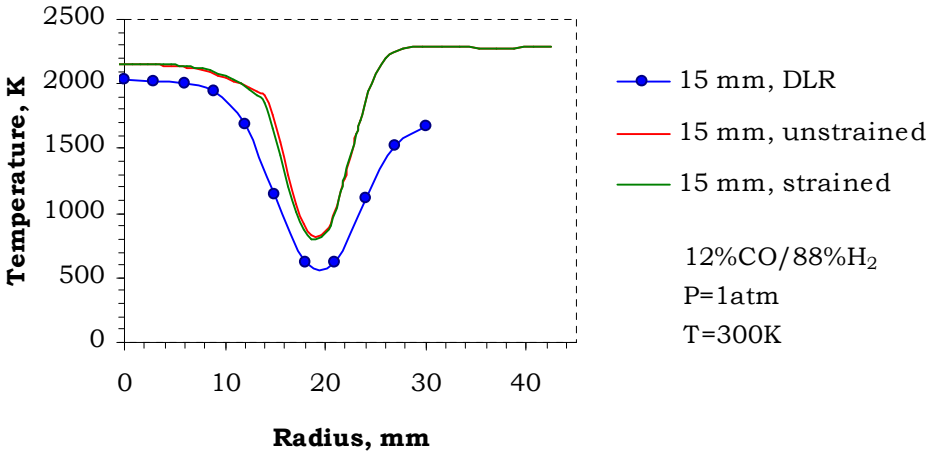

Figure F 23: Predicted temperature profiles for fuel mixture 12%CO/88%H_2 for strained and unstrained flames at 15 mm downstream of the burner nozzle; experimental measurements of methane flame plotted as a reference

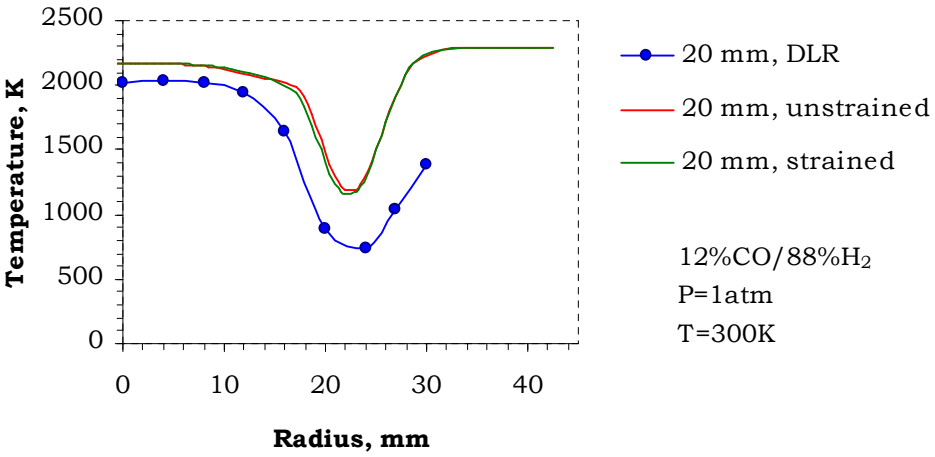

Figure F 24: Predicted temperature profiles for fuel mixture 12%CO/88%H_2 for strained and unstrained flames at 20 mm downstream of the burner nozzle; experimental measurements of methane flame plotted as a reference

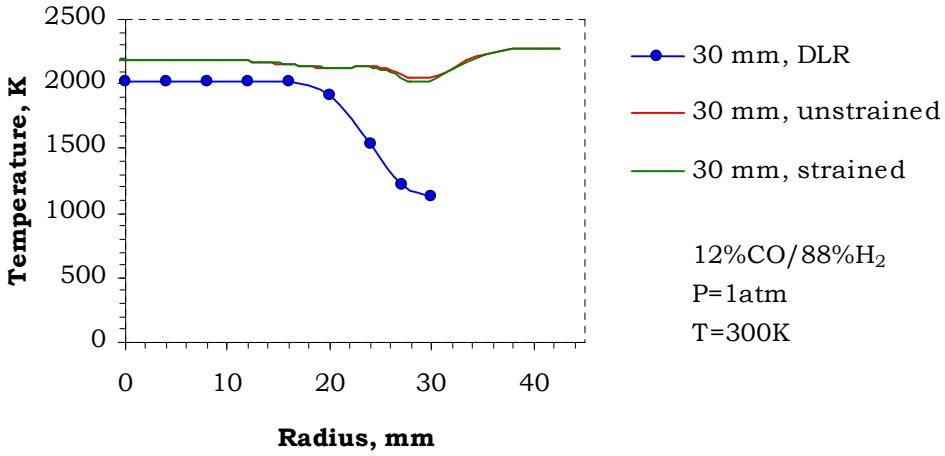

Figure F 25: Predicted temperature profiles for fuel mixture 12%CO/88%H_2 for strained and unstrained flames at 30 mm downstream of the burner nozzle; experimental measurements of methane flame plotted as a reference

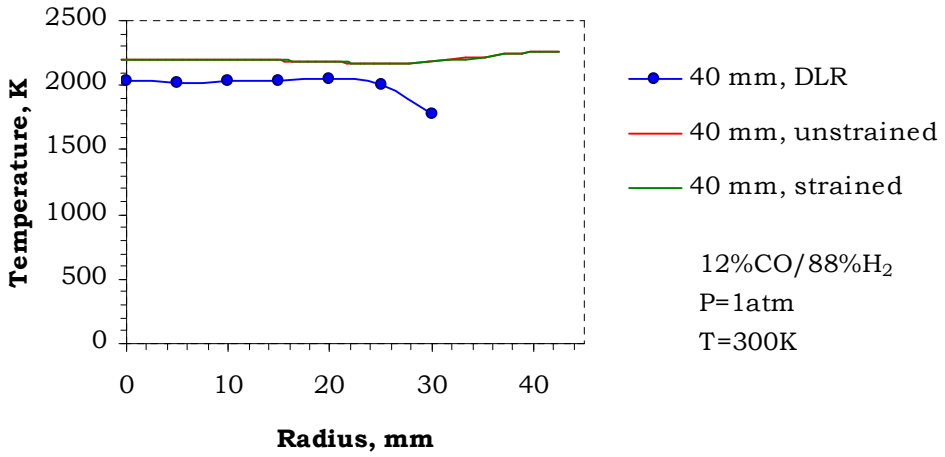

Figure F 26: Predicted temperature profiles for fuel mixture 12%CO/88%H_2 for strained and unstrained flames at 40 mm downstream of the burner nozzle; experimental measurements of methane flame plotted as a reference

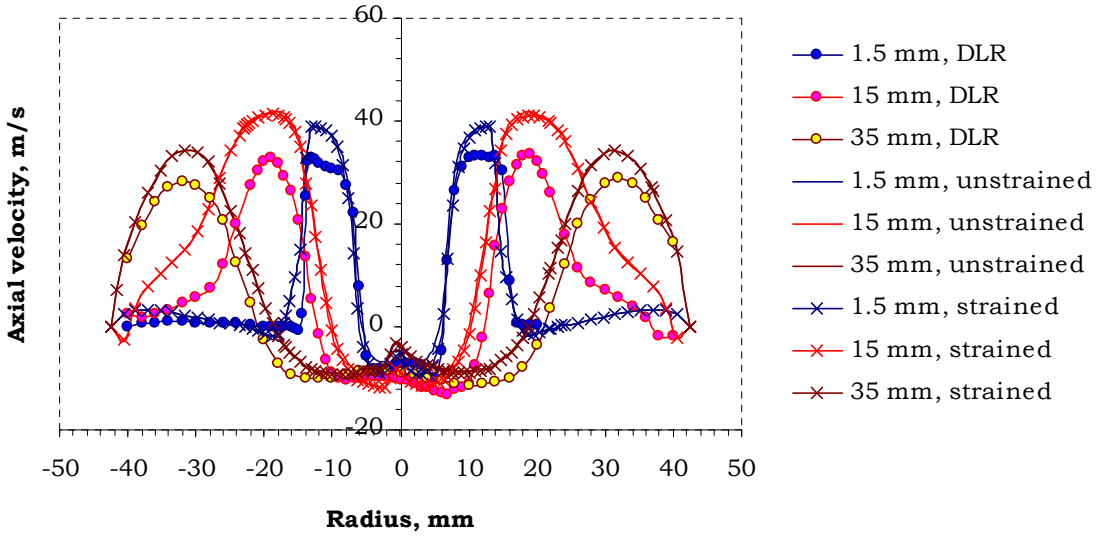

Figure F 27: Predicted axial velocities for 12%CO/88%H_2 fuel mixture compared with experimental measurements for methane

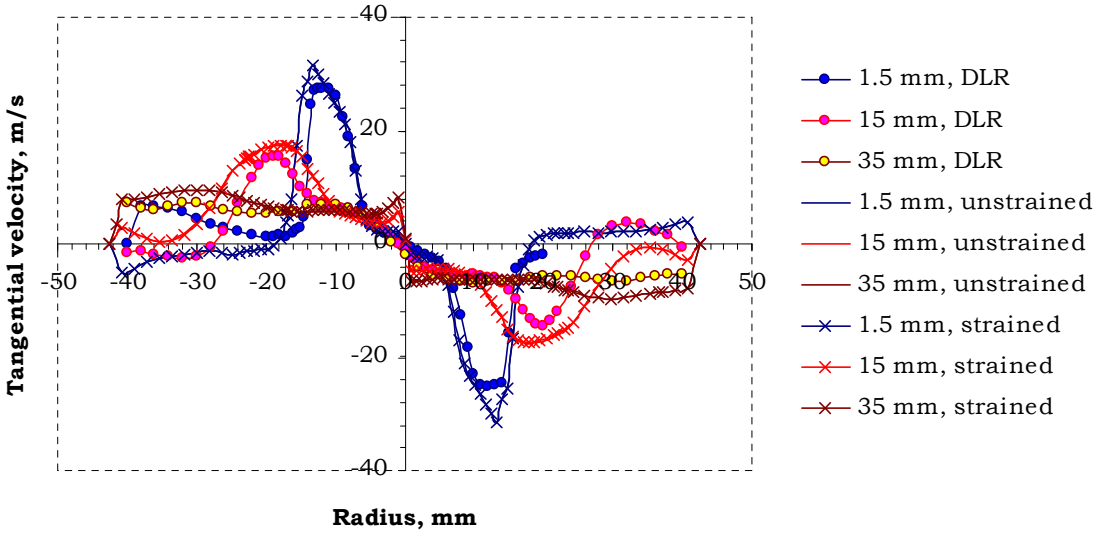

Figure F 28: Predicted tangential velocities for 12%CO/88%H_2 fuel mixture compared with experimental measurements for methane

1.5%CO/28.5%H_2/70%N_2 – second fuel mixture

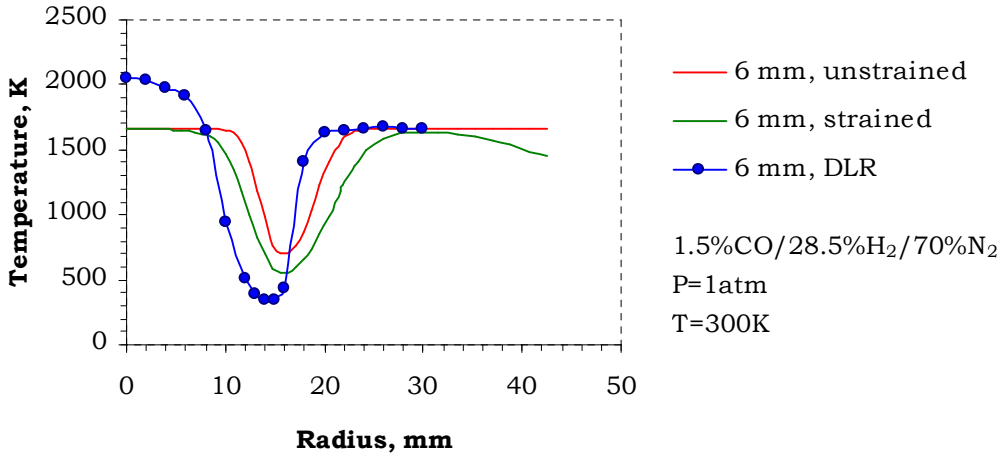

Figure F 29: Predicted temperature profiles for fuel mixture 1.5%CO/28.5%H_2/70%N_2 for strained and unstrained flames at 6 mm downstream of the burner nozzle; experimental measurements of methane flame plotted as a reference

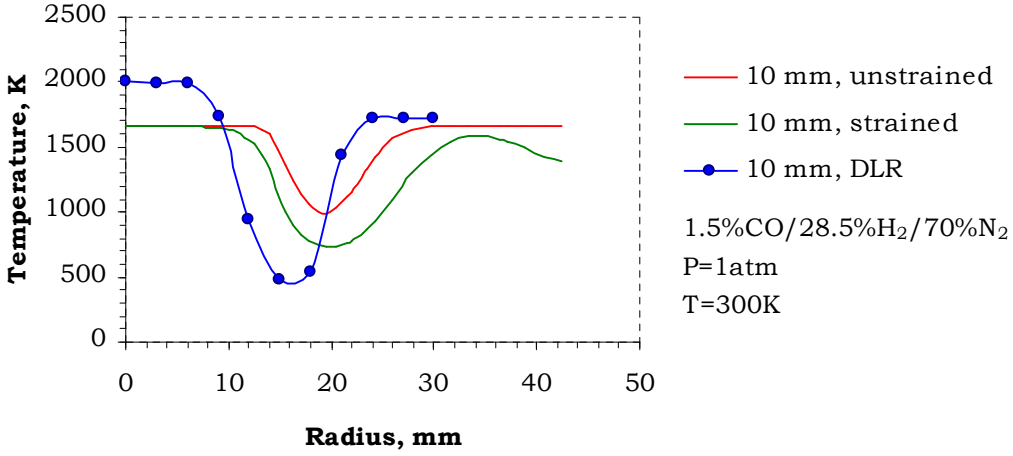

Figure F 30: Predicted temperature profiles for fuel mixture 1.5%CO/28.5%H_2/70%N_2 for strained and unstrained flames at 10 mm downstream of the burner nozzle; experimental measurements of methane flame plotted as a reference

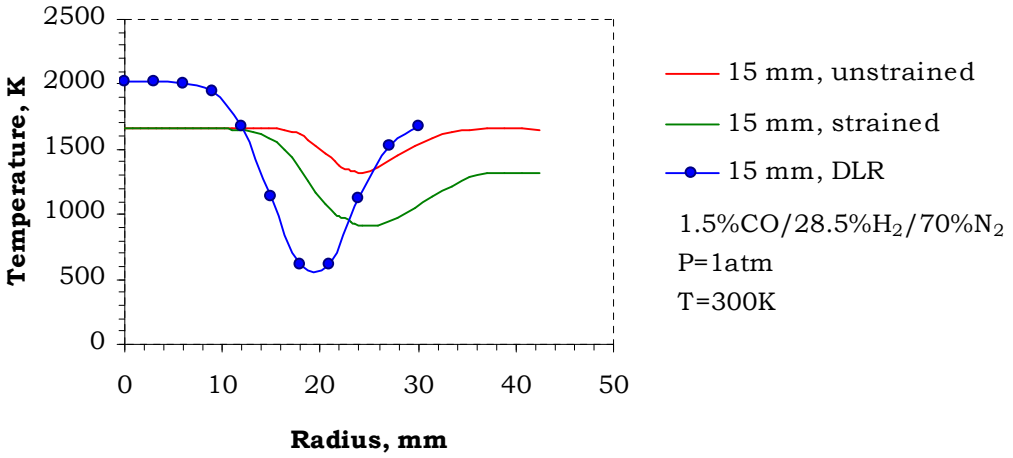

Figure F 31: Predicted temperature profiles for fuel mixture 1.5%CO/28.5%H_2/70%N_2 for strained and unstrained flames at 15 mm downstream of the burner nozzle; experimental measurements of methane flame plotted as a reference

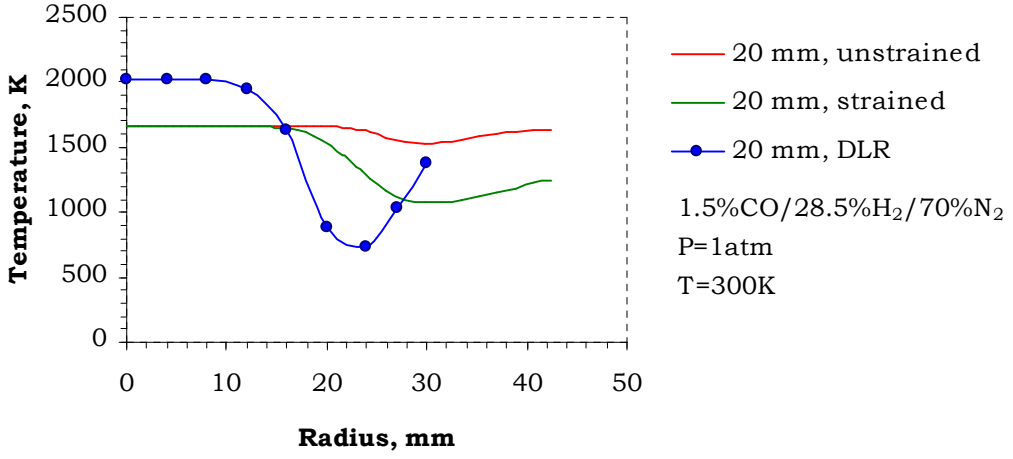

Figure F 32: Predicted temperature profiles for fuel mixture 1.5%CO/28.5%H_2/70%N_2 for strained and unstrained flames at 20 mm downstream of the burner nozzle; experimental measurements of methane flame plotted as a reference

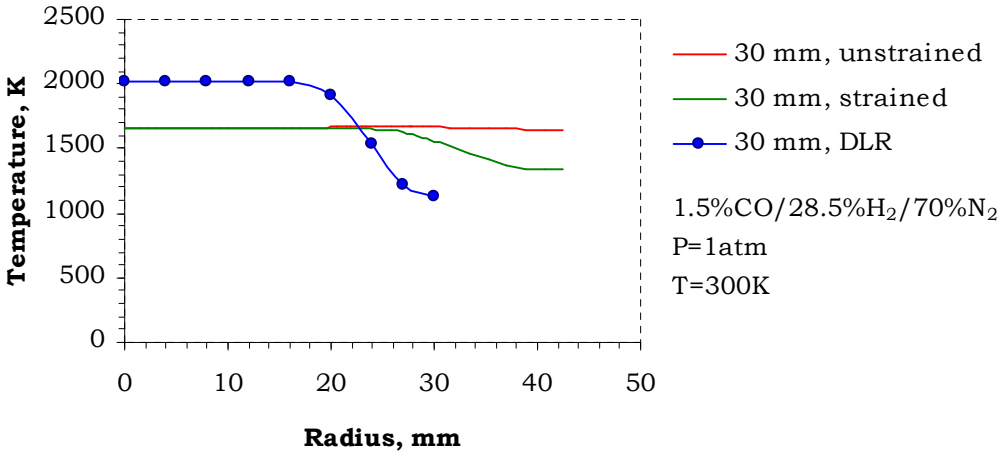

Figure F 33: Predicted temperature profiles for fuel mixture 1.5%CO/28.5%H_2/70%N_2 for strained and unstrained flames at 30 mm downstream of the burner nozzle; experimental measurements of methane flame plotted as a reference

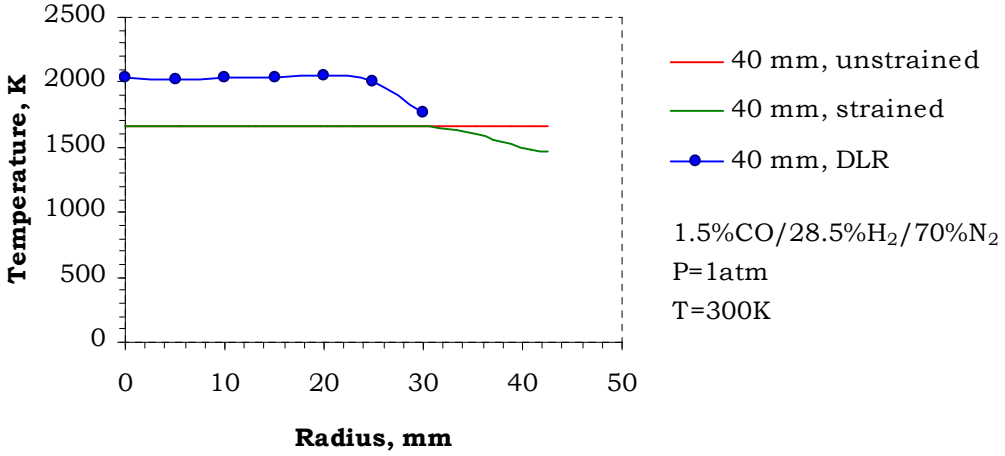

Figure F 34: Predicted temperature profiles for fuel mixture 1.5%CO/28.5%H_2/70%N_2 for strained and unstrained flames at 40 mm downstream of the burner nozzle; experimental measurements of methane flame plotted as a reference

50%CO/50%H_2 – third fuel mixture

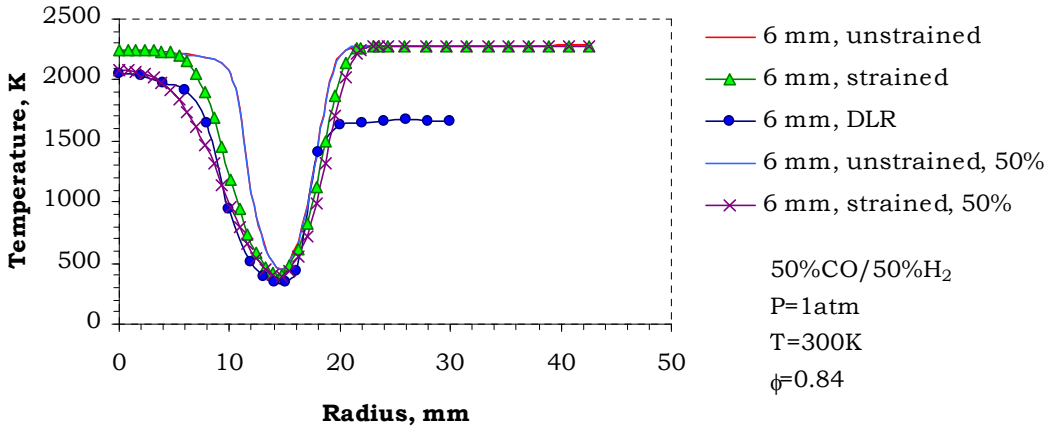

Figure F 35: Predicted temperature profiles for fuel mixture 50%CO/50%H_2 for strained and unstrained flames (50% - increased air mass flow by 50%) at 6 mm downstream of the burner nozzle; experimental measurements of methane flame plotted as a reference

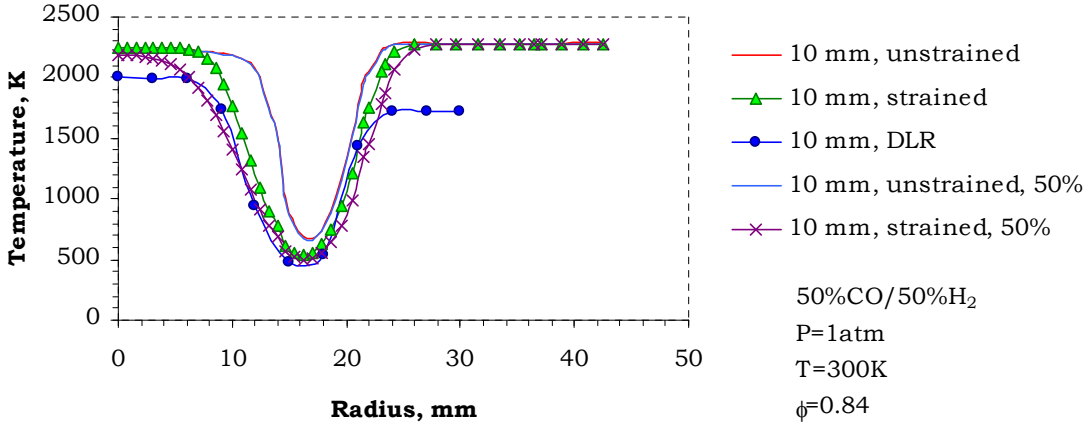

Figure F 36: Predicted temperature profiles for fuel mixture 50%CO/50%H_2 for strained and unstrained flames (50% - increased air mass flow by 50%) at 10 mm downstream of the burner nozzle; experimental measurements of methane flame plotted as a reference

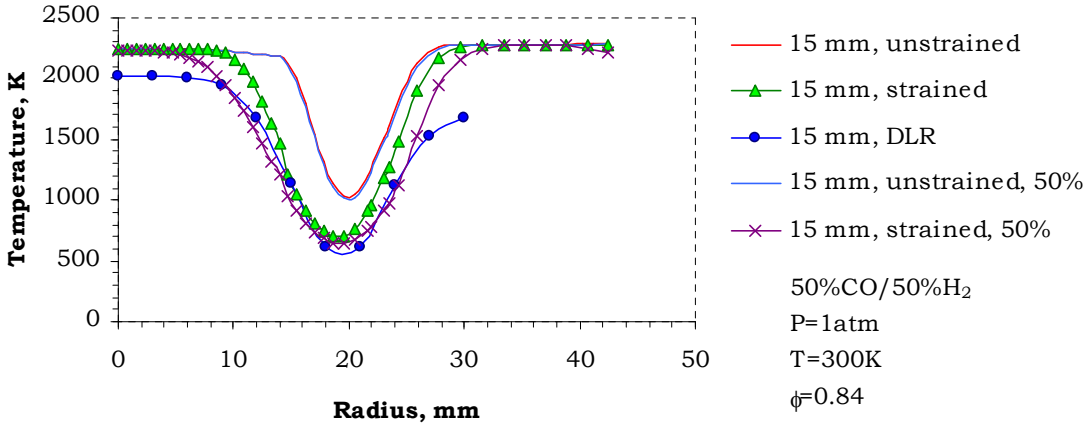

Figure F 37: Predicted temperature profiles for fuel mixture 50%CO/50%H_2 for strained and unstrained flames (50% - increased air mass flow by 50%) at 15 mm downstream of the burner nozzle; experimental measurements of methane flame plotted as a reference

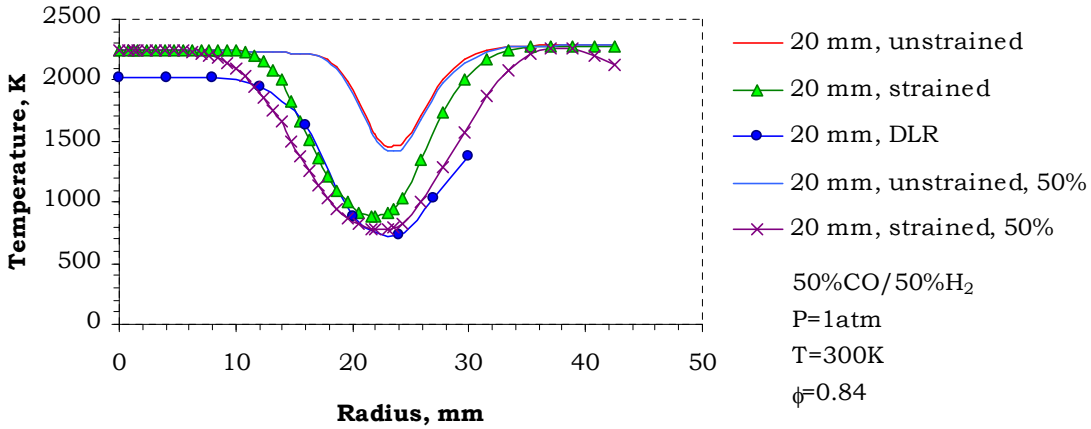

Figure F 38: Predicted temperature profiles for fuel mixture 50%CO/50%H_2 for strained and unstrained flames (50% - increased air mass flow by 50%) at 20 mm downstream of the burner nozzle; experimental measurements of methane flame plotted as a reference

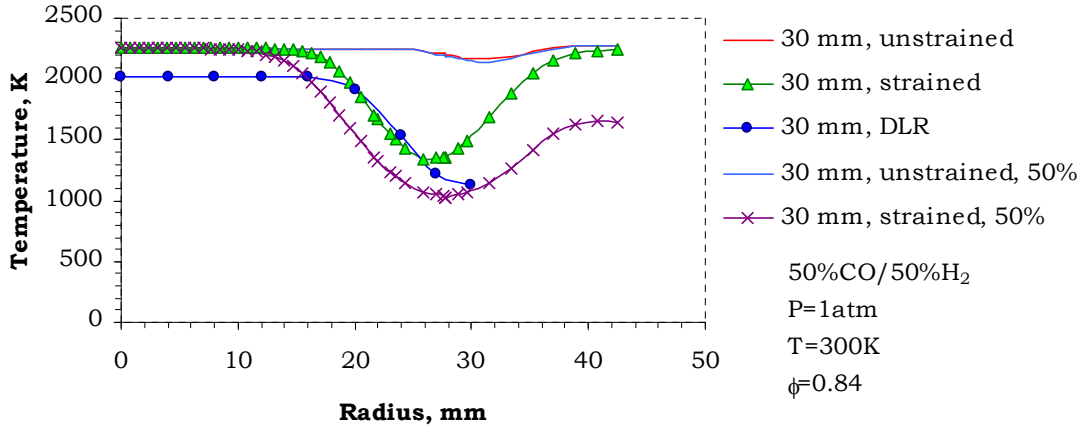

Figure F 39: Predicted temperature profiles for fuel mixture 50%CO/50%H_2 for strained and unstrained flames (50% - increased air mass flow by 50%) at 30 mm downstream of the burner nozzle; experimental measurements of methane flame plotted as a reference

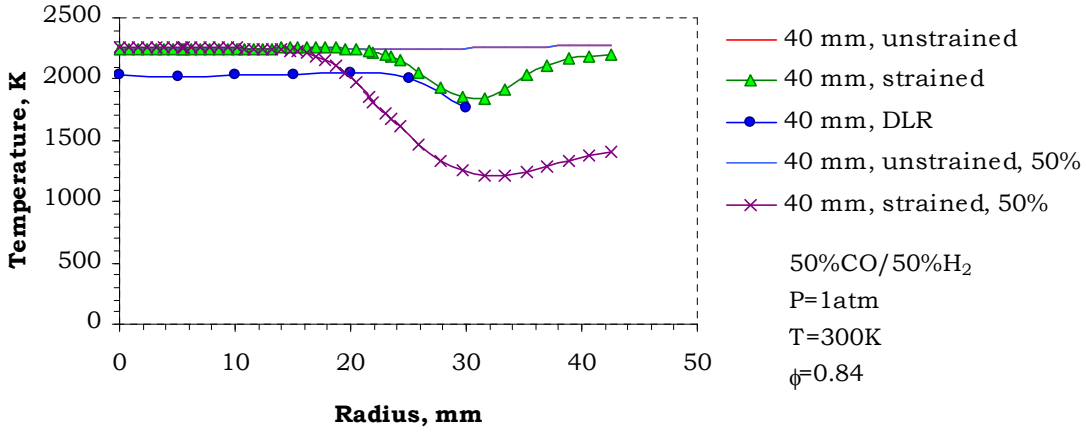

Figure F 40: Predicted temperature profiles for fuel mixture 50%CO/50%H_2 for strained and unstrained flames (50% - increased air mass flow by 50%) at 40 mm downstream of the burner nozzle; experimental measurements of methane flame plotted as a reference

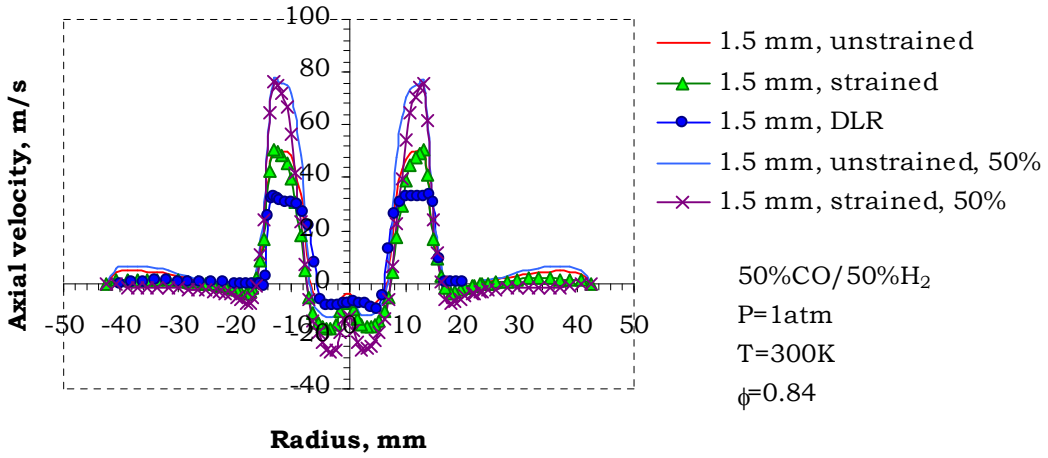

Figure F 41: Predicted axial velocity profiles for fuel mixture 50%CO/50%H₂ for strained and unstrained flames (50% - increased air mass flow by 50%) at 1.5 mm downstream of the burner nozzle; experimental measurements of methane flame plotted as a reference

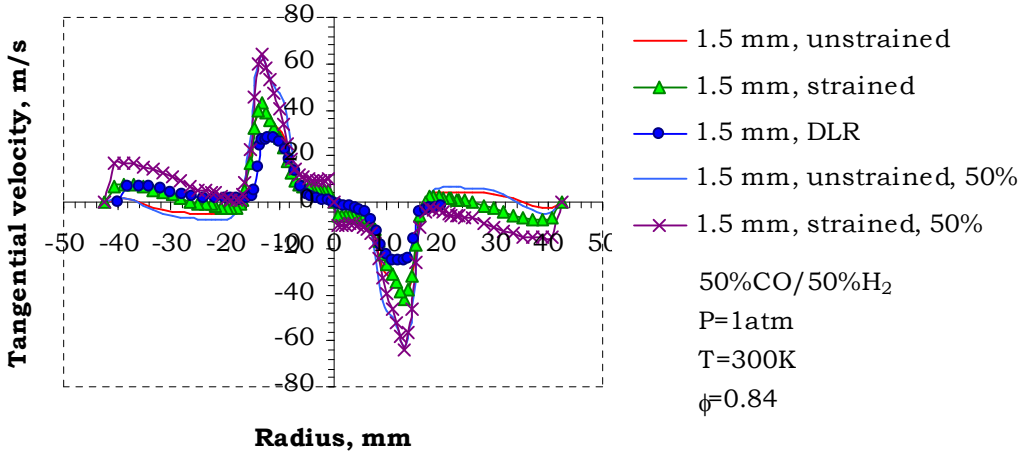

Figure F 42: Predicted axial velocity profiles for fuel mixture 50%CO/50%H₂ for strained and unstrained flames (50% - increased air mass flow by 50%) at 1.5 mm downstream of the burner nozzle; experimental measurements of methane flame plotted as a reference